AN INTEGRATED SOLAR HEAT PUMP SYSTEM FOR COOLING, WATER HEATING AND DRYING

YE SHAOCHUN

NATIONAL UNIVERSITY OF SINGAPORE

2009

AN INTEGRATED SOLAR HEAT PUMP SYSTEM FOR COOLING, WATER HEATING AND DRYING

YE SHAOCHUN

A THESIS SUBMITTED

FOR THE DEGREE OF DOCTOR OF PHILOSOPHY

DEPARTMENT OF MECHANICAL ENGINEERING

NATIONAL UNIVERSITY OF SINGAPORE

2009

ACKNOWLEDGEMENTS

The author wishes to express his sincere appreciation of the guidance and advice given by his supervisor Associate Professor Hawlader M. N. A. The assistance, suggestions as well as the information provided by Professor Hawlader led to his completion of research.

The author is also extremely grateful for the valuable help and generosity from Mr. Jahangeer S/O K. Abdul Halim and Mr. Yeo Khee Ho. Special appreciation must be extended to all lab officers and technicians in the Thermal Division Lab and Engineering Workshop, for the great assistance provided in carrying out the experiment, especially, Mr. Anwar Sadat and Mrs. Roslina Bte Abdullah.

Finally, the author would like to show his thankfulness to his parents and wife, for their patience and support throughout this work.

TABLE OF CONTENTS

SUMMARY

An integrated solar system has been developed to provide water heating, drying and air conditioning. Experiments have been conducted under the meteorological conditions of Singapore to evaluate its performance. Mathematical models for different components and processes are included in a simulation program to predict its performance for different operating conditions. Experimental results were compared with predicted values and good agreement has been obtained. The mathematical model for the evaporator-collector included a 2-dimensional transient approach, where two-phase flow was involved. The system has shown good potential for implementation to commercial and residential applications and would give a new dimension in the process of replacement of conventional energy with renewable energy sources.

The three applications (water heating, drying and air conditioning) can be served simultaneously or independently. A large fraction of the energy requirements is met by a combination of energy collected from the sun, the ambient and the energy recovered from a vapor compression heat-pump system, which serves as an air-conditioner. The presence of evaporator-collector, which is in parallel connection with the room evaporator, enables the system to operate round the clock. The series connection of the water condenser and air condenser ensures complete condensation of the refrigerant before it reaches the expansion valve.

Under the meteorological conditions of Singapore, a series of experiments were conducted to evaluate the system performance. In the full mode operation (water heating, drying and air-conditioning including evaporator-collector), comfortable room conditions were obtained with stabilized room temperatures ranging from 19℃

to23℃; the temperature of 400 liters water in the tank could be raised to 60℃ in 75 minutes and the COP values was found between 4 to 7 with the average of about 5.

Besides the full mode operation, the experiments were also conducted under four more different operation modes with the use of control valves bypassing one (or more) of the four main system components (two condensers and two evaporators), respectively. When the water condenser is bypassed, the moisture content of drying material in the drying chamber can be reduced from 0.9 to 0.09 in 20 minutes in the drying process. When air condenser is bypassed, system performance becomes more sensitive to the water temperature in the water condenser. When the room evaporator for air conditioning is bypassed, heat available from the condensers is highly depended on the heat from solar evaporator collector. The performance of water heating and drying both decline and become sensitive to the solar radiation. When the solar evaporator-collector is bypassed, system performance is not much affected by the meteorological condition, like the other operation modes.

An innovative unglazed solar evaporator-collector with two-phase is developed and utilized in this system. This type of collector can be locally made and relatively much cheaper than the conventional collector. Refrigerant R-134a is used as the working fluid due to the better thermodynamic and environmental performance. A transient two-dimensional mathematical model of the evaporator-collector has been developed to predict temperature distribution and useful energy gain. Both experimental and analytical results show the fact that the two-phase unglazed solar evaporator-collector, instead of losing energy to the ambient, gained a significant amount due to low operating temperature of the collector. As a result, the collector efficiency attains a value greater than 1, when conventional collector equation is used. This analysis shows that the two-phase unglazed solar evaporator-collector

has good potential for application in the tropics.

From the parametric study, it was observed that the ambient temperature, solar radiation, relative humidity, compressor speed, area of evaporator-collector and the temperature of water in water condenser have significant effect on the system thermal performance as well as the evaporator-collector performance.

The results obtained from simulation and experiments are in good agreement under different operation modes. Based on the validated simulation model of the system, an economic optimization was performed to identify the best collector size for a given load and its distribution, using two methods, life cycle savings (LCS) and payback period. The load pattern is determined based on a typical small hotel with the air-con room area of 500 m^2, daily hot water demand of 18m^3 and daily drying demand of 90kg. It was seen that the life cycle saving method lead to the prediction of the optimum collector area of 55 m^2. The payback period method of analyses predicted the optimum collector area of 45 m^2. The minimum payback period is about 1.5 years.

The system shows good potential for implementation in commercial and residential applications and would give a new dimension in the process of replacement of conventional energy with renewable energy sources.

NOMENCLATURE

Abbreviation	Description	Unit
A_c	Collector area	m^2
C	Clearance volumetric ratio	dimensionless
COP	Coefficient of performance	dimensionless
C_F	Fuel Cost	$/MJ
C_D	Collector area related cost	$/MJ.m^2
C_I	Collector area independent cost	$/MJ
C_s	System Cost	$
C_{RF}	Capital recovery factor	dimensionless
C_b	Bond conductance	W/m.K
C_p	Specific heat capacity	kJ/K
D	Bore of compressor	m
D_i	Inner diameter of tube	m
H	Specific enthalpy of refrigerant	kJ/kg
h	Heat transfer coefficient	W/m^2K
h_{fi}	Tube internal heat transfer coefficient	W/m^2K
h_w	Convection heat transfer coefficient	W/m^2K
h_r	Radiation heat transfer coefficient	W/m^2K
i	Discount rate	W/m^2
I	Solar radiation	W/m^2
k	Thermal conductivity	W/m.K
L	Stroke of compressor	m
L_t	Length of tube	m
m	Mass flow rate of refrigerant	kg/s

m_w	Mass flow rate of water	kg/s
M	Mass of water in the water tank	kg
M_c	Moisture content	dimensionless
N	Rotational speed of compressor	rpm
NTU	Number of transfer unit	dimensionless
n	Polytropic index of compressor	dimensionless
P	Pressure	Pa
Q_s	Solar heat gain	MJ
Q_{ac}	Heat gain in air-con room	W
Q_u	Useful energy gain	W
R	Thermal resistance	m^2K/W
S	Absorbed Solar Radiation	W/m^2
t	Time	s
T	Temperature	℃
T_{fi}	Inlet temperature of working fluid	℃
T_a	Ambient Temperature	℃
T_{wo}	Outlet temperature of water	℃
T_{wmax}	Maximum water temperature	℃
U_L	Overall heat transfer loss coefficient	W/ m^2K
V	Volume	m^3
V_a	Velocity of air flow	m/s
V_p	Piston displacement per cylinder	m^3/min
W	Distance between tubes (Pitch)	m
W	Compressor work	W
x	vapor quality	

X_{tt}	Lockhart-Martinelli Parameter	dimensionless
Z_0	Length at which single phase commences	m

Greek Letters

α	Solar absorptance	dimensionless
τ	Transmittance absorptance product	
σ	Stefan-Boltzman constant,	$5.67\times10^{-8}W/m^2K^4$
ε	Absorber surface emittance	dimensionless
ŋ	Efficiency	dimensionless
ρ	Density	kg/m^3
μ	Viscosity	Kg/m·s
ν	Specific volume	m^3/kg
ω	Humidity ratio of air	kg/kg
δ	Thickness of plate	m

Subscripts

a	air
c	collector
db	dry bulb
i	inlet
o	outlet
r	refrigerant
tp	Two-phase
v	vapor
w	water
wb	wet bulb

LIST OF FIGURES

LIST OF TABLES

CHAPTER 1 INTRODUCTION

1.1 Background

In view of the growing global energy needs and concern for environmental degradation, the possibility of running thermal system using the energy from the sun has been receiving considerable attention in recent years. Solar energy is clean and almost inexhaustible of all known energy sources. The low temperature thermal requirement of a heat pump makes it an excellent match for the use of solar energy. A combination of solar energy and heat pump system can bring about various thermal applications for domestic and industrial use, such as water heating, solar drying, space cooling, space heating and refrigeration. Unlike thermosyphon solar water heaters, solar heat pump systems offer opportunity to upgrade low-grade energy resources from the surroundings as well as solar energy and make use of it for domestic and industrial applications [1].

The concept of direct expansion solar-assisted heat pump (DX-SAHP) was first proposed in an experimental study by Sporn and Ambrose [2]. Based on these studies, Chaturvedi and Shen [3] performed an investigation on the steady state thermal performance of a DX-SAHP and indicated that this system offers significant advantage in terms of superior thermal performance.

Approximately, half of the primary energy is consumed in water heating, air conditioning and laundry drying in urban households. A conventional vapor compression air-con system throws the heat from a heat source (air-con room) to the ambient without making an effort to recover it. Furthermore, the performance of a conventional heat pump system is greatly limited by the heat source.

In this study, an attempt has been made to recover the heat from condenser(s) and utilized it for water heating and drying applications by developing a solar-assisted heat-pump system.

The major components of this system are solar evaporator-collector, room evaporator, water cooled condenser, air cooled condenser, expansion valves and compressor. R-134a is used as working fluid due to the environmental and thermodynamic considerations. In the present study, two evaporators, connected in parallel, can increase the system cooling and heating coefficient of performance (COP) significantly. One of the evaporators performs as solar collector which absorbs solar radiation and ambient energy; while the other evaporator performs as an air conditioner and absorbs heat from a space for cooling purpose, which means space cooling. The energy from these two heat sources, plus the energy added by compressor, is used for water heating and air heating used in this application for clothes drying. Hence, the solar assisted heat pump system performs as a water heater, clothes dryer and air conditioner.

The solar evaporator-collector is an essential component in a SAHP, because it is the only component which can absorb solar radiation. In conventional solar heating system, the solar collector is glazed or evacuated to reduce the heat loss to the ambient. The complex structure of the glazed or evacuated solar collector makes the whole solar system more expensive. The first two-phase collectors developed by Sporn and Ambrose [2] were double glazed. They used double glazed collector which also act as evaporator for the heat pump with R-12 as the working fluid. They found that removal of glazing or back insulation did not affect performance of collector significantly. This could probably be attributed to refrigerant used and the meteorological conditions of Arizona, where the relative humidity is low.

The collector operating temperature in a solar-assisted heat pump system can be lower than the ambient temperature. In this case, an un-glazed solar evaporator collector is used. The simple structure of the un-glazed solar collector makes it an economical type of solar collector. However, its performance is highly dependent upon the environment, because its surface is exposed directly to the ambient. To improve the performance of un-glazed solar collector, a clear understanding of influence of the environment is required.

An unglazed two-phase collector without any insulation was first used in the heat pump system developed by Franklin et al. [4]. Chaturvedi et al. [5, 6] found a variation of the evaporator temperature from 0°C to 10°C above the ambient temperature under favorable solar conditions. Many authors [7-9] reported that, for the ambient temperature of above 25°C, the evaporator could be operated at an elevated temperature. Hawlader et al. [1] performed analytical and experimental studies on a solar-assisted heat pump using unglazed evaporator-collector, using a steady-state one-dimensional mathematical model.

However no one has investigated the effect of condensation phenomenon caused by high relative humidity (RH) on the surface of un-glazed solar collector. The effect of condensation on the collector performance was investigated in this study. A transient two-dimensional mathematical model of the evaporator- collector has been developed to predict temperature distribution and useful energy gain. A series of experiments were performed under the meteorological conditions of Singapore to validate the model.

Two models are most widely used for calculating pressure drop in two-phase flow. They are Martinelli Nelson's method for separated flows and Owen's homogeneous

equilibrium model for misty or bubbly flow [10]. The homogeneous equilibrium model is simple in determining the pressure drop in two-phase flow.

1.2 Objectives

The objectives of the present work are as follows:

1. To develop and construct a solar assisted heat-pump system for air-conditioning, water heating and drying;
2. To conduct a series of experiments under the meteorological conditions of Singapore to evaluate the system performance;
3. To develop appropriate mathematical models for different components of the system, especially a two-dimensional transient mathematical model of the unglazed solar flat plate evaporator-collector;
4. To developed a simulation program to predict the performance of the system and validate it by the experimental data;
5. To compare predicted results with experimental values for the purpose of validation;
6. To optimize the systems to determine the optimum size of a system for different applications.

1.3 The scope

The thesis starts with an introduction of the present work in Chapter 1. Chapter 2 presents a literature review. Description of experimental setup and procedure are included in Chapter 4. The mathematical model and simulation work are introduced in Chapter 4. Chapter 5 shows an analysis of results and discussion. Lastly, conclusions are made in Chapter 6.

CHAPTER 2 LITERATURE REVIEW

This chapter includes a comprehensive literature review of the previous work on solar-assisted heat pump system.

2.1 Solar heat pump system

Over the last decade, a number of investigations have been conducted by researchers for the design, modeling and testing of solar-assisted heat pump systems (SAHPS) [1, 3, 11-17]. These studies undertaken on solar heat pump systems can be broadly classified into three groups: (i) SAHPSs for water heating [1, 12, 14, 18-23], (ii) SAHPSs with storage (conventional type) for space heating [13, 15, 17, 24-33], (iii) SAHPSs with direct expansion for space heating [12, 34-37] .

2.1.1 SAHPSs for water heating

Chaturvedi et al. [12] investigated a variable capacity direct expansion SAHPS, which was used for domestic hot water application. This system employs a bare solar collector, which acts as the evaporator of the system. A variable frequency drive modulates the compressor speed to maintain a proper matching between the heat pump capacity of the compressor and the evaporative capacity of the collector under widely varying ambient conditions. Their experimental results indicated that the coefficient of performance of the system can be improved significantly by lowering the compressor speed as ambient temperature rises from winter to summer.

The characteristic of an integral-type solar-assisted heat pump (ISAHP) was investigated by Huang and Chyng [18, 19]. An ISAHP system with a 105-liter water

storage tank using a bare collector and a small reciprocating-type compressor with input power of 250W was built and tested in the study. It consisted of a Rankine refrigeration cycle and a thermosyphon water heating loop that were integrated together to form a package heater. Solar energy and ambient energy were absorbed at the collector/ evaporator and pumped to the storage tank. A performance model was derived and found to be able to fit the experimental data very well for the ISAHP by these investigators. The COP values for the ISAHP built in the study were in the range 2.5–3.7 depending on the water temperatures. The highest COP value in the tests was 3.83 [18].

Chyng et al. [14] conducted a system simulation study of an ISAHP water heater. Their model assumed a quasi-steady process for all the components in the system except the storage tank. The simulation results agreed well with the experimental values. The COP values were found higher than 2.0 for most of the time in a year and the daily operating time varied from 4 to 8 hours. The analysis indicated that the expansion device does not need to be controlled online. Using the 1-year simulation results, a universal daily performance correlation of the system was derived.

A long-term reliability test was carried by Huang and Lee [20] on an ISAHP system. The prototype has been running continuously for more than 13,000 hours with a total running time larger than 20,000 hours during the 5 years. The measured energy consumption was 0.019 kWh/L of hot water at 57℃ that was less than the backup electric energy consumption of the conventional solar water heater, which ranges from 0.02 to 0.05 kWh/L.

Hawlader et al. [22], Hawlader and Jahangeer [23] designed, fabricated, and tested a

SAHP dryer and water heater. They investigated the performance of the system under the meteorological conditions of Singapore. The system consisted of a variable-speed reciprocating compressor, evaporator-collector, storage tank, air-cooled condenser, auxiliary heater, blower, dryer, dehumidifier, and air collector. The drying system was designed in such a way that some of the components could be isolated depending on the weather conditions and usage pattern. A simulation program was also developed to evaluate the performance of the system and the influence of different variables by these researchers. The values of COP obtained from the simulation and experiment varied between 5 and 7, whereas the SF values of 0.61 and 0.65 were obtained from the simulation and experiment, respectively.

2.1.2 SAHPSs with storage (conventional type) for space heating

Badescu [17, 25, 26] studied on model of a sensible heat thermal energy storage (TES) device integrated into a SAHPS for space heating and performed first law (energy) and second law (exergy) analysis of this system. He found that both the heat pump COP and exergy efficiency decreased when increasing the length of thermal energy storage. Also, the monthly thermal energy stored by this unit and the monthly energy necessary to drive the heat pump compressor increased by increasing this unit length. Besides this, his preliminary results indicated that the photovoltaic array could provide all the energy required by the heat pump compress or, if an appropriate electrical energy storage system would be provided.

Yamankaradeniz and Horuz [13] investigated the characteristics of a SAHP both analytically and experimentally for clear days during the 7 months of the winter season in Istanbul, Turkey. They developed a heoretical model and a computer program was written on this basis. The characteristics such as, daily average

collector efficiency and solar radiation, monthly average heat transfer at the condenser, monthly average cooling capacity, and COP were examined.

Huang et al. [27] studied analytically the thermal performance of two different schemes of SAHPSs. In the first scheme, the evaporator of the heat pump is taken directly as the solar collector and always maintained at the ambient temperature. As there is no heat loss from the collecting plate, the thermal efficiency of the collector is high and equals the solar absorptivity of the collecting plate. In the second scheme, the evaporator is placed in a novel fresh water solar pond/tank with high efficiency. Since the evaporator operates at a relatively high temperature, the COP value is increased. Their calculation results indicated that the COP of a SAHPS using the second scheme was considerably higher than that of the first scheme.

Yumrutas and Kaska [31] designed, constructed and investigated an experimental SAHP system for space heating with a daily energy storage tank to evaluate its performance. The heating system basically consisted of a plate solar collector, a heat pump, a cylindrical storage tank, measuring units, and a heating room located in Gaziantep, Turkey (37.181N). The effects of climatic conditions and certain operating parameters on the system performance were studied by these authors. They found that COP was about 2.5 for a lower storage temperature at the end of a cloudy day and it was about 3.5 for a higher storage temperature at the end of a sunny day, and it fluctuated between these values in other times.

Kaygusuz [28-30] investigated the performance of a combined solar heat pump system with energy storage in encapsulated phase change material (PCM) packing for residential heating in Trabzon, Turkey. An experimental set-up was constructed. The experimental results were obtained from November to May during the heating

season for two heating systems. His experimental studies indicated that the parallel heat pump system saved more energy than the series heat pump system, because it used both air and solar as a heat source for evaporator while the series system used only solar energy.

Axaopoulos et al. [24] conducted a comparison of the performance of a SAHPS with that of a conventional thermosyphon solar system (CTSS). Their experimental studies were monitored from 1993 to 1997 during summer and winter periods. The performance of CTSS was seriously affected by weather conditions, whereas SAHPS could always operate with no significant variation and with a COP above 3.0. A comparison between the two systems proved the performance of the SAHPS to be better than that of CTSS under all climatic conditions.

Yumrutas et al. [33] investigated the annual performance of a SAHPS with seasonal underground energy storage and the annual water temperature distribution in the storage tank using an iterative computational procedure based on the analytical solution of the problem. It appeared that the heating system was a technically realistic alternative to fossil fuel-fired systems. The results showed that earth type and system size had considerable effects on the system performance.

Kuang et al. [15] carried out an experimental study of SAHP performance and concluded that the thermal storage tank was an important component in solar heating systems, which could modulate the mismatch between solar radiation and the heating load. In this system, the tank temperature was so close to ambient air temperature that its heat loss to the surroundings was very low. As a result, good insulation of the water tank was not critical. An auxiliary energy source was necessary for the SAHP system. It was analyzed and demonstrated that the use of

an auxiliary heater inside the storage tank resulted in wastage of energy due to the large heat loss from the storage tank. Hence, the auxiliary energy consumption was higher. The use of an auxiliary heater at the load point was economically feasible.

2.1.3 SAHPSs with direct expansion for space heating studies

Torres-Reyes et al. [38] and Cervantes and Torres Reyes [39] studied both analytically and experimentally a SAHP, with a direct expansion of the refrigerant within the solar collector and performed a thermodynamic optimization. The maximum exergy efficiency, defined as the ratio of the outlet to the inlet exergy flow in every component of the heat pump cycle, was determined taking into account the typical parameters and performance coefficients.

Aziz et al. [34] conducted the studies on thermodynamic analysis of two-component, two-phase flow in solar collectors with application to a direct-expansion SAHP. Their results showed that changes in the mass-flow rate and absorbed solar heat flux had significant effects on the collector tube length and refrigerant heat transfer coefficient. Variations of the tube inlet diameter and collector pressure had a negligible effect on the collector size, but a significant effect on the heat transfer coefficient.

The increase in the vapor quality of the refrigerant mixture was gradual over the major length of the tube, with a rapid rise taking place near the end of the tube. The method used in this study can be easily extended to incorporate matching between the collector size and compressor heat-pumping capacity.

2.2 Two-phase flat plate solar collector

Literature review for two-phase solar collector in heat pump system will include the following areas:

- System analysis and modeling;
- System design and parameter optimization;
- Properties of two-phase flow refrigerant mixture.

2.2.1 System analyses and modeling

Two phase flow in collectors was first considered by Sporn and Embrose [2]. They used double glazed collector which also act as evaporator for the heat pump with R-12 being the working fluid. They did not demonstrate the full potential of the concept due to a mismatched, oversized compressor. They also did experiments by removing the glazing and found that the removal did not affect the performance significantly. They found that removal of glazing or back insulation does not affect performance of two-phase flow solar collector significantly.

In the two-phase flow literature, two models of calculating pressure drop are most widely used and they are known as Martinelli Nelson's method for separated flows and Owen's homogeneous equilibrium model for misty or bubbly flow [40]. The homogeneous equilibrium model is the simplest method determining the pressure drop in two-phase flow and makes the basic assumption that the two phases have the same velocity.

Adopting an equilibrium, homogeneous, two-phase model mentioned above, Chaturvedi et al. [41] carried out preliminary theoretical performance studies

concerning a solar-assisted heat pump that uses a bare collector as the evaporator. The analysis was subject to limitation of a constant temperature evaporator with no superheating or sub cooling.

The first comprehensive work on two-phase solar collector was carried out by Soin et al. [7]. They investigated the thermal performance of a thermosyphon collector containing boiling acetone and petroleum ether and developed a modified form of the Hottel-Whillier-Bliss equation (HWB) [42] to account for the fraction of liquid level in the collector with glazed. The steady-state thermal efficiency η_B containing a modified heat-removal factor F_R, in HWB equation, for two-phase solar collector was firstly defined by Al-Tamimi and Clark [8], accounting for the boiling and the sub cooled portions of the collector. They conducted a detailed study of flow boiling in solar collector [9]. They developed an analytical model to investigate the effect of sub cooling the liquid entering the collector and the level of fluid in the collector on collector efficiency. They defined Z* to be the fraction of the collector required to heat the fluid to its boiling temperature. Mainly based on the results of Al-Tamini and Clark's [8] research, ASHRAE 109-A test standard for two-phase solar collectors was established in 1984 [43]. This standard defined five sets of conditions for two-phase collector thermal efficiency.

Ahmed et al. [44] developed and defined a new generalized heat removal factor, Fs and a new overall thermal loss coefficient, U_L for two-phase flat-plate collector. Further modification on U_L was done by them [45]

First steady-state system simulations was made with TRNSYS by Freeman et al. [46]. The first thermodynamic model to analyze two-phase solar collector was developed by Chaturvedi et al. [5]. The equilibrium homogeneous theory was used to model

the two-phase flow in solar collectors.

O' Dell et al. [47] developed a design method for heat pumps with refrigerant filled solar collectors. They obtained the heat gain at condenser and the COP as function of evaporation temperature.

Numerical calculations of the collector efficiencies for double-glazed two-phase flat-plate collector employing R-11 were carried out by Kishore et al. [48]. They firstly express the collector efficiency as a function of the saturation temperature and liquid level by combining their experimental data. Ramos et al. [49] also carried out theoretical investigation on two-phase collectors assuming laminar homogeneous flow and experimentally confirmed by them. Mathur et al. [50] developed a method calculating boiling heat transfer coefficient in two phase thermosyphon loop. The first detailed model for boiling solar collector using TRNSYS was developed by Price et al. [51].

All the modeling or methods of analyses described earlier assume homogeneous flow in two-phase mixture. The first theoretical model concerning non-homogenous for two-phase flow thermosyphon in the collector and condenser was carried out by Yilmaz [52]. His results show that homogenous model is not sufficient to describe the two phase flow in the collector. Variation of the properties of the working fluid and water with temperature are taken into account.

Considering the effect of long-wave radiation and wind speed, a modified form of the Hottel-Whillier-Bliss solar collector efficiency function for unglazed solar collector characterization is investigated by Morrison and Gilliaert [53].

Using the approach of element analyze of the steady one-dimensional two-phase energy conservation equations, a mathematical model for natural circulation

two-phase solar collector with cover was developed by Radhwan et al. [54]. Torres Reyes et al. [36] conducted the first exergy analysis on a solar-assisted heat pump with two-phase collector-evaporator. They analyzed and experimentally confirmed that the largest irreversibilities in SAHP system occurred in collector-evaporator because a significant fraction of the total solar radiation absorbed is poorly employed. Similar investigation and results were obtained by Cervantes [35].

Most of the researches before 1999 were for steady-state in two-phase flow. Hussein was the first to theoretically and experimentally investigate a two phase closed thermosyphon flat plate solar collector under transient conditions [55]. He improved the model in 2002 [56].

2.2.2 System design and parameter optimization

The first two-phase collectors developed by Sporn and Embrose [2] were double glazed. Bare two-phase collector without any insulation was firstly used by Franklin et al. [25] in heat pump system. But the data was so limited that no definite conclusion could be drawn.

Freeman et al. [46] analytically investigated the influence of collector area, number of glazing, main storage volume to collector area ratio, and heat pump coefficient of performance by using his simulation model developed in TRNSYS. Chaturvedi et al. [3] designed a direct expansion solar assisted heat pump, in which a bare flat plate collector also acted as the evaporator for the refrigerant, Freon-12. The COP and the solar collector efficiency ranged from 2.0 to 3.0 and from 40% to 70%, respectively. Similar experimental result were obtained by Morgan et al. [11].

Detailed effect of collector cover was investigated by O′ Dell et al. [47]. They found

that uncovered collector heat pump systems have better performance than both conventional air-source heat pumps and covered collector heat pump systems over a wide range of collector areas for space heating. However, Krakow et al. [57] found that, for cold climates (mean daily temperature varies between -10C and -6C), solar source direct expansion heat pump systems with glazed solar collectors are preferable to systems with unglazed solar collectors. Chaturvedi et al. [58] further investigated the effects of various parameters on direct expansion solar heat pump system performance [29]. He concluded that the long-term performance of the system is governed strongly by collector area, compressor RPM, load temperature and refrigerant, while the remaining parameters have only weak influence.

Chaturvedi et al. [5] concluded that the overall performance of the heat pump system with two-phase solar collector depends largely on the proper match between the heat pumping capacity of the compressor and the evaporation of the collector. He indicated that the increase of collector area for a given compressor results in improved COP and depressed collector efficiency. A dual RPM compressor used by Krush [59] in 1980 was for the first time to achieve capacity control by matching the heat pump output and the load. A variable capacity direct expansion solar assisted heat pump developed by Chaturvedi et al. [12] could maintain the collector–evaporator temperature in the design range by using compressor capacity modulation.

Reviews of the development of heat pumps with direct expansion solar collectors were done by Shinobu et al. [60] and Ito [61]. Series of advantages of two-phase solar thermosyphon are summarized by Pluta et al. [62]. Day et al. [63] classified SAHP system to parallel, series and dual system and found that series system has the highest COP.

First detailed analysis on the effect of evaporator-collector geometry on SAHP system performance is conducted by Ito et al. [64]. His results indicated that COP is only reduced by 4% if the pitch of refrigerant tube soldered to the copper plate changed from 100mm to 190mm and COP reduced little if the 1mm thickness copper plate replaced by 0.5 thickness.

Joudi et al. [65] was the first to investigate the influence of system loading on the performance of two-phase thermosyphon solar cycle. Different kinds of complicated load patterns were used in his research.

Huang et al. [19] developed a new type of solar assisted heat pump by integrating a Rankine refrigeration cycle and a water thermosyphon loop using R-134a as the refrigerant. The COP lies in the range 2.5–3.7 at water temperature between 61 and 25C. Hawlader et al. [1] experimentally and theoretically analyzed a direct expansion solar assisted heat pump using R-134a. A variable speed compressor was used to ensure proper match between the collector–evaporator load and the compressor capacity. Their results show that the performance of the system is influenced by the area of the collector, the speed of the compressor and the solar irradiation. The COP lies in the range 4–9 at water temperature between 30 and 50℃

Chata et al. [16] developed a graphical procedure for several refrigerants for sizing the solar collector area and the heat pump compressor displacement capacity.

2.2.3 Properties of two-phase flow refrigerant

Effects of fluid properties and pipe diameter on two-phase flow patterns in horizontal flow was investigated by Weisman et al. [66] in 1978. The fluid properties studied by them are liquid viscosity, liquid density, interfacial tension and gas

density. The pipe diameter varied from 1.2 to 5 cm. They presented dimensionless correlations which fit the experimental data well.

Most of research before 1987 used refrigerant R-12 or R22 as the working fluid[67]. An international treaty [68], named "The Montreal Protocol on Substances That Deplete the Ozone Layer", was adopted to protect the ozone layer by phasing out the production of a number of substances believed to be responsible for ozone depletion. The proposal was opened for signature on September 16, 1987 and came into force on January 1, 1989. It announced that, as a result of the ban on R-12 due to the Montreal agreement, the results from studies before 1987 are of a very limited value and studies using newly proposed refrigerants need to be conducted. As one of the most promising alternative for R-12 or R22, R134a has been paid much attention from 1990's till now.

Eckels and Pate [69] firstly obtained the heat transfer data for R-134a during two-phase flow in a short tube. The evaporation and condensation heat transfer coefficients for R-134a were 35-45% and 25-35% increase over R-12, respectively. Hambraeus [70] was the first to discover that oil free R134a's heat transfer coefficient is higher than R-22 and continue to decrease with increase of oil content. Torikoshi et al. [71] investigated the heat transfer and pressure drop characteristics of R134a in a short horizontal heat transfer tube and compared to those of R32 and a mixture of R32/R134a inside tubes [72]. Wattelet et al. [73] compared the evaporative characteristics of R-134a, MP-39, and R-12 at low mass fluxes in a short tube. Murata et al. [74] measured heat transfer coefficient and pressure drop of a mixture of R123 and R134a in both smooth and spirally grooved short tubes.

The first detailed experimental investigation of two-phase flow of a mixture of

R-134a with PAG oil through short tube was completed by Kim et al. [75]. He also proposed a semi-empirical model of two-phase flow of refrigerant-134a through short tube orifices [76]. Bassi et al. [77] investigated the in-tube condensation of mixture of R134a and ester oil. He obtained an empirical correlation for the properties of R134a for two-phase flow.

All the experimental results on R134a mentioned above were obtained using short tube. Liu [78] investigated R-134a heat transfer coefficient and pressure drop using a 10.8m long tube. He found that the heat transfer coefficient for R-134a decreased for mass velocity above 270kg/m^2.s.

Natan et al. [79] theoretically analyzed a system of two parallel pipes with common inlet and outlet manifolds that undergoes a process of heating and evaporation. The results show that the solution is not unique and one can obtain multiple solutions even for the case of equal heating of the two pipes. Minzer et al. [80] checked experimentally the validity of the simulation results of multiple steady state solutions presented by Natan et al. [79]. Choi et al. [81] developed a generalized correlation for the prediction of R134a flow rate through short tube and confirmed it through a set of experiments.

Applying the R134a to the whole solar assisted heat pump system, Abou-Ziyan et al. [82] found that R-134a is better than R-404a to replace R-22 for low temperature applications. Aziz et al. [34] extend the experimental analysis to a mixture of R123 and R134a. Esen et al. [83] conducted the experimental investigation of a two-phase closed solar thermosyphon system. Three identical small-scale solar water heating systems, using refrigerants R-134a, R407C, and R410A, were tested and the results were compared.

In the latest research on R-134a two-phase flow in solar heat pump system was conducted by Chata et al. [16], where a computer program [84] was employed to predict the refrigerant properties involved in the energy balance across the collector. A graphical procedure for several refrigerants (including R134a) for sizing the solar collector area and the heat pump compressor displacement capacity was proposed.

2.3 Economic Analyses

An economic analysis was performed based on several figures of merit such as, annualized system cost, net life cycle savings, payback period, internal rate of return, and a few others.

Wijeysundera and Ho [85] have shown that the above four methods can be broadly grouped into two. The annualized system cost and the net life cycle savings methods of analyses lead to identical optimum conditions, predicting the same collector area, as shown in a later section. Similarly, the payback period and internal rate of return lead to an exactly identical expression for the optimum condition.

Barley and Winn [86], Brand- emuehl and Beckman [87], and Lunde [88] have used life cycle savings as the figure of merit in the optimization of solar systems. Chang and Minardi [89] used annualized system cost as the optimization criteria for a solar hot water system. In the life cycle savings and annualized system cost analyses, the future expenses and benefits are expressed in terms of dollars in hand, which requires assumptions on future discount rate, inflation rate and fuel price escalation rate. Thus, the conversion of all future earnings to present worth dollars involves a certain degree of uncertainty. Moreover, most customers are interested in the pay-back period of the system.

Michelson [90] and Boer [91] used the minimum payback period for economic optimization of solar systems which requires fewer assumptions about future costs. Gordon and Rabl [92] used the internal rate of return as the criterion for the optimization of a solar process heat plant. Two cost parameters, which are collector cost/m^2 and the cost of diesel/GJ, were taken into account in El-Nashar's [93] study on the economics of solar assisted multiple stack distillation plants.

A comprehensive economic analysis was conducted by Hawlader et al. [94] for a solar water heating system at the Changi International Airport in Singapore. Different economic optimization criteria were applied and compared. It was found out, using life cycle savings and annualized life cycle cost calculations, that the optimum collector area was around 1200 m^2, while analyses using the payback period and internal rate of return showed optimum collector area of 1000 m^2. For the economic variables used in these analyses, the minimum payback period is around 14 years, which was considered rather high.

Mills et al. [95] described a design approach taken to use existing commercial flat plate absorber and tank components in a new way to maximize solar contribution and minimize material usage in the construction of the system. The design criterion used is not maximum peak efficiency, but minimum annual backup energy supplied to the system to meet an annual load. This corresponds to meeting a minimum greenhouse emissions requirement in embodied CO_2 during manufacture and pollution from backup energy supplied.

Using life-cycle savings as the criteria, Kalogirou [96] proposed an artificial intelligence methods to optimize a solar-energy system. His method greatly reduces the time required by design engineers to find the optimum solution and in many cases reaches a solution that could not be easily obtained from simple modeling programs or by trial-and-error.

Kulkarni et al. [97] proposed a methodology to determine the design space for analysis and optimization of solar water heating systems. They optimized the solar water heating system by minimizing annual life cycle cost.

2.4 Other areas of applications of multi-function solar system

2.4.1 Drying

The combination of solar energy and heat pump system can support various thermal applications for domestic and industrial use, such as water heating, solar drying, space cooling, space heating, refrigeration, etc. Drying is widely used in industries such as agriculture, food, chemical, paper, timber and textile. It is an energy intensive process that easily accounts for up to 15% of all industrial energy usage, often with relatively low thermal efficiency, 20-25% [98]. Heat pump assisted dryer has been extensively used by industry for many years.

Nevertheless, a limited number of studies have been reported on laundry drying utilizing heat pump assisted dryer. Braun et al. [99] compared the energy efficiency of air heat pump tumbler clothes dryer with a conventional air vented dryer. The heat pump dryer presented offers up to 40% improvement in energy efficiency over the electric dryer, as against 14% projected improvement by open cycle and closed dryers using heat recovery heat exchangers. Conde et al. [100] discussed current tumbler dryer technology and its shortcoming, and an economically viable and simple solution for energy conservation in laundry drying was proposed.

The heat pump assisted dryer is mainly used for drying timber and other temperature sensitive materials such as agricultural products, confectionery and ceramics. Different methods of drying have been reported including solar drying, heat pump drying, drying by superheated steam and microwave convection drying. There are numerous studies of related work in the literature.

Sharma et al. [101] presented an experimental investigation of three different types of solar dryer based on the principle of natural as well as forced convection. They

are cabinet-type natural convection solar dryer, multi-stacked natural convection solar dryer and indirect-type multi-shelf forced convection.

Many computer simulation or modeling has been developed to evaluate the performance of solar assisted heat pump system. A prototype heat pump assisted mechanical drying system was designed, constructed and tested for drying wool by Oktay et al. [102]. The dryer was shown to be capable of specific moisture extraction rates ranging from 0.65 to 1.75 kg/kWh. The heating coefficient of performance of the dryer was found to be between 2.47 and 3.95.

In other study, Pendyala et al. [103, 104] developed a mathematical model for an integrated heat pump assisted dryer and compared the performance of a heat pump assisted dryer using R11 and R12. Chou et al. [105] presented a mathematical model of a heat pump assisted dryer. In their study, a term named 'contact factor', defined as the ratio of the actual moisture removal rate to the maximum possible moisture removal rate of the dryer, was introduced in the mathematical model. Their results indicated that the non dimensional contact factor of a dryer is insensitive to dryer air inlet temperature. A performance chart to guide the selection of the heat-pump dryer components was also proposed.

In conventional dryers, humid air from dryer outlet is exhausted to the ambient, which leads to a loss of both sensible and latent heat. A more efficient approach would be to remove moisture and recover heat from the dryer outlet stream using a heat pump. A solar assisted heat pump rice drying system was developed by Best et al. [106, 107] as an alternative to conventional mechanical dryers. The experiment was conducted by modifying a 7 kW R-22 air conditioning unit, which was combined with a solar collector for a better control of temperature and humidity.

They showed a comparison of three experimental drying curves for three different operation modes, and found that the recirculation mode with heat pump was the most energy efficient, which offered the shortest drying time and lowest moisture content. Hawlader et al. [22] investigated the use of conventional vapor compression heat pump using R134a for water heating and agriculture drying. This paper reported higher energy efficiency with heat recovery method resulting in lower energy consumed for each unit of water removed in the dryer.

2.4.2 Air Conditioning

More and more buildings are being equipped with air-conditioning systems. This is where solar air conditioning can be considered. Florides et al. [108] classified solar cooling systems into three categories: namely, solar sorption air-conditioning (include absorption and adsorption), solar-mechanical systems and solar-related systems. Researches on solar air-conditioning grew quickly in the 1970s. Most of the recent research in solar air-conditioning is focused on absorption and adsorption..

Among adsorption chillers, desiccant coolers and the absorption systems, the absorption systems has the highest market penetration [109]. The market share of adsorption systems is significantly lower. The desiccant cooling technique has the advantage of the lowest driving temperatures and, therefore, has a large potential for market penetration. An experimental investigation on solar-assisted heat pump air conditioning system using water as working fluid had been reported by Tleimat and Howe [110]. In their studies, it was shown that the use of solar energy in space heating and cooling results in large energy savings.

Based on the above, not many studies have been done on the 3-in-1 solar assisted-heat pump system for air-conditioning, water heating and drying. Further

study was needed in this field to determine the full potential of such integrated solar assisted-heat pump system. Therefore, an experimental setup was constructed to achieve this goal. Experiments were conducted followed by a simulation study. An economic optimization based on the analytical method mentioned above may be used to determine the feasibility of the system.

CHAPTER 3 EXPERIMENTS

This chapter includes details of the experimental apparatus related to the integrated solar assisted heat pump system for air-conditioning, water heating and drying. A description of the experimental rig, instrumentation and test procedure are also included. The system was designed, built and experiments were conducted under the meteorological conditions of Singapore.

3.1 System configuration

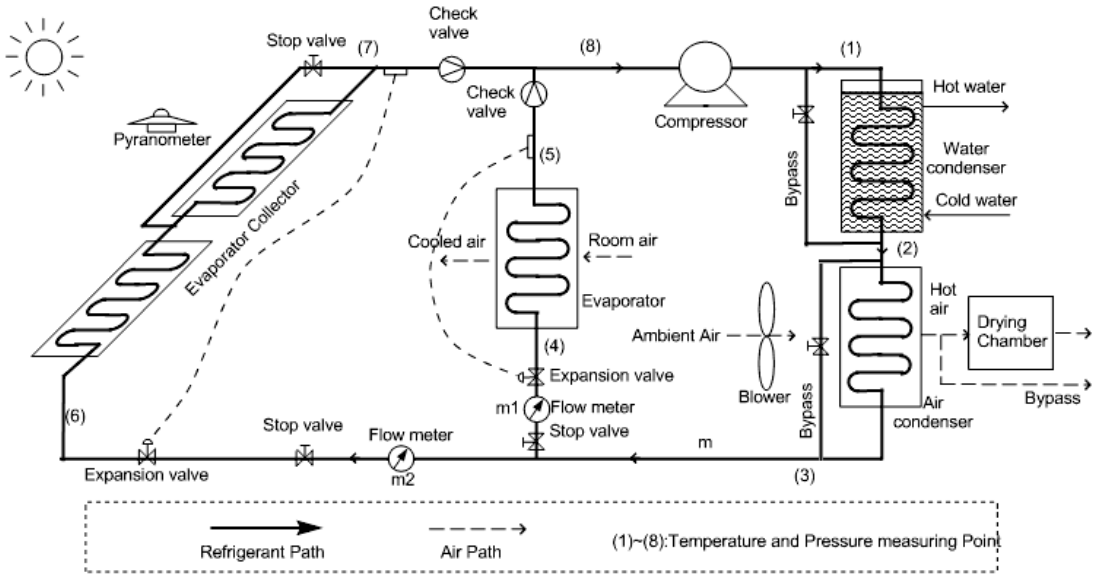

Figure 3.1 Schematic diagram of the solar assisted heat pump system

A solar assisted heat pump system was designed and built, as shown in Figure 3.1. The system is located on the rooftop of a four-storey building at the National University of Singapore.

The various components of the system are: evaporator-collector, evaporator, variable speed reciprocating compressor, air-cooled and water-cooled condensers, drying chamber, blower and other control devices. The evaporator-collector is made

of a copper absorber plate coated with black paint. Underneath the absorber plate, serpentine copper tubes of 9 mm diameter are brazed to enable the refrigerant to flow. The evaporator-collector and evaporator are connected in parallel with individual expansion valves. The air-cooled and water cooled condensers are connected in series.

The system consists of two flow paths: refrigerant flow path and air flow path. Bypass arrangements are also made for the solar collectors, evaporator and water tank for different usage patterns and operating conditions.

Figure 3.2 includes a photograph of the integrated system.

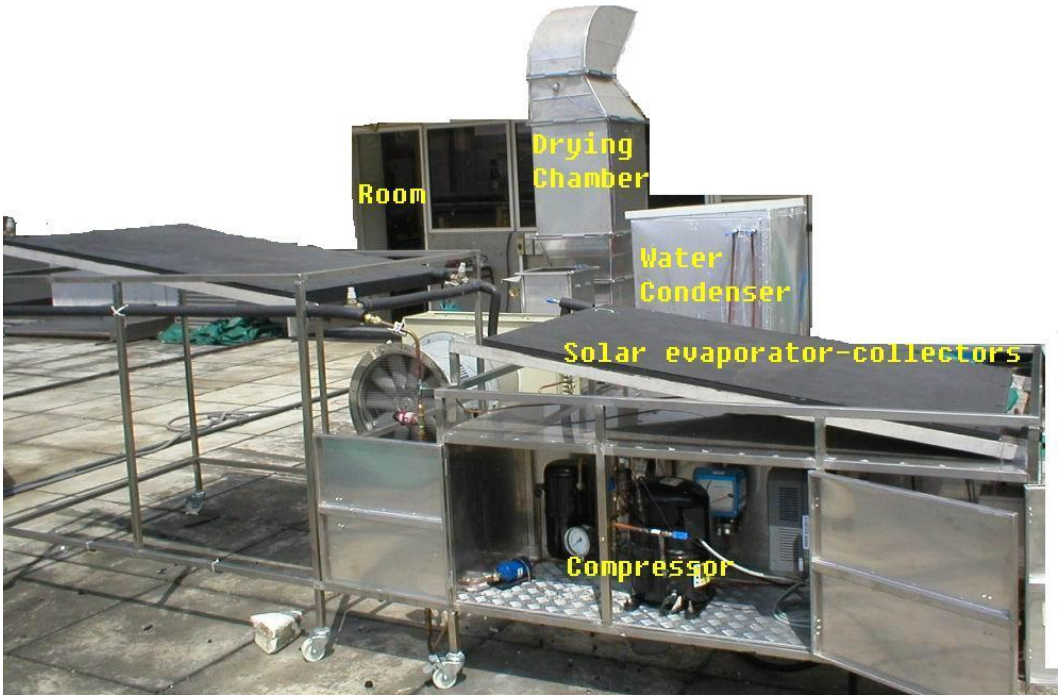

Figure 3.2 A photograph of the experiment set-up

The system component layout is shown in figure 3.3.

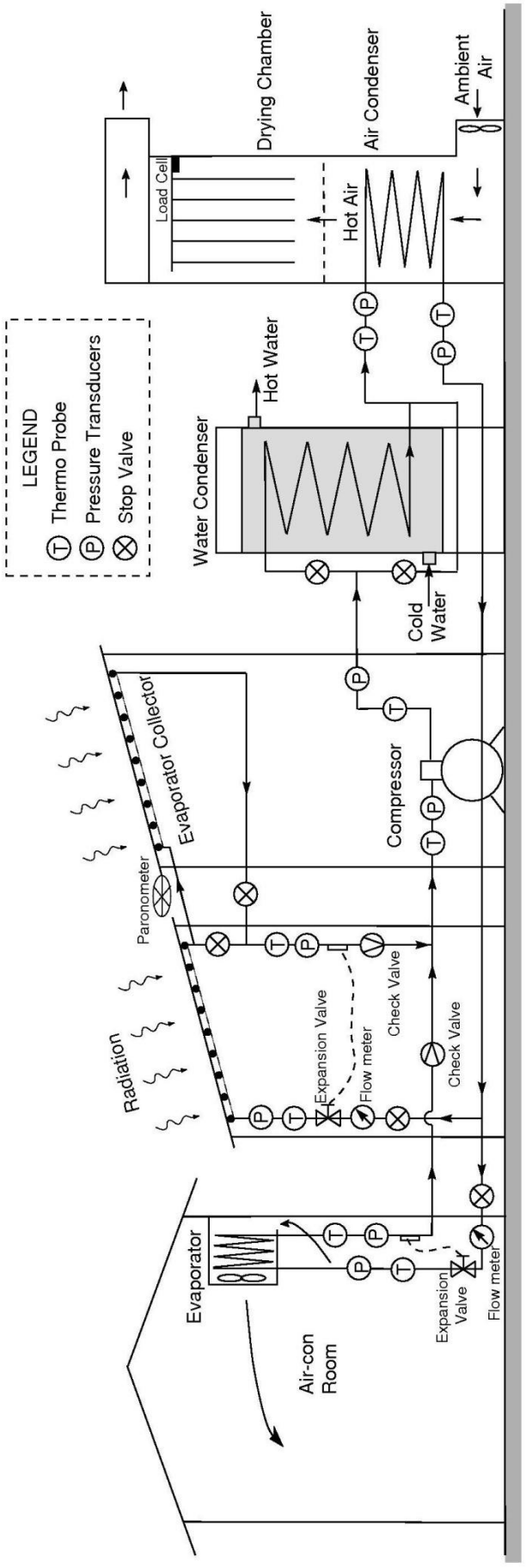

Figure 3.3 System component layout design of the solar assisted heat pump system

3.1.1 Refrigerant flow path

The refrigerant flow path of the system includes a hermetic type reciprocating compressor, evaporator, evaporator collector, water cooled condenser, air cooled condenser and expansion valves. The two evaporators are connected in parallel whereas the two condensers are connected in series, as shown in Figure 3.1.

After complete condensation, liquid refrigerant splits into two ways. Each of them expands through a flow regulating device, superheat controlled thermostatic expansion valve, reaching the evaporator in the room and evaporator-collectors located on the roof-top for collection of solar and ambient energy.

In the evaporator, the refrigerant vaporizes by receiving heat from room air. The air in the room is cooled through the finned tubes by releasing heat to the cold refrigerant inside the tubes. The evaporator outlet superheat level was automatically controlled by the thermostatic expansion valve. It senses the evaporator outlet temperature by a sensing bulb clamped to the outlet of evaporator, as shown in Figure 3.1. Based on the feedback from feeler bulb, thermostatic expansion valve automatically regulates the flow rate of fluid in proportion to the rate of evaporation to maintain the outlet superheat level.

In the solar evaporator-collector, the two-phase refrigerant flow through the serpentine copper tubes brazed underneath the absorber plate, as shown in figure 3.4. It is heated by incident solar radiation and the energy absorbed from the ambient air through a absorber plate, as shown in figure 3.5. The refrigerant superheat level at evaporator-collector outlet was also automatically controlled by the thermostatic expansion valve.

Check valves are installed after both of the evaporators to prevent refrigerant back flow, as shown in figure 3.1. Refrigerants arriving from the solar evaporator collector and the room evaporator are mixed together and enter into the suction side of the compressor. At this point, electrical / mechanical energy is added to the refrigerant to increase its temperature and pressure. The high pressure and temperature refrigerant vapor from the compressor outlet first enters the coil immersed in the water of the condenser tank and then passes through the air-cooled condenser. The heat of condensation from the superheated refrigerant vapor is recovered both in air and water-cooled condensers, which otherwise would have been wasted in normal circumstances. The energy recovered in the water-cooled condenser heats the water, whereas, the energy released in air-cooled condenser heats the air for drying purposes. The air-cooled condenser also ensures complete condensation of the refrigerant vapor, often with a little bit of sub-cooling, to ensure complete condensation before it enters expansion valves. The saturated / sub-cooled liquid refrigerant splits into two paths and enters into evaporator in the room and outdoor solar evaporator-collectors, and the cycle repeats. R134a is used as the refrigerant due to its better thermodynamic performance [82].

3.1.2 Air flow path

The air flow path consists of a blower, air cooled condenser, drying chamber and a fan-duct system, as shown in figure3.10 and figure 3.11. The blower draws ambient air into the air-cooled condenser. Air flows over the finned exterior surface of the condenser and heat transfer occur between air and refrigerant. The drying chamber contains drying material, wet clothes or towels in the present study, hung vertically to have good exposure to the incoming hot air from the air-cooled condenser. Humid air is then vented out to the atmosphere after drying.

3.1.3 Bypass arrangements

The three applications of the system are: air-conditioning, water heating and drying, which can be served simultaneously or independently. Therefore, bypass arrangements are made for the solar collectors and water tank for different usage patterns and operating conditions, as shown in Figure 3.1.

The solar evaporator-collector can be bypassed by closing the stop valve before the collectors. Then all of the refrigerant will flow through the evaporator in the room. This mode is proper for the cases that both solar radiation and ambient temperature is low.

The second solar evaporator-collector can be bypassed so that the total collector area can be reduced to half. It is to investigate the effect of collector area on the system performance.

The water-cooled condenser can be bypassed. In this case, the heat of condensation from the superheated refrigerant vapor is recovered only in air-cooled condenser, as in conventional air-conditioning system. This action will increase the amount of heat for dying and reduce drying time.

The air-cool condenser can be bypassed to save the energy consumption of blower. However, for the safety of system, it is not recommended to bypass to the air-cool condenser to ensure complete condensation of refrigerant under any circumstance.

3.2 Design of Components

All of the components were designed to meet the desired thermal load. The system consist of evaporator-collector, evaporator, variable speed reciprocating compressor, air-cooled and water-cooled condensers, drying chamber, blower, liquid receiver, sight glasses, frequency inverter and thermostatic expansion valve. The major components of the system are discussed in this section. The system components' specification and characteristics are shown in Table 3.1.

Table 3.1 Specification and characteristics of system components

1. Solar Evaporator-Collector		
a.	Area	1.5m^2 $\times$2
b.	Absorber plate	2mm thick copper plate(copper tube is bonded to the absorbing plate in a serpentine fashion)
c.	Surface treatment	Black paint coating. Absorptivity: 90%, Emissivity: 90%
d.	Back insulation	Made of fiberglass wool of thickness 50mm
e.	Collector tilt	10 degrees
2. Evaporator (forced draft with two fans)		
a.	Type	Cross flow fin and tube
b.	Fan rotational speed	1325RPM
c.	Total air flow rate	0.42kg/s
3. Compressor		
a.	Type	Reciprocating hermetic type
b.	Cooling capacity	13 kW
c.	Motor power	3.7 kW
d.	Bore	49.5mm
e.	Stroke	23.0mm
f.	Motor speed	2900RPM (maximum)
4. Water cooled condenser (water tank)		

a.	Size	300 liters (dimensions: 0.6m x 0.6m x 0.83m)
b.	Condenser coil	Spiral shape copper tube with the length of 30 m
c.	Insulation	Made of polyurethane of thickness 50mm
5. Air cool condenser		
a.	Type	Air cooled fin (Aluminum) and tube (Copper)
b.	Face area	0.6m x 0.85m = 0.51m^2
c.	Number of rows	22
d.	Tubes per row	3
e.	Tube diameter	9.5 mm
6. Drying Chamber		
a.	Dimension	0.6m x 0.6m x 0.4m
b.	Material	Stainless steel
c.	Insulation	Internally insulated with armaflex
7. Blower		
a.	Type	Axial flow fan
b.	Air flow rate	1500m^3/hour
c.	Motor speed	1440RPM(maximum)
d.	Static pressure	200Pa
8. Expansion Valves		
a.	Type	Thermostatic expansion valve(superheat controlled)
b.	Capacity	1.5kW & 5.5kW
9. High/Low Pressure Cut-off (safety device)		
a.	High pressure limits	10-20 bar
b.	Low pressure limits	0-5 bar
10. Frequency Inverter		
a.	Capacity	5kW
b.	Frequency range	0-50Hz, 3 phase

3.2.1 Evaporator-collector

In the present study, two 1.5m x 1.0 m unglazed collector plates, made of copper were designed and fabricated. A copper tube of 9 mm diameter was soldered at the back of each absorber plate in serpentine form with spacing of 100mm, as shown in the Figure 3.4. Adequate insulations were provided at the back of the collector to cover the refrigerant tube and the lower plate surface. No glass cover was used on the top surface i.e. unglazed collector.

Fig 3.4.The lower surface of collector

There is a bypass line from the exit of the first evaporator-collector to the exit of second evaporator-collector, which allows operation of only one or both evaporator-collectors. As shown in Figure 3.5, the two evaporator-collectors are fixed on the top of a stainless steel frame work with a tilt of 10 degree. The top surface of collector is painted black with absorptance of 90% and emittance of 90%.

Figure 3.5 Photograph of the evaporator-collector

The two-phase refrigerant from the expansion valve flows through the serpentine copper tubes brazed underneath the absorber plate and heated by incident solar radiation and heat from the ambient air through the absorber plate. The evaporator-collector plate temperature at different sections is measured by means of T-type copper-constantan thermocouples. The temperatures inside the refrigerant tube at inlet and outlet of two collectors are measured by means of thermal probes. The pressures at these points are measured by means of pressure transducers and pressure gauges. These temperatures and pressures are monitored and stored continuously in a data logger.

3.2.2 Evaporator

A direct-expansion evaporator with two fans, as shown in Figure 3.6, was designed and fabricated, and placed in a room in NUS engineering block EW2 for cooling purposes.

Figure 3.6 Evaporator with two fans for space cooling

Heat transfer occurs in the direct expansion type coil where the refrigerant flows inside the tubes and room air flows over the finned-coil surface. The room dimension and internal cooling load description are shown in Figure 3.7.

Temperatures and pressures at evaporator inlet and outlet are measured and stored in the data-logger used for the evaporator-collector. A thermal probe is used to monitor the room temperature.

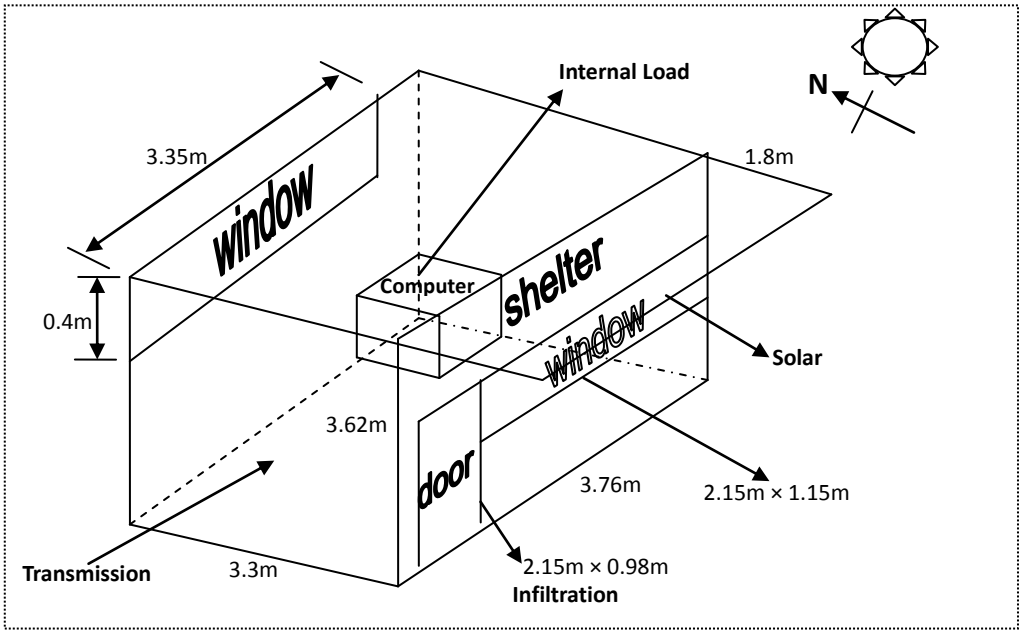

Figure 3.7 The room at roof top of NUS Workshop 2 building

3.2.3 Compressor

A hermetic type reciprocating compressor was used in the present study, as shown in Figure 3.8. In order to control the compressor cooling capacity and study the system performance under different operating conditions, a frequency inverter is used to vary the compressor speed. The frequency can be varied from 30Hz to 50Hz. With the frequency of 50Hz, the compressor power consumption is 3.7 kW and the cooling capacity is 13kW. The circulating refrigerant, R134a, enters the compressor as vapor, preferably slightly superheated, which is compressed to a high pressure and temperature before it is released to the condensers.

For safety of the compressor, a high pressure and low pressure cut-off strategy is used. It switches off the compressor if the pressure goes outside the range limits. The range limit of the pressure at compressor outlet is set to 10-20 bar and that of the pressure at compressor inlet is set to 0-10 bar.

Figure 3.8 Hermetic type reciprocating compressor

Temperatures and pressures at compressor inlet and outlet were measured and stored in a data acquisition system. The power consumption of the compressor was measured by a wattmeter.

3.2.4 Water cooled condenser

The water cooled condenser also served as water tank for hot water storage. It consists of a copper coil immersed in a tank filled with water, as shown in Figure 3.9.

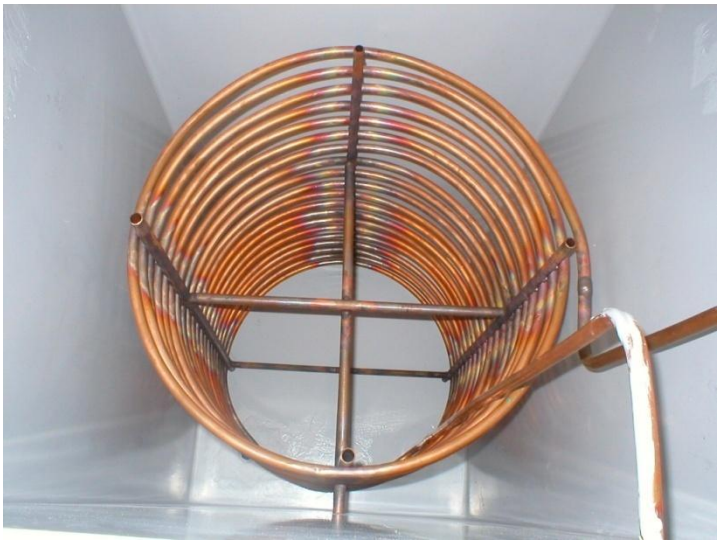

Figure 3.9 Photograph of copper coil in the water storage tank

The maximum volume of the water tank is 360 liters (dimension: 1.2m x 0.6m x 0.6m.) The superheated refrigerant from the compressor was cooled by the water from a superheated discharge temperature to saturated condition. To prevent heat losses from water tank, the condenser was properly insulated and covered with polyurethane. The water temperature is measured continuously by a thermal probe immersed in the water. A bypass arrangement is designed for this water-cooled condenser to enable operation of the system without water heating function.

3.2.5 Air-cool condenser and drying chamber

An air-cool condenser integrated to a drying chamber was designed and fabricated to perform drying, as shown in Figure 3.10.

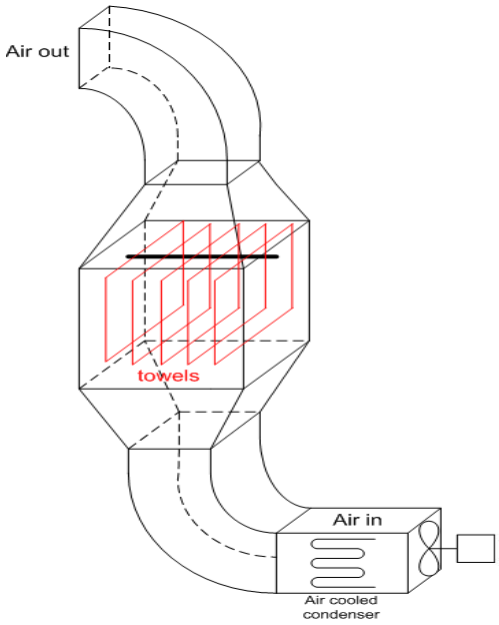

Figure 3.10 Schematic diagram of the air-cool condenser and drying chamber

The refrigerant from water-cooled condenser was subjected to further cooling in an air-cooled condenser to ensure complete condensation, with a little bit of sub-cooling, if possible. Air flowed over the finned exterior surfaces and heat transfer occurred between air and refrigerant. After being heated, the air was used for drying clothes. After passing through the dryer, the humid air was vented out to the atmosphere.

A perforated plate was placed after the diffuser in order to achieve uniform air flow velocity. To change drying materials in the drying chamber without closing blower operation, a bypass arrangement was designed for the air flow path. A load cell was mounted on the bracket hanging the drying materials. It measured the variation of drying load continuously and stored them in a data logger. Two thermal probes were placed in the duct after the air-cooled condenser and at the exit of drying chamber to monitor the air temperature before and after drying.

When the water-cooled condenser was bypassed, the superheated refrigerant from

compressor was condensed only by air-cooled condenser and provides much more heat to the air. Investigation was conducted in this study to compare the drying performance at the conditions with/without water-cooled condenser.

A photograph of the air-cool condenser integrated drying chamber is shown below in figure 3.11.

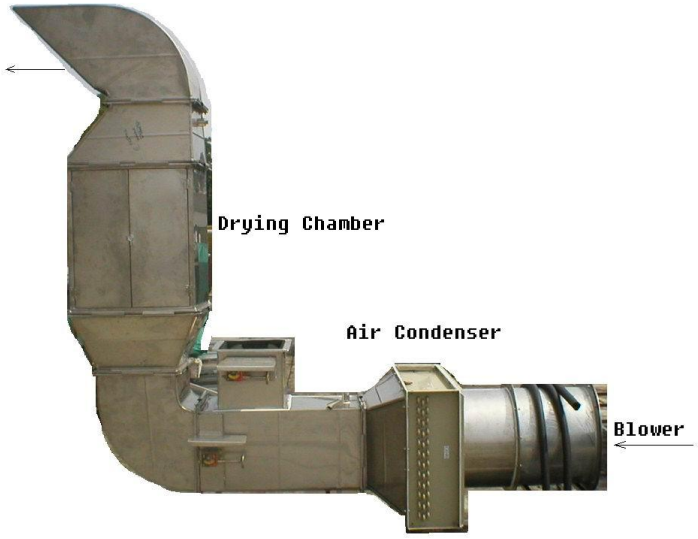

Figure 3.11 photograph of the air-cool condenser integrated drying chamber

3.3 Instrumentation

A well-equipped instrumentation system was deployed for this experiment to measure the various parameters in order to perform a complete system performance analysis. A description of the instruments used in the present study is included in this section.

3.3.1 Temperature Measurement

Thermal probes and thermocouples are used for the measurement of temperatures of air stream, refrigerant and ambient. The thermal probes and thermocouples used were type T copper-constantan and were calibrated using a standard thermometer. The accuracy (uncertainty) of temperature measurements is $\pm 0.2^{o}C$. These temperature sensors were connected to a data logger.

3.3.2 Pressure Measurement

The refrigerant pressures at different locations were measured using piezoresistive type pressure transducers. The accuracy of pressure measurements is 0.25 N/m^2. All these pressure transducers were connected to the data logger to monitor and record pressures continuously. For the convenience of operation, pressure gauges were also installed at different locations.

3.3.3 Moisture Content Measurement

Moisture contents of the product under drying were monitored continuously by a compression type load cell. The capacity of the load cell was 6kg, with an accuracy of 0.5%. The load cell is calibrated using standard deadweights.

3.3.4 Flow Rate Measurement

Figure 3.12 The flow meter for refrigerant R134a flow

The mass flow rate of the refrigerant was measured using a positive displacement type flow meter, as shown in figure 3.12. Whereas for air, a vane type anemometer was used to measure the air flow velocity. With the cross sectional area measured, the volumetric flow rate of air was obtained. The accuracy of flow rate measurement is 0.01 kg/s.

3.3.5 Solar Radiation Measurement

Figure 3.13 The pyranometer for the measurement of solar radiation

A pyranometer was used for the measurement of solar radiation and it is placed near to the solar collector, as shown in figure 3.13 and figure 3.5. The pyranometer was carefully positioned in order not to caste any shadow on the collector surface.

3.3.6 Relative humidity Measurement

A whirling hygrometer is used to measure the wet and dry bulb temperature. Dew point and relative humidity can be determined by reference to a psychrometric chart. The accuracy is +/- 2% RH.

Figure 3.14 The whirling hygrometer for the measurement of relative humidity

3.3.7 Data Acquisition System

In the present study, a HP data logger with 40 channels was used for recording of different parameters. The measuring signals (altogether 32) were digitized and stored at regular intervals. All quantities were monitored continuously and stored at 5 minutes interval. The stored data were then transferred to a computer for analyses.

3.4 Test procedure

The experiment conducted includes water heating, clothes drying and space cooling. The dryer in the present study was designed for laundry drying only and towels were used in the experiment. Before the experiment was started, some preparation works has to be done as follows:

3.4.1 Preparation works

1. 300~360 liter of water at ambient temperature was filled into the water tank.

2. Ten towels were wetted first and then dried by 'manual spinning'. Towels were wetted to a moisture content of about 130% ~ 150% and then hung onto the clothes hanger after measuring their weight using the weighing machine. This is to ensure the weight measured have a good degree of agreement with the weight of towels recorded by the load cell. Moisture contents (dry basis) were obtained using the following equation:

$$M_c = [(W_w - W_d) / W_d] \times 100\%$$

   where W_w, W_d are the weights of wet and bone dry towels, respectively.

3. Refrigerant is charged into the system until 12 bar of pressure was reached.

4. Set the frequency of the inverter to a particular value.

5. Choose the operation area of evaporator-collector by turning the valves.

6. Check for the proper positioning of all the valves according to desired running mode.

7. Check for all the electrical circuits and instrumentation system.

8. Check the high and low pressure cut-off limits for compressor to proper values.

3.4.2 Running the system

After the completion of initial preparation, the system was ready for experiment. Normally, the compressor requires a minimum of two hours "run-in" to attain specified performance. During the experiment, once the water temperature reaches 60^0C, the hot water (60^0C) was discharged and cold water (30^0C) was fed into the water tank, with flow rate of 5 liter/min, for continuous heating. Whereas for the drying process, it continues until moisture content of 6% [111] is reached. When this stage was reached, one drying run was completed and the system was prepared for the next drying run.

During the experiment the sight glass was checked to ensure the system was functioning properly. The discharge temperature and pressure were checked at regular intervals. If the temperature or pressure went beyond the set cut-off limit and the system did not cut off automatically, the system was switched off manually and checked. After every run, the water in the condenser was flushed out and replaced before the starting of the next experiment.

3.4.3 System operation modes

The system can be operated in 5 operation modes by setting the bypasses of the system:

1. **Full mode:**

   Water heating, drying and air-conditioning including evaporator-collector

   No component is bypassed. The three functions are used simultaneously with the assisted power from solar evaporator-collector.

2. **NoWC mode:**

   Drying and air conditioning including evaporator-collector:

   Water condenser is bypassed. The Air condenser serves as the single condenser.

3. **NoAC mode:**

   Water heating and air conditioning including evaporator-collector:

   Air condenser is bypassed. The water condenser serves as the single condenser.

4. **NoRE mode:**

   Water heating and drying including evaporator-collector:

   Close the stop valve before the evaporator in the room. All of the refrigerant flows through the solar evaporator-collector.

5. **NoEC mode:**

   Water heating, drying and air conditioning without evaporator-collector:

   Close the stop valve before the solar evaporator-collectors. All of the refrigerant flows through the evaporator in the room.

3.5 Error analysis

An error analysis for collector efficiency and COP has been undertaken based on Moffiat's equation of uncertainty in result [112]. A sample calculation of errors related to collector efficiency is presented in APPENDIX E.

CHAPTER 4 MATHEMATICAL MODEL AND SIMULATION

Mathematical equations describing the performance of different components of the solar assisted heat pump system are described in this chapter. These equations will be used in a simulation program to predict the performance of the system.

4.1 Meteorological condition

Meteorological data is important to get the actual thermal performance and optimum size of the system. In order to achieve the exact thermal performance of the heat pump assisted solar hot water system, local meteorological data has been used and these are discussed in this section.

4.1.1 Climatic condition of Singapore

As the country is located near the equator (1°21′ N, 103°55′ E), Singapore has a uniform temperature, high humidity and a reasonable rainfall throughout the year. The daily ambient temperature variation is relatively small, while annual temperature variation is about 1.9℃. As stated earlier, the relative humidity (RH) is generally high and, in the early hours of the morning, it reaches around 90%, while it drops to around 60% at about solar noon. The mean monthly temperature variations are not more than 1.1℃ from the mean annual of 26.6℃. The mean maximum and minimum daily temperature are 30.7℃ and 23.7℃.

In Singapore, the month of December consistently shows itself as the wettest month of the year while July, generally, has the lowest average monthly rainfall. The annual mean rainfall in Singapore is 2381 mm. Two main seasons in Singapore are the Northeast monsoon and Southwest monsoon. Northeast monsoon starts in late

November and ends in March, whereas Southwest monsoon usually starts in the second half of May and ends in September. In between these two seasons, there are shorter inter monsoon periods. Rain frequently occurs during the early part of Northeast monsoon.

Figure 4.1 shows the Meteorological conditions, i.e. solar radiation, ambient temperature, relative humidity and wind speed, for a typical day (in March) in Singapore.

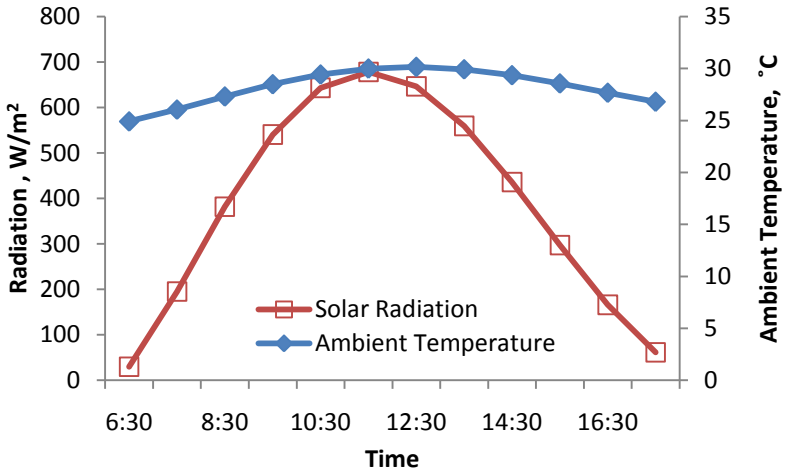

(a) Variation of monthly ambient temperature and solar radiation

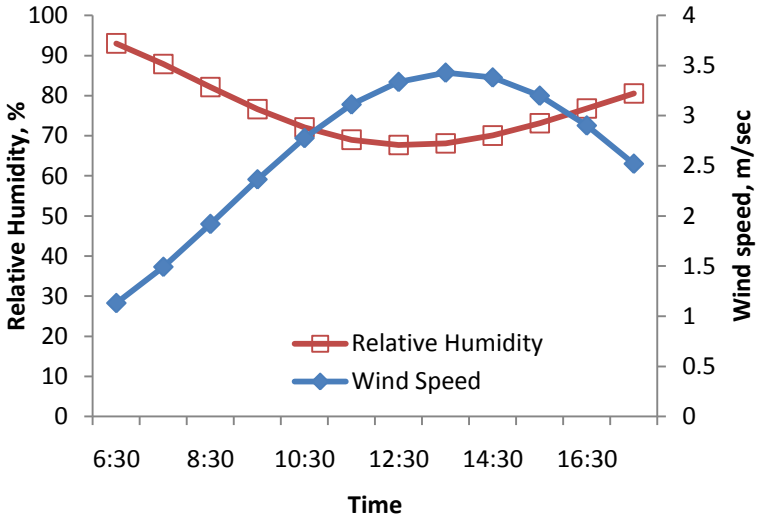

(b) Variation of monthly relative humidity and wind speed

Figure 4.1 Meteorological conditions for a typical day (in March) in Singapore

4.1.2 Model of Meteorological data of Singapore

Meteorological data is very important for the design, performance evaluation and optimization of solar thermal systems. It also provides necessary information for thermal load calculations. A model to describe Singapore' s meteorological conditions has been developed by Hawlader et al. [112]. This model predicts the monthly average daily values of solar radiation, ambient temperature, wind speed, and relative humidity, as described by the following equation:

$$X = \sum_{n=0}^{7} a_n t^n \tag{4.1.1}$$

where,

X = Hourly values of the variables (solar radiation, ambient temperature, relative humidity, and wind speed),

a_n = Coefficient of polynomial equation,

t = Station time, which is 8 hours ahead of GMT.

The values of the coefficient are given in tabular form in appendix A.

4.2 Evaporator-collector model

A transient two-dimensional mathematical model of the evaporator-collector has been developed to predict temperature distribution and useful energy gain.

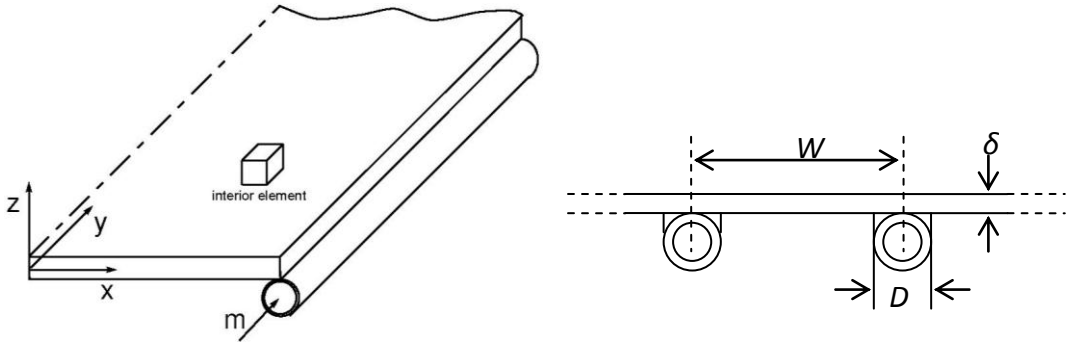

(a) (b)

Figure 4.2 Geometry of the unglazed solar evaporator collector

4.2.1 Governing equations for the mathematical model

The function of an evaporator collector is to deliver the heat absorbed on the collector surface to the fluid in the tube. Because the copper plate is thin and conductivity is high, the temperature variation in z-direction can be considered as negligible. However, the heat transfer in y-direction, as shown in Figure 4.2, cannot be considered negligible because of the fact that the fluid temperature is not constant along the length of the tube. For this reason, the governing equation is derived to predict the performance of the evaporator collector by considering heat transfer in both x and y directions.

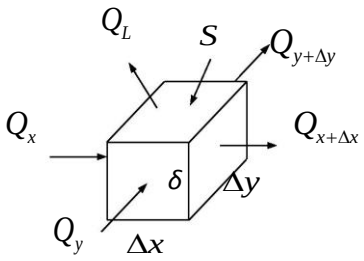

Figure 4.3 Energy balance in a control volume in the interior area of collector

An energy balance on the control volume (interior area as seen in Figure 4.2a) is shown in Figure 4.3 gives:

$$Q_x + Q_y + Q_u - Q_{x+\Delta x} - Q_{y+\Delta y} = \rho c_p(\delta \Delta x \Delta y)\frac{\partial T}{\partial t} \tag{4.2.1}$$

The term $\rho c_p(\delta \Delta x \Delta y)\frac{\partial T}{\partial t}$ represents the change of internal energy in the elemental control volume. δ is the thickness of the plate.

The terms $Q_u, Q_{x+\Delta x}$ and $Q_{y+\Delta y}$ are given by:

$$Q_u = q_u\left(\Delta x \Delta y\right);$$

$$Q_{x+\Delta x} = Q_x - k\delta \Delta x \Delta y \frac{\partial^2 T}{\partial x^2};$$

$$Q_{y+\Delta y} = Q_y - k\delta \Delta x \Delta y \frac{\partial^2 T}{\partial y^2}$$

Substituting these three terns into equation (4.2.1) gives the partial differential equation (PDE):

$$\frac{q_u}{k\delta} + \frac{\partial^2 T}{\partial x^2} + \frac{\partial^2 T}{\partial y^2} = \frac{\rho c_p}{k}\frac{\partial T}{\partial t} \tag{4.2.2}$$

Where

$$q_u = S - Q_L = S - U_L(T - T_a) \tag{4.2.3}$$

$$S = I(\tau\alpha) = I\alpha$$

This partial differential equation (4.2.2) requires one initial condition and four

boundary conditions for its solution.

The initial condition for all temperature values are set as ambient temperature:

At t=0 : $$T = T_a \tag{4.2.4}$$

The four boundary conditions are as follows:

a. The boundary at $y = 0 \text{ and } 0 < x < \frac{(W-D)}{2}$**.**

Because the boundary at $y = 0$ is exposed to the ambient, so

At y=0 : $$Q_y = q_y(\delta\Delta x) = -U_L(T_{y1} - T_a)(\delta\Delta x) \tag{4.2.5}$$

where, $T_{y1} = T\big|_{y=0 \text{ and } 0<x<\frac{(W-D)}{2}}$

At $y = 0$**,** the energy flow in the control volume is shown in figure 4.4:

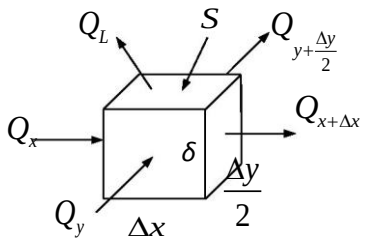

Figure 4.4 Energy balance on the control volume at $y = 0$

The energy balance on the control volume is:

$$Q_x + Q_y + Q_u - Q_{x+\Delta x} - Q_{y+\frac{\Delta y}{2}} = \rho c_p(\delta\Delta x\frac{\Delta y}{2})\frac{\partial T_{y1}}{\partial t} \tag{4.2.6}$$

The terms $Q_{y+\frac{\Delta y}{2}}$ are given by:

$$Q_{y+\frac{\Delta y}{2}} = -k\delta\Delta x\frac{\partial T_{y1}}{\partial y} \tag{4.2.7}$$

Substituting it into equation (4.2.6), the partial differential equation (PDE) for the boundary at $y = 0 \text{ and } 0 < x < \frac{(W-D)}{2}$ is:

$$\frac{q_u}{k\delta} + \frac{\partial^2 T_{y1}}{\partial x^2} - \frac{2}{k\Delta y} U_L \left(T_{y1} - T_a\right) + \frac{2}{\Delta y}\frac{\partial T_{y1}}{\partial y} = \frac{\rho c_p}{k}\frac{\partial T_{y1}}{\partial t} \tag{4.2.8}$$

The other three partial differential equations for boundaries are derived using similar method.

b. The boundary at $y = L \text{ and } 0 < x < \frac{(W-D)}{2}$**:**

$$\frac{q_u}{k\delta} + \frac{\partial^2 T_{y2}}{\partial x^2} - \frac{2}{k\Delta y} U_L \left(T_{y2} - T_a\right) - \frac{2}{\Delta y}\frac{\partial T_{y2}}{\partial y} = \frac{\rho c_p}{k}\frac{\partial T_{y2}}{\partial t} \tag{4.2.9}$$

c. The boundary at $x = 0 \text{ and } 0 < y < L$**:**

$$\frac{q_u}{k\delta} + \frac{\partial^2 T_{x1}}{\partial y^2} - \frac{2}{\Delta x}\frac{\partial T_{x1}}{\partial x} = \frac{\rho c_p}{k}\frac{\partial T_{x1}}{\partial t} \tag{4.2.10}$$

d. Boundary condition at $x = \frac{(W-D)}{2} \text{ and } 0 < y < L$**:**

$$\frac{q_u}{k\delta} - \frac{2}{D}\frac{\partial T_{x2}}{\partial x} - \frac{\left(T_{x2} - T_f\right)}{k\delta D\left(\frac{1}{h_{fi}\pi D_i} + \frac{1}{C_b}\right)} = \frac{\rho c_p}{k}\frac{\partial T_{x2}}{\partial t} \tag{4.2.11}$$

where,

$$T_{y2} = T\big|_{y=L \text{ and } 0<x<\frac{(W-D)}{2}} \quad ; \quad T_{x1} = T\big|_{x=0 \text{ and } 0<y<L} \quad ; \quad T_{x2} = T\big|_{x=\frac{(W-D)}{2} \text{ and } 0<y<L}$$

The four corner points are special conditions of boundary conditions. The PDE for them are derived by the same energy balance method as for boundary conditions.

4.2.2 The overall heat transfer coefficient UL

As shown in figure 4.5, the plate on the tube has 5 parts of heat gain. The shade region is the bond material.

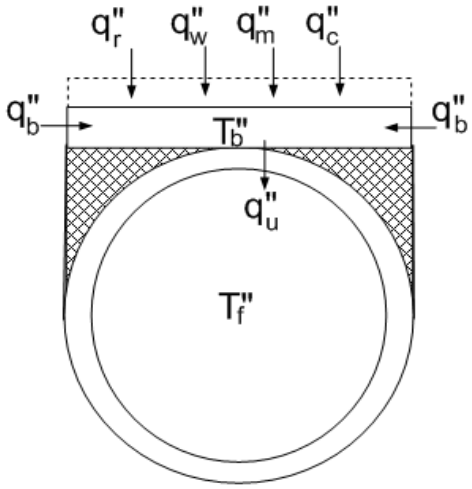

Figure 4.5 Cross-section of plate and the tube

The energy released to the fluid is $q_u^{"}$, and

$$q_u^{"} = q_b^{"} + [q_r^{"} + q_w^{"} + q_m^{"} + q_c^{"}] \tag{4.2.12}$$

Where, $q_u^{"}$ is decided by the flow condition inside the tube.

$$q_u^{"} = \frac{(T_b - T_f)}{\left[\frac{1}{h_{fi}\pi D_i} + \frac{1}{C_b}\right]} \tag{4.2.13}$$

where,

$$h_{fi} = \begin{cases} h_l = 0.023\,\mathrm{Pr}^{0.4}\,\mathrm{Re}^{0.8}\,\dfrac{k_l}{D} \\ h_v = 0.023\,\mathrm{Pr}^{0.4}\,\mathrm{Re}^{0.8}\,\dfrac{k_v}{D} \\ h_{tp} = 2.44 h_l X_{tt}^{-0.863} \end{cases} \tag{4.2.14}$$

Lockhart-Martinelli Parameter X_{tt} [10] is used for two-phase flow

$$X_{tt} = (1-x)^{0.9}\left(\frac{\rho_l}{\rho_v}\right)^{-0.5}\left(\frac{\mu_l}{\mu_v}\right)^{0.1} \quad (4.2.15)$$

C_b is the bond conductance [1] is used for two-phase flow

$$C_b = \frac{k_b \cdot D}{\left(1-\frac{\pi}{4}\right)\cdot\frac{D}{2}} \quad (4.2.16)$$

The effect of condensation is built into the overall heat transfer coefficient, which can be separated into three parts: wind heat transfer coefficient h_w, the radiation heat transfer coefficient h_r and the condensation heat transfer coefficient h_{cond}

$$U_L = h_w + h_r + h_{cond} \quad (4.2.17)$$

where,

$$h_w = 2.8 + 3V_a \quad (4.2.18)$$

$$h_r = \sigma\varepsilon_p \frac{\left(T_p^4 - T_{sky}^4\right)}{\left(T_p - T_a\right)} \quad (4.2.19)$$

$$T_{sky}^4 = 0.0552T_a^{1.5} \quad (4.2.20)$$

Here, T_{sky} and T_a are both in degree Kelvin [1].

For the condensation heat transfer coefficient h_{cond}, if T_p is greater than T_{dew}, condensation will not occur, which means that $h_{cond}=0$

If $T_p<T_{dew}$ $$h_{cond} = 1.13RH_a\left[\frac{g\rho_w^2 k_w^3 \cos\phi h_{fg}}{\mu_w L_p (T_a - T_p)}\right]^{1/4} \quad (4.2.21)$$

Dew point Temperature: $$T_{dew} = \frac{243.12\ln(P_v/611.12)}{17.62-\ln(P_v/611.12)} \quad (4.2.22)$$

Partial Vapor Pressure: $$P_v = RH_a \times e^{\left(\ln 611.2 + \frac{17.62T_a}{243.12+T_a}\right)} \quad (4.2.23)$$

4.2.3 Numerical solution method

The partial differential equations (4.2.2) are written in difference forms using Crank-Nicholson method, where each term is expressed by the following equation:

$$\begin{aligned}
&\frac{\partial^2 T}{\partial x^2} = \frac{1}{2}\left(\left.\frac{\partial^2 T}{\partial x^2}\right|^{j} + \left.\frac{\partial^2 T}{\partial x^2}\right|^{j+1} \right) = \frac{1}{2}\left(\frac{T^{j}_{m+1,n} + T^{j}_{m-1,n} - 2T^{j}_{m,n}}{\Delta x^2} + \frac{T^{j+1}_{m+1,n} + T^{j+1}_{m-1,n} - 2T^{j+1}_{m,n}}{\Delta x^2} \right) \\
&\frac{\partial^2 T}{\partial y^2} = \frac{1}{2}\left(\frac{T^{j}_{m,n+1} + T^{j}_{m,n-1} - 2T^{j}_{m,n}}{\Delta y^2} + \frac{T^{j+1}_{m,n+1} + T^{j+1}_{m,n-1} - 2T^{j+1}_{m,n}}{\Delta y^2} \right) \\
&\frac{\partial T}{\partial t} = \frac{T^{j+1} - T^{j}}{\Delta t}
\end{aligned} \tag{4.2.22}$$

Substituting these terms into PDE, finite difference approximation for the partial differential equation (4.2.2) is derived as follows:

$$\begin{aligned}
&T^{j+1}_{m,n-1} + T^{j+1}_{m-1,n} + T^{j+1}_{m+1,n} + T^{j+1}_{m,n+1} + \left(-4 - \frac{U_L}{r} - \frac{2p}{r} \right) T^{j+1}_{m,n} \\
&= -\left(T^{j}_{m,n-1} + T^{j}_{m-1,n} + T^{j}_{m+1,n} + T^{j}_{m,n+1} \right) + \left(4 + \frac{U_L}{r} - \frac{2p}{r} \right) T^{j}_{m,n} - \frac{2}{r}\left(S + U_L T_a \right)
\end{aligned} \tag{4.2.23}$$

The other finite difference approximations for boundary and corner conditions are derived similarly, which is presented in detail in appendix-B: "Numerical solution of PDE using Crank-Nicholson method"

After setting the initial condition described in equation (4.2.4), variation of temperature distribution on the evaporator-collector can be calculated by Gauss-Seidel iteration method using the finite difference approximation.

4.3 Modeling of components (excluding evaporator-collector)

This section explores the mathematical modeling of the other components of the system. The main components covered in the model are the compressor, water condenser, air condenser, expansion valve, evaporator-collector, room evaporator and drying chamber.

4.3.1 Compressor

An open type reciprocating compressor coupled with an electric motor and a frequency inverter is used in the heat pump. Different compressor speeds can be obtained by changing the frequency using the frequency inverter. The compressor model assumes a polytropic compression with a constant polytropic index, n, and the different equations are expressed as follows:

Piston displacement per cylinder:

$$V_d = \frac{\pi D^2 L N}{4} \tag{4.3.1}$$

Volumetric efficiency of the compressor can be expressed as:

$$\eta_v = 1 + C - C\left(\frac{p_2}{p_1}\right)^{1/n} \tag{4.3.2}$$

Where, C is the clearance volumetric ratio and determined from compressor manufacturer 's data.

Mass flow rate flowing through the compressor can be expressed as:

$$\dot{m} = \frac{V_d N \eta_v}{v_1 \times 60} \tag{4.3.3}$$

Work required for driving the compressor:

$$W = \dot{m}\frac{p_1 v_1}{\eta_c}\frac{n}{n-1}\left[\left(\frac{p_2}{p_1}\right)^{\frac{n-1}{n}} - 1\right] \tag{4.3.4}$$

Discharge state of the refrigerant:

$$T_{c,o} = T_{c,i}\left(\frac{p_2}{p_1}\right)^{\frac{n-1}{n}} \tag{4.3.5}$$

$$v_2 = v_1\left(\frac{p_1}{p_2}\right)^{\frac{1}{n}} \tag{4.3.6}$$

4.3.2 Water cooled Condenser

The water condenser is a combination of heat exchanger and hot water storage tank. The water cooled condenser consists of copper coil in spiral fashion immersed in a tank filled with water, as shown in figure 3.9. The superheated refrigerant releases heat in water condenser and becomes saturated or sub-cooled. The schematic diagram of water condenser is presented as follow:

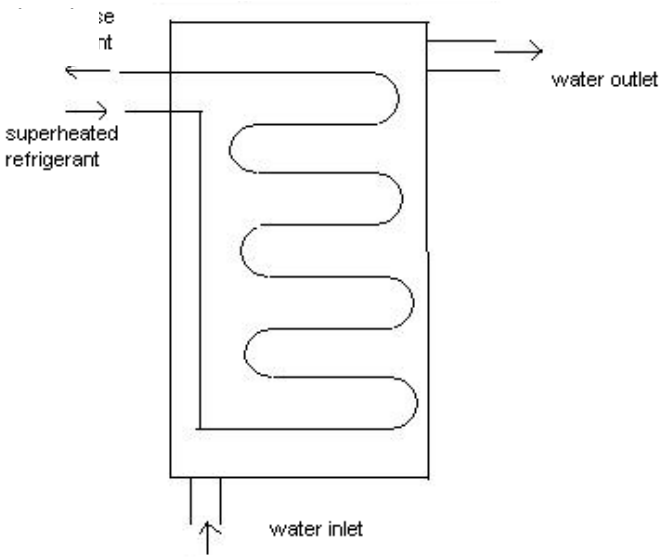

Figure 4.6 Schematic diagram of water tank

Water is heated to required temperature and then maintained by controlling the

cold water supply rate (same as hot water discharge rate).

$$MC_{pw}\frac{dT_w}{dt}+m_wC_{pw}(T_w-T_{wi})=Q_{wc}-U_{l\_wc}A_{wc}(T_w-T_a) \tag{4.3.7}$$

At heating period, temperature increasing rate is determined as:

$$MC_{pw}\frac{dT_w}{dt}=Q_{wc}-U_{l\_wc}A_{wc}(T_w-T_a) \tag{4.3.8}$$

The cold water supply rate mw to maintain the water temperature can be obtained by following equation:

$$m_wC_{pw}(T_w-T_{wi})=Q_{wc}-U_{l\_wc}A_{wc}(T_w-T_a) \tag{4.3.9}$$

Refrigerant goes through vapor and two phase region as shown in Figure 4.7.

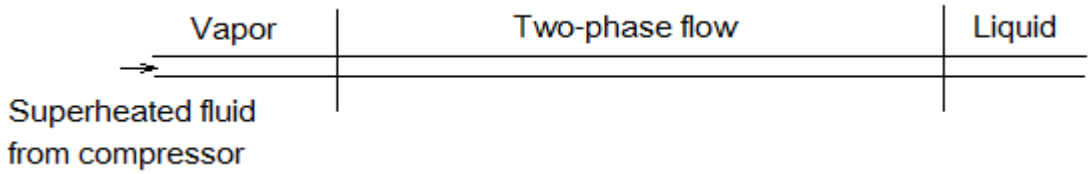

Figure 4.7 Regions of refrigerant flow in water condenser

In vapor region:

$$Q_v=m_r\times(H_{in}-H_{sat}) \tag{4.3.10}$$

Length of tube in vapor region:

$$L_v=\frac{Q_v}{\pi D_i h_v LMTD_v} \tag{4.3.11}$$

where,

$$LMTD_v=\frac{\Delta T_o-\Delta T_i}{\ln(\Delta T_o/\Delta T_i)} \tag{4.3.12}$$

In two phase flow region:

$$\frac{dQ_{tp}}{dL}=\pi D_i h_{tp}(T_{sat}-T_w) \tag{4.3.13}$$

$$dx = \frac{dQ_{tp}}{m_r H_{fg}} \tag{4.3.14}$$

The useful energy gain in the two-phase region is:

$$Q_{tp} = \int_{x=0}^{x=1} d\,Q_{tp} = \int_{L=0}^{L=L_{tp}} \pi D_i h_{tp} (T_{sat} - T_w) dL \tag{4.3.15}$$

Total length of the water condenser tube is defined as L_{tot}. If refrigerant is fully condensed before it reaches the end of tube, heat released in liquid region is:

$$Q_l = m_r C_{pr} (T_{sat} - T_{r\_o}) = L_l \pi D_i h_l LMTD_l \tag{4.3.16}$$

where,

$$LMTD_l = \frac{\Delta T_o - \Delta T_i}{\ln(\Delta T_o / \Delta T_i)} \tag{4.3.17}$$

$$L_l = L_{tot} - L_{tp} - L_v \tag{4.3.18}$$

Total energy released by refrigerant Q_{ref}, which is equivalent to the energy absorbed by the water Q_{wc}, is the sum of energy released in three regions.

$$Q_{wc} = Q_{ref} = Q_v + Q_{tp} + Q_l \tag{4.3.19}$$

4.3.3 Drying chamber

Figure 3.10 shows a schematic diagram of the drying chamber. Basically, the drying chamber consists of a simple fan-duct system and an air cooled condenser. As shown in the diagram, the blower draws ambient air into the duct. Air flows over the finned exterior and heat transfer occur between air and refrigerant. After being heated, the air is used for drying towels. Humid air is then vented out to the atmosphere after drying. A perforated plate is placed after the diffuser in order to uniform the air flow velocity.

Heat received by air,

$$Q_a = m_a \times c_{pa} \times (T_{ao} - T_{ai}) \tag{4.3.20}$$

Condenser heat rejection in terms of maximum temperature,

$$Q_a = m_a \times c_{pa} \times \varepsilon_{conda} \times (T_{a\max} - T_{ai}) \tag{4.3.21}$$

Where, effectiveness of the condenser, $\varepsilon_{conda} = 1 - \exp(-NTU_{conda})$

Number of transfer units of condenser, $NTU_{conda} = \dfrac{(UA)_{conda}}{m_a \times c_{pa}}$

In the drying process, water vapor is added to air adiabatically. The water removal rate during drying is

$$m_w = m_a \times (\omega_{in} - \omega_{out}) \tag{4.3.22}$$

The saturated specific moisture (ωs) equations [115] were derived, using the linear regression method as,

(i) For T < 30℃,

$$\omega_s = 10^{-5} \times \exp(5.937415 + 0.073119 \times T - 0.00002865 \times T^2 + 0.00000149 \times T^3)$$

(ii) For T > 30℃,

$$\omega_s = 10^{-4} \times \exp(3.572565 + 0.078293 \times T - 0.0004318 \times T^2 + 0.000002873 \times T^3)$$

The specific enthalpy of air was determined from the following equation

$$h_a = 1.006979 \times T + \omega_s \times (2501 \times T + 1.805 \times T) \tag{4.3.23}$$

4.3.4 Thermostatic expansion valve

Two thermostatic expansion valves are used in this system which are fitted to the solar evaporator-collector and the room evaporator. A thermostatic expansion valve

is a component that controls the level of superheat at the outlet of the evaporator, i.e. solar evaporator-collector and the room evaporator. This is accomplished by use of a temperature sensing bulb filled with a similar gas as in the system that causes the valve to open against the spring pressure in the valve body as the temperature on the bulb increases. For the modeling of the thermostatic expansion valve, an isenthalpic expansion process is assumed. Therefore,

$$h_{f,i} = h_{f,o} \tag{4.3.24}$$

4.3.5 Room Evaporator

The rate of sensible heat transfer from the tube surface to the air d_{qs} can be calculated by the convection equation, which is shown below.

$$d_{qs} = h_c \times A \times (t_a - t_i) \tag{4.3.25}$$

The rate of mass transfer from air to the wetted tube surface is

$$d_m = h_D \times A \times (\omega_a - \omega_i) \tag{4.3.26}$$

Thus, the heat transfer due to the condensation or evaporation d_{qL} is given by

$$d_{qL} = h_D \times A \times (\omega_a - \omega_i) \times h_{fg} \tag{4.3.27}$$

Thus, the total heat transfer is

$$d_{qt} = d_{qs} + d_{qL} = \frac{h_c \times A}{c_{pm}} (h_a - h_i) \tag{4.3.28}$$

where, $c_{pm} = c_p + \omega_a \times c_{ps}$

The total heat is absorbed by refrigerant and thus space cooling is achieved. The cooling capacity during a cooling process is given by

$$Q_c = m_a \times (h_{air-out} - h_{air-in}) \quad (4.3.29)$$

4.4 Model for economic analysis

Economic analysis is the most important part to determine the practical feasibility of a system. For this purpose an economic analysis has been carried out for the integrated solar heat pump system. The details are given below.

4.4.1 Economic evaluation methodology

The economic analysis of solar energy systems involves multiple variables. In general, all the components in the system will have some effect on the thermal performance and the costs. In practice, the problem often reduces to a simpler one of determining the size of a solar system for a given load, with storage capacity and other parameter fixed in relation to collector area. For solar systems, the performance is more sensitive to collector area than any other variables. Therefore, in this analysis, the primary index for the size of the solar system is chosen to be the area of the evaporator collector.

The following are the types of cost encountered in the solar system analysis:

1) Capital equipment cost

2) Acquisition cost

3) Operation cost

4) Interest charges

5) Insurance and miscellaneous charges, taxes

6) Recurring or one-time cost associated with the system and salvage value.

4.4.2 Process of optimization

The optimization of solar systems can be broadly divided into three stages [94]:

a) Optimization criterion. The thermal performance of the system is to be optimized. The economic cost, e.g. annual cost, life cycle cost, etc., is to be minimized.

b) Thermal performance evaluation. The thermal performance of the system can be evaluated by using hour-by-hour simulation over a long period of time.

c) Optimization procedure. The influence of one variable on the function can be considered at a time and the maximum/minimum can be evaluated. This can be applied to two variables at a time to give contours from which the optimum can be determined. Alternatively, a differential expression can be developed for the function and the maximum/minimum can be estimated by obtaining the point at which the partial derivative is zero.

In this study, economic optimization is carried out by writing a differential expression, and the minimum/maximum is obtained by finding the point where the partial derivative is zero. The thermal performance of the system for a given load is evaluated by using hour-by-hour simulation of the system.

4.4.3 Analysis

Several economic figures of merit have been used as the criteria for the evaluation and optimization of a solar system, as described below.

(A) Life cycle costing:

(i) Annualized life cycle cost

(ii) Net life cycle savings

(B) Payback period.

(C) Internal rate of return.

Life cycle cost includes the sum of all costs over the life of the system or selected period of analysis, in today's dollars, taking into account the time value of money. This is done by using the annualized life cycle costs method or the life cycle savings (LCS) method.

It can be seen from analysis [85] that the governing equation describing the optimum condition becomes identical for annualized life cycle cost and the net life cycle saving and predicts the same collector area. Similarly, the analysis of internal rate of return and payback period lead to an identical equation, giving the same collector area, which is different from the one described earlier. For this reason, the life cycle cost and payback period will be investigated in this study.

Life cycle cost and payback period are the two merits, which have been used as the criteria for the evaluation and optimization of a solar integrated heat pump system.

Life cycle cost includes the sum of all costs over the life of the system, in current value, taking into account the time value of money. This is done by using the life cycle savings (LCS) method.

Boer [91] defines the payback period as the time at which first costs and annual expenses with compounded interest equal the total saving on energy costs with compounded interest.

The annualized life cycle cost and the net life cycle savings methods express the future expenses and benefits in terms of dollar, which requires assumptions on

future discount rate, inflation rate and fuel escalation rate. Thus the conversion of all future earnings to present worth involves a certain degree of uncertainty. However, the payback period method requires fewer assumptions about future costs.

4.4.4 Net Life Cycle Savings

Life cycle savings (LCS) are the difference between a reduction in fuel cost and an increase in expenses.

$$LCS = \frac{\left(Q_s + Q_{ac} + W\right) C_F}{C_{RF}\left(i'', n\right)} - C_s \tag{4.4.1}$$

It should be noted that, the reduction in fuel cost for this integrated solar system is (Q_s+Q_{ac}+W), which is different from that of single function solar system. Normally, the reduction in fuel cost for solar system is equal to the solar heat gain, Q_s. However, the reduction in fuel cost for this integrated solar heat pump system is the energy release in two condensers, which can also expressed as the combination of solar heat gain, air conditioning heat gain and compressor work input.

The maximum LCS occurs at the point:

$$\begin{aligned} &\frac{\partial}{\partial A}\left(LCS\right) \\ &= -C_D C_{RF}\left(i', n\right) + \frac{\partial\left(Q_s + Q_{ac} + W\right)}{\partial A} \frac{C_F C_{RF}\left(i'', n\right)}{C_{RF}\left(i'', n\right)} \\ &= 0 \end{aligned} \tag{4.4.2}$$

4.4.5 Payback Period

The minimum payback period, using discounted auxiliary fuel cost is given by the following equation:

$$\frac{C_s}{\left(Q_s + Q_{ac} + W\right)} = \frac{C_F}{C_{RF}\left(i", n_p\right)} \tag{4.4.3}$$

Payback period n_p is:

$$n_p = \frac{\ln[1-(i-e)x]}{\ln\left(\frac{1+e}{1+i}\right)} \tag{4.4.4}$$

Where, $x = \frac{C_s}{(Q_s + Q_{ac} + W)C_F}$

Differentiating equation 4.4.3 with respect to the area (A):

$$\frac{\partial\left(Q_s + Q_{ac} + W\right)}{\partial A} = \frac{\left(Q_s + Q_{ac} + W\right)C_D}{C_D A + C_I} \tag{4.4.5}$$

4.4.6 Coefficient of Performance (COP)

For the water condenser, where the heat is released by the refrigerant and absorbed by the water, the COP is given by

$$COP = \frac{Thermal\ Energy\ released\ by\ the\ condenser}{Energy\ input\ to\ compressor} \tag{4.4.6}$$

For the cooling effect, the performance indicator is cooling COP, defined as below:

$$COP_{cooling} = \frac{Thermal\ Energy\ absorbed\ by\ the\ evaporator}{Energy\ input\ to\ compressor} \tag{4.4.7}$$

4.4.7 Solar Collector Efficiency

The efficiency of the solar evaporator-collector is given by the conventional expression:

$$\eta_c = \frac{Useful\ energy\ gain\ by\ the\ evaporator\text{-}collector,\ Q_u}{Solar\ Energy\ available\ on\ the\ evaporator\text{-}collector,\ A_c I} \tag{4.4.8}$$

This efficiency illustrates the relationship between the total energy gain via the solar

evaporator-collector and the product of collector area and solar irradiation.

4.4.8 System Energy Conversion Ratio (ECR)

The energy conversion ratio (ECR) of the system is defined as the following expression:

$$ECR = \frac{Total\ energy\ \ for\ usefull\ effects(co\,oling\ and\ heating)}{Total\ Energy\ Input\,(Compressor,blowers\ and\ energy\ gain\ via\ collector)} \quad (4.4.9)$$

4.5 Simulation Algorithm

To determine the performance of the system, the analytical model of each component was used in a simulation program. The following is an overview of the simulation's algorithm:

1. Input conditions, such as meteorological conditions, collector area and compressor running frequency, are given.

2. Using the input conditions, the program calculates the refrigerant temperature at the outlet of the evaporator collector. This subroutine calculates the evaporator collector's efficiency and the refrigerant temperature at the outlet. Initially, based on the refrigerant properties, the subroutine will determine the phase of the refrigerant, and the corresponding equations used. Useful energy absorbed in each segment of the model will increase the energy level of the refrigerant until its exit condition from the evaporator collector is found. The efficiency of the collector is found from the energy gain of the refrigerant compared to radiation on the collector.

3. Similar calculation methods are used in the room evaporator subroutine. The subroutine for the evaporator will also calculate the variation of room temperature.

4. Refrigerant leaving the room evaporator mixing with the refrigerant from evaporator collector. The temperature and pressure of the refrigerant after mixing is calculated. This is the inlet condition for the compressor.

5. Simulation the compressor work and the temperature of refrigerant leaving the compressor. The temperature value at the compressor outlet becomes the inlet value for the water condenser coil.

6. The water condenser subroutine comes next. It calculates the heat transfer that took place in the water condenser. Feed water temperature is same as ambient temperature.

7. Temperature at the outlet of condenser coil becomes the input for the water condenser tank. This subroutine calculates the temperature leaving the tank.

8. Taking collector efficiencies, water production, and temperature values at certain points, the coefficient of performance and performance ratio is calculated.

9. The program displays all the desired values. The results are then saved into MS Excel format.

4.5.1 Flow chart of simulation program

To determine the thermal performance of the system a simulation program has been developed. The procedure of the simulation strategy is as follows:

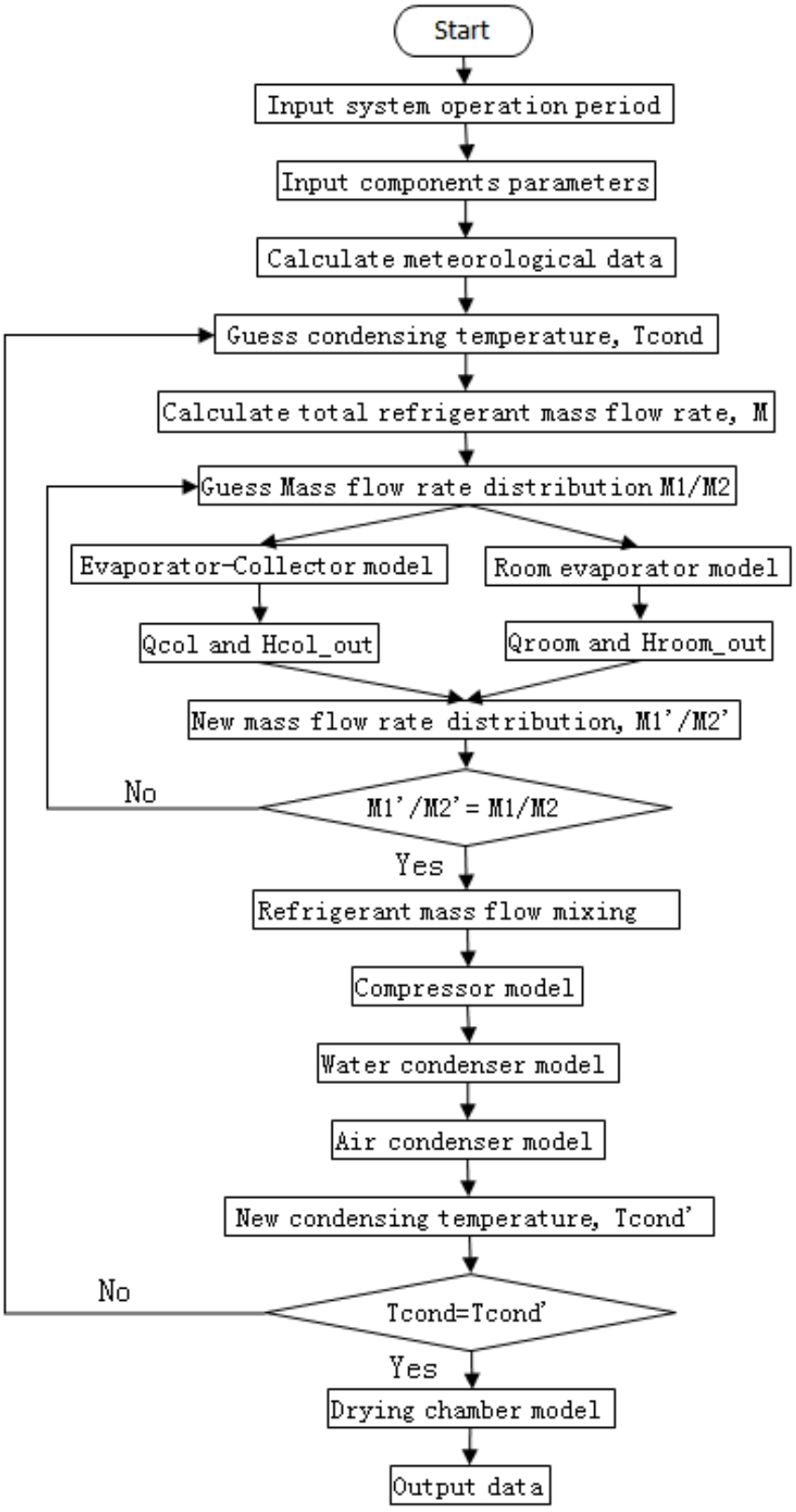

Figure 4.8 Flow diagram of simulation model

CHAPTER 5 RESULTS AND DISCUSSION

5.1 Experimental results

A series of experiment has been conducted under the meteorological conditions of Singapore. The results obtained from experiments and analyses are presented in this section.

The present experiment set-up was designed to operate under different modes with the use of control valves:

1. Water heating, drying and air-conditioning with evaporator-collector (Full mode)

2. Drying and air conditioning with evaporator-collector (Bypass water condenser)

3. Water heating and air conditioning with evaporator-collector (Bypass air condenser)

4. Water heating and drying with evaporator-collector (Bypass room evaporator)

5. Water heating, drying and air conditioning without evaporator-collector (Bypass evaporator–collector)

In this section, the experimental results obtained under different modes are presented and compared. Here, the influence of different modes of operation on the performance of the system has been observed and discussed.

Meteorological Conditions

The climate of Singapore is characterized by relatively uniform temperature, high humidity and abundant rainfall Figure 5.1.1 shows the measured meteorological

data for Singapore for a typical day (12 September 2004, one of the days of the experiments). As seen from Figure 5.1.1, both solar radiation (global) and wind speed vary in an unpredictable manner with time. The ambient temperature reaches the highest point at around 2pm and relative humidity rises to as high as 95% in the early hours of the morning.

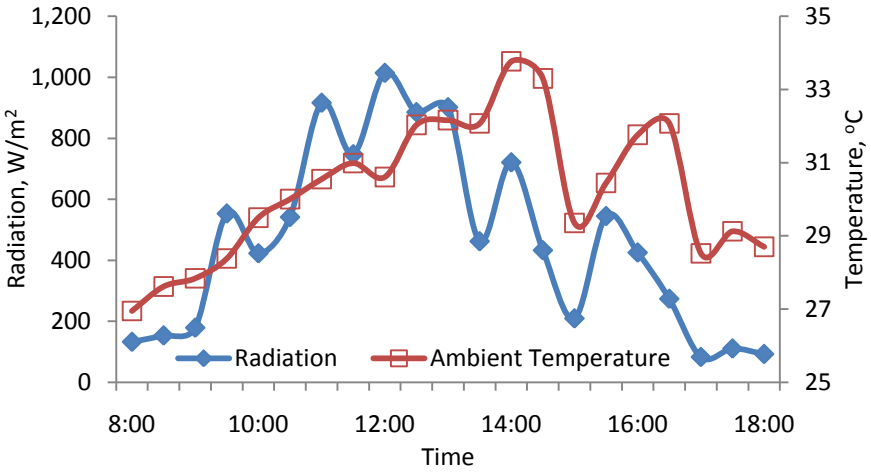

(a) Variation of solar radiation and ambient temperature

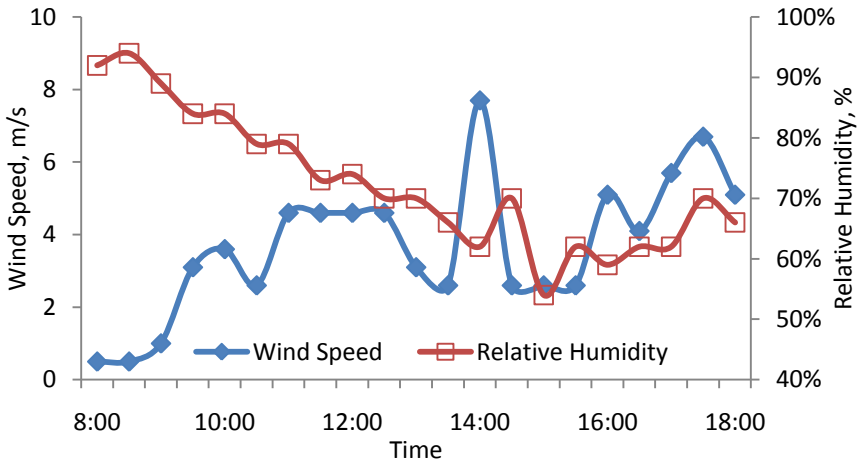

(b) Variation of relative humidity and wind speed

Figure 5.1.1 Measured meteorological data for a typical day in Singapore

5.1.1 Full mode operation

In full mode operation, with two condensers, water condenser and air condenser, and double evaporators, room evaporator and evaporator-collector, the present system can provide water heating, drying and air-conditioning simultaneously. Experiments under full mode operation were conducted from 10am to 16:30pm.

Water heating

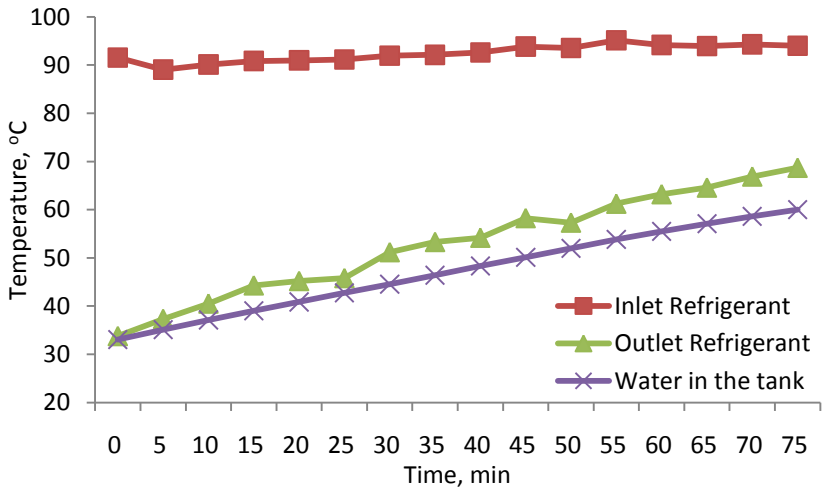

Figure 5.1.1.1 Variation of temperatures of water and refrigerant with time

Figure 5.1.1.1 shows the change in refrigerant temperature at inlet and outlet of water-cooled condenser and water temperature in the tank with time using two solar collectors. The temperature of the 400 liters of water in the tank increases in a steady manner and rises from 33℃to 60℃ in 75 minutes.

As seen from the figure, the outlet refrigerant temperature increased with the rise of water temperature while the inlet refrigerant temperature remained at around 90℃. It lead to a decline of the temperature difference between the inlet and outlet refrigerant with the rise of water temperature.

An energy analysis was conducted for the experimental data and the results are shown in figure 5.1.1.2. With the rise of water temperature, the condensing heat

released from the refrigerant declined due to a reduction in temperature deference between the refrigerant and water.

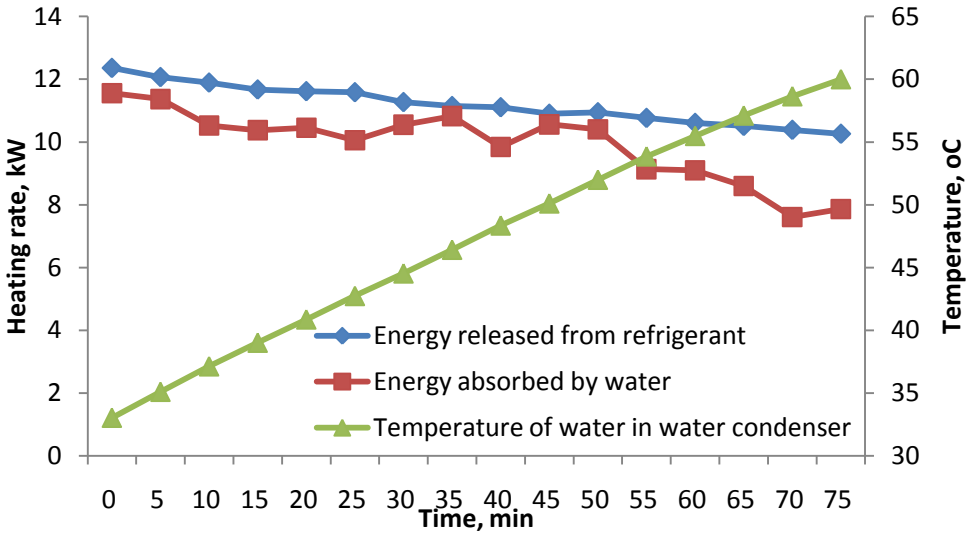

Figure 5.1.1.2 Variation of heating rate with time using two collectors

Most of the heat released by the refrigerant was absorbed by water, with a little dissipation to the ambient. The increase of the gap between the energy released by the refrigerant and the energy absorbed by the water indicates that the energy dissipated to the ambient is rising with the rise of water temperature

Drying

After passing through the water condenser, the refrigerant is allowed to flow through an air condenser to ensure that the refrigerant is fully condensed. In this study, the air at the inlet of air condenser is defined as "inlet air"; the air at the exit of the air condenser (inlet of drying chamber) is called "heated air" and the air at the exit of the drying chamber is addressed as "discharged air".

Textile with the bone dry weight of 1.5kg was wetted by "manual spinning" so that the initial moisture content is around 1. They are hanged in the drying chamber in a uniform pattern.

As seen from Figure 5.1.1.3, the refrigerant temperature at the air condenser inlet

increased from 33℃ to 68℃ due to the fact that water temperature in the water condenser increased from 30℃ to 60℃, as seen in figure 5.1.1.2.

With the rise of refrigerant temperature at the inlet of the air condenser, the gap between the air temperatures at the inlet and exit of the air condenser increased, indicating an increase in the energy absorbed by the air condenser. For the air condenser, the temperature difference between inlet and outlet air is up to 7℃ when the inlet refrigerant temperature reaches 68℃, while only 1.5℃ when inlet refrigerant temperature is 37℃.

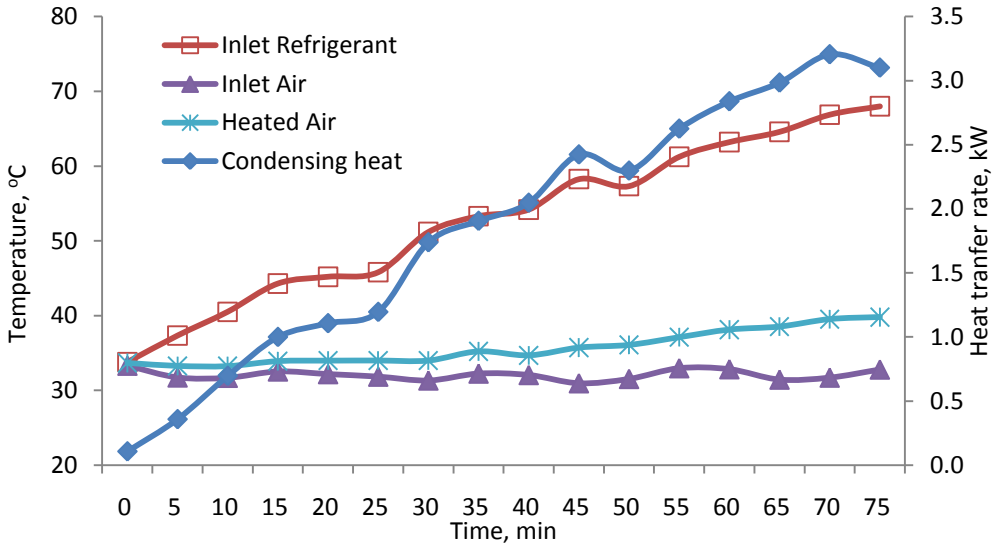

Figure 5.1.1.3 Variation of temperature of refrigerant and air for air condenser

The energy release by refrigerant to the air for drying increased with the rise of water temperature. When water temperature is 30℃, only 0.2kW condensing heat released for drying and it went up to 3kW when water temperature was 60℃. It indicated that the drying effect is highly depended on the water temperature in the water condenser when system is operated in full mode.

Figure 5.1.1.4 shows the variation of air temperature and moisture content of material during the drying process. In this drying process, temperature of the water in the water condenser was maintained at 60℃ by controlling the water flow rate. It

enabled the stabilization of the temperature of air for drying.

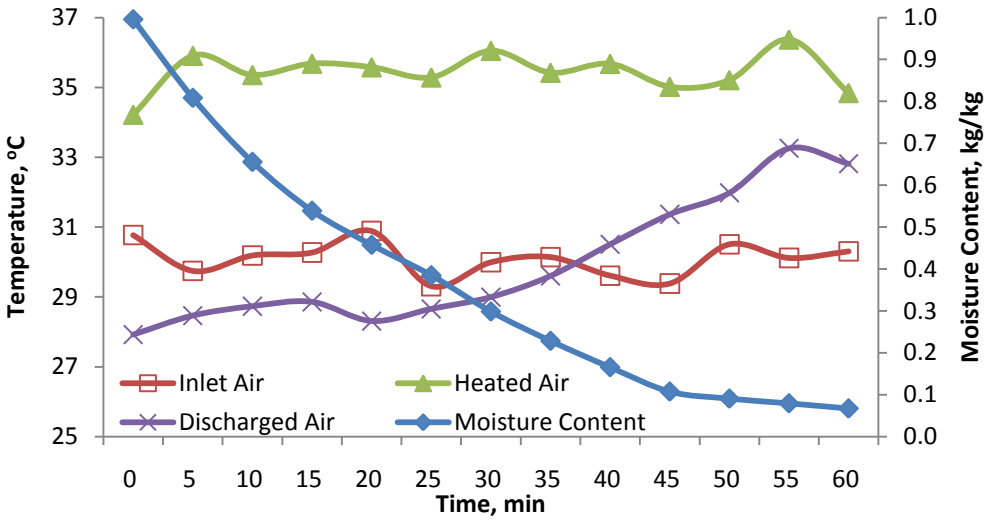

Figure 5.1.1.4 Variation of air temperature and moisture content with time

As seen in the figure, the inlet air, with the temperature of around 30℃ and RH of 0.6, was heated to around 36℃ in air condenser. This warm air flowed through the drying chamber and discharged after releasing heat in the drying process. Textile with the bone dry weight of 1.5kg was wetted and hanged in the drying chamber. The moisture content of material was reduced from 0.9 to 0.09 in 60 minutes. The drying falls mostly in the falling rate region. With the declination of moisture content, the temperature difference between the inlet and outlet of the drying chamber declined gradually. In full mode operation, the heated air temperature is normally lower than 40℃ because the refrigerant from compressor condensed in water condenser and released most of condensing heat before it went through the air condenser to heat the ambient air.

Specific Moisture Extraction Rate (SMER) is the most commonly used criterion for characterizing the performance of dryers. It is defined as the ratio of the moisture removed in kg to the energy input in kWh. Figure 5.1.1.5 shows the variation of SMER with time in full mode operation. A maximum of SMER value of 0.68 kg/kWh

is observed. As seen from the figure, the SMER values decline with time. This is due to the fact that, as drying proceeds, the moisture removal rate decreases.

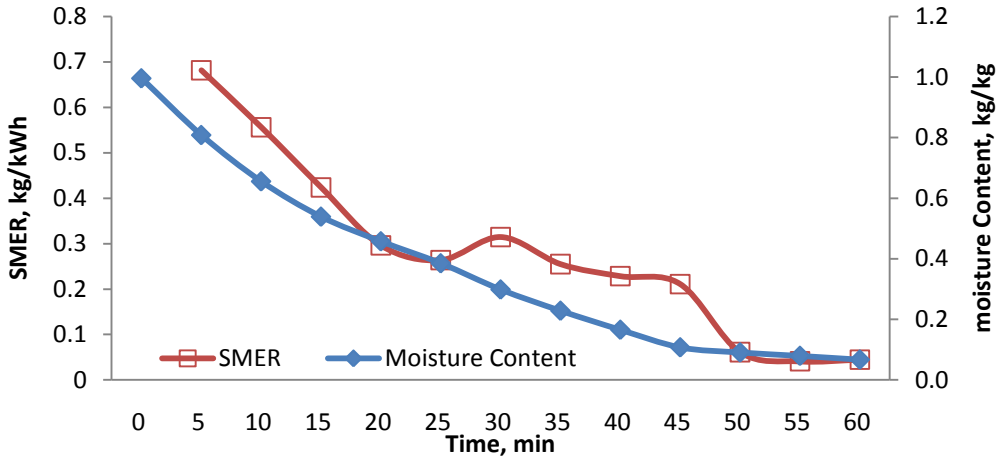

Figure 5.1.1.5 Variation of air temperature and moisture content with time

Air-conditioning

As seen from figure 5.1.1.6, room temperature was cooled from 27℃ to 20℃ in one hour and became stable.

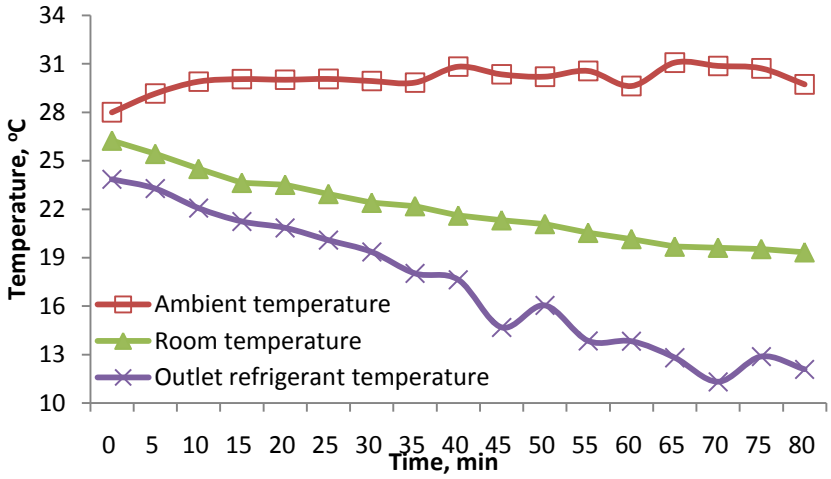

Figure 5.1.1.6 Variation of temperature of ambient, room and outlet refrigerant.

In the room evaporator, refrigerant after expansion valve absorbed heat from room air and became superheated at evaporator outlet. As seen from the figure 5.1.1.6, temperature of refrigerant at room evaporator outlet was reduced due to a decline in room temperature, leading to a reduction in heat transfer.

For a constant mass flow rate of refrigerant through the room evaporator, heat absorbed by the refrigerant declined with time, as the room temperature approaches the desired condition.

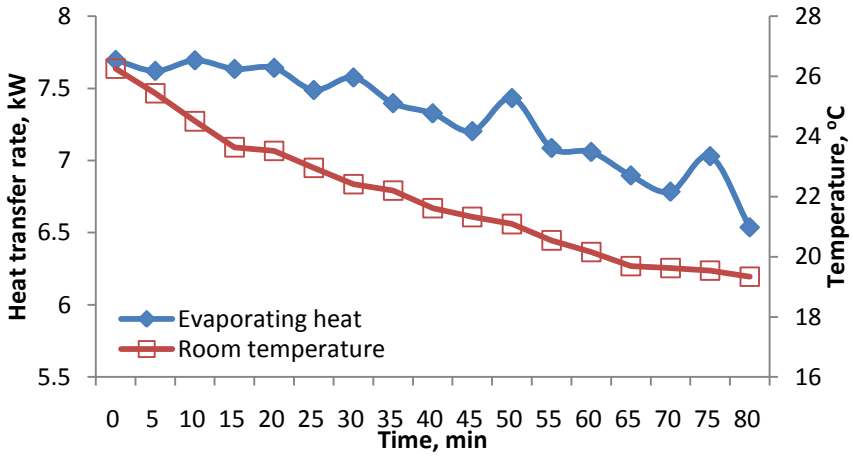

Figure 5.1.1.7 Variation of room temperature and evaporating heat with time.

As seen from the figure 5.1.1.7, evaporating heat of room evaporator dropped from 7.8kW to 6.6kW when the room temperature went down from 26℃ to 20℃.

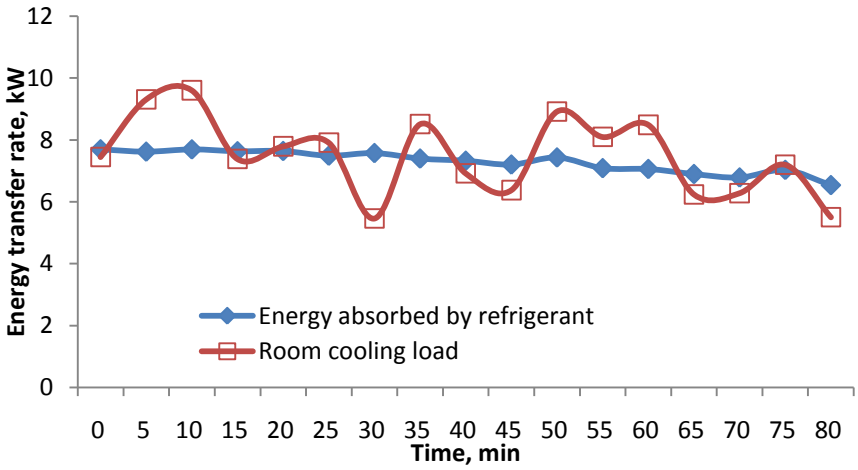

Figure 5.1.1.8 Energy balance in room evaporator with time.

Figure 5.1.1.8 presents an analysis of energy balance for the room evaporator. Energy absorbed by the refrigerant was compared with the room cooling load. Room cooling load means the heat transfer rate required to change the room temperature, as presented in figure 5.1.1.6. As seen from figure 5.1.1.8, energy

absorbed by refrigerant shows a declining trend because the room temperature is dropping. It matched the room cooling load reasonably well.

Evaporator-collector

After passing through the expansion valve, flows through the two evaporator-collectors and absorbs solar and ambient energy.

Figure 5.1.1.9 shows the variation of average absorber surface temperature of evaporator-collector and irradiation with time. In this case, two collectors are used with the area of $3m^2$.

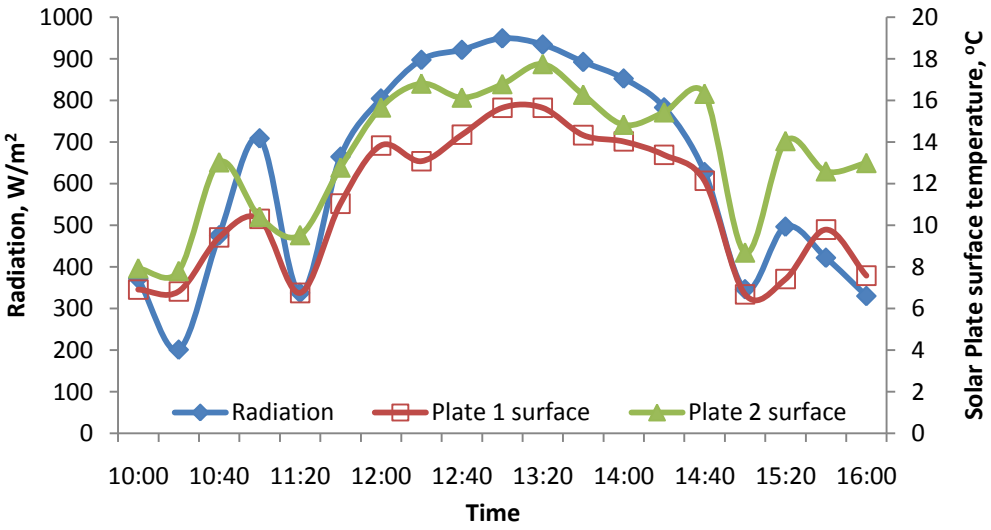

Figure 5.1.1.9 Variation of collector surface temperature and irradiation with time.

As seen from the figure, the evaporator-collector surface temperatures show similar variation as the solar irradiation. It can be explained that the surface temperature is affected mainly by the instantaneous solar irradiation.

It is also found that the surface temperature of second evaporator-collector is always higher than the first one. It is contributed by the higher average refrigerant temperature in second evaporator-collector due to the fact that the refrigerant in certain section of the second evaporator-collector is in a superheated state.

Useful energy gain by the evaporator-collector is a combination of energy gain due

to irradiation and also the energy gain from the ambient. Figure 5.1.1.10 illustrated the effect of solar radiation on the useful energy gain. It shows that the total useful energy gain by the evaporator-collector increases with the rise of radiation.

However, unlike the normal solar collector, the amplitude of fluctuation of the useful energy gain by this evaporator-collector is less than that of solar radiation. This can be attributed to the fact that it not only absorbs energy from radiation but also from ambient due to its low surface temperature (lower than ambient, as shown in figure 5.1.1.9), leading to a relatively steady useful energy gain.

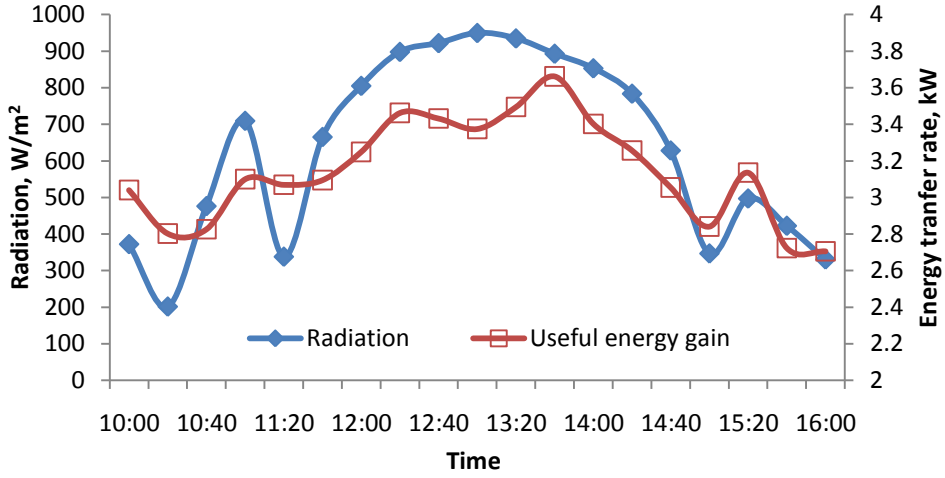

Figure 5.1.1.10 Variation of useful energy gain and irradiation with time.

The variation of collector efficiency and irradiation with time for the total collector area of 3m^2 is shown in figure 5.1.1.11.

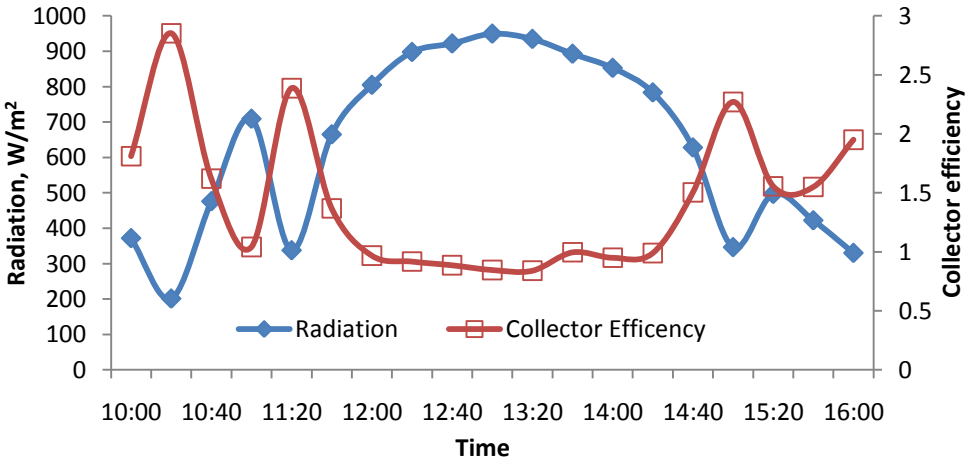

Figure 5.1.1.11 Variation of solar collector efficiency and irradiation with time

Collector efficiency is defined as the rate of total useful energy gain to the total irradiation on the collector surface. As seen from the figure, evaporator-collector efficiency ranges from 0.9 to 2.9 at day time. The evaporator-collector efficiency of one or more than one can be attributed to the fact that the collector absorbs energy from ambient as well. Because of the influence of this energy absorbed from ambient, instead of heat losses from the collector, the collector efficiency remains fairly high even with the drop in solar radiation, as seen from the Figure 5.1.1.11.

Figure 5.1.1.12 shows the relationship between solar collector efficiency and the $(T_a\text{-}T_{fi})/I$. The useful energy gain can be written in the following form:

$$Q_u = A_c F_R [\alpha I + U_L (T_a - T_{fi})]$$

Where F_R is called the collector heat removal factor:

The collector efficiency can be expressed by a conventional definition as:

$$\eta = \frac{Q_u}{A_c I} = F_R \alpha + F_R U_L \frac{(T_a - T_{fi})}{I}$$

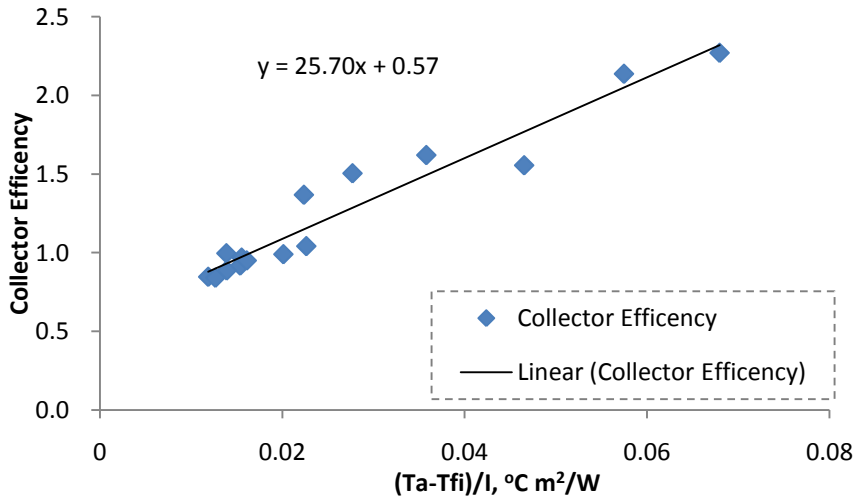

Figure 5.1.1.12 Variation of solar collector efficiency with (Ta-Tfi)/I

From the trend line in the figure, given the plate absorptance α of 0.9:

$$\begin{cases} F_R\alpha = 0.57 \\ F_R U_L = 25.7 \\ \alpha = 0.9 \end{cases}$$

Heat removal factor F_R and overall heat loss coefficient U_L can be calculated as:

$$\begin{cases} F_R = \dfrac{F_R\alpha}{\alpha} = \dfrac{0.57}{0.9} = 0.64 \\ U_L = \dfrac{F_R U_L}{F_R} = \dfrac{25.7}{0.64} = 40.3\ \mathrm{W/m^2C} \end{cases}$$

System Performance

The solar assisted heat pump system for water heating, drying and air-conditioning in the present work has two condensers and two evaporators in full mode operation. It is important to analysis the distribution of condensing heat in two condensers and the energy absorbed by the two evaporators.

Figure 5.1.1.13 shows the variation of water temperature in the water condenser and the heated air temperature in air condenser. It also shows the heat released from refrigerant in the two condensers and the sum of these two quantities.

In this case, the 400L water in the water condenser is kept on heating without discharging when the temperature of water is lower than 60℃. Once the water in the tank reaches a temperature of 60℃, it is replaced by supply water at about 30℃.

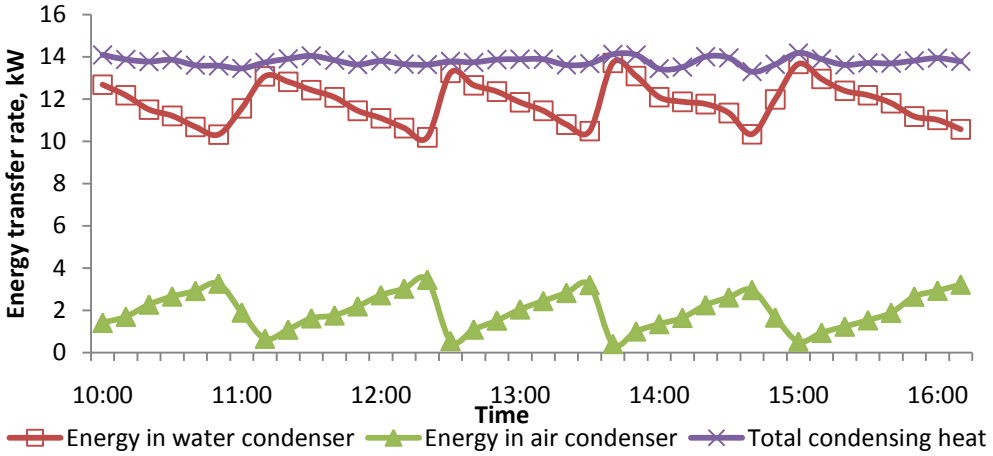

(a)

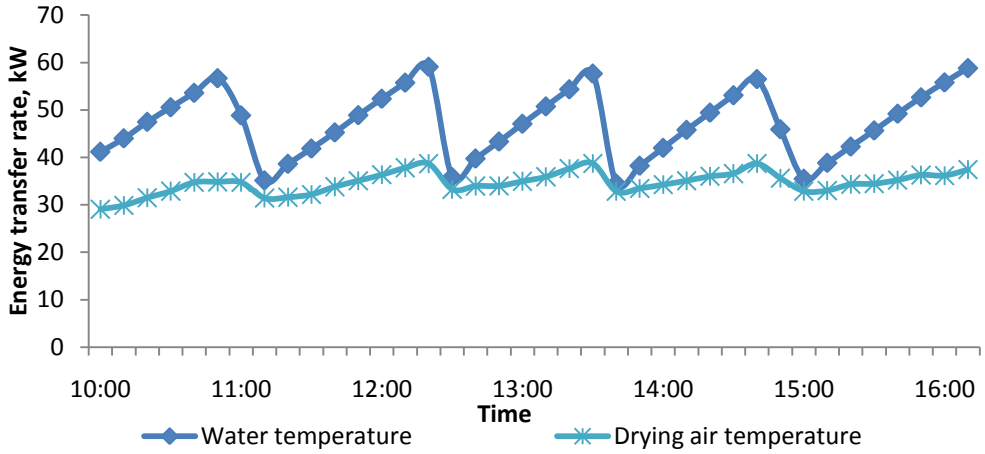

(b)

Figure 5.1.1.13 Variation of heat transfer and temperature in condensers with time

From the figure, it can be seen that the energy released in water condenser is affected mainly by the water temperature. If the water temperature in the water tank is higher, the heat released by the refrigerant to water is reduced, which may be attributed to a reduction of temperature difference between the refrigerant and water in water condenser. As a result, the temperature of the refrigerant at the exit of water condenser is higher. The heat rejection in water condenser is 13kW when water is 30℃ while it is 10kW when water temperature is 60℃.

The refrigerant from water condenser is then condensed further in air condenser. As seen from the figure, the heat released in air condenser increased with decline of heat delivered to the water condenser. The condensing heat rejection in air condenser is 0.7kW when water is 30℃ while it is 3.5kW when water temperature is 60℃. As a result, the temperature of heated air increases with the increase in energy delivered at the air condenser.

Compared to the air temperature of 45℃ to 50℃, which is controlled by the electrical power, in conventional electrical dryer, the drying air temperature in this multifunction solar heat pump system can only up to 40℃ (when ambient

temperature is 33℃) and also highly effected by the water temperature in full mode operation. However, the series connection of two evaporators ensured the fully condensing of refrigerant, leading to a stability of total condensing heat rejection, as shown in the Figure 5.1.1.13. The total condensing heat is maintained at 14kW despite the fluctuation of water temperature.

Figure 5.1.1.14 shows the variation of energy absorbed in the two evaporators, which are in parallel arrangement, and the sum of these two quantities. As shown in the figure, with the rise of water temperature, the evaporating heat absorbed by the room evaporator was slightly decreased, caused by the increase of evaporating temperature. The rate of heat absorption by the room evaporator is maintained in the range of 6.8kW to 7.8kW.

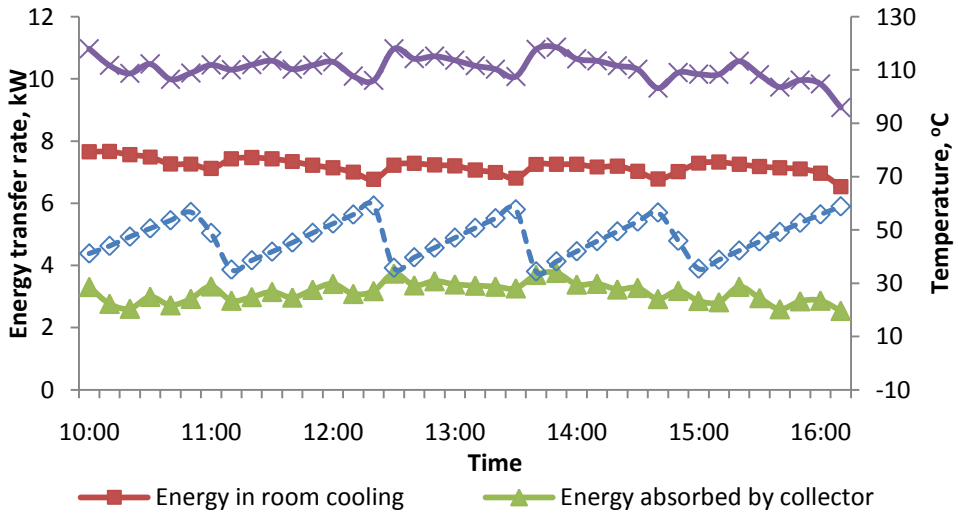

Figure 5.1.1.14 Variation of heat transfer in evaporators with time

The effect of radiation on the evaporating heat rejection in solar evaporator -collector is analyzed in the discussion on figure 5.1.1.10. As seen from figure 5.1.1.14, it is also slightly affected by water temperature for the same reason of variation of evaporating heat in room evaporator.

The total evaporating heat in two evaporators is maintained in the range of 10kW to

12kW. There is a boost of it when the water temperature drops from 60℃ to 30℃ rapidly. It is attributed to the decline of evaporating temperature caused by the decrease of condensing temperature.

The effect of water temperature on the system coefficient of performance (COP) is illustrated in Figure 5.1.1.15. As seen from the figure, notable enhancement of COP occurs when the water temperature rapidly drops from 60℃ to 30℃. It indicated that the system overall heating performance at the water temperature of 60℃ is better than that of 30℃. The COP of the system raised between 4.5 and 6.5 for the condition considered here.

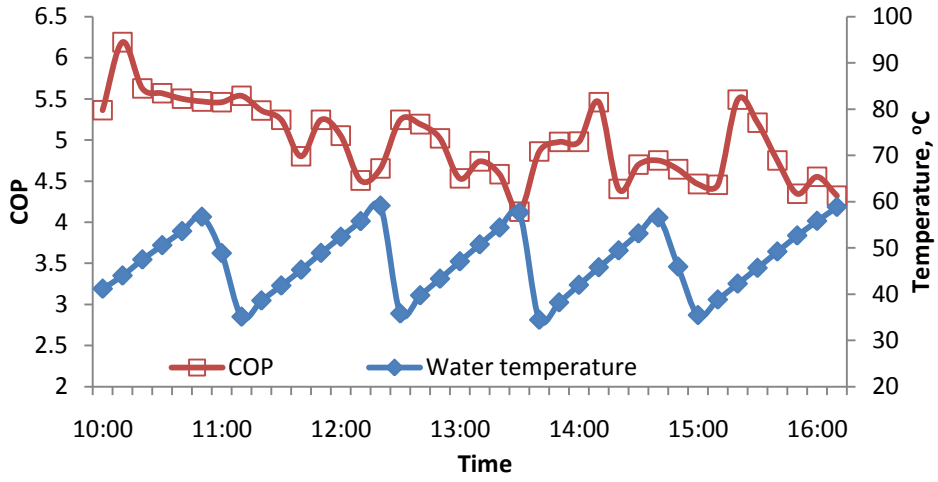

Figure 5.1.1.15 Variation of COP and water temperature with time

The variation of the energy conversion ratio (ECR) of the system is illustrated in Figure 5.1.1.16. As seen from the figure, ECR varied between 3.0 to 4.0 with the average of 3.3 for the condition considered here. It indicated that, with the use of solar evaporator-collector, every 1kW of energy input to the system can generates 3.3 kW effect of cooling, water heating and drying.

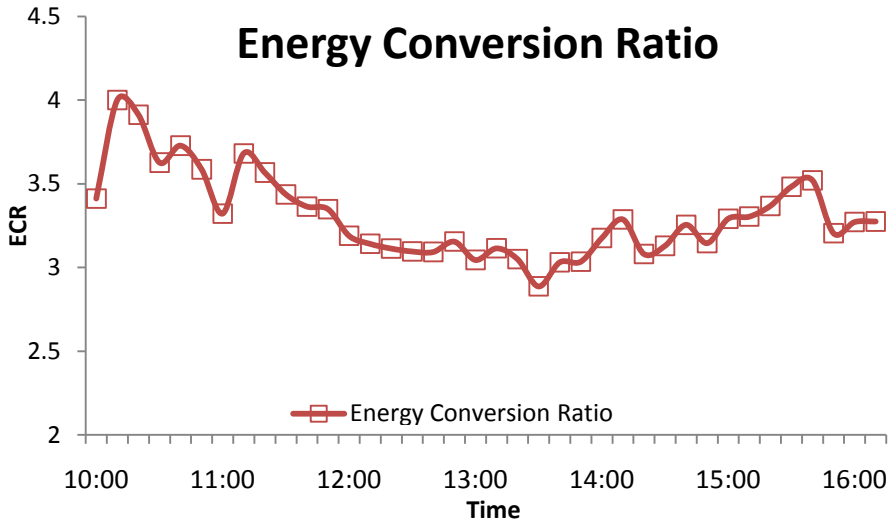

Figure 5.1.1.16 Variation of energy conversion ratio (ECR)

The average energy distribution in each of the major components of the system is presented in figure 5.1.1.16.

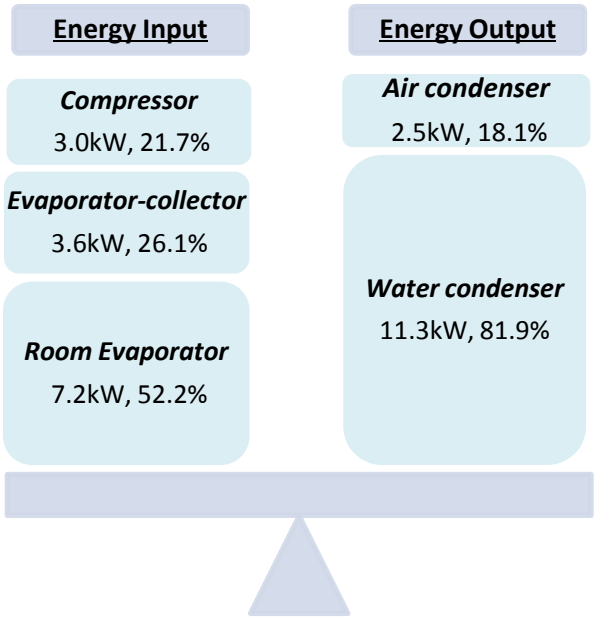

Figure 5.1.1.16 Energy distribution in system components

5.1.2 Drying and air conditioning with solar evaporator-collector

The temperature of heated air for dying is lower than 40℃ and highly depended on the water temperature under full mode operation. The water condenser can be bypassed when there is no demand of hot water or demand of fast drying. When water condenser is bypassed, the system operation mode is called "No water condenser mode" (NoWC mode). The system performance in NoWC mode operation is presented and discussed in this section.

Drying

Figure 5.1.2.1 shows the variation of air temperature and moisture content of material in drying process in NoWC mode operation. In this drying process, the refrigerant from compressor is solely condensed by the air condenser.

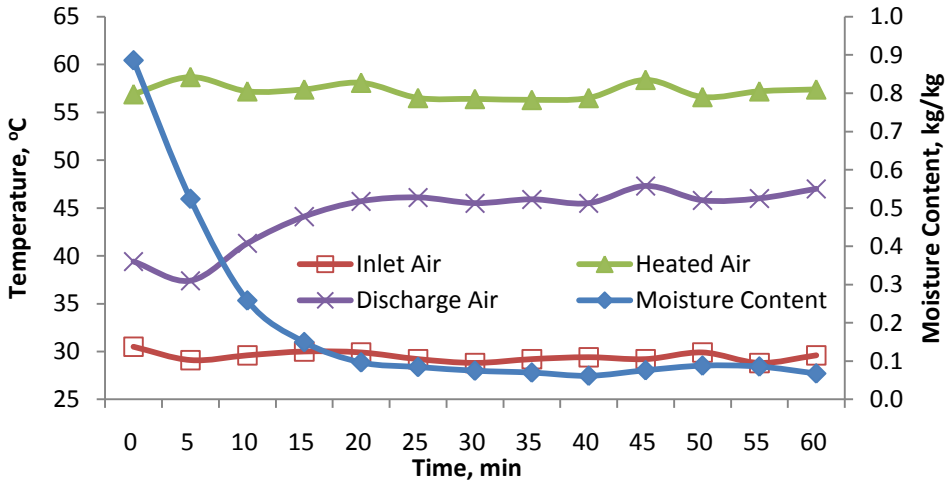

Figure 5.1.2.1 Variation of air temperature and moisture content with time

As seen in the figure, ambient air, with the temperature of around 30℃ and RH of 0.6, was heated by the refrigerant from the compressor, where the temperature was about 85℃ at air condenser inlet. The temperature of heated air for drying is more than 55℃. This hot air was allowed to flow through the drying chamber and discharged. Textile with the bone dry weight of 1.5kg was wetted and hanged in the drying chamber. The moisture content of material was reduced from 0.9 to 0.09 in

20 minutes. With the decline of moisture content, the temperature difference between the heated air and discharged air was reduced gradually.

Compared to the drying time of 60 minutes in full mode operation, drying time for NoWC mode operation is much shorter because of the higher drying temperature, due to the fact that all the condensing heat is release in air condenser.

Air-conditioning

As seen from figure 5.1.2.2, room temperature was cooled from 27℃ to 20℃ in 1.5 hour before it became stable. Heat transferred from room air to refrigerant through the evaporator decreased with the decline of room temperature, because of the reduced temperature difference between room air and refrigerant in the evaporator. The rate of heat absorption for cooling is in the range of 6.5kW to 7kW.

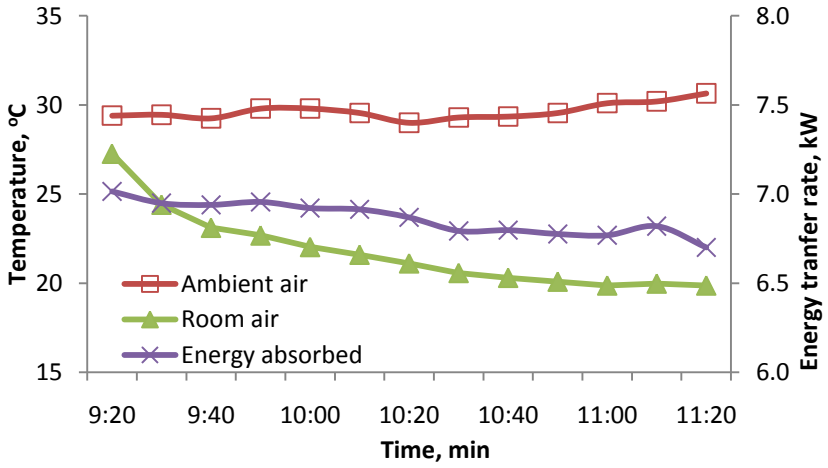

Figure 5.1.2.2 Variation of ambient temperature, room temperature and evaporating heat with time.

Compared to the cooling process in full mode operation, the cooling speed and the evaporating heat transfer rate for NoWC mode is slightly lower due to the decline of condensing heat caused by the absence of water condenser.

Evaporator-collector

Figure 5.1.2.3 described the effect of solar irradiation on the useful energy gain by

the evaporator collector.

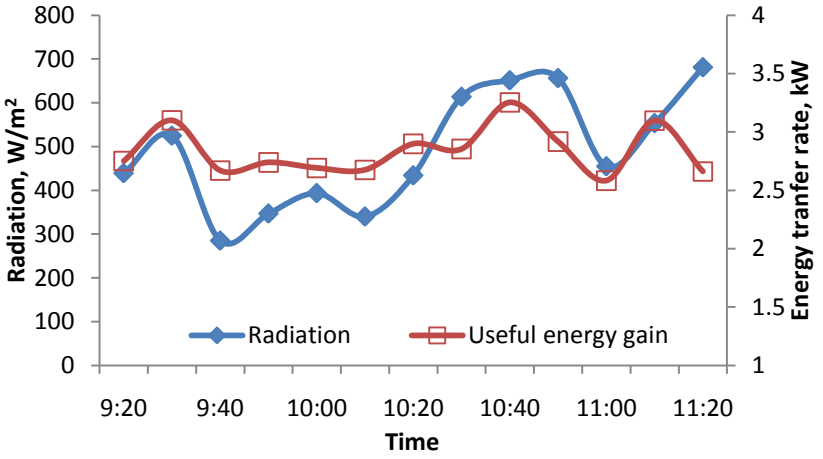

Figure 5.1.2.3 Variation of useful energy gain and irradiation with time.

It shows that the total useful energy gain by the evaporator-collector increases with the rise of radiation. However, the amplitude of the fluctuation of useful energy gain is less than that of solar radiation. This can be attributed to the fact that it not only absorbs energy from radiation but also from ambient due to its low surface temperature, leading to a relatively steady useful energy gain. Compared to the total useful energy gain of around 3kW in full mode operation, that in NoWC mode is slightly lower due to an increase in evaporator-collector inlet temperature.

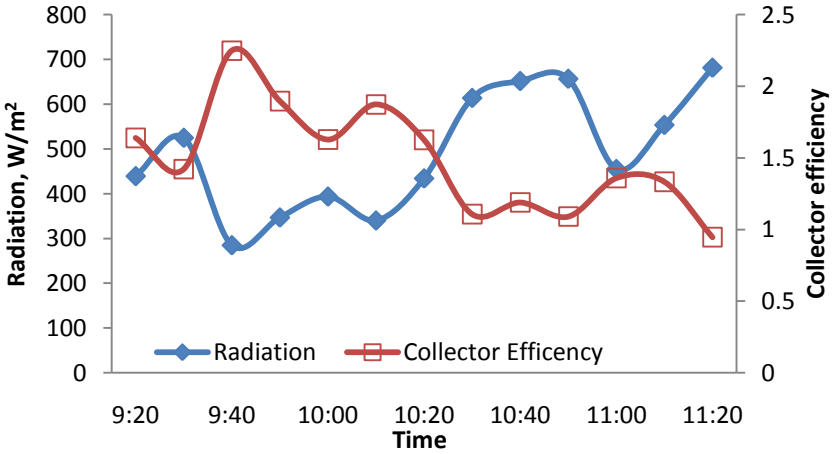

Figure 5.1.2.4 Variation of collector efficiency and irradiation with time

In Figure 5.1.2.4, the variation of collector efficiency and irradiation with time for the

total collector area of 3m^2 is shown. As seen from the figure, evaporator-collector efficiency ranges from 0.9 to 2.3. Same as the full mode operation, the evaporator-collector efficiency varied in the opposite trend of the fluctuation of solar radiation in NoWC mode.

System Performance

Figure 5.1.2.5 presented the variation of evaporating heat absorption in the two evaporators, condensing heat released in air condenser and system heating COP with time in NoWC mode operation.

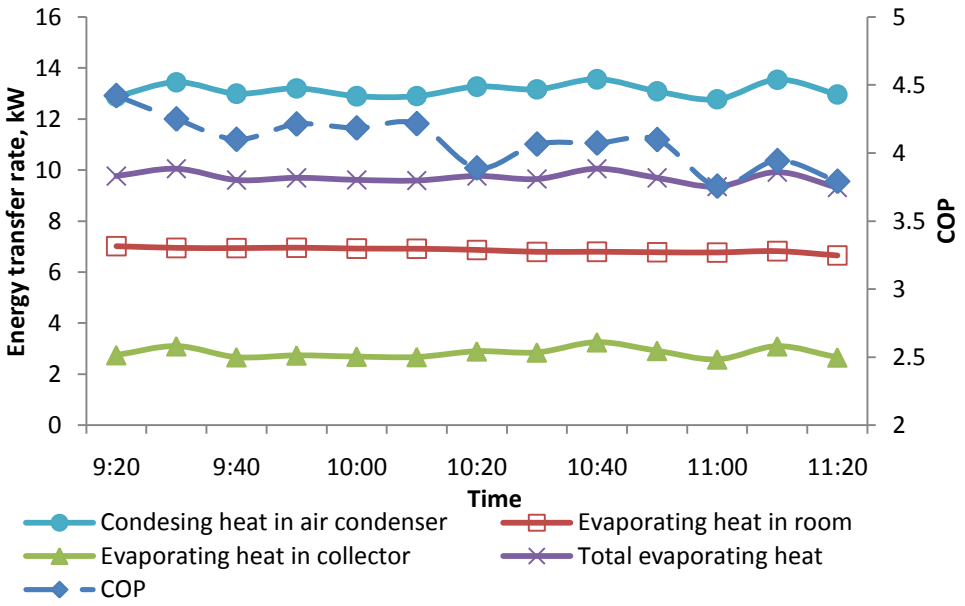

Figure 5.1.2.5 Variation of energy distribution and system COP with time

As seen from figure 5.1.2.5, without water condenser, the heat rejection rate in air condenser is very stable in NoWC mode operation. This leads to a stable condition of the room evaporator, where the energy absorbed remained constant.

Compared to the energy distribution in full mode operation, the condensing heat rejection in air condenser to heat the air for dying is remarkably enhanced to 13.2kW. However, it is still lower than the total condensing heat (14kW) in the double condensers of full mode operation. In NoWC mode operation, both

evaporating heat in the room evaporator and in the evaporator-collector is slightly lower than that in full mode operation.

As discussed in 5.1.1, the system COP in full mode operation will be affected by both water temperature and solar irradiation. However, without water condenser, the system COP in NoWC mode operation is not affected by water temperature. As seen in Figure 5.1.2.6, COP increase and decrease with the rise and fall of solar radiation.

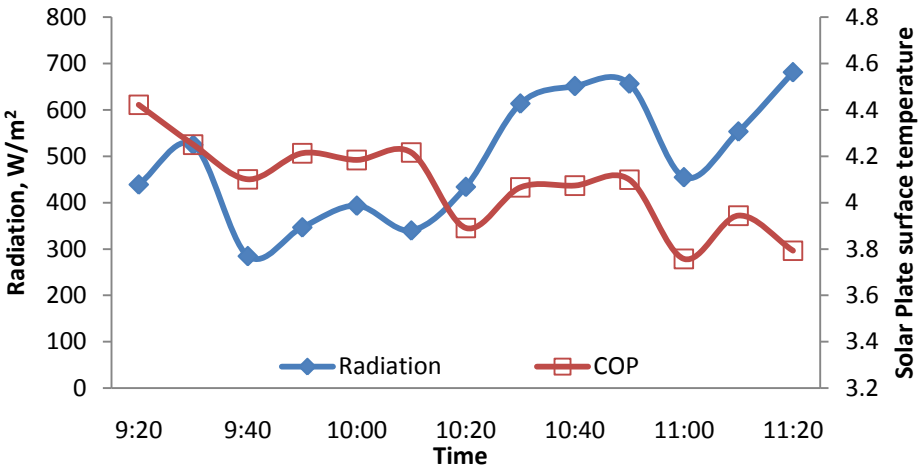

Figure 5.1.2.6 Variation of solar radiation and system COP with time

COP is in a slight declining trend in the whole operation. It might be due to a decrease of evaporating heat provided by room evaporator as a result of an increase of evaporator operating temperature, which is described in figure 5.1.2.2

The average COP of NoWC mode is around 4.2, which is lower than that of full mode operation, which is around 4.7, due to the fact that the condensing effect of double condenser is better than that of single air condenser. However, without the effect of water temperature, the amplitude of the fluctuation of COP of NoWC operation is less than that of full mode.

5.1.3 Water heating and air conditioning with solar collector

When air condenser is bypassed, the system operation mode is called "No air condenser mode" (NoAC mode). In this operation mode, the system can serve water heating and air conditioning. The system performance in NoAC mode operation is presented and discussed in this section.

Water heating

Figure 5.1.3.1 shows the variation of energy released in water condenser and the temperatures of refrigerant and water in the heating process in NoAC mode operation. In this heating process, the refrigerant from compressor is solely condensed by the water condenser.

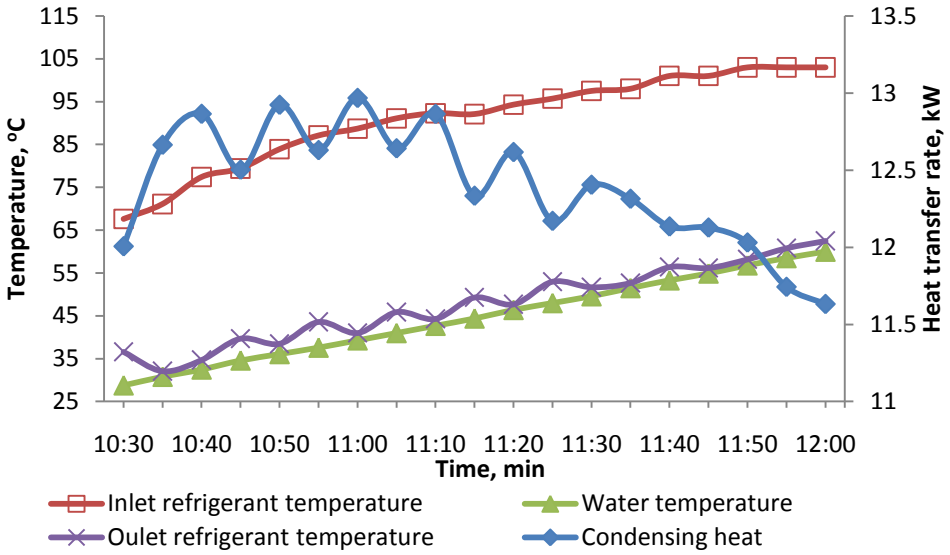

Figure 5.1.3.1 Variation of water and refrigerant temperatures and condensing heat in water condenser with time

As seen from the figure, 400L of water is heated from 28℃ to 60℃ in 90 minutes. The heating speed is slightly lower than that in full mode. Both inlet and outlet refrigerant temperature increased with the rise of water temperature, as seen in the figure. The heat released in water condenser declined from 13kW to 11.6kW when the water temperature increased from 28℃ to 60℃. Condensing heat rejection rate

in NoAC mode operation is similar to full mode operation. However, the temperature of inlet refrigerant was rising and reached the value of over 100℃ when water temperature was 60℃, while it is relatively stable at 90℃ in full mode operation. It can be explained by the fact that the enthalpy of refrigerant at evaporators outlet increase with the rise of enthalpy of refrigerant at the evaporator inlet, caused by the enhancement of condensed refrigerant temperature.

Air-conditioning

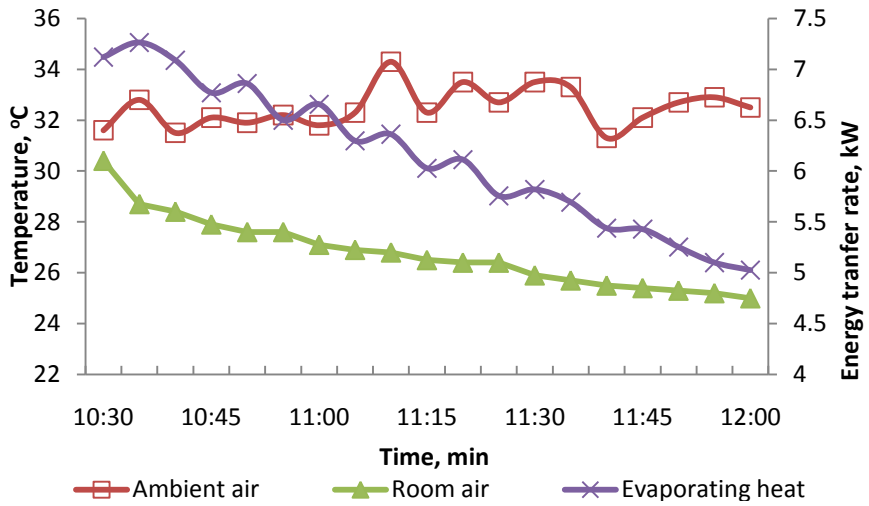

Figure 5.1.3.2 Variation of temperatures and evaporating heat in room with time

Figure 5.1.3.2 illustrated the variation of room temperature and ambient temperature with time. It also includes the variation of heat absorption rate in room evaporator with time. As seen from figure 5.1.3.2, room temperature was cooled from 30℃ to 25℃ in one and a half hour. Heat transfer from room air to refrigerant through the evaporator decreased notably with the decline of room temperature. It can be attributed to a combined effect of the decreased of room temperature and an increase in refrigerant evaporating temperature. The rate of heat absorption for cooling is in the range of 5kW to 7kW.

The effect of water temperature on the air-conditioning performance is shown in figure 5.1.3.3. As seen from the figure, the evaporating temperature in the room

evaporator increased with the rise of water temperature. It can be explained by the fact that evaporating pressure is raised by the rise of condensing pressure, caused by the condensing temperature.

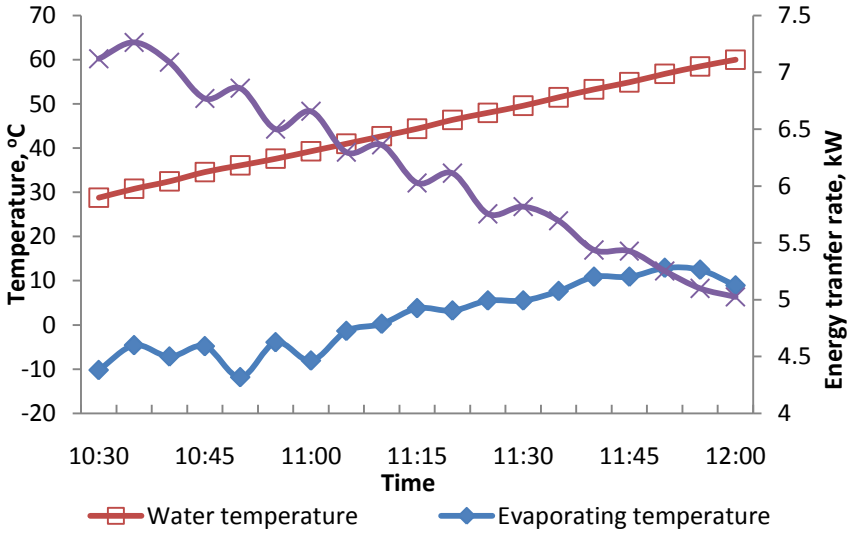

Figure 5.1.3.3 Variation of water temperature, evaporating temperatures and evaporating heat in room evaporator with time

The evaporating heat in room evaporator reduced dramatically with the rise of water temperature. It is because of not only the fall of temperature difference between the room air and evaporating refrigerant but also the increase of refrigerant enthalpy at evaporator inlet (water condenser outlet), caused by the rise of water temperature.

Evaporator-collector

Figure 5.1.3.4 illustrated the variation of collector plate temperature, ambient temperature, solar radiation and the water temperature with time. As seen from the figure, the surface temperature of both plate increased with the rise of water temperature and solar radiation. It is the combination result of the enhancement of inlet refrigerant enthalpy caused by the rise of water temperature and the rise of solar radiation level.

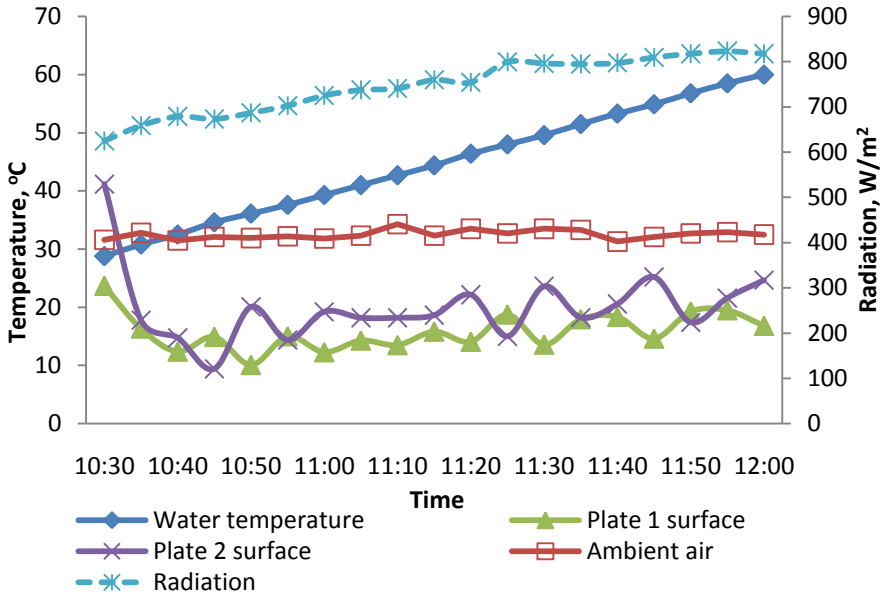

Figure 5.1.3.4 Temperature variation of water, plate and ambient with time.

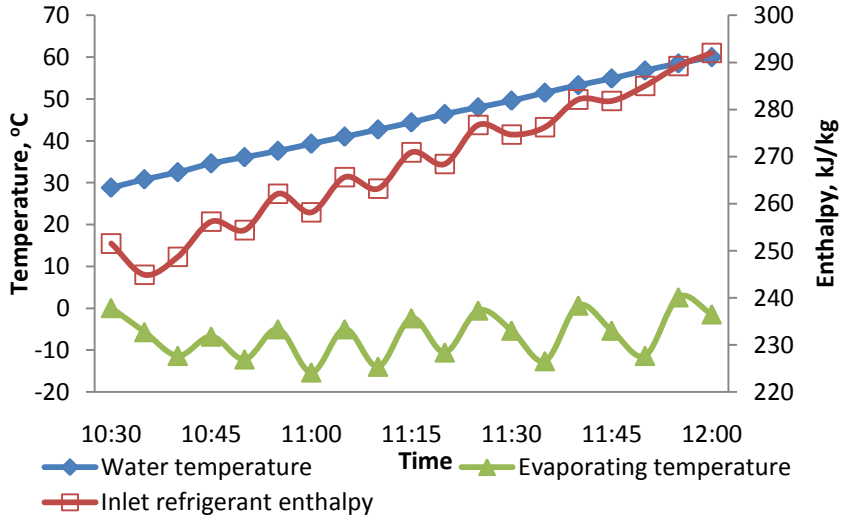

Figure 5.1.3.5 Variation of water temperature, evaporating temperature and refrigerant enthalpy at evaporator-collector inlet with time.

It is shown in figure 5.1.3.5 that both of the evaporating temperature and the refrigerant enthalpy at the inlet of evaporator-collector increased with the rise of water temperature in water condenser. As seen from the figure, the evaporating temperature in the evaporator-collector increased with the rise of water temperature. It can be explained by the fact that evaporating pressure is increased due to a rise of condensing pressure, caused by the condensing temperature. As

seen from the figure, the refrigerant enthalpy at evaporator-collector inlet (water condenser outlet) also increased with the rise of water condensing temperature.

In spite of the slow rise of solar radiation, the useful energy gain by the evaporator-collector reduced dramatically with the rise of water temperature, as seen in figure 5.1.3.6. It is because of the increase of refrigerant enthalpy at evaporator inlet (water condenser outlet). The useful energy gain is 2.6kW when water temperature is 60℃, lower than the useful energy gain of 3.3kW in full mode operation.

The solar collector efficiency also declined with the rise of water temperature, as seen in figure 5.1.3.6. It is 0.8 when water temperature is 60℃

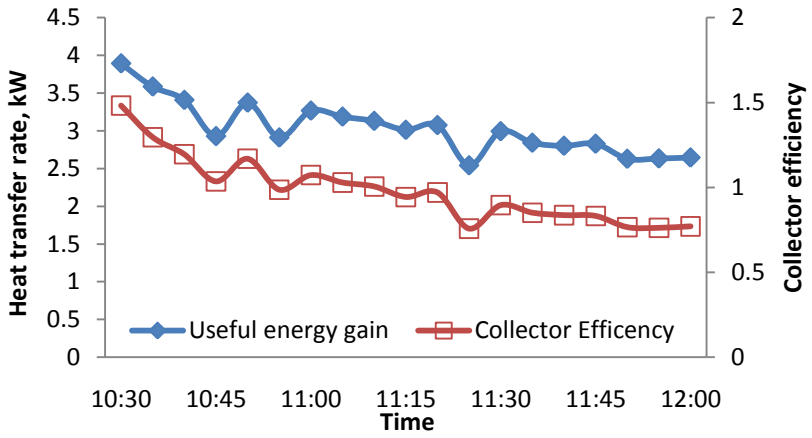

Figure 5.1.3.6 Variation of useful energy gain and collector efficiency with time.

Compared to full mode operation, the evaporator-collector performance of NoAC mode operation is highly depended on the water temperature, due to the fact that the absence of air condenser caused the fluctuation of status of condensed refrigerant with the rise and fall of water temperature.

System Performance

Figure 5.1.3.7 presented the variation of evaporating heat in the two evaporators and heat released in water condenser with time in NoAC mode operation. As seen from the figure, in spite of the stable status of radiation, all of the evaporating heat

in the two evaporators and condensing heat released in water condenser declined with the rise of water temperature in NoAC mode operation.

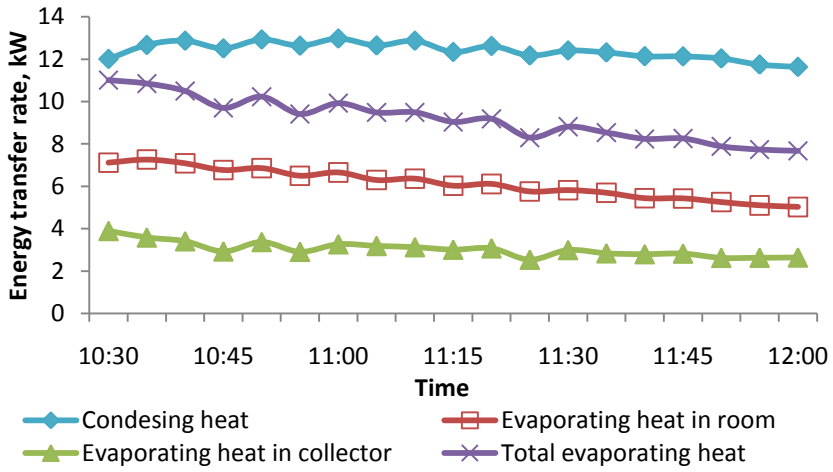

Figure 5.1.3.7 Variation of energy distribution with time

Compared to the COP in full mode operation, the COP of NoAC mode operation is at same level when water temperature is around 30℃ but lower at the condition of water temperature of 50℃ to 60℃. The COP dropped to 3 when the water is heated to 60℃, as seen in figure 5.1.3.8.

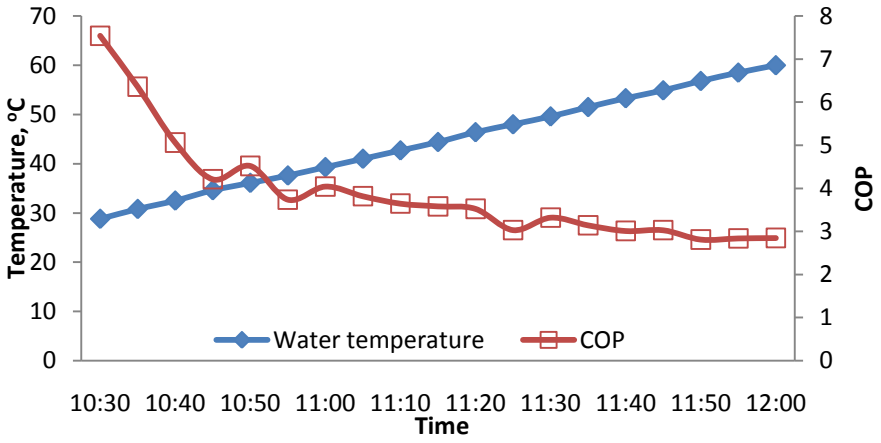

Figure 5.1.3.8 Variation of water temperature and system COP with time

The high COP at beginning may be attributed to low initial water temperature of 28℃, which was 33℃ in the experiment of full mode operation.

5.1.4 Water heating and drying with solar collector

When the room evaporator for air conditioning is bypassed, the system operation mode is called "No room evaporator mode" (NoRE mode). In this operation mode, the system can serve water heating and drying. Without the room evaporator, all the evaporating heat will be solely absorbed by the solar evaporator-collector. The system performance in NoRE mode operation is presented and discussed in this section.

Experiment was conducted in NoRE mode operation from 10am to 16:30pm.

Water heating

In the experiment, 400L of water in the water condenser was heated without discharging when it is lower than 60℃. It is replaced by 400L water at ambient temperature (around 30℃) when it reached 60℃.

Figure 5.1.4.1 shows the variation of heat released in water condenser and the temperature of refrigerant and water in the heating process in NoRE mode operation.

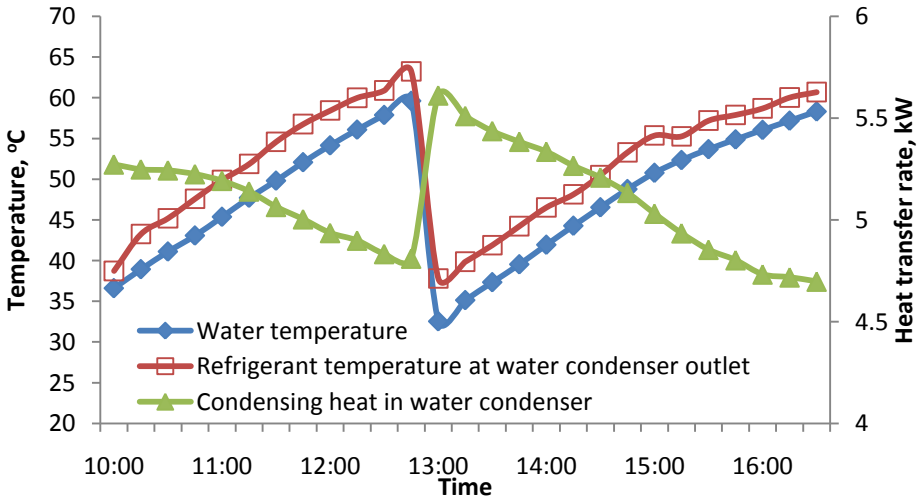

Figure 5.1.4.1 Variation of temperature and condensing heat with time

As seen from the figure, water temperature only increased by 7℃~9℃ in every one

hour. With the rise of water temperature, heat released in water condenser dropped gradually from 5.5kW to 4.7kW. Both of the water heating speed and the condensing heat releasing rate in NoRE mode are much lower than that of full mode and NoAC mode. It can be explained by the fact that the evaporating heat is provided by the solar evaporator-collector only.

Without room evaporator, the condensing heat in NoRE mode is mainly from the heat of solar evaporator collector, which is influenced by the irradiation. Hence, in NoRE mode, the performances of water heating and drying, which are driven by condensing heat, is highly affected by solar radiation and ambient temperature.

Figure 5.1.4.2 illustrated how the solar radiation affects the water heating speed in NoRE mode. Temperature of 400L water was raised in the rate of 0.15℃/minute when radiation is 900W/m^2. It dropped to 0.075℃/minute when the radiation is less than 100W/m^2. The fluctuations of the two lines show similar trend.

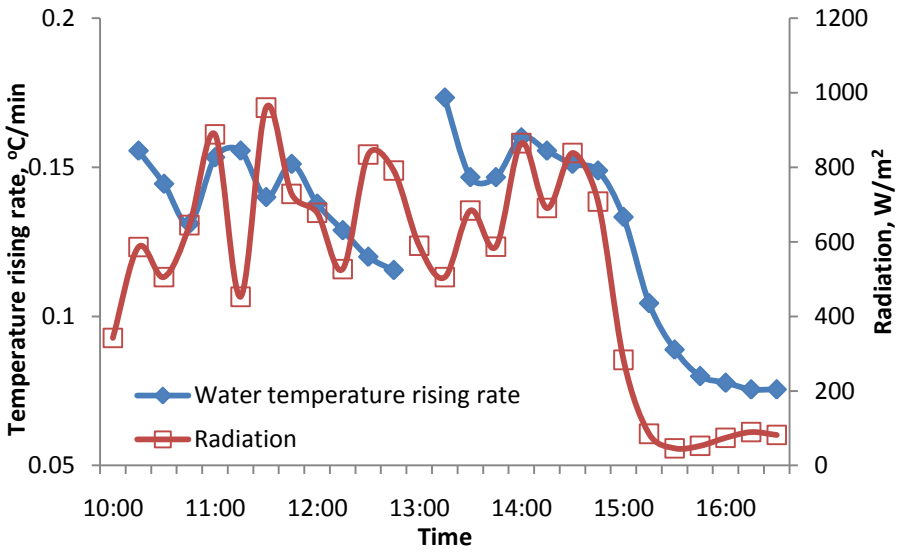

Figure 5.1.4.2 Variation of water temperature rising rate and radiation with time

Drying

Figure 5.1.4.3 shows the variation of ambient temperature, heated air temperature

for dying and heat released in air condenser in NoRE mode operation with time.

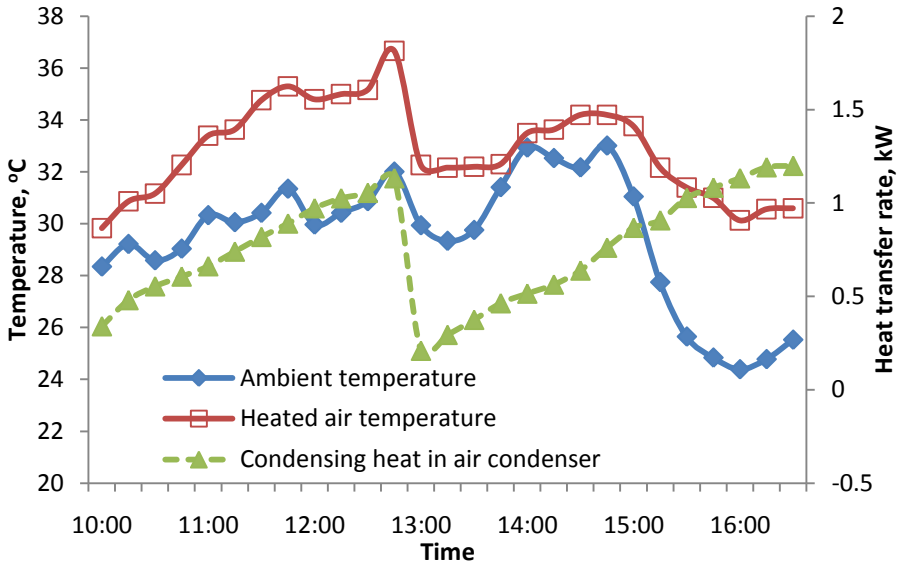

Figure 5.1.4.3 Variation of ambient temperature, heated air temperature and condensing heat with time.

As seen in the figure, ambient air, with the temperature of around 30℃ and RH of 60%, was heated in the air condenser by the refrigerant arriving from water condenser. With the rise of water temperature, as shown earlier in figure 5.1.4.1, the temperature difference between the inlet air and heated air increased. It means that the energy absorbed by air increased. The temperature difference between inlet air and heated air is up to 5℃ when the water temperature reaches 60℃, while only 1℃ when water temperature is 37℃. Temperature enhancement of air in air condenser in NoRE mode is less than that in full mode due to lower temperature of the refrigerant. As a result, if the heated air in NoRE mode is used for drying, the drying time must be longer than the drying time, which is one hour for 1kg textile drying, in full mode.

The energy released by the refrigerant to the air for drying increased with the rise of water temperature. When water temperature is 30℃, condensing heat is only 0.2kW and rose to 1.2kW when water temperature is 60℃. This phenomenon is similar to

that in full mode operation. However, the value of condensing heat of air condenser in NoRE mode is only around half of that in full mode, caused by a drop of total evaporating heat as a result of the absence of room evaporator.

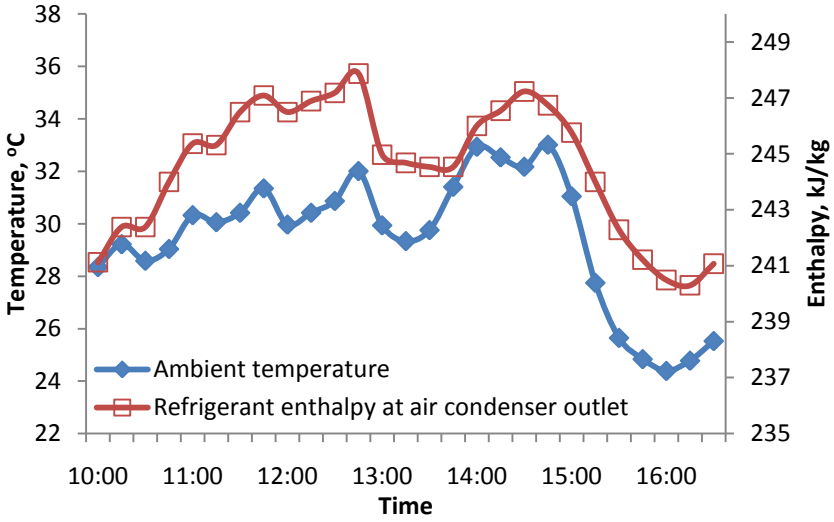

Figure 5.1.4.4 Variation of ambient temperature and air condenser outlet refrigerant enthalpy with time.

As illustrated in figure 5.1.4.4, the status of condensed refrigerant is highly depended on the temperature of ambient air, which is blown through the air condenser. As seen from the figure, with the fall of ambient temperature, the condenser outlet refrigerant enthalpy drop, this is good for evaporator performance as well as the system performance.

Evaporator-collector

In NoRE mode operation, all condensed refrigerant flows through the evaporator-collector. Figure 5.1.4.5 shows the variation of surface temperature of the two evaporator-collector plates and radiation with time. As seen from the figure, both plate surface temperature decline with the fall of radiation. Surface temperature of plate 2 is always higher than that of plate 1. These are similar with the full mode operation due to the same reasons.

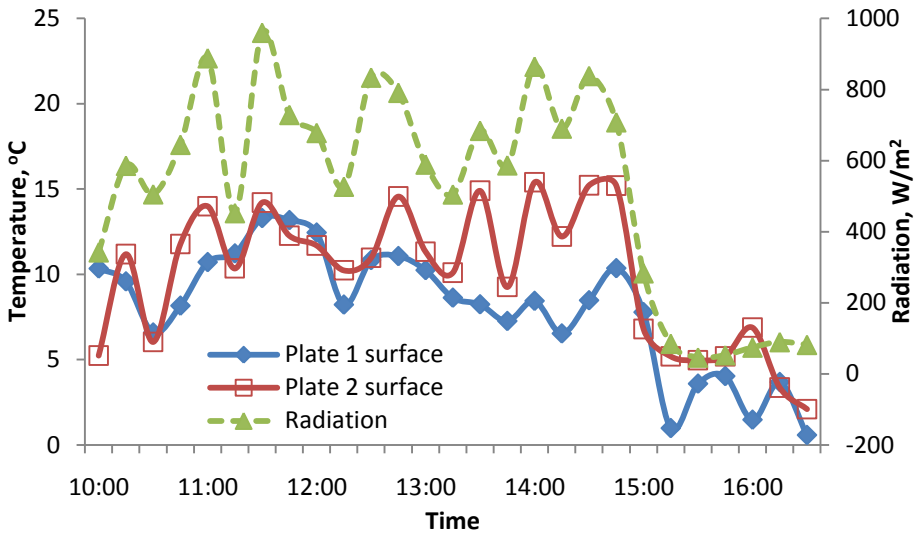

Figure 5.1.4.5 Variation of plate surface temperature and radiation with time.

However, the temperature difference between the two plates in NoRE mode is less than that of full mode operation. It might be due to the increase of two phase region in evaporator-collector, caused by the increase of refrigerant mass flow rate as a result of absence of room evaporator.

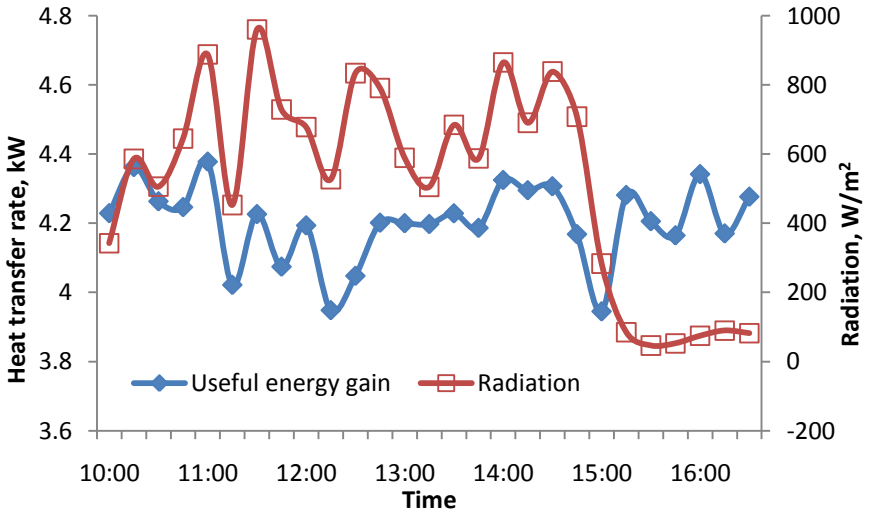

Figure 5.1.4.6 Variation of useful energy gain and radiation with time.

For the same reason, the collector useful energy gain in NoRE mode, which is in the range of 4 kW to 4.4 kW, as shown in figure 5.1.4.6, is higher than that of full mode for the same radiation condition. It is also noted that, when the radiation is lower

than 100W/m^2 after 15:00pm, the collector useful energy gain is maintained at the level of 4.2 kW. It is attributed to the dramatically drop of the refrigerant enthalpy at condenser outlet caused by the fall of ambient temperature, as shown in figure 5.1.4.4. Thus, it can be concluded that the variation of evaporator-collector useful energy gain is a combination result of both radiation and ambient temperature.

As seen from the figure, the amplitude of fluctuation of useful energy gain is less than that of radiation due to the existence of energy gain from ambient cause by the fact that plate surface temperature is lower than ambient temperature.

For the above reason, collector efficiency increase due to a fall of solar irradiation, where the ambient gain remained constant, as shown in Figure 5.1.4.7. This pattern of variation is similar to full mode operation.

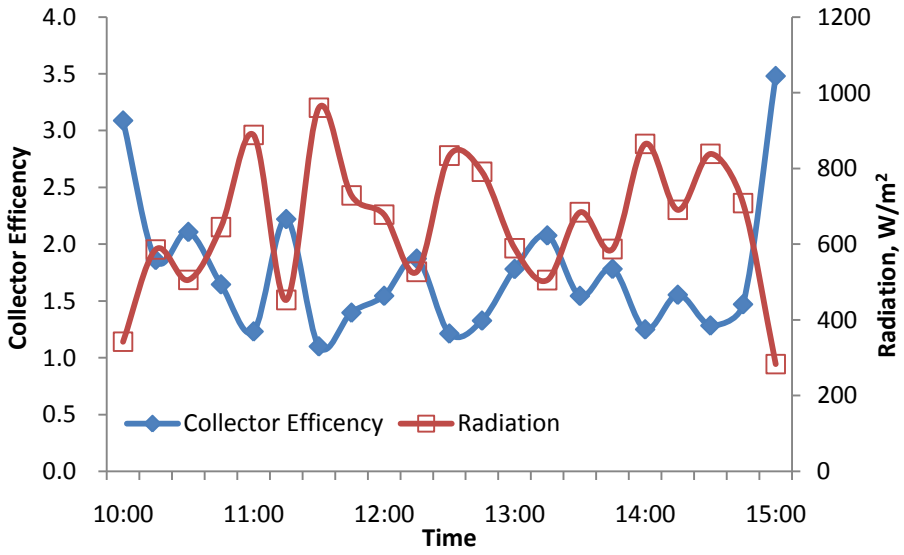

Figure 5.1.4.7 Variation of collector efficiency and radiation with time.

Variation of refrigerant enthalpy at the evaporator-collector outlet and radiation with time is shown in figure 5.1.4.8. As seen from the figure, the status of refrigerant at collector outlet is mainly determined by the radiation level.

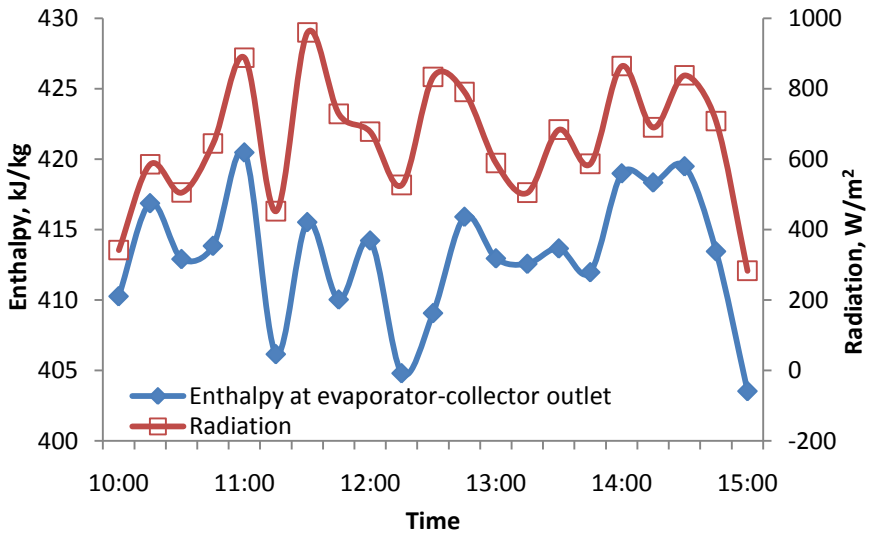

Figure 5.1.4.8 Variation of enthalpy at evaporator-collector outlet and radiation with time.

Unlike the full mode operation, in which the refrigerant at the compressor is the mixture of refrigerant from room evaporator and evaporator-collector, in NoRE mode, the refrigerant flowing into the compressor is all from the evaporator-collector. It means the status of refrigerant at compressor suction in NoRE mode is mainly determined by the evaporator-collector performance, which is highly affected by the radiation.

System performance

Figure 5.1.4.9 presented the variation of system COP and solar irradiation with time in NoRE mode operation. As seen from the figure, higher the solar radiation, higher the system COP due to more evaporating heat absorbed by the unglazed solar evaporator-collector.

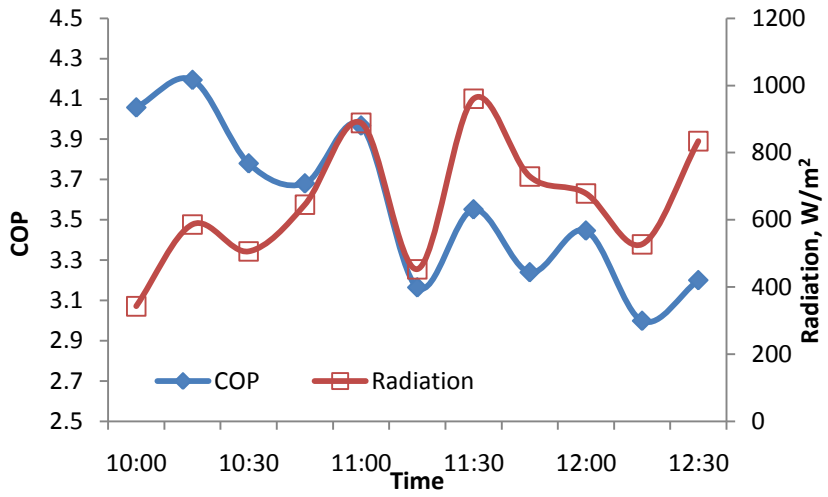

Figure 5.1.4.9 Variation of system COP and solar irradiation with time

Beside the solar radiation, system COP is also affected by the water temperature by influencing the condensing heat. COP dropped gradually from 4.2 to 3.2 with the rise of water temperature.

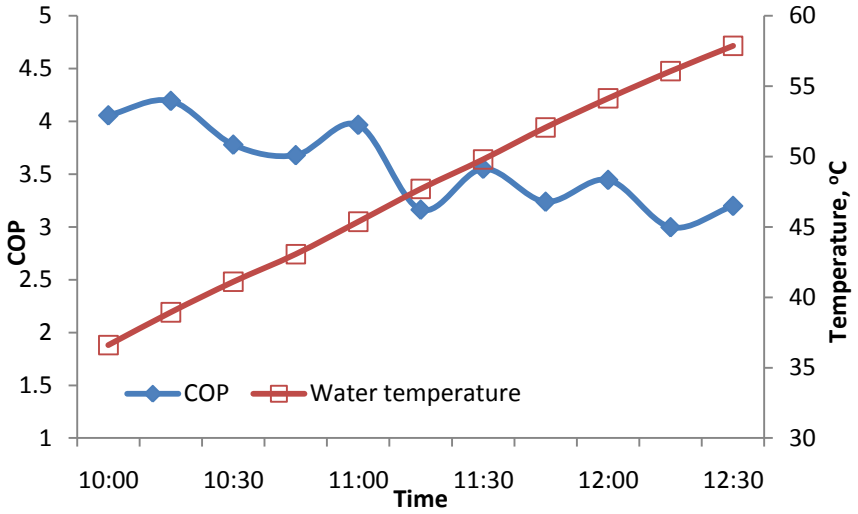

Figure 5.1.4.10 Variation of system COP and water temperature with time

5.1.5 Water heating, drying and air conditioning without solar collector

When the solar evaporator-collector is bypassed, the operation mode is called "No evaporator-collector mode" (NoEC mode). Without the solar evaporator-collector, all the evaporating heat is solely absorbed by the room evaporator. The system performance in NoEC mode operation is presented and discussed in this section.

Water heating

Figure 5.1.5.1 shows the variation of heat released in water condenser and the temperature of refrigerant and water in NoEC mode operation.

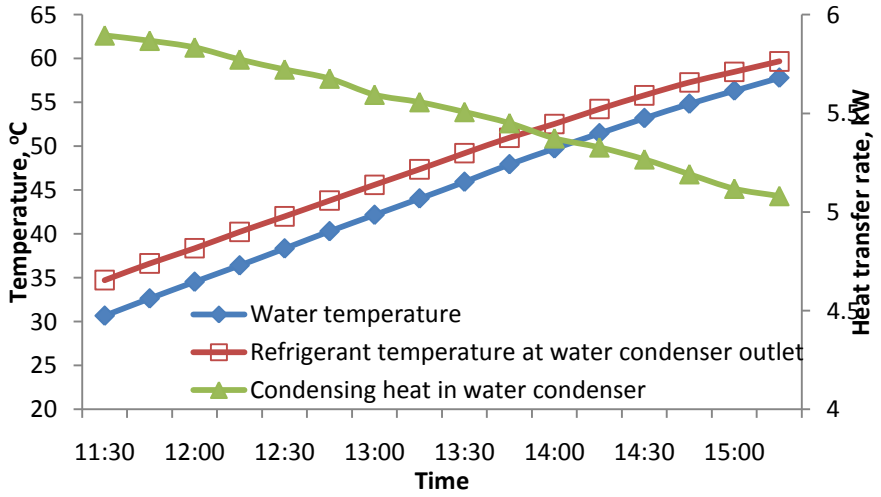

Figure 5.1.5.1 Variation of water and refrigerant temperature and condensing heat with time

As seen from the figure, 400L of water is heated from 30℃ to 60℃ in 3 and half hours. The heating speed is much lower than that in full mode operation. Condenser outlet refrigerant temperature increased with the rise of water temperature. The heat released in water condenser declined from 6kW to 5.1kW when the water temperature increased from 30℃ to 60℃.

The water heating performance can also be presented by water temperature rising rate (temperature increase per minute), as seen from figure 5.1.5.2. With the decline of heat released in water condenser, the temperature rising rate for 400L water drop

from 0.13℃/min to 0.1℃/min. It is similar with that in NoRE mode but much lower than that in full mode and NoAC mode.

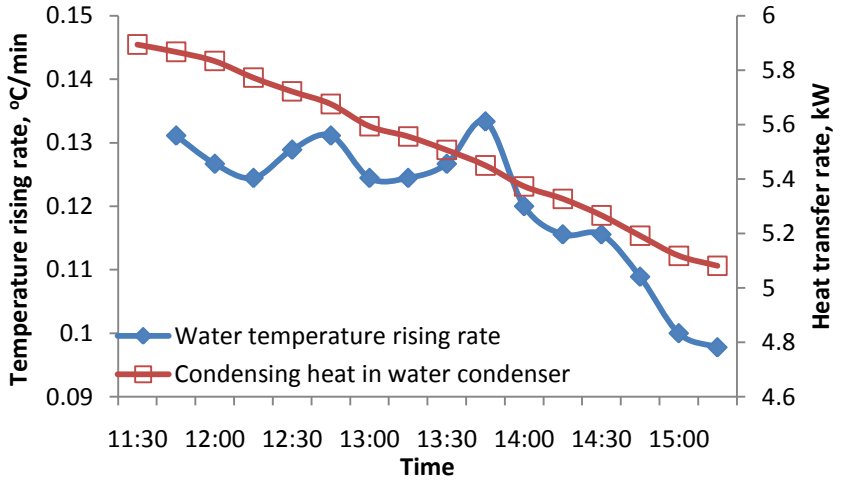

Figure 5.1.5.2 Variation of water and refrigerant temperature and condensing heat in water condenser with time

Drying

Figure 5.1.5.3 shows the variation of air and refrigerant temperature and condensing heat in air condenser in NoEC mode operation with time.

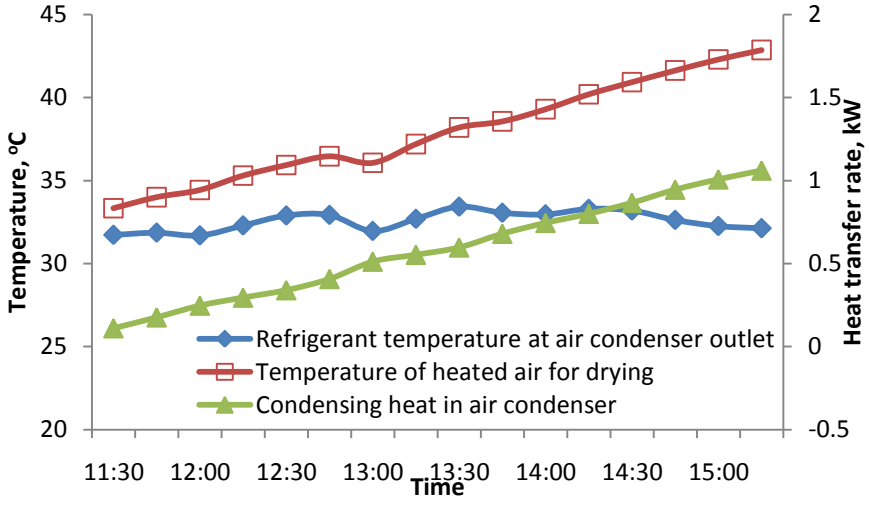

Figure 5.1.5.3 Variation of air and refrigerant temperature and condensing heat in air condenser

As seen from the figure, with the rise of inlet refrigerant temperature, the condensing heat in air condenser increased from 0.11kW to 1.1kW. As a result, the

heated air temperature increased up to 42℃, when water temperature was 60℃.

One of the purposes of air condenser is to ensure that refrigerant is fully condensed no matter how high is the temperature of water in the water condenser. As a result, the refrigerant temperature at air condenser outlet is maintained in sub-cooled condition at 32℃, as plotted in figure 5.1.5.3.

As discussed in 5.1.4, the status of refrigerant at air condenser outlet is highly depended on the ambient temperature. Figure 5.1.5.4 shows the variation of ambient temperature and air condenser outlet refrigerant enthalpy with time.

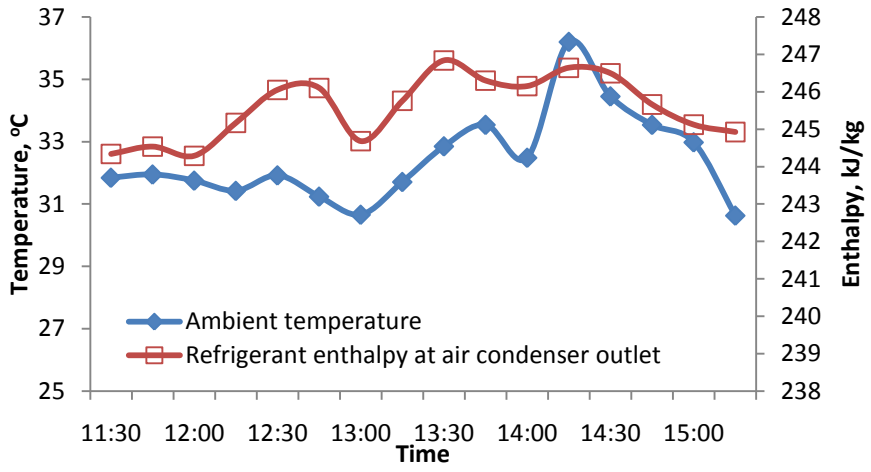

Figure 5.1.5.4 Variation of ambient temperature and refrigerant enthalpy at condenser outlet with time

As seen from the figure, the condenser outlet refrigerant enthalpy increased with the rise of ambient temperature.

Air-conditioning

In NoEC mode operation, the entire condensed refrigerant flows through the room evaporator. Figure 5.1.5.5 illustrated the variation of evaporating heat and room and ambient temperature with time. The evaporating heat in room evaporator dropped from 4.4kW to 4.15kW with the fall of room temperature, as presented in figure 5.1.5.5. It is at similar level with the evaporating heat of NoRE mode but much lower

than the total evaporating heat in full mode operation.

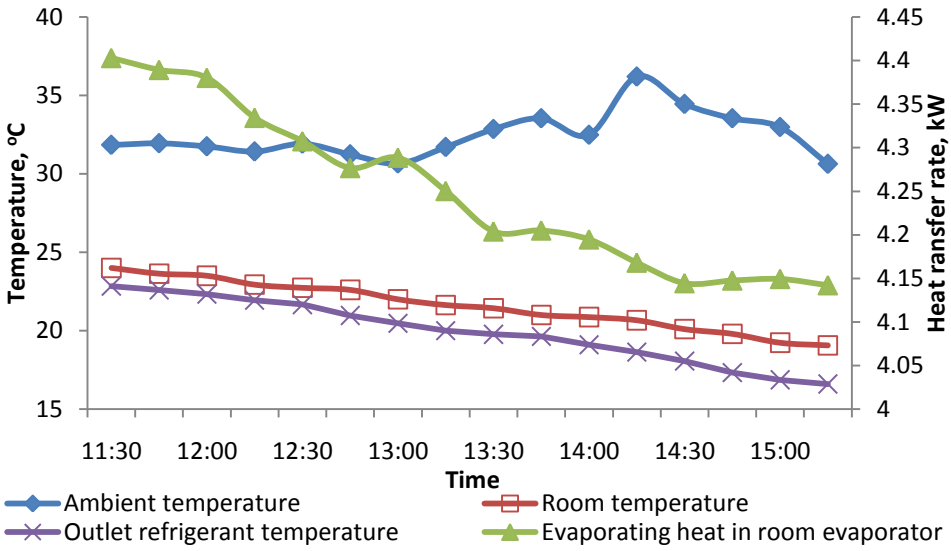

Figure 5.1.5.5 Variation of temperatures and evaporating heat in room evaporator with time

As seen from the figure, the room is cooled from 24℃ to 18℃ in 3.5 hours. The refrigerant temperature at evaporator outlet deceases with the fall of room temperature. Unlike full mode operation, the heat absorbed by room evaporator provides all the system evaporating heat. It means the condition of refrigerant at compressor inlet in NoEC mode, as well as the system performance, is mainly determined by the refrigerant condition at room evaporator outlet, which is highly affected by the room temperature and cooling load.

System performance

In absence of solar evaporator-collector, the system performance in NoEC mode is not much affected by the meteorological condition, like the other operation modes.

The heat released in the two condensers and the evaporating heat, together with the system COP, are plotted in figure 5.1.5.6. Like full mode operation, the total heat released in the two condensers in NoEC mode is constant. System COP is dropped from 3.7 to 3.1 with the decline of evaporating heat.

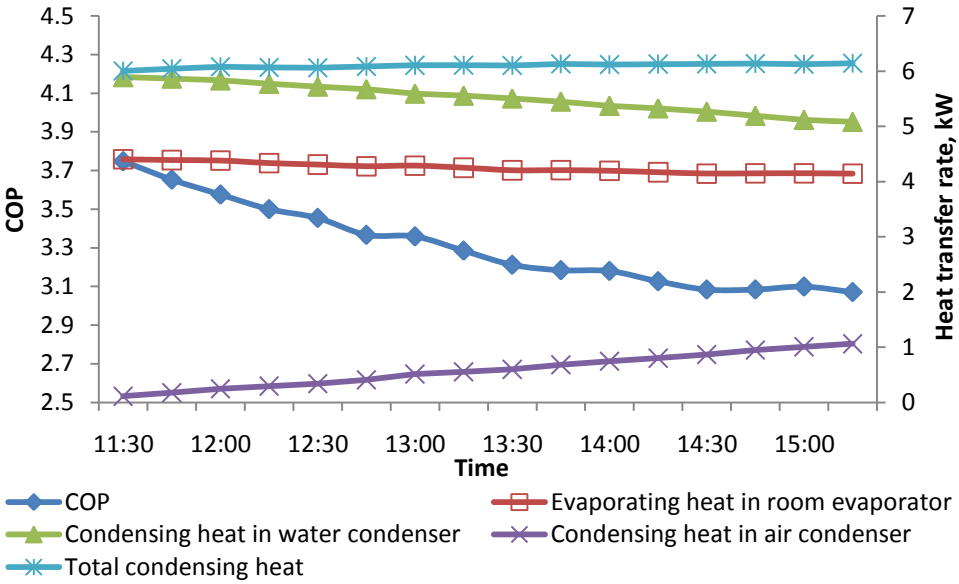

Figure 5.1.5.6 Variation of condensing and evaporating heat and COP with time

The relationship between COP and room temperature in NoEC mode is illustrated in figure 5.1.5.7.

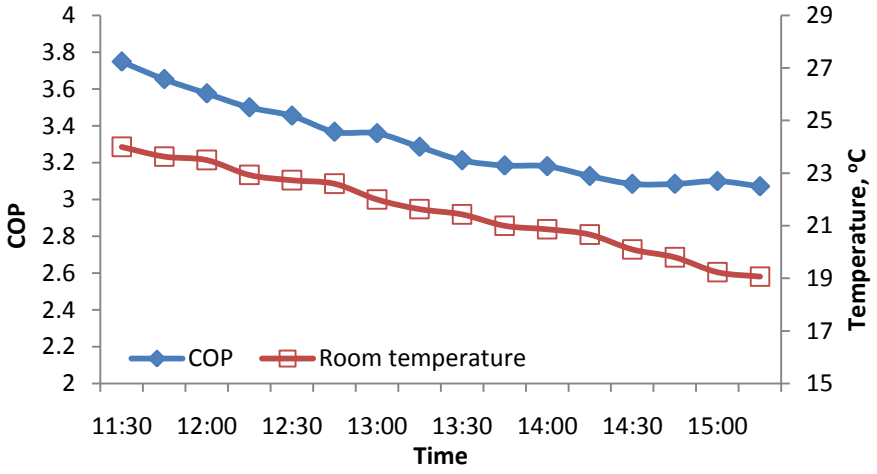

Figure 5.1.5.7 Variation of room temperature and COP with time

As seen from the figure, the system COP is highly depended on the room temperature due to the change in the evaporating heat.

5.1.6 Comparison with Conventional Heat Pump System

A conventional vapor compression air conditioning system throws the heat from a heat source (air-con room) to the ambient air without making an effort to recover it. Furthermore, the performance of a conventional heat pump system is greatly limited by the heat source. In this study, an attempt was made to recover the condenser heat and investigate the performance of a conventional heat pump with an additional heat source: solar energy.

Compared to the conventional heat-pump system, the present three-in-one solar heat-pump system has three main advantages:

- Evaporator-collector can absorb the radiation and ambient energy. By increasing the superheat level at the compressor inlet, evaporator-collector reduced the work input of compressor in comparison to the conventional heat-pump system.
- Water condenser and air condenser in series ensures complete condensation of the refrigerant vapor resulting improved thermodynamic performance.
- Water condenser and air condenser in three-in-one solar heat-pump system utilized the condensing heat, which is totally thrown away in conventional heat-pump system.

A series of experiments were conducted to evaluate the system performance and subsequent comparison of the two systems. As shown in table 5.2, Q_{RE}, Q_{EC}, Q_W and Q_A are all utilized in 3-in-1 solar heat pump system, whereas only Q_{RE} is utilized in conventional heat pump system.

Table 5.2 System performance comparison (Average radiation at 500 W/m^2)

	Q_{EC}(kW)	Q_{RE}(kW)	W(kW)	Q_W(kW)	Q_A(kW)	$COP_{cooling}$	$COP_{heating}$
Conventional heat pump	N/A	7.1	3.1	N/A	10.2	2.3	3.3
3-in-1 solar heat pump	3.5	7.2	3.0	11.4	2.6	2.4	4.7

- Evaporator-collector absorbed significant radiation and ambient heat. Work input of compressor W (kW) is reduced by 5 %.

- With better condensing effect, 3-in-1 solar heat pump' s cooling COP is better than that of conventional heat pump.

5.2 Simulation and validation

The mathematical model, which is developed and presented in Chapter 4, is used to develop a simulation program to predicted system performance in full mode, NoWC mode and NoRE mode, with the same input parameters as in experiments. Simulation results are presented and validated by experiment data in this section.

5.2.1 Full mode operation

In the system simulation for full mode operation, the input process parameters, such as meteorological condition, collector area, compressor speed and other variables for different components, are set as same as the experiment conducted and presented in section 5.1.1.

Water heating

Figure 5.2.1.1 shows the comparison between the simulation and experimental results of condensing heat and water temperature in water condenser under full mode operation.

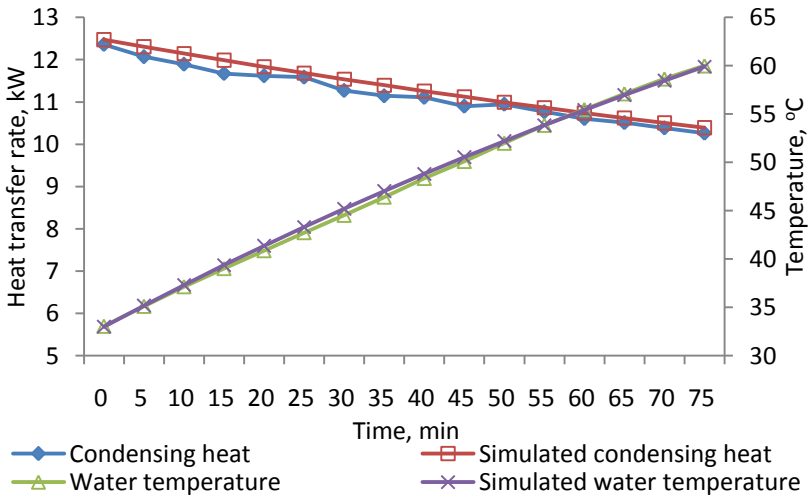

Figure 5.2.1.1 Comparison of predicted and measured condensing heat and water temperature in water condenser with time

As seen from the figure, the predicted and measured variation in condensing heat

and water temperature agree fairly well. Both simulation and experimental results indicated that, in full mode, the temperature of the 400 liters water increases in a steady manner and rises from 33℃ to 60℃ in 75 minutes. With the rise of water temperature, the condensing heat released from the refrigerant in water condenser declined from 12.5kW to 10.5kW.

Drying

Figure 5.2.1.2 shows the comparison between the simulation and experimental results of condensing heat and heated air temperature for drying in air condenser in full mode operation. As seen from the figure, the predicted and measured variation in condensing heat and heated air temperature agree fairly well. It is shown by both predicted and measured data that, in full mode, the condensing heat in air condenser increased from 0.5kW to 3kW with the rise of water temperature.

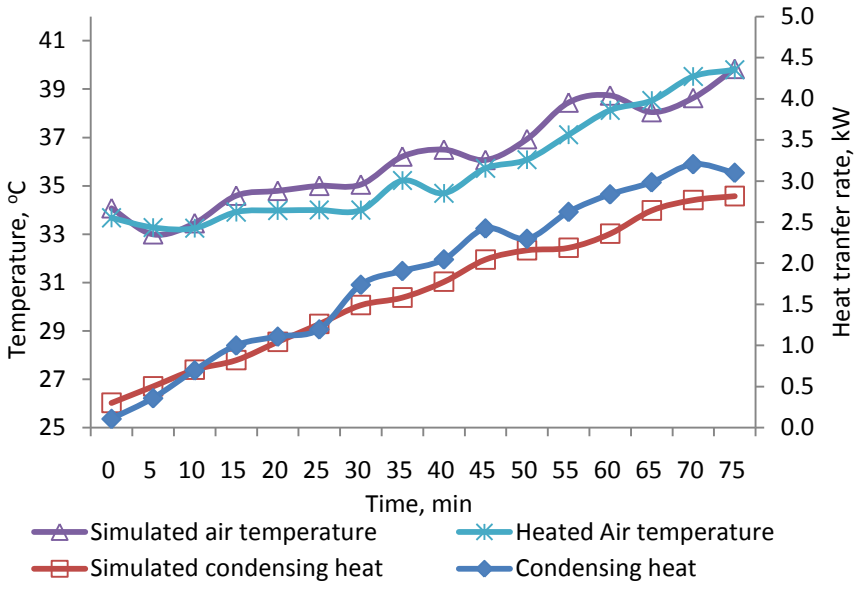

Figure 5.2.1.2 Comparison of predicted and measured condensing heat and heated air temperature in air condenser with time

The comparison of the simulation and experimental results of moisture contents with time in full mode operation is shown in figure 5.2.1.3. In this drying process, temperature of the water in the water condenser was maintained at 60℃ by

controlling the water flow rate. It enabled the stabilization of the temperature of air for drying. Textile with the bone dry mass of 1.5kg was wetted and hangs in the drying chamber.

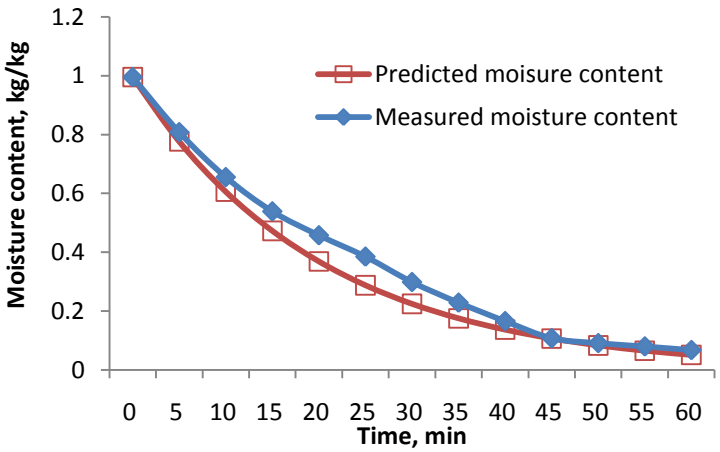

Figure 5.2.1.3 Comparison of predicted and measured moisture content

As seen from the figure, the predicted variation in moisture content of material in drying process was found to be in good agreement. It reduced moisture from 1 to 0.09 in 60 minutes.

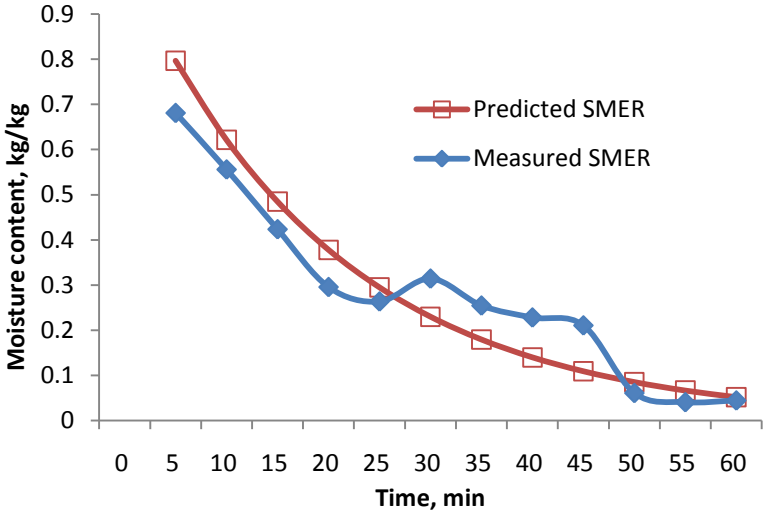

Figure 5.2.1.3 Comparison of predicted and measured SMER with time

Specific Moisture Extraction Rate (SMER) is the most commonly used criterion for characterizing the performance of dryers involving heat pump system. Figure

5.2.1.4 shows the comparison of predicted and measured variation of SMER with time in full mode operation. A maximum of predicted SMER value of 0.79 kg/kWh was obtained, which is slightly higher than the maximum, 0.69kg/kWh, obtained from experiments. As seen from figure 5.2.1.3, the values of both predicted SMER and measured SMER decline with time. The measured and predicted values agree fairly well, as shown in figure 5.2.1.3

Air-conditioning

The comparison of the simulation and experimental results of evaporating heat absorbed by room evaporator for cooling with time in full mode operation is shown in figure 5.2.1.4.

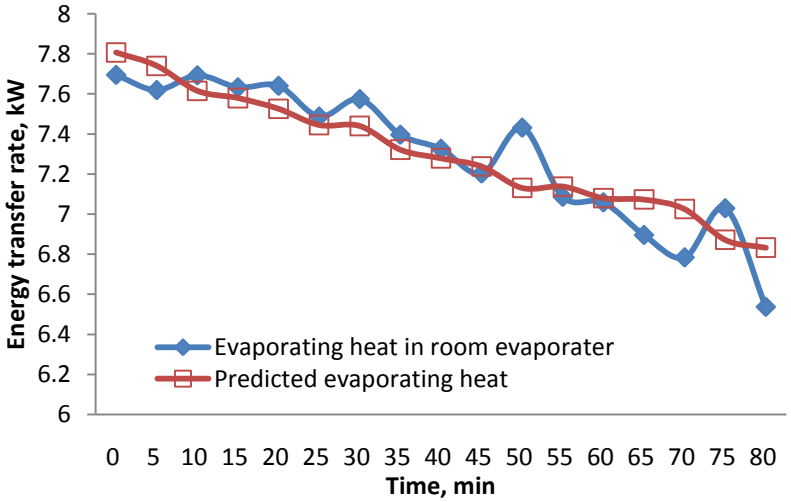

Figure 5.2.1.4 Comparison of predicted and measured evaporating heat in room evaporator with time

As seen from the figure, the predicted variation of energy transferred from the air-con room (evaporating heat) was found to be in good agreement with measured values. It declined from 7.8kW to 6.6kW gradually in about 80 minutes.

Figure 5.2.1.5 presented the comparison of predicted and measured variation of room temperature with time in full mode operation.

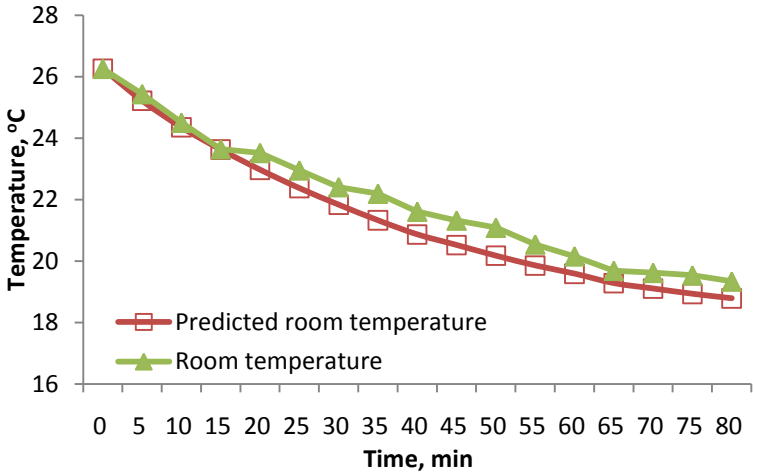

Figure 5.2.1.5 Comparison of predicted and measured room temperature with time

As seen from the figure, the predicted room temperature dropped slightly faster than measured result. It might be due to the fact that the door for the air-con room was opened several times during the experimental process for people moving in and out, which was not taken into account in the simulation process.

Evaporator-collector

Useful energy gain is a combination of energy gain from irradiation and the ambient. The contribution of these two parts is obtain by simulation analysis and presented in figure 5.2.1.6.

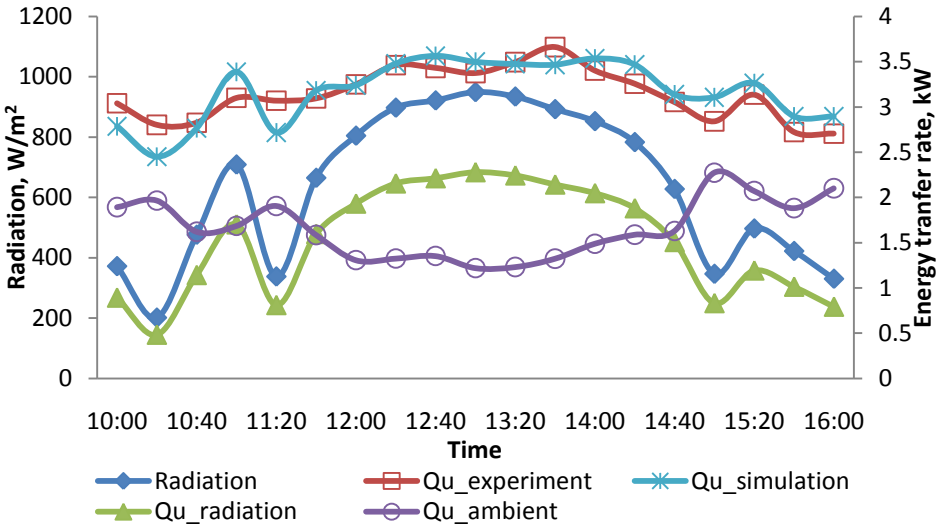

Figure 5.2.1.6 Comparison of predicted and measured useful energy gain and solar radiation with time

As seen from figure 5.2.1.6, the energy from radiation $Q_{u\_radiation}$ is highly depended on the radiation level. In contrast to $Q_{u\_radiation}$, energy absorbed from the ambient, $Q_{u\_ambient}$, is relatively constant. It decreased with the rise of radiation due to the fact that the temperature difference between ambient and collector dropped caused by the increase of plate surface temperature as a result of an increase of irradiation. It shows that predicted Q_u has a reasonably good agreement with experimental values in full mode operation. Both of them varied in the range from 2.5kW to 3.7kW with the change of radiation.

Unlike normal solar collector, the amplitude of fluctuation of useful energy gained by this evaporator-collector is less than that of radiation. This can be attributed to the fact that it not only absorbs energy from radiation but also from ambient due to its low surface temperature, leading to a relatively steady useful energy gain.

In figure 5.2.1.7, the variation of predicted and measured collector efficiency and solar radiation are plotted against time. As a result of good agreement between experimental and predicted value of useful energy gain, the simulated collector efficiency matched the experimental results fairly well.

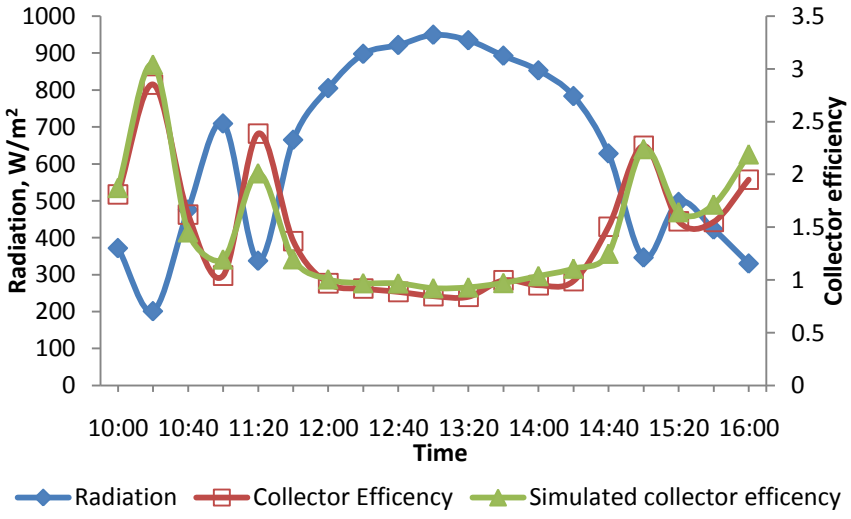

Figure 5.2.1.7 Comparison of predicted and measured collector efficiency and solar radiation with time

System performance

The comparison of results of coefficient of performance (COP) obtained from simulation and experiments in full mode operation is shown in figure 5.2.1.8

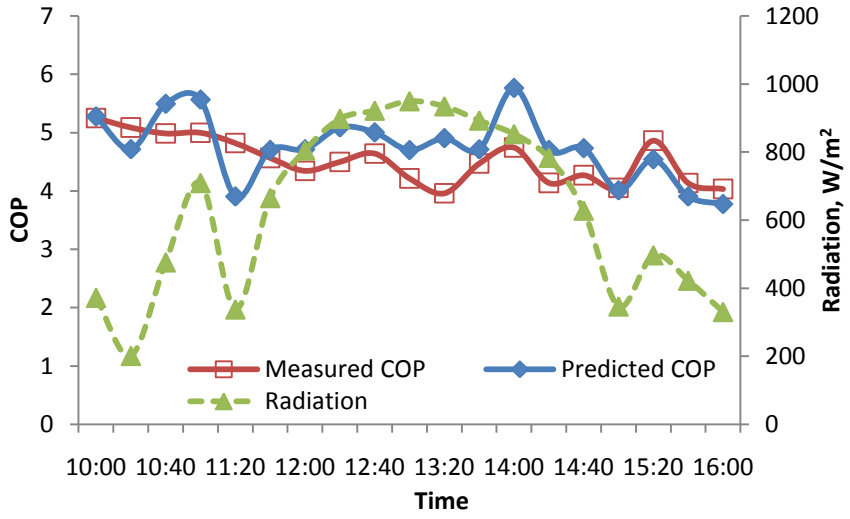

Figure 5.2.1.8 Comparison of predicted and measured COP and radiation with time

It is shown that the fluctuation of solar radiation lead to a rise or fall of both simulated and experimental COP for the system. It is caused by the variation of energy absorbed in solar evaporator-collector with the change of solar irradiation.

As seen from the figure 5.2.1.8, the variation of predicted system COP is in good agreement with the measured value.

The agreements between the simulation and experimental results for full mode operation proved that the mathematical model is validated for full mode operation.

5.2.2 NoWC mode operation

In the system simulation for NoWC mode operation, the input process parameters, such as meteorological condition, collector area, compressor speed and other components parameters, are set as same as the experiment conducted and presented in section 5.1.2.

Drying

Figure 5.2.2.1 shows the comparison of predicted and measured heated air temperature and discharged air temperature in drying process As seen from the figure, the predicted and measured heated air temperature and discharged air temperature agreed fairly well.

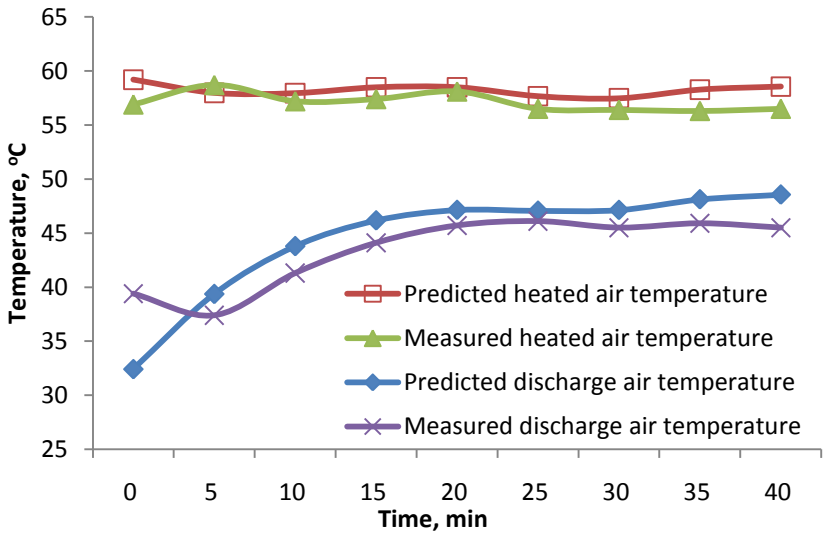

Figure 5.2.2.1 Comparison of predicted and measured heated air temperature and discharged air temperature in drying process

Without the effect of water temperature in NoWC mode, the heated air temperature is constant in the range of 55~60℃. At the beginning of the drying process, the heated air was cooled to around 40℃ by the material with high moisture content in the drying chamber and discharged. While with the decrease of material moisture content, the temperature difference between discharged air and

heated air dropped to a level of about 12℃

In figure 5.2.2.2, the predicted and measured moisture content were plotted against time. At the start of drying process, textile with the bone dry mass of 1.5kg was wetted and hanged in the drying chamber. The agreement of predicted and measured results indicated that the simulation model describing the dying process is a true representation of the actual process.

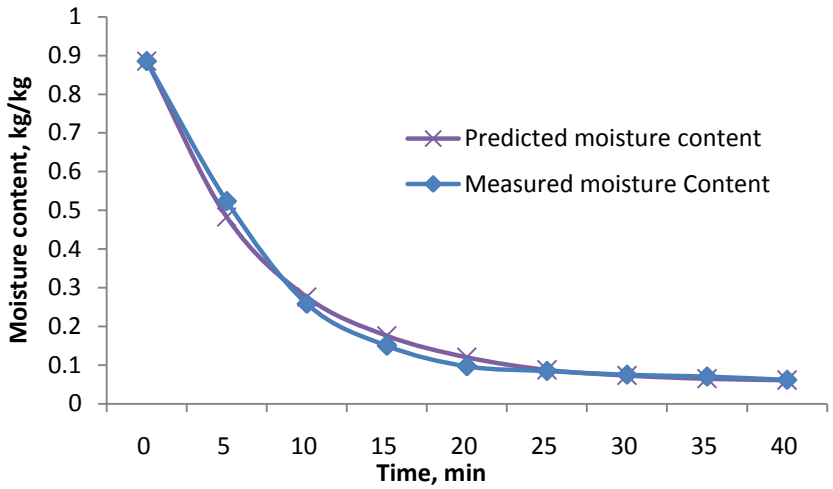

Figure 5.2.2.2 Comparison of predicted and measured moisture content in drying process

In NoWC mode, all the condensing heat is released in air condenser. Thus, the drying performance is greatly enhanced compared to full mode operation. As seen from the figure, the moisture content of material reduced from 0.9 to 0.09 in 25 minutes, which is much shorter than that in full mode operation.

Figure 5.2.2.3 shows the comparison of predicted and measured variation of SMER with time in NoWC mode operation. A maximum predicted SMER value of 1.7 kg/kWh was obtained, which is slightly higher than the maximum experimental value of 1.5kg/kWh. As seen from the figure, both predicted and measured SMER values decline with time and their variations agree fairly well. Both predicted and measured SMER values in NoWC mode operation were found much more than

those in full mode operation described earlier.

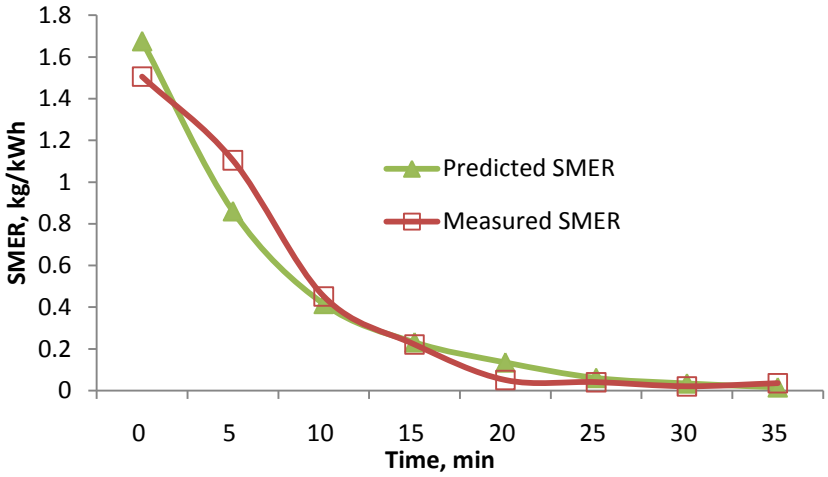

Figure 5.2.2.3 Comparison of predicted and measured SMER in drying process

Air-conditioning

Figure 5.2.2.4 shows a comparison of predicted and measured variation of room temperature with time in NoWC mode operation.

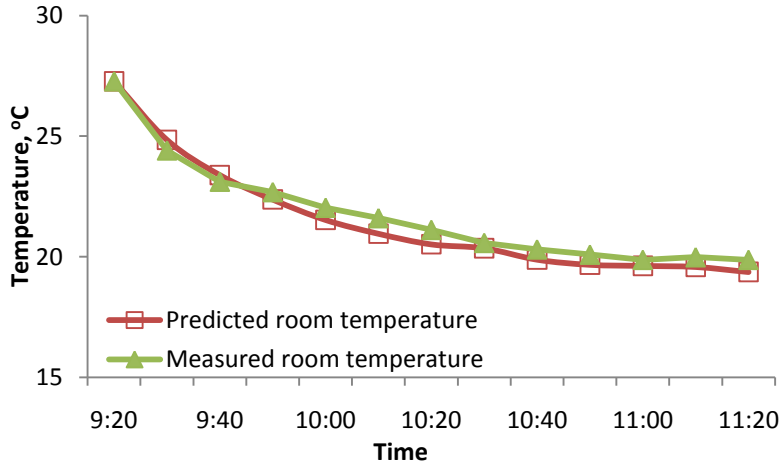

Figure 5.2.2.4 Comparison of predicted and measured room temperature with time

As seen from the figure, the predicted room temperature dropped slightly faster than measured result, due to the same reason in full mode operation. Both experimental and simulated value of room temperature were found to stabilized at about 19℃.

The comparison of the simulation and experimental results of energy absorbed by the room evaporator for cooling with time in NoWC mode operation is shown in figure 5.2.2.5. As seen from the figure, the predicted variation of evaporating heat was found to be in good agreement with measured values. It reduced from 7.1kW to 6.7kW gradually in about 2 hours.

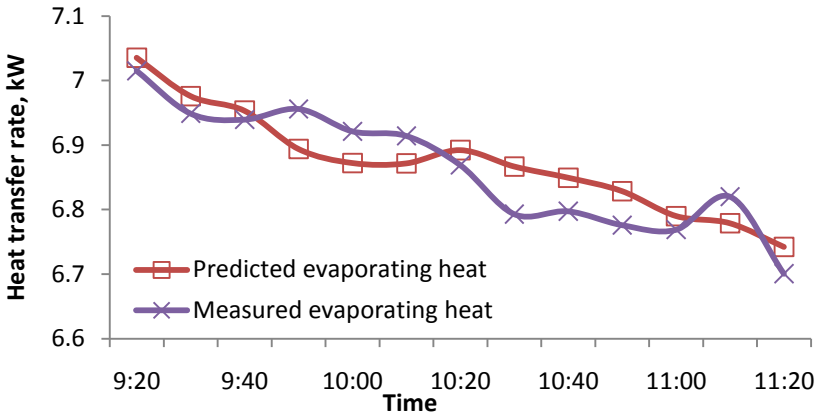

Figure 5.2.2.5 Comparison of predicted and measured evaporating heat in room evaporator with time

Evaporator-collector

In figure 5.2.2.6, measured and predicted values of useful energy gain, Qu, by the unglazed solar evaporator-collector and solar irradiation are plotted against time.

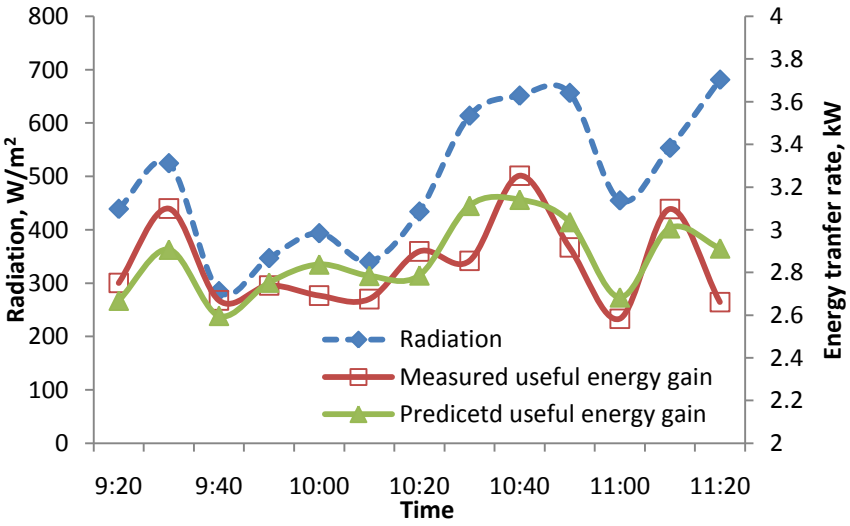

Figure 5.2.2.6 Comparison of predicted and measured useful energy gain by evaporator-collector with time

As seen from the figure, the predicted Qu has a reasonably good agreement with experimental values in NoWC mode operation. Both of them varied in the range from 2.6kW to 3.2kW with the change of radiation.

In figure 5.2.2.7, the variation of predicted and measured collector efficiency and solar radiation are plotted against time.

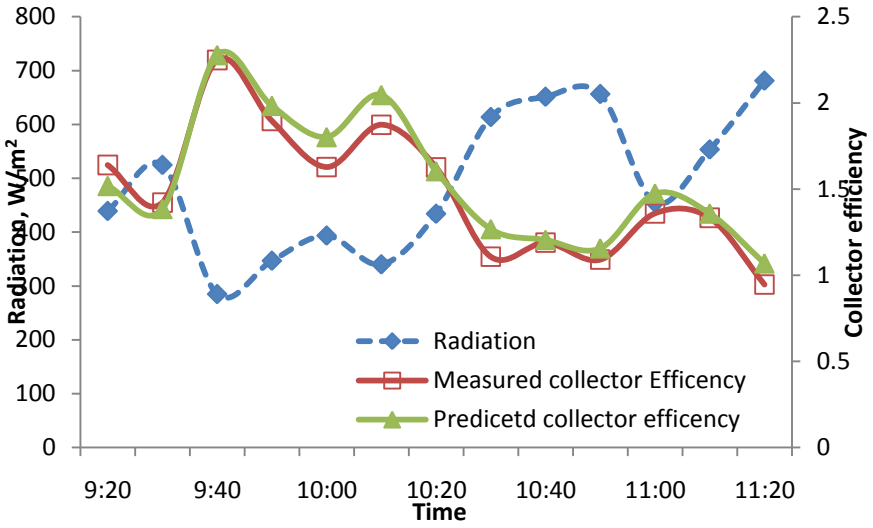

Figure 5.2.2.7 Comparison of predicted and measured collector efficiency with time

As a result of good agreement between measured and predicted values of useful energy gain, the simulated collector efficiency matched the experimental results fairly well, as seen from the figure 5.2.2.7. It is also found that the collector performance in NoWC mode operation is similar to that in full mode.

System performance

The comparison of results of simulated and experimental condensing heat and total evaporating heat in NoWC mode operation is shown in figure 5.2.2.8. As seen from the figure, the variation of predicted condensing heat and evaporating heat are in a good agreement with the measured data.

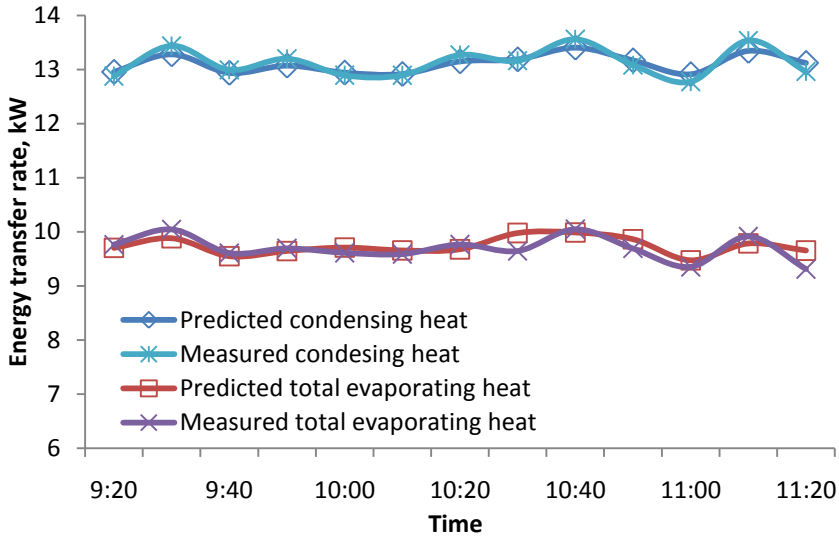

Figure 5.2.2.8 Comparison of predicted and measured condensing heat and total evaporating heat with time

In figure 5.2.2.9, the predicted and measured values of system coefficient of performance (COP) were plotted against time. As seen from the figure, the system COP was slightly affected by the radiation. The agreement between predicted and measured values of COP indicated that the simulation model can describe the system performance in NoWC mode adequately.

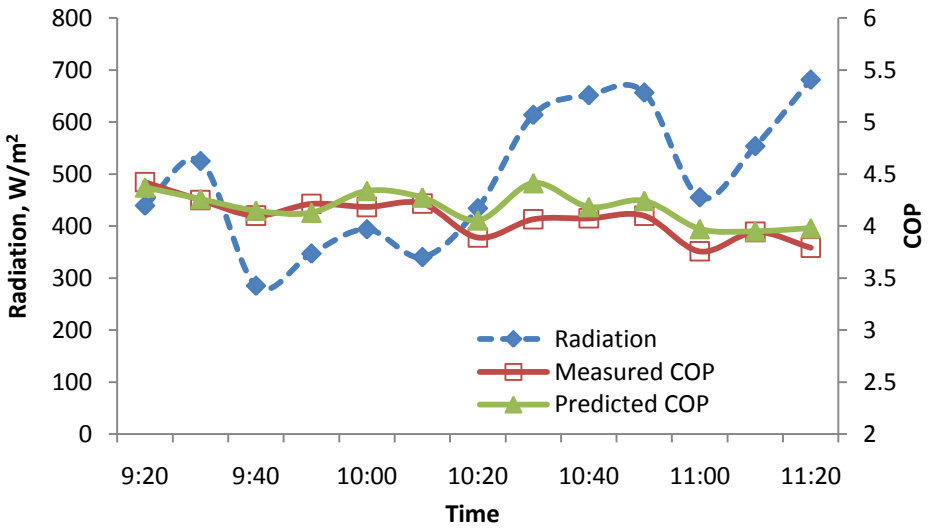

Figure 5.2.2.9 Comparison of predicted and measured system COP with time

5.2.3 NoRE mode operation

In the system simulation for NoRE mode operation, the input process parameters, such as meteorological condition, collector area, compressor speed and other components parameters, are set as same as the experiment conducted and presented in section 5.1.3.

Water heating

Figure 5.2.3.1 shows the comparison between the simulation and experimental results of condensing heat in water condenser with time in the water heating process in NoRE mode operation.

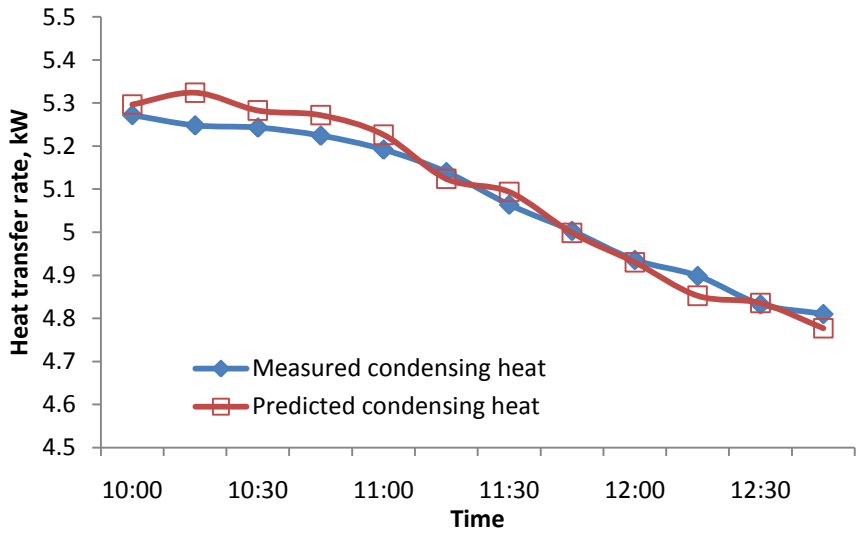

Figure 5.2.3.1 Comparison of predicted and measured condensing heat in water condenser with time

As seen from the figure, the predicted and measured variation in condensing heat and water temperature agree fairly well.

The simulation and experimental values of water temperature in water condenser in NoRE mode operation is plotted against time in figure 5.2.3.2

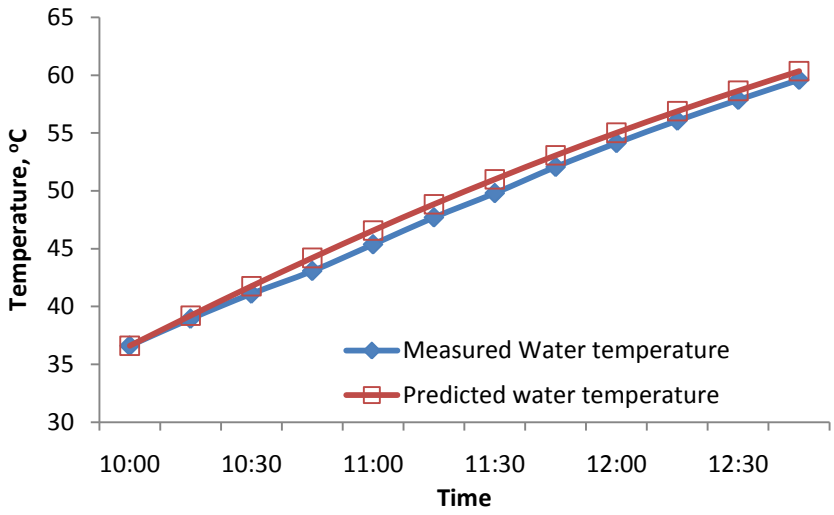

Figure 5.2.3.2 Comparison of predicted and measured water temperature with time

Both simulation and experimental results indicated that, in NoRE mode, the temperature of the 400 liters water increased in a steady manner and rises from 35℃ to 60℃ in 165 minutes. With the rise of water temperature, the condensing heat released from the refrigerant in water condenser declined from 5.3kW to 4.9kW.

The water heating performance in NoRE mode is lower than full mode due to absence of energy absorbed by the room evaporator.

Drying

Figure 5.2.3.3 shows a comparison between the simulation and experimental condensing heat in air condenser with time in NoRE mode operation. As seen from the figure, the predicted and measured results agree fairly well.

It is shown by both predicted and measured data that, in NoRE mode, the condensing heat in air condenser increased dramatically from 0.35kW to 1.1kW with the rise of water temperature. Howerver, like water condensing heat, air condensing heat in NoRE mode is less than full mode for same reason.

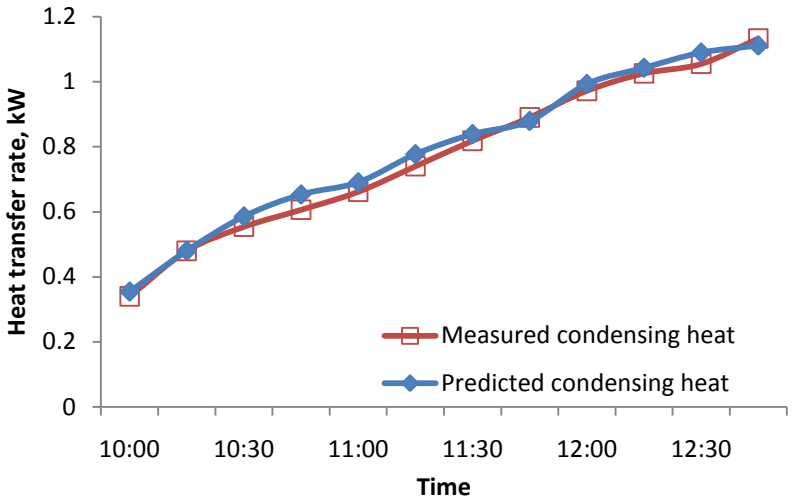

Figure 5.2.3.3 Comparison of predicted and measured condensing heat in air condenser with time

Figure 5.2.3.4 shows the comparison between the simulation and experimental heated air temperature for drying with time in NoRE mode operation. As seen from the figure, the predicted and measured results agree fairly well. Both of them are affected by the ambient temperature.

As a result of rise of the condensing heat in air condenser, the difference between the heated air temperature and ambient temperature is enhanced, as seen from the figure 5.2.3.4.

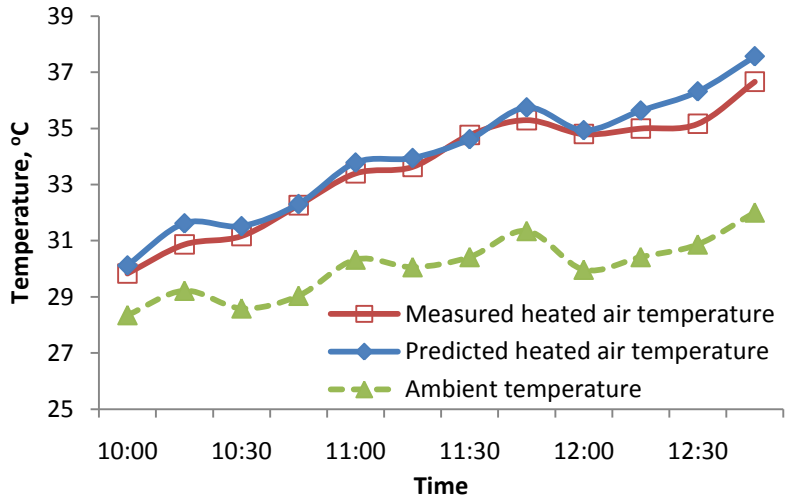

Figure 5.2.3.4 Comparison of predicted and measured heated air temperature with time

Evaporator-collector

In figure 5.2.3.5, measured and predicted useful energy gain, Qu, by the unglazed solar evaporator-collector and solar irradiation are plotted against time.

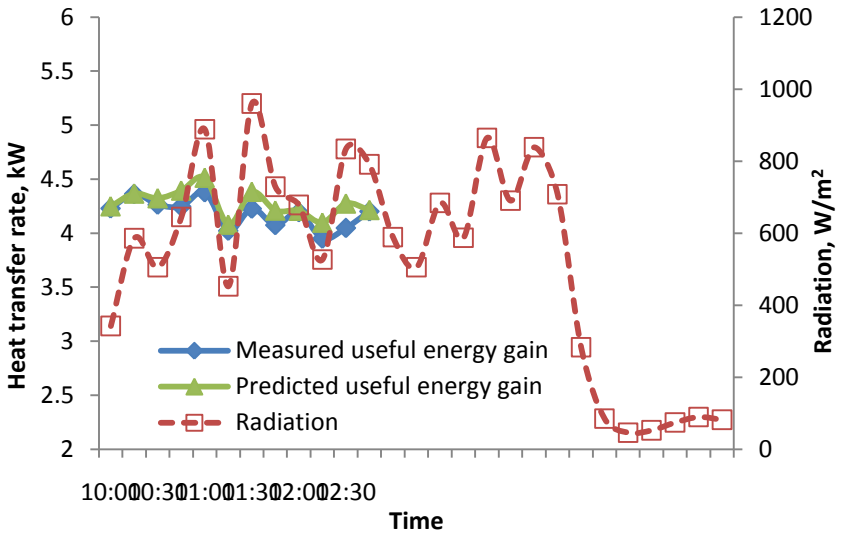

Figure 5.2.3.5 Comparison of predicted and measured collector useful energy gain with time

It shows that predicted Qu has a reasonably good agreement with experimental values in NoRE mode operation. Both of them varied in the range from 4.0kW to 4.5kW with the change of radiation.

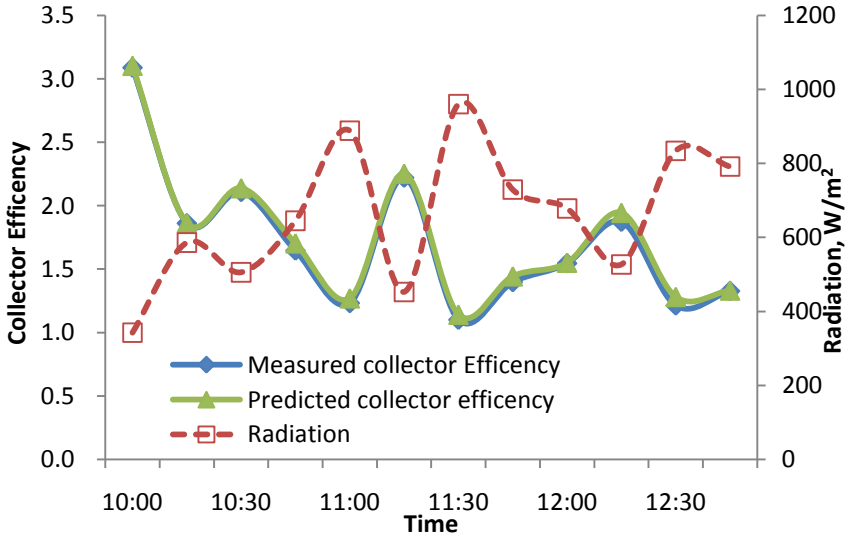

Figure 5.2.3.6 Comparison of predicted and measured collector efficiency with time

The useful energy gain in NoRE mode is greater than full mode due to the fact that the refrigerant mass flow rate is increased as a result of absence of room evaporator. As a result of good agreement of useful energy gain prediction, the simulated collector efficiency matched the experimental results fairly well, as seen from the figure 5.2.3.6. .

System performance

The comparison of results of simulated and experimental system coefficient of performance (COP) in NoRE mode operation is shown in figure 5.2.3.7 As seen from the figure, the system COP has a decline trend with the rise of water temperature.

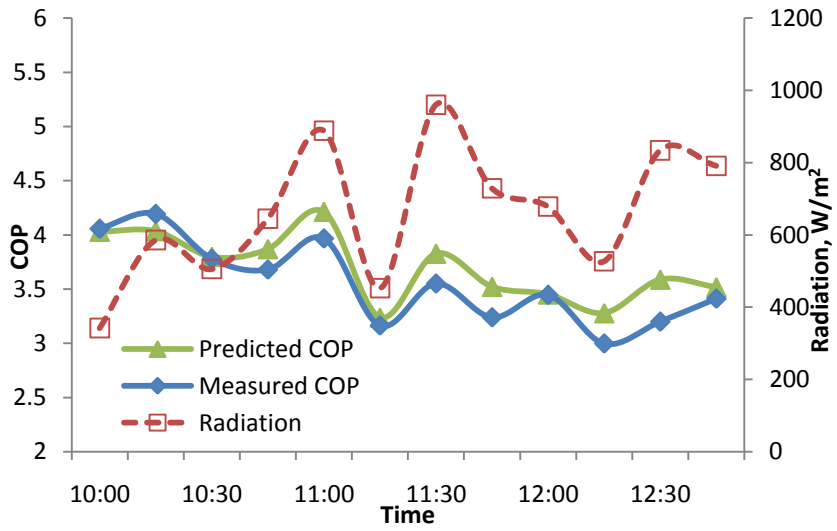

Figure 5.2.3.7 Comparison of predicted and measured system COP with time

The agreement between predicted and measured COP shows that the simulation model can describe the system performance closely under NoRE mode operation.

5.3 Analysis of Un-glazed evaporator-collector

The unglazed evaporator-collector is the essential component in this integrated solar heat pump system. The system performance is greatly depended on this evaporator-collector performance. Without glazed cover, this collector is directly exposed to the ambient and is obviously more sensitive to the ambient condition such as radiation, ambient temperature wind speed and relative humidity.

With the help of validated simulation program, a detail investigation of the evaporator-collector has been carried out under different operating conditions.

5.3.1 Temperature distribution in the plate

In current study, a two-dimensional (2-D) mathematical model of the evaporator -collector has been developed and utilized. In this model, the plate heat transfer in both x direction (vertical to the tube) and y direction (parallel to the tube) are taken into account. The temperature distributions in the plate under different conditions can be predicted by using this 2-D model. The coordinate system for the illustration of temperature distribution is shown in figure 5.3.1.1.

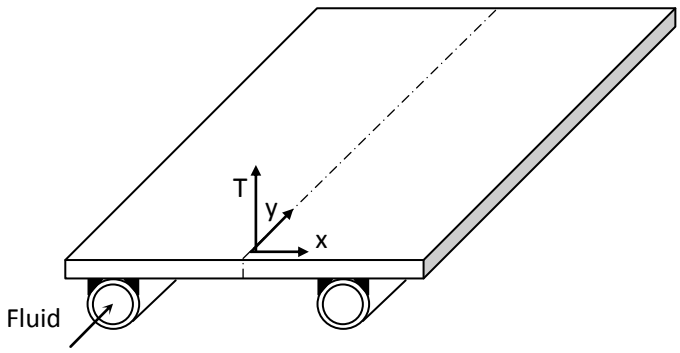

Figure 5.3.1.1 Geometry and coordinate system of evaporator collector

The characteristic curve for the temperature distributions in the evaporator collector under the conditions of radiation at 900W/m^2 and 300W/m^2 are calculated by the method presented in section 4.2.3, as shown in figure 5.3.1.2.

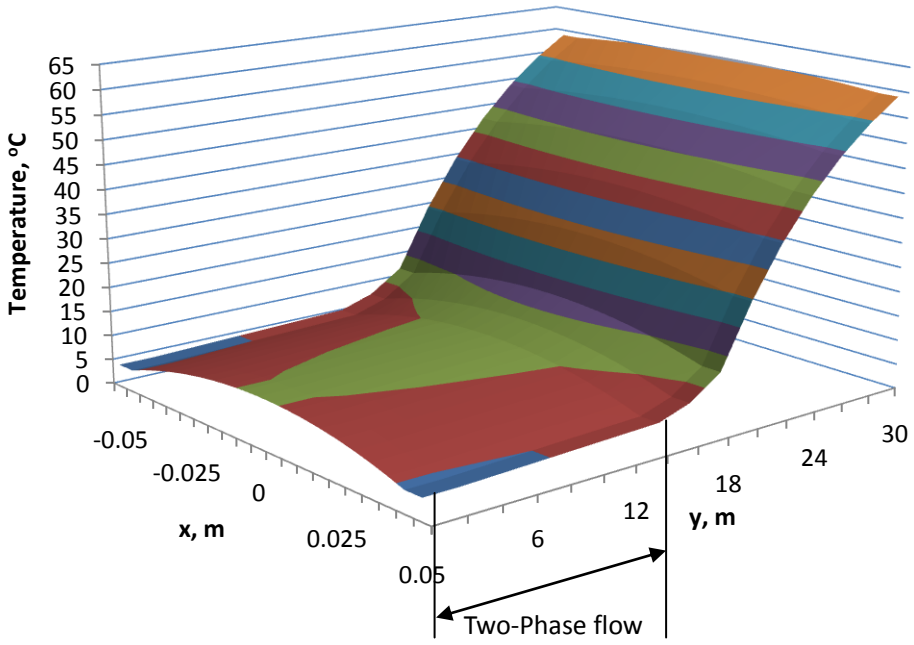

(a) Radiation = 900W/m^2

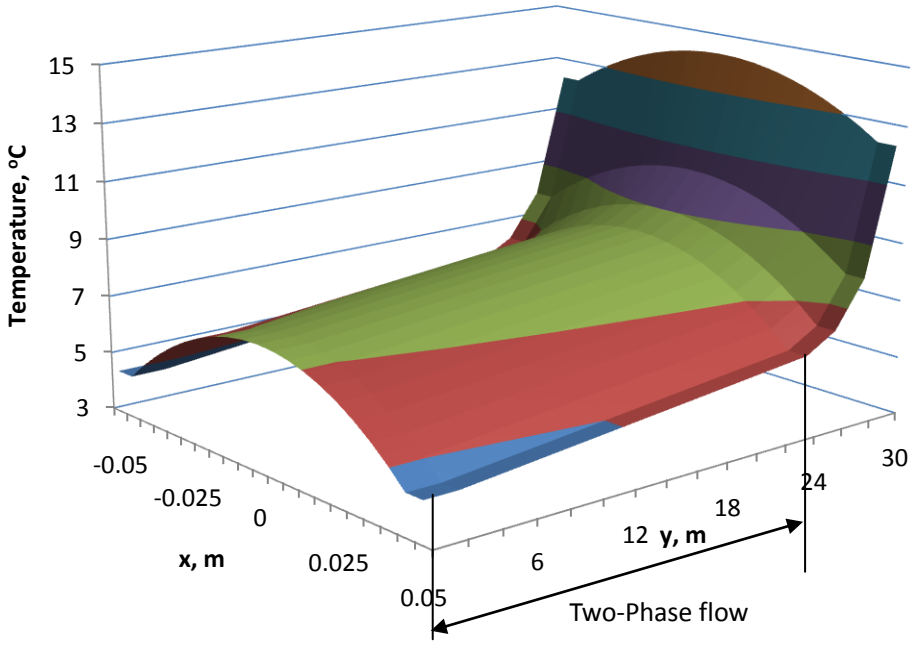

(b) Radiation = 300W/m^2

Figure 5.3.1.2 Temperature distribution in the plate

It described the temperature distribution when the system has run for half hour. It

was found that the temperature decreased in x direction. The decreasing rate at the part near the tube is higher than that at the part near the centre line between tubes.

The variation of temperature of the plate in y direction is almost constant in two-phase flow region. Temperature of the plate varies in the range from 4 to 12℃ in two-phase region. However, it increased rapidly in single phase region caused by the increase of refrigerant temperature in single phase flow.

As shown in figure 5.3.1.2, the length of two-phase flow under irradiation of 300W/m^2 is much longer than that under irradiation of 900W/m^2.

5.3.2 Analysis along the tube.

The condensed refrigerant after expansion valve entered the unglazed evaporator-collector in two-phase status. The vapor quality of this two-phase flow gradually increases to 1 and the refrigerant vapor become superheat before it reaches the compressor. To investigate the development of the parameters, such as vapor quality, heat transfer coefficient and plate temperature, at different locations along the tube, an analysis along the tube under different conditions is carried out by the validated simulation program. The other conditions are chosen as follows:

Ambient Temperature=30℃, Mass flow rate=0.012kg/s,
Wind Speed=3.5m/sec, Condensed refrigerant = 35℃
Relative humidity=70%, Total tube length=30m

The simulation result of the development of vapor quality along the tube under different solar radiation is shown in figure 5.3.2.1.

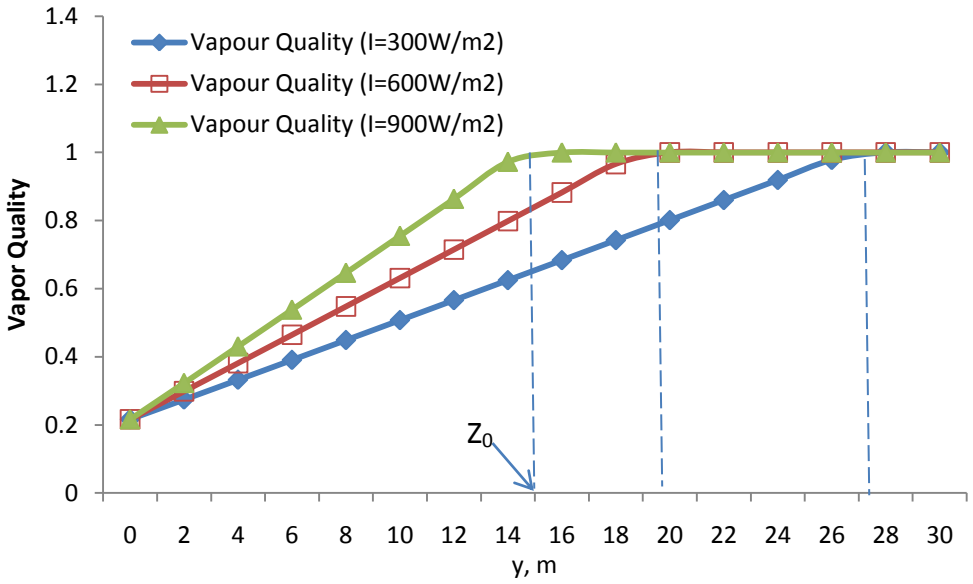

Figure 5.3.2.1 Development of vapor quality along the tube under different solar radiation.

The point where vapor quality becomes 1 is the end of two-phase flow. The length of two-phase flow in the tube is defined as Z_0. As seen from the figure, Z_0 is greatly

affected by the level of radiation. The higher is the solar radiation, the shorter is the length of two-phase flow.

Development of heat transfer coefficient inside the tube in different solar radiation is presented in figure 5.3.2.2.

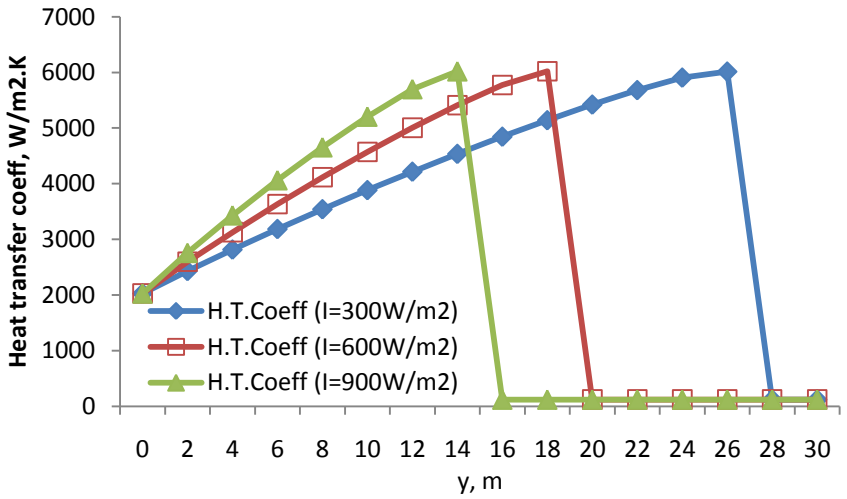

Figure 5.3.2.2 Development of heat transfer coefficient inside the tube at different solar radiation levels.

As seen from the figure, the heat transfer coefficient increase with the rise of vapor quality in two-phase flow and dramatically dropped in single-phase region.

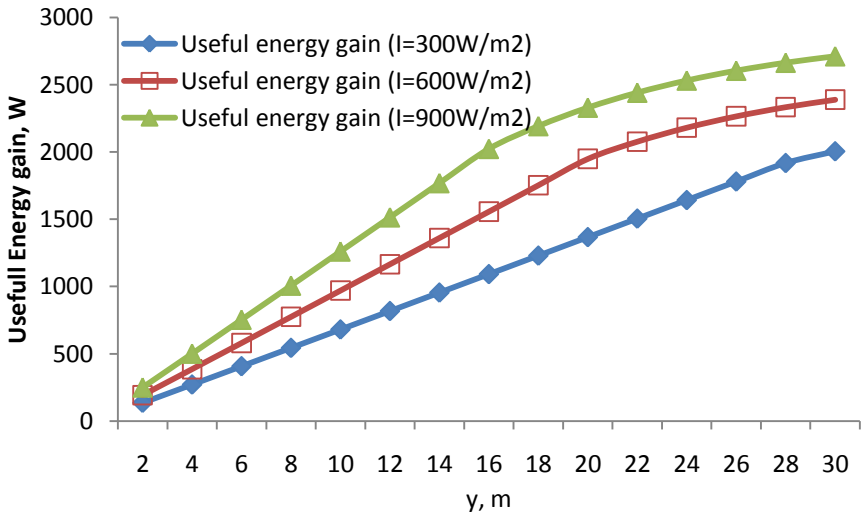

Figure 5.3.2.3 Development of energy gain by the refrigerant along the tube at different solar radiation levels.

Figure 5.3.2.3 shows the development of energy gain by the refrigerant along the tube in different solar radiation. As seen from the figure, the increase of energy gain in single-phase flow is much slower than that in two-phase, as a result of the fall of heat transfer coefficient inside the tube. It means the useful energy gain per unit length in two-phase region is much higher than that in single-phase region. For the total tube length, the higher solar radiation, the higher total useful energy gain.

The energy gain by the refrigerant in the evaporator-collector is a combination of energy gain from radiation and ambient. The development of energy gain from radiation and ambient along the tube in different solar radiation is presented in figure 5.3.2.4

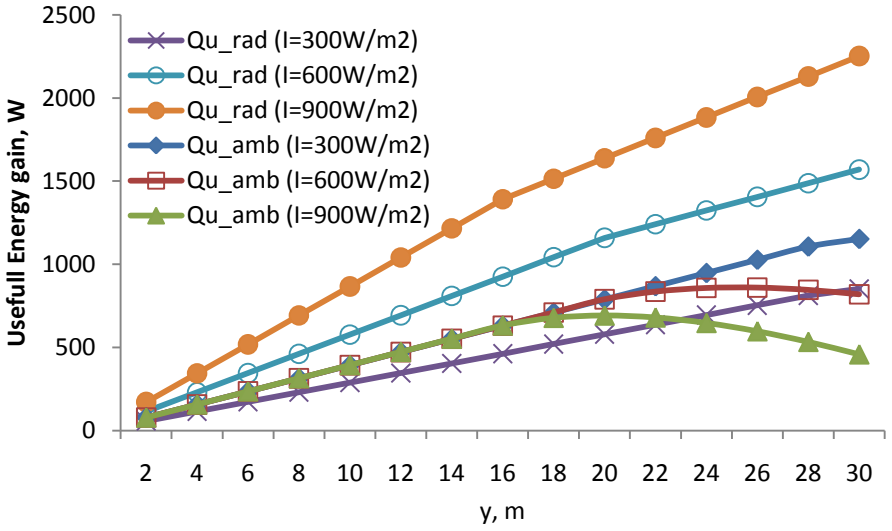

Figure 5.3.2.4 Development of energy gain from radiation and ambient along the tube in different solar radiation

As seen from the figure, in two-phase flow region, the solar radiation affects the collector useful energy gain mainly by affecting the useful energy gain from radiation. In two-phase flow region, the higher is the solar radiation, the higher is the Qu_rad. However, the variation of useful energy gain from ambient, Q_{u_amb}, is almost same in two-phase flow for three radiation conditions considered here.

The increasing rate of Qu_rad dropped slightly in single phase flow due to the drop of heat transfer coefficient inside the tube. In contrast, the increasing rate of useful energy gain from ambient dropped remarkably and even become negative in single phase flow. It is due to the rise of plate temperature caused by the increase of refrigerant temperature in single phase flow.

Development of collector plate surface temperature above the tube (x=W/2) along the tube length under different solar radiation is presented in figure 5.3.2.5.

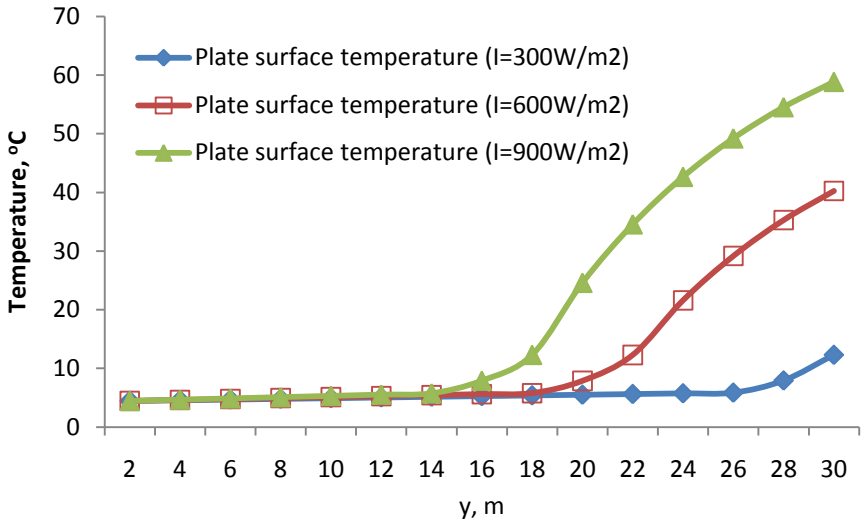

Figure 5.3.2.5 Development of collector plate surface temperature with tube length in different solar radiation.

The plate surface in two-phase flow is not much different for three radiation conditions. It is close to the refrigerant temperature, which is almost constant in two-phase flow. However, the plate surface temperature increased due to an increase of refrigerant temperature in single phase flow.

5.3.3 Effect of solar radiation on collector performance

The effect of solar radiation on collector performance is analyzed in this section. Results of different parameters for the mass flow rates of 0.009kg/s, 0.012kg/s and 0.015kg/s are presented against the solar radiation ranging from 100W/m^2 to 1000W/m^2. The other conditions are chosen as follows:

Ambient Temperature=30℃, Relative humidity=70%.
Wind Speed=3.5m/sec, Condensed temperature=35℃

As indicated in 5.3.1, the collector performance is mainly determined by the length of two-phase flow, Z_0. Figure 5.3.3.1 presented the length of two-phase flow against solar radiation for different refrigerant flow rate. It should be noted that the maximum of the length of two-phase flow is the total tube length, which is 30m.

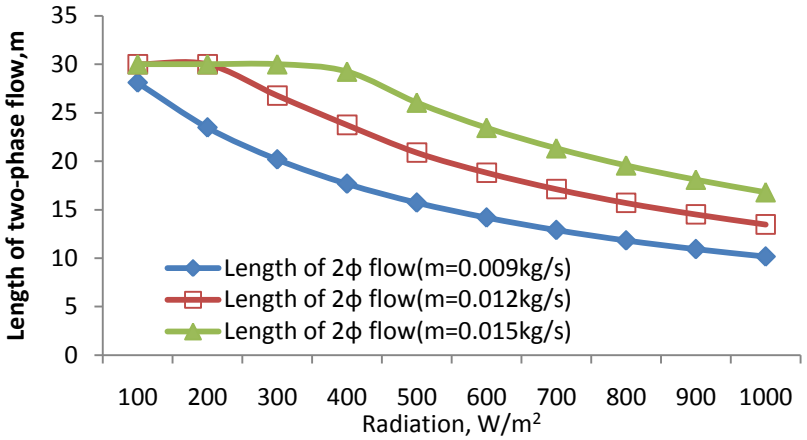

Figure 5.3.3.1 Variation of length of two-phase flow with solar radiation for different refrigerant flow rate

As seen from the figure, with the rise of radiation, the length of two-phase flow, Z_0, decreased gradually, because of the rise of useful energy gain per unit tube length. It is also noted that, the higher mass flow rate, the longer length of two-phase flow. It can be attributed to the fact that the higher mass flow rate leads to a higher requirement of heat gain for same enhancement of vapor quality of the refrigerant.

The effect of radiation and mass flow rate on the collector performance is further

analyzed in terms of total useful energy gain, as presented in figure 5.3.3.2.

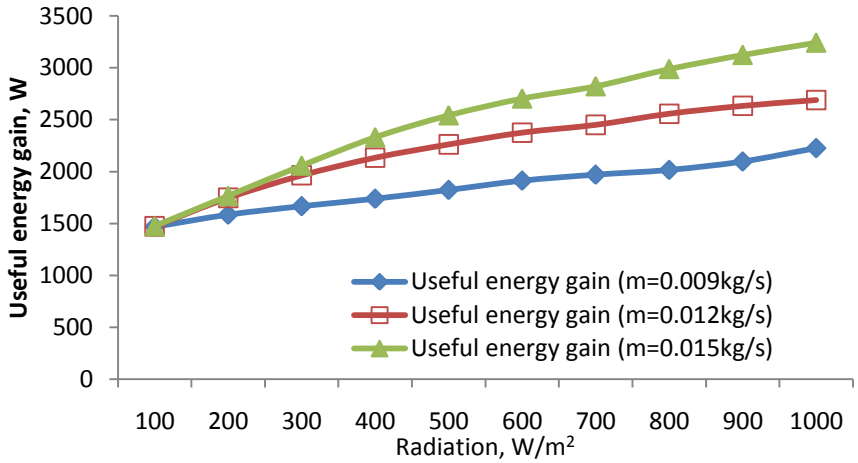

Figure 5.3.3.2 Variation of total useful energy gain with solar radiation for different refrigerant flow rate.

As seen from the figure 5.3.3.2, for a certain mass flow rate, the useful energy gain increased with the rise of radiation, which is also presented and discussed in figure 5.3.1.3. The lower mass flow rate, the faster useful energy gain increasing rate.

The differences of the useful energy gains for different mass flow rates in low radiation condition ($I<300W/m^2$) is less than that in high radiation conndition ($I>600W/m^2$), as seen from the figure 5.3.3.2. It can be explained by the facts that the ratios of length of two-phase flow to total tube length(30m) for different mass flow rates in low radiation condition are equal or close to 1, as seen in figure 5.3.3.1, and the useful energy gains for different mass flow rates in two phase flow region are almost same, as described in figure 5.3.2.3.

The total useful energy gain of evaporator-collector consists of two parts: energy gain from radiation and energy gain from ambient. These two parts for different mass flow rates are plotted against radiation separately in figure 5.3.3.3 and figure 5.3.3.4. The energy gain from radiation, Qu_rad, increases remarkbly with the rise of radiation, as seen from figure 5.3.3.3. The mass flow rate has little effect on Qu_rad.

However, the energy gain from ambient for different mass flow rate conditions decreased with the rise of solar radiation, as seen from figure 5.3.3.4. It was caused by the rise of plate temperature in single phase flow region as a result of rise of radiation, as presented in figure 5.3.1.5.

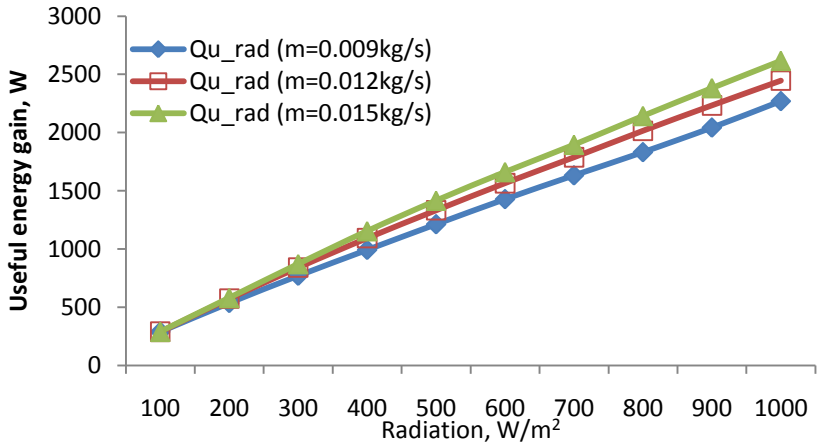

Figure 5.3.3.3 Variation of energy gain from radiation with solar radiation for different refrigerant flow rates.

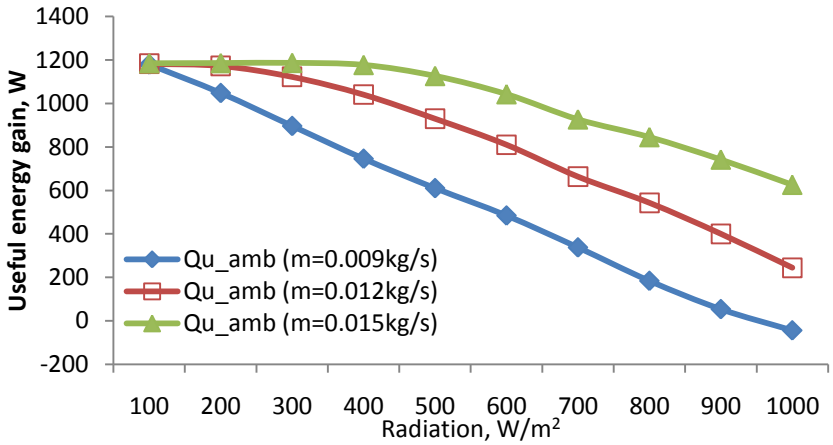

Figure 5.3.3.4 Variation of energy gain from ambient with solar radiation for different refrigerant flow rates.

The energy gain from ambient increased with the rise of mase flow rate, leading to the increase of length of two-phase flow, where the plate temperature is almost constant and much lower than ambibent, as seen from figure 5.3.2.5

The results above pointed to the conclusion that solar radiation has positive effect

on the energy gain from radiation and negatvie effect on the energy gain from ambient. It makes the total useful energy gain relatively stable in different radiation conditions, as described in figure 5.3.3.2.

Another important parameter for the evaporator-collector performance is collector efficiency. Collector efficiency of evaporator-collector for different mass flow rates are plotted against solar radiation in figure 5.3.3.5.

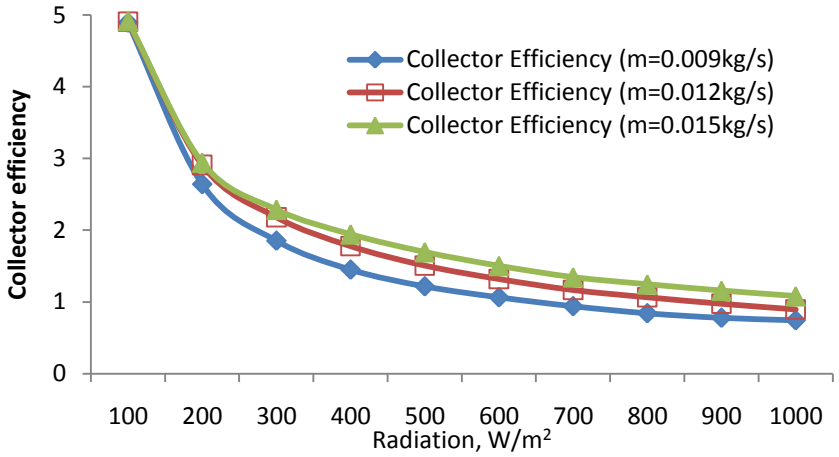

Figure 5.3.3.5 Variation of collector efficiency with solar radiation for different refrigerant flow rates.

As seen from the figure, the collector efficiency decreased rapidly with the rise of radiation in low radiation level. The rate of decrease reduced gradually as the radiation level increased. The high efficiency in low radiation condition is caused by the part of energy gain from ambient in low radiation condition, presented in figure 5.3.3.4. With the combination of energy from radiation and ambient, the collector efficiency is close to 1 for different mass flow rate even in high radiation condition.

For a specific value of solar radiation, the collector efficiency increases when mass flow rate increase. It is because that the higher mass flow rate leads to a higher requirement of heat gain for same enhancement of vapor quality of the refrigerant.

5.3.4 Effect of ambient temperature on collector performance

The effect of ambient temperature on collector performance is analyzed in this section. Results of different parameters for the mass flow rates of 0.009kg/s, 0.012kg/s and 0.015kg/s are presented against the ambient temperature ranged from 20℃ to 40℃. The other conditions are chosen as follows:

Solar radiation=600W/m^2, Relative humidity=70%,
Wind Speed=3.5m/sec, Condensed Temperature=35℃.

The lengths of two-phase flow for different refrigerant mass flow rate are plotted against solar radiation in figure 5.3.4.1.

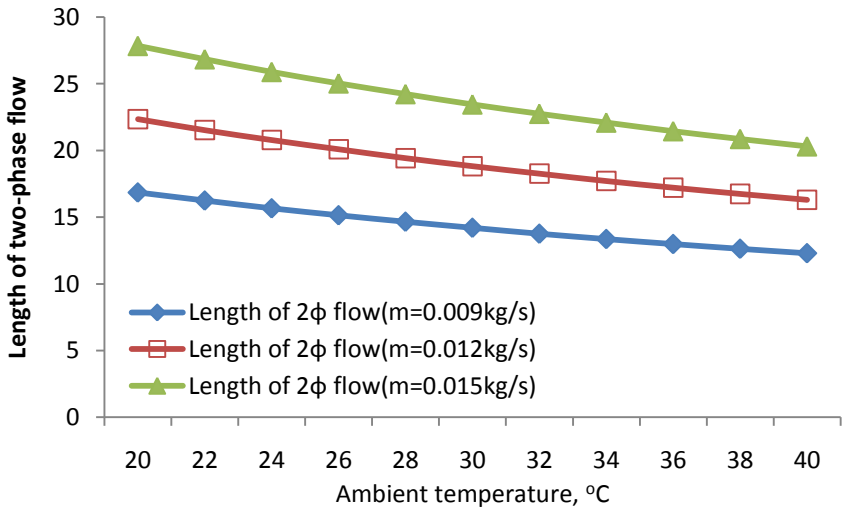

Figure 5.3.4.1 Variation of length of two-phase flow with ambient temperature for different refrigerant flow rates

As seen from the figure, the length of two-phase flow slightly decreased with the rise of ambient temperature. It can be attributed to the fact that higher ambient temperature causes higher temperature difference between ambient and fluid leading to a higher useful energy gain per unit length from ambient.

For a specific value of ambient temperature, the length of two-phase flow increase when mass flow rate increase. It can be attributed to the fact that higher mass flow

rate causes more heat requirement for same vapor quality enhancement of the refrigerant.

The effect of ambient temperature on the collector performance is further analyzed in terms of total useful energy gain, as presented in figure 5.3.3.2. It shows that the total useful energy gain increase gradually when ambient temperature increase, resulting in the increase of temperature difference between ambient and fluid.

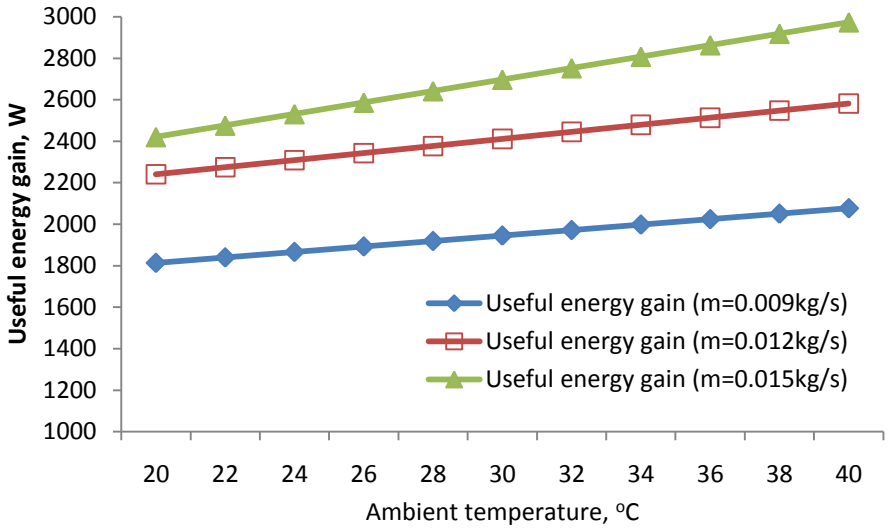

Figure 5.3.4.2 Variation of useful energy gain from radiation with ambient temperature for different refrigerant flow rates.

The effect of ambient temperature on the total useful energy gain is then investegated in terms of energy gain from radiation and energy gain from ambient separately . These two parts energy gain for different mass flow rates are plotted against ambient temperature separately in figure 5.3.4.3 and figure 5.3.4.4.

As seen from figure 5.3.4.3, the energy gain from radiation, Qu_rad, is stable with the variation of ambient temperature. However, the energy gain from ambient, Qu_amb, increase rapidly when the ambient temperature increase, as shown in figure 5.3.4.4.. It indicated that the effect of ambient temperature on the total useful energy gain is mainly in the part of energy gain from ambient.

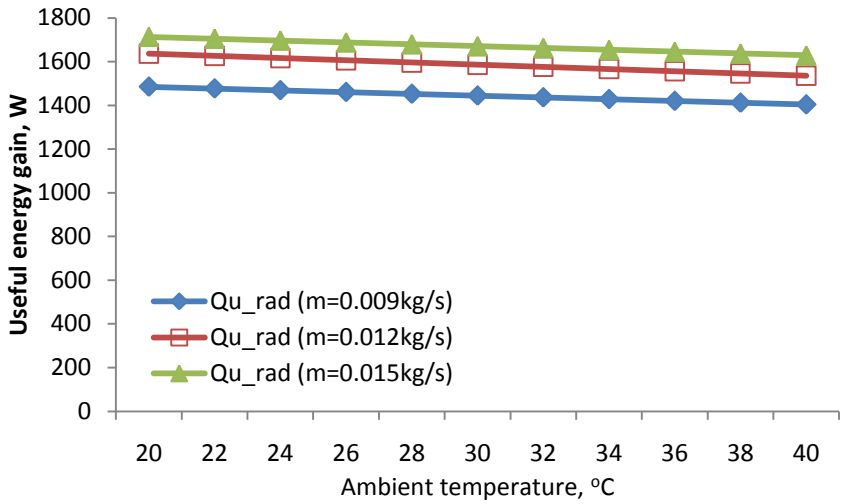

Figure 5.3.4.3 Variation of energy gain from radiation with ambient temperature for different refrigerant flow rates.

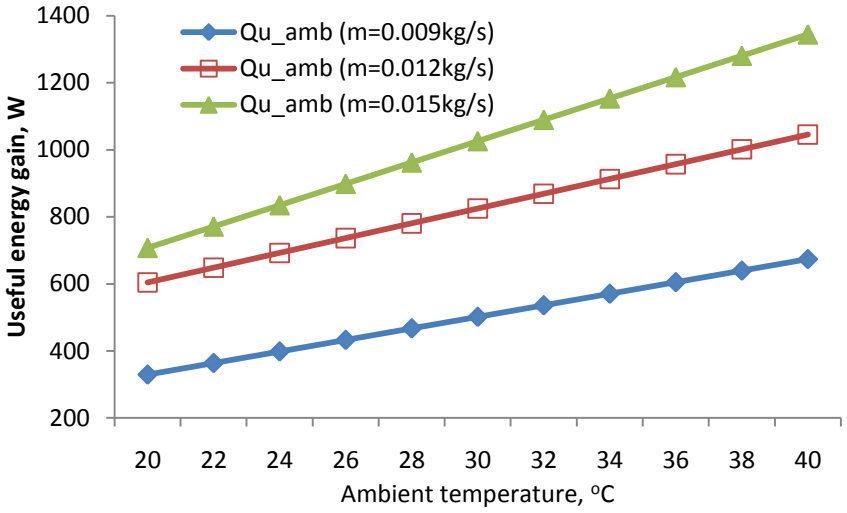

Figure 5.3.4.4 Variation of energy gain from ambient with ambient temperature for different refrigerant flow rates.

Collector efficiency curves of evaporator-collector for different mass flow rates are plotted against ambient temperature in figure 5.3.4.5. As seen from the figure, with the rise of ambient temperature, collector efficiency increases slightly as a result of rise of total useful energy gain.

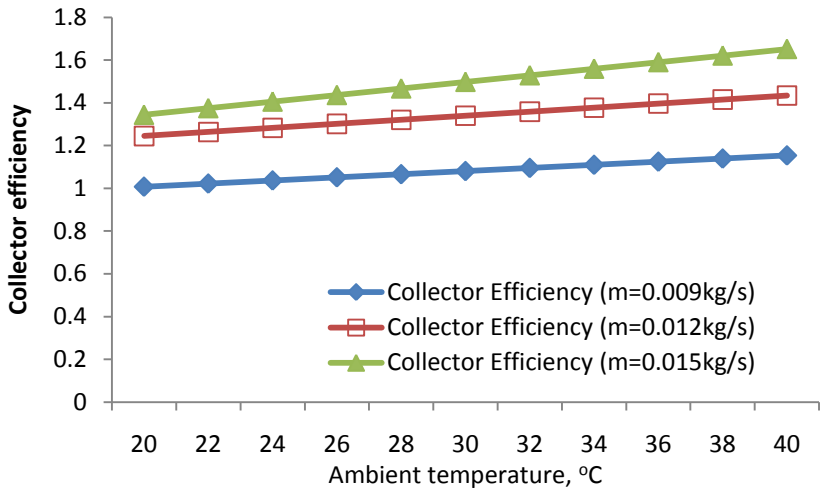

Figure 5.3.4.5 Variation of collector efficiency with ambient temperature for different refrigerant flow rates.

For a specific value of ambient temperature, the collector efficiency of evaporator-collector increase when mass flow rate increase, leading to the rise of total useful energy gain.

5.3.5 Effect of relative humidity (RH) on collector performance

When the plate temperature is lower than the environment dew point, condensation of water vapor in the ambient will occur on the plate surface. A water film is formed on the surface of evaporator-collector. Latent heat is released, which is mostly transferred to the fluid. This part of heat gain of collector only occurs when plate temperature is lower than the dew point.

The effect of relative humidity (RH) on collector performance is analyzed in this section. Results of different parameters for the mass flow rates of 0.009kg/s, 0.012kg/s and 0.015kg/s are presented against RH ranged from 10% to 100%. The other conditions are chosen as follows:

Solar radiation=600W/m^2, Ambient temperature=30℃,
Wind Speed=3.5m/sec, Condensed temperature=35℃.

Variation of the dew points for different ambient temperature with relative humidity (RH) is shown in figure 5.3.5.1. As seen from the figure, with the rise of RH, dew point increase and reach the value of ambient temperature when the RH is 100%.

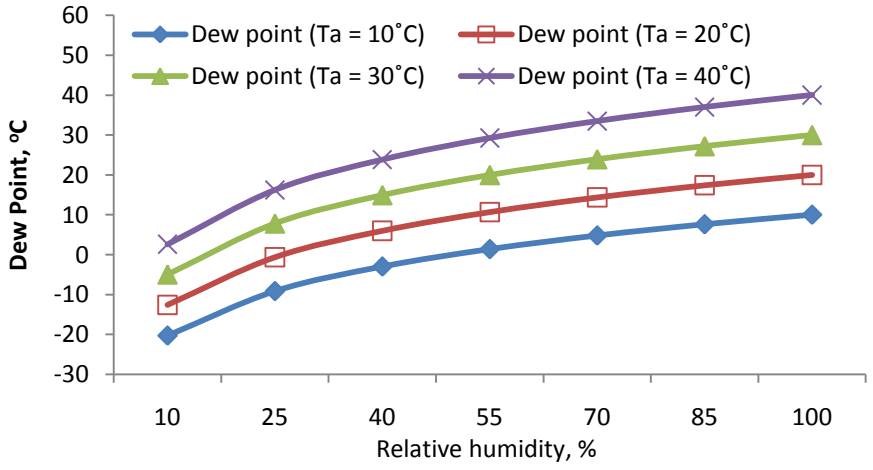

Figure 5.3.5.1 Variation of dew point with RH for different ambient temperature

The lengths of two-phase flow for different ambient temperature are plotted against RH in figure 5.3.5.2.

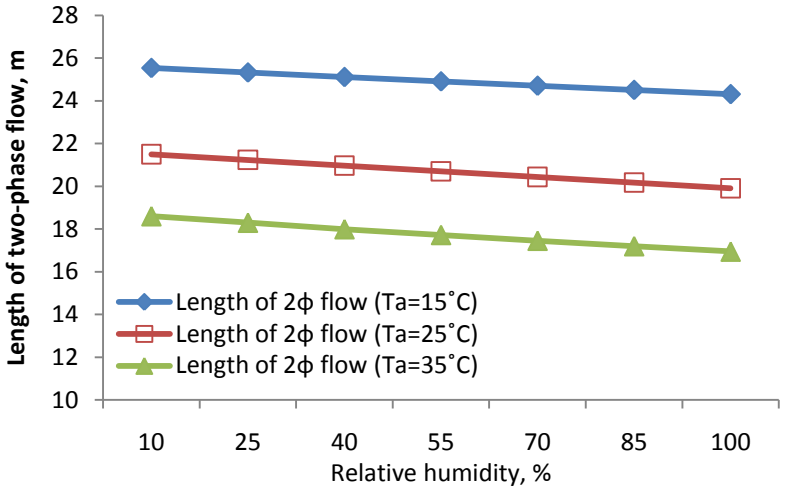

Figure 5.3.5.2 Variation of length of two-phase flow with RH for different ambient temperature

It shows that the length of two-phase flow decreases with rise of relative humidity. It is because higher RH causes higher condensation heat transfer coefficient, leading to higher heat gain from ambient per unit tube length. For a specific value of RH, when ambient temperature increase, the length of two-phase flow decrease, as a result of the rise of total useful energy gain.

The effect of RH on collector performance is analyzed in terms of total useful energy gain, as presented in figure 5.3.5.3. It shows that the total useful energy gain increase gradually when RH increase, resulting higher heat gain from ambient.

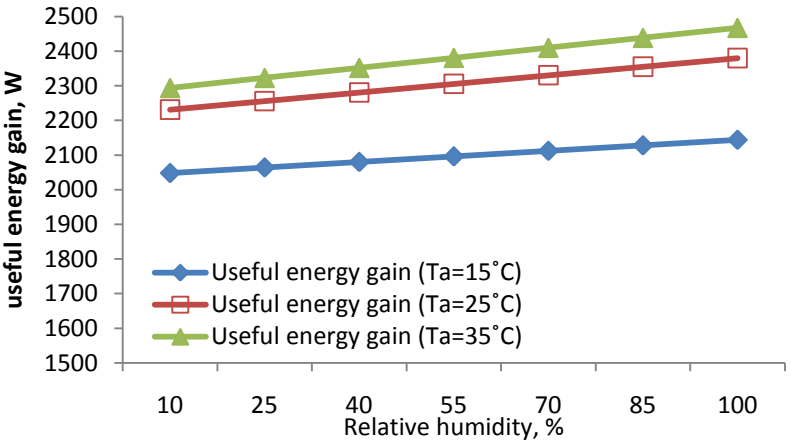

Figure 5.3.5.3 Variation of useful energy gain with RH for different ambient temperature.

For a specific value of RH, when ambient temperature increase, the total useful energy gain increase, as presented in figure 5.3.5.3. It can be attributed to the fact that higher ambient temperature causes higher temperature difference between ambient and fluid leading to a higher useful energy gain from ambient.

Useful energy gain from radiation and ambient for different ambient temperature are plotted against RH separately in figure 5.3.4.3 and figure 5.3.4.4.

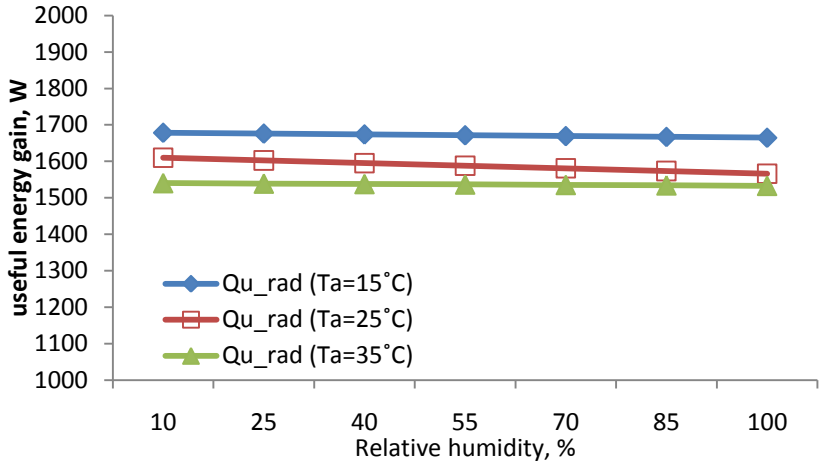

Figure 5.3.5.4 Variation of energy gain from radiation with RH.

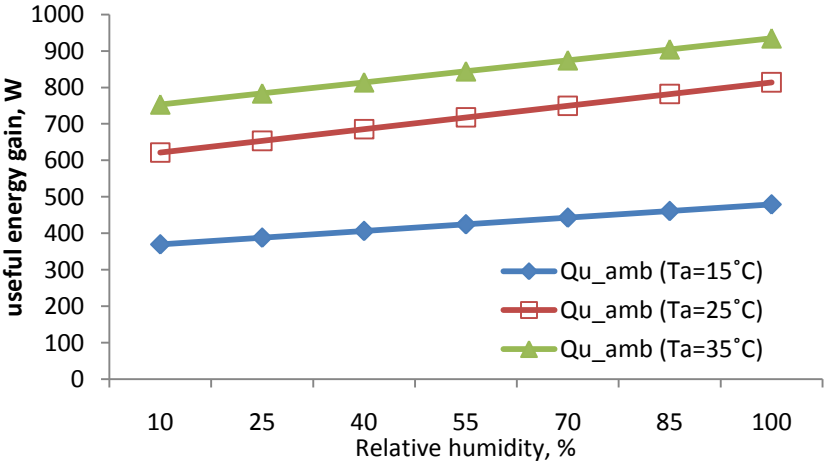

Figure 5.3.5.5 Variation of energy gain from ambient with RH.

As seen from figure 5.3.5.4, the energy gain from radiation, Qu_rad, is stable with variation of RH. However, the energy gain from ambient, Qu_amb, increase gradualy when the RH increase, as shown in figure 5.3.5.5. It indicated that the effect of RH

on the total useful energy gain is mainly in the part of energy gain from ambient by influncing the condensation heat transfer.

Collector efficiency of evaporator-collector for different ambient temperature are plotted against RH in figure 5.3.5.6. As seen from the figure, with the rise of RH, collector efficiency increase, as a result of rise of total useful energy gain.

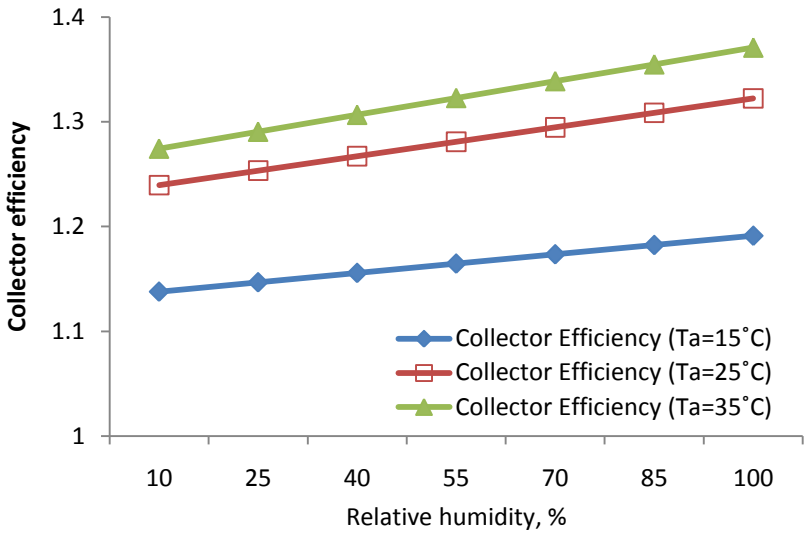

Figure 5.3.5.6 Variation of collector efficiency with RH for different ambient temperature.

For a specific value of RH, when ambient temperature increase, the collector efficiency of evaporator-collector increase, as a result rise of total useful energy gain.

5.3.6 Effect of condenser exit temperature on collector performance

Once condensed in the condenser, refrigerent is in liquid state, in which enthalpy is only a function of temperature. It is then throttled by expansion valve in a constant enthapy process and entered evpaorator-collector in a two-phase state. It means the enthalpy of refrigerant at evaporator-collector inlet is determined by the refrigerent temperature at the exit of condenser.

The effect of refrigerant temperature at the exit of condenser on collector performance is analyzed in this section. Results of different parameters for the mass flow rates of 0.009kg/s, 0.012kg/s and 0.015kg/s are presented against refrigerant temperature at the exit of condenser ranging from 30℃ to 70℃. The other conditions are chosen as follows:

Solar radiation=600W/m^2, Ambient temperature=30℃
Wind Speed=3.5m/sec, Relative humidity=70%.

The variation of the length of two-phase flow with refrigerant temperature at the exit of condenser for different mass flow rates is shown in figure 5.3.6.1.

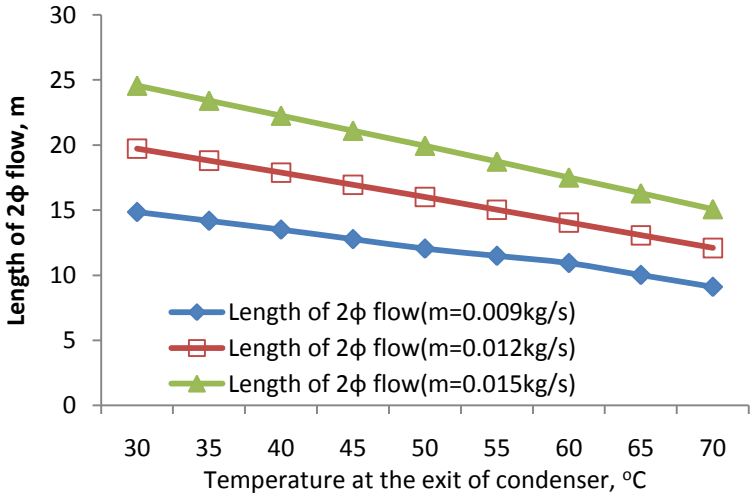

Figure 5.3.6.1 Variation of length of two-phase flow with temperature at the exit of condenser for different refrigerant flow rates

As seen from the figure, the length of two-phase flow reduces with the rise of

refrigerant temperature at the exit of condenser. It can be attributed to the fact that higher refrigerant temperature at the exit of condenser causes higher refrigerant entry enthalpy leading to a lower energy gain requirement for enhancing the vapor quality to 1. For a specific value of refrigerant temperature at the exit of condenser, when mass flow rate increase, the length of two-phase flow increase, as a result of rise of heat requirement for enhancing the vapor quality to 1.

The effect of temperature at the exit of condenser on the collector performance is further analyzed in terms of total useful energy gain, as shown in figure 5.3.6.2. It shows that the total useful energy gain decrease gradually when temperature at the exit of condenser increase, shortening the length of two-phase flow.

As discussed in 5.3.1, the useful energy gain per unit length in two-phase is much higher than that in single-phase. Therefore, when refrigerant temperature at the exit of condenser increase, total useful energy gain decrease, caused by the fall of the ratio of length of two-phase flow to the total tube length, as shown in figure 5.3.6.2.

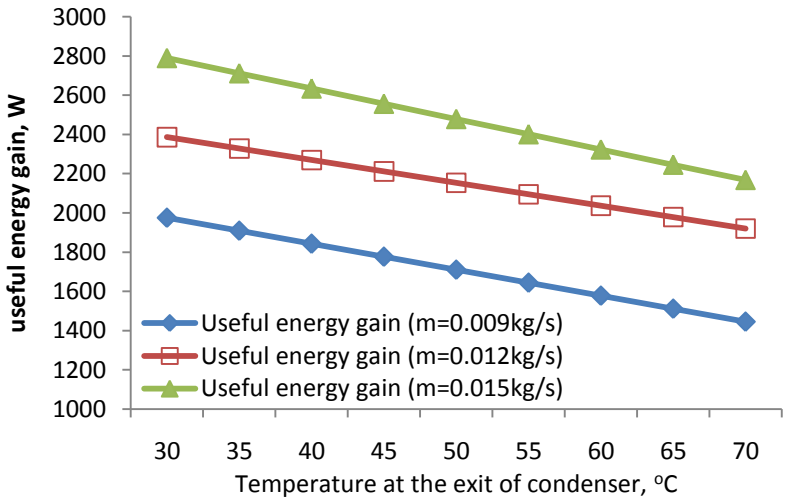

Figure 5.3.6.2 Variation of useful energy gain with temperature at the exit of condenser for different refrigerant flow rates.

The effect of temperature at the exit of condenser on the total useful energy gain is

then investigated in terms of useful energy gain from radiation and useful energy gain from ambient separately. These two parts of energy gain for different mass flow rates are plotted against temperature at the exit of condenser separately in figure 5.3.6.3 and figure 5.3.6.4.

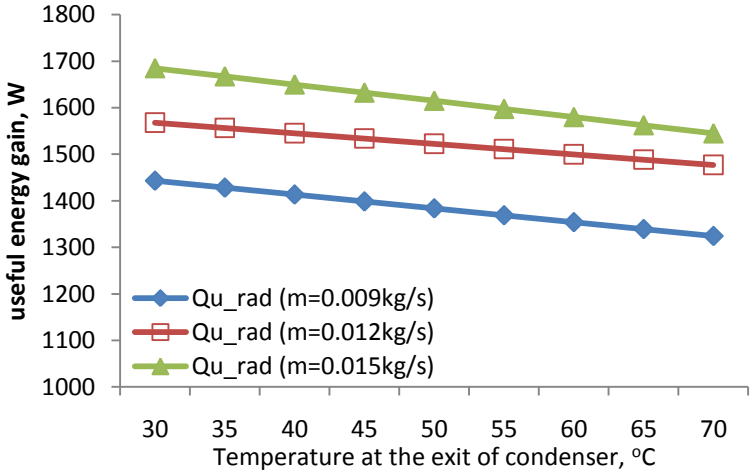

Figure 5.3.6.3 Variation of energy gain from radiation with temperature at the exit of condenser for different refrigerant flow rate.

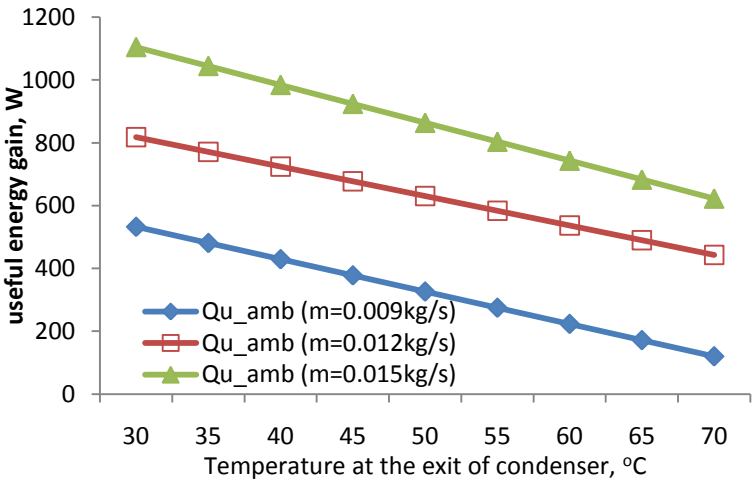

Figure 5.3.6.4 Variation of energy gain from ambient with temperature at the exit of condenser for different refrigerant flow rates.

As seen from figure 5.3.6.3 and figure 5.3.6.4, both the energy gain from radiation, Qu_rad, and the energy gain from ambient, Qu_amb, decrease when the refrigerant temperature at the exit of condenser increase, because both Qu_rad per unit length and Qu_amb per unit length in two-phase region are much higher than those in

single phase region, as discussed in 5.3.1. When compared with the response of Q_{u_rad} to the increase of temperature at the exit of condenser, Q_{u_amb} is more sensitive to the change of refrigerant temperature at the exit of condenser, as seen in figure 5.3.6.3 and figure 5.3.6.4. It can be attributed to the fact that Q_{u_amb} per unit length dropped dramatically when fluid becomes superheated vapor (even drop to negative) while the Q_{u_rad} per unit length only reduce a little, as shown in figure 5.3.1.4 and figure 5.3.2.4.

Collector efficiency of evaporator-collector for different mass flow rates are plotted against refrigerant temperature at the exit of condenser, as shown in figure 5.3.6.5. With the rise of refrigerant temperature at the exit of condenser, collector efficiency decreases as a result of decline of total useful energy gain.

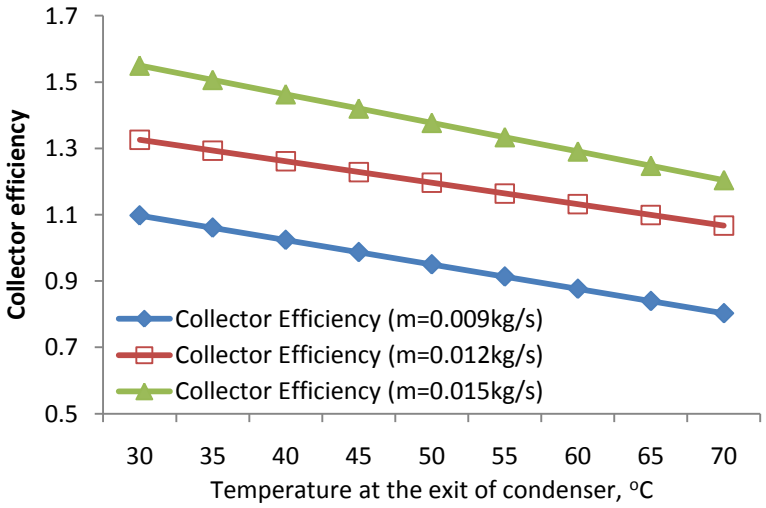

Figure 5.3.6.5 Variation of collector efficiency with temperature at the exit of condenser for different refrigerant flow rates.

5.3.7 Comparison of 1-D and 2-D models

In the present study, a two-dimensional (2-D) mathematical model of the evaporator-collector has been developed. In this model, heat transfer inside the plate in both x direction (vertical to the tube) and y direction (parallel to the tube) are taken into account. However heat transfer inside in y direction is neglected in conventional one-dimensional (1-D) model.

The comparison of simulation results using 1-D and 2-D mathematical model of the evaporator-collector is presented in this section. Different parameters are presented against solar radiation ranged from 100W/m^2 to 1000W/m^2. The other conditions are chosen as follows:

Ambient temperature=30℃, Wind Speed=3.5m/sec,
Mass flow rate=0.012kg/s, Relative humidity=70%
Refrigerant temperature at the exit of condenser=35℃

Simulation results of useful energy gain and collector efficiency from 1-D and 2-D models are plotted against solar radiation in figure 5.3.7.1.

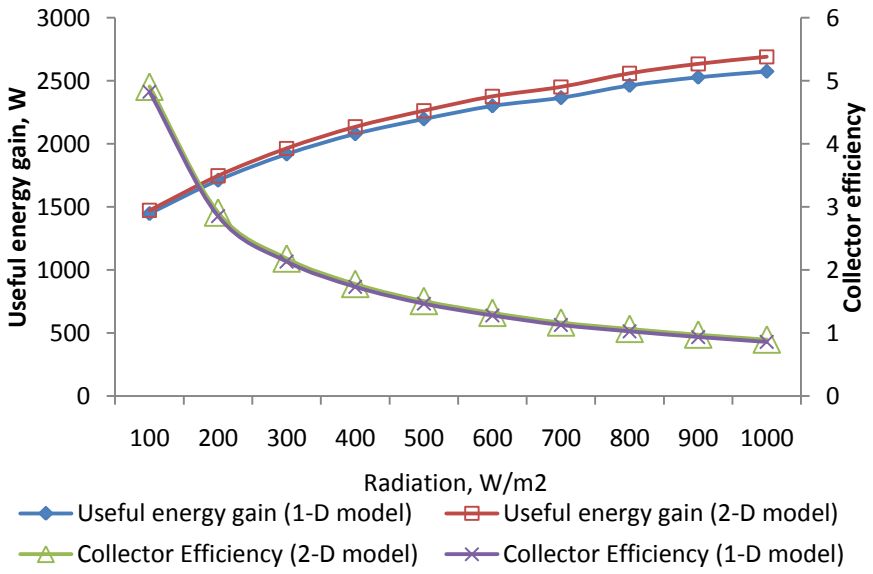

Figure 5.3.7.1 Comparison of useful energy gain and collector efficiencies for 1-D simulation model and 2-D simulation model.

As seen from the figure, simulation results using 1-D and 2-D mathematical model of the evaporator-collector are very close. The average difference is only 3% of the 2-D result. The difference of results between 1-D and 2-D mathematical model is mainly due to the heat transfer inside the plate in y direction, caused by the rapid change of refrigerant temperature in single-phase region, which is neglected in 1-D model. As mentioned earlier in figure 5.3.3.1, the higher radiation, the longer length of single-phase flow. Therefore, the difference between the results from 1-D and 2-D model increases with the rise of radiation, as shown in figure 5.3.7.1. The maximum difference, which is 4.3% of 2-D result, occurs at radiation I=1000W/m^2.

It can be concluded that 1-D model, which is simpler than 2-D mode, can be used when allowance error is more than or equal to 5%.

5.4 System parametric study

The performance of this solar assisted heat pump water heating, drying and air-conditioning system is sensitive to a lot of operation variables. To identify the important variables, a series of numerical investigation have been performed. The area of one piece of evaporator-collector is 1.5 m^2. In the present study, evaporator-collectors are connected in series. The effect of each parameter on thermal performance has been discussed in this section.

5.4.1 Effect of compressor speed

Figure 5.4.1.1 shows the variation of collector useful energy gain as a function of compressor speed with different colletor areas. As compressor speed increases, useful energy gain of the collectors with area of 3.0m^2 and 4.5m^2 increases, which is due to the rise of mass flow rate inside the evaporator-collector..

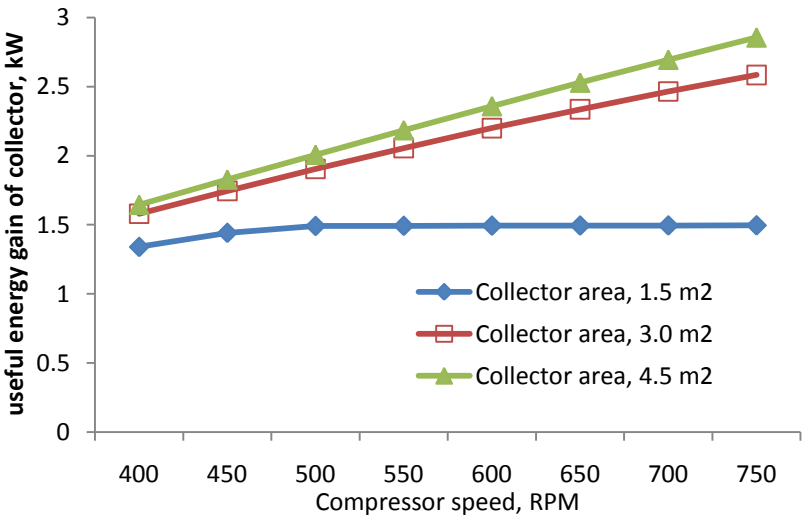

Figure 5.4.1.1 Variation of collector useful energy gain with compressor speed for different collector area.

However, the useful energy gain of the collector with area of 1.5m^2 did not increase as the other two collectors. It can be attributed to the fact that, for collector with area of 1.5m^2 (total tube length of 15m), most of the flow is in two-phase regoin

and mass flow rate did not affect the useful energy gain per unit length much in two-phase region .

Figure 5.4.1.2 shows the variation of collector efficiency as a function of compressor speed with different colletor area. As compressor speed increases, efficiency of the collectors with area of 3.0m^2 and 4.5m^2 increases, which is due to the rise of useful energy gain. The efficiency of the collectors with area of 1.5m^2 only increase in low flow rate condition, caused by the variation of useful energy gain, as shown in figure 5.4.1.1.

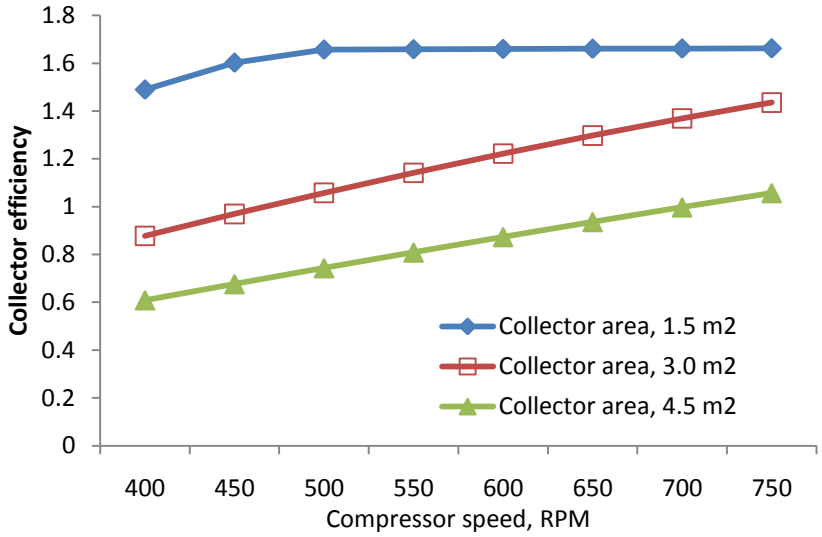

Figure 5.4.1.2 Variation of collector efficiency with compressor speed for different collector area.

Figure 5.4.1.3 shows the variation of system COP as a function of compressor speed with different colletor area. As compressor speed increases, COP of the systems with collectors area of 3.0m^2 and 4.5m^2 reduce slightly, which is due to the fact that the increment of useful energy gain of the evaporator-collector and room evaporator is slightly lower than the rise of compressor work input when compressor speed increase.

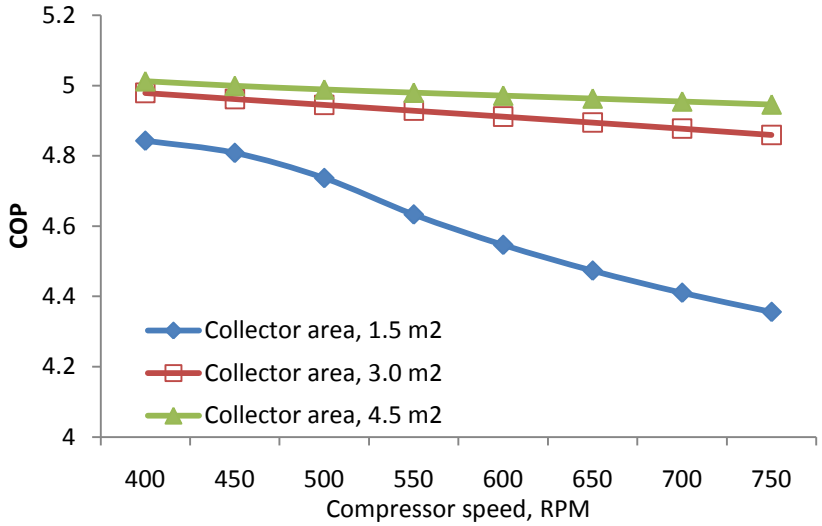

Figure 5.4.1.3 Variation of COP with compressor speed for different collector area.

However, COP of the system with collector area of 1.5m^2 decline rapidly with the rise of compressor speed. It can be attributed to the fact that, for the systems with collector area of 1.5m^2, the increment of useful energy gain of the evaporator-collector and room evaporator is much lower than the rise of compressor work input, because of the steady state of the useful energy gain, as shown in figure 5.4.1.1.

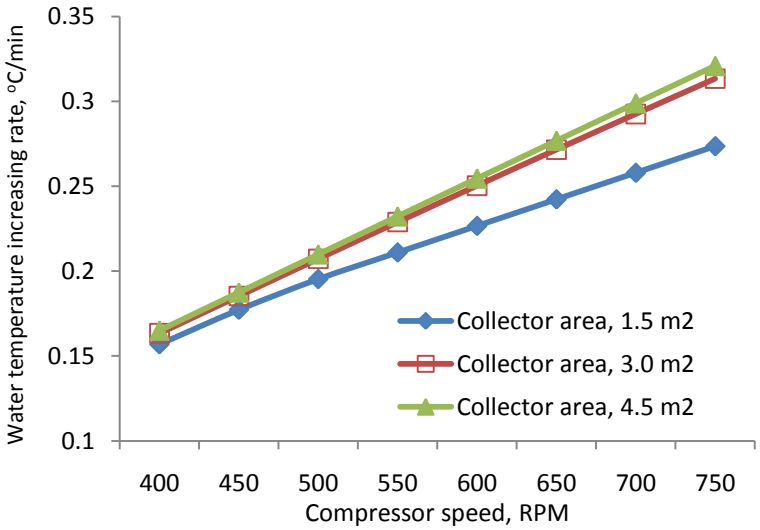

Figure 5.4.1.4 Variation of water temperature increasing rate with compressor speed for different collector area.

Figure 5.4.1.4 shows the water heating rate (℃/min) as a function of compressor speed with different colletor areas. As compressor speed increases, the rising rate of water temperature increases steadily.

Heat transfer in each system components are plotted against compressor speed with colletor area of 3m^2 in figure 5.4.1.5. As compressor speed increases, energy transfer in each system components increases.

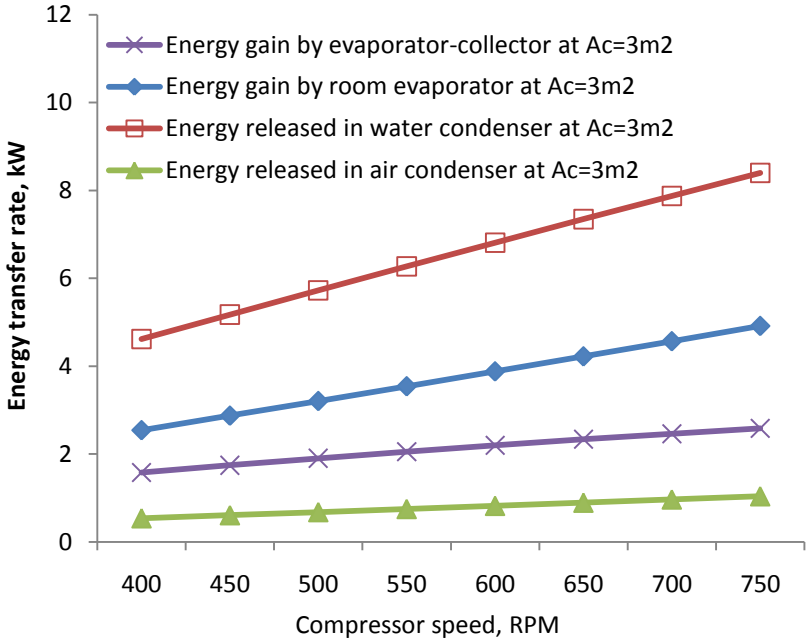

Figure 5.4.1.5 Variation of heat transfer in each component with compressor speed.

The increasing rate of energy transfered in water condenser is faster than that of energy released in air condenser, which is due to the fact that these two condensers are connected in series and condensing heat is released to water condenser before the refrigerant reaches the air condenser.

5.4.2 Effect of solar radiation

Figure 5.4.2.1 shows the variation of collector useful energy gain as a function of solar radiation with different colletor areas. As solar radiation increases, useful energy gain increases.

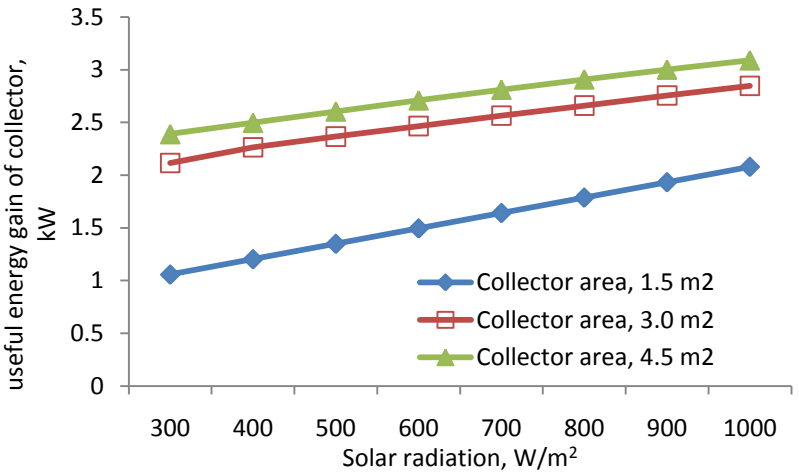

Figure 5.4.2.1 Variation of collector useful energy gain with solar radiation for different collector area.

The difference between the useful energy gains of the collectors with area of 3.0m^2 and 4.5m^2 is less than that of 1.5m^2 and 3.0m^2, which is due to the fact that the effect of solar radiation on the useful energy gain in two-phase flow is much greater than in single phase flow, as dicussed in figure 5.3.1.3.

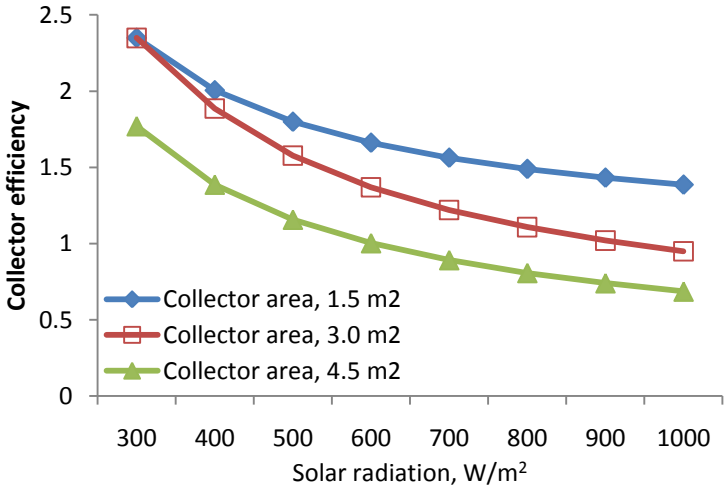

Figure 5.4.2.2 Variation of collector efficiency with solar radiation for different collector area.

Figure 5.4.2.2 shows the variation of collector efficiency as a function of solar radiation with different colletor area. As solar radiation increases, efficiency of the collectors decreases, which is due to the fact that the increment of useful energy gain of the evaporator-collector is slightly lower than the rise of solar radiation, which is the denominator of the collector efficiency.

Figure 5.4.2.3 shows the variation of COP as a function of solar radiation with different colletor area. As solar radiation increases, COP of the systems increases.

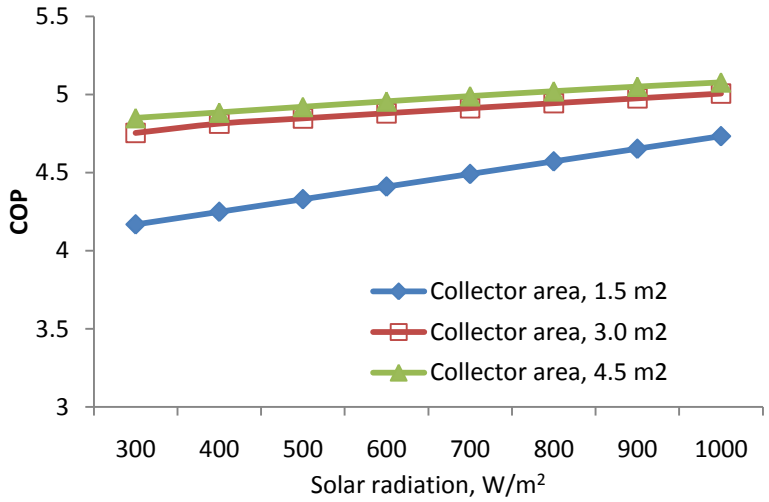

Figure 5.4.2.3 Variation of system COP with solar radiation for different collector area.

The COP enhancement of system with collector area increase from 1.5m^2 to 3.0m^2 is much more than that of collector area increase from 3.0m^2 to 4.5m^2. It is due to the fact that the difference between the useful energy gains of the collectors with area of 3.0m^2 and 4.5m^2 is less than that of 1.5m^2 and 3.0m as presented in figure 5.4.2.1.

Due to a similar reason, the difference between the water temperature increasing rates in the system with collector area of 1.5m^2 and 3.0m^2 is much more than that of collector area of 3.0m^2 and 4.5m^2, as seen in figure 5.4.2.4. It can be conclude that this solar system performance is not in proportion to the collector area.

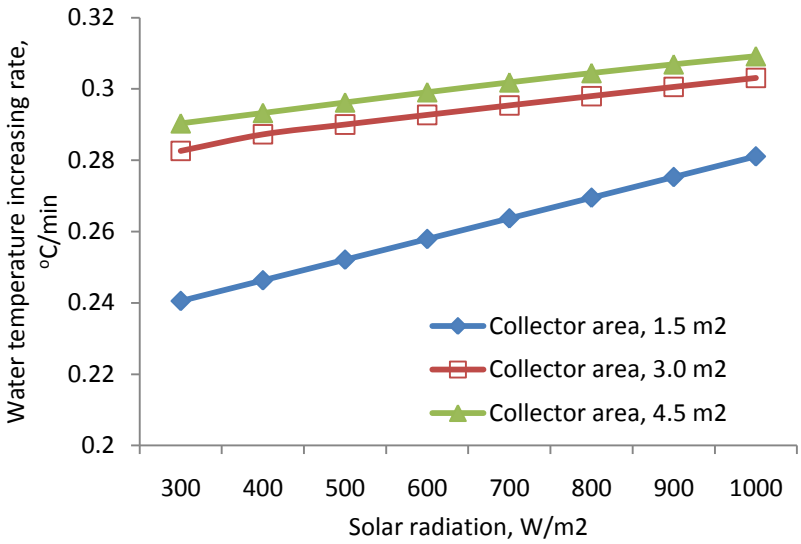

Figure 5.4.2.4 Variation of water temperature rising rate with solar radiation for different collector area.

Heat transfer in each system components is plotted against solar radiation with colletor area of 3m^2 in figure 5.4.2.5. As seen from the figure, solar radiation did not affect the heat transfer in each system component as much as mass flow rate.

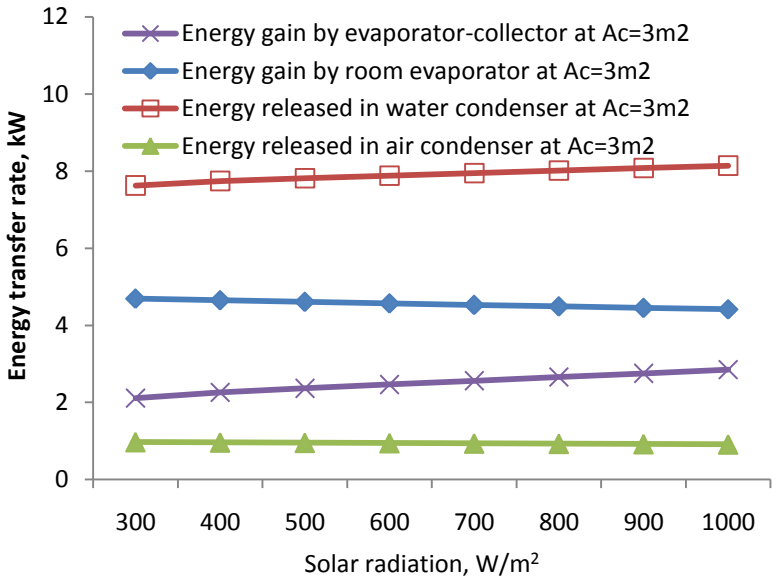

Figure 5.4.2.5 Variation of heat transfer in each component with solar radiation.

5.4.3 Effect of ambient temperature

Figure 5.4.3.1 shows the variation of collector useful energy gain as a function of

ambient temperature with different solar radiations.

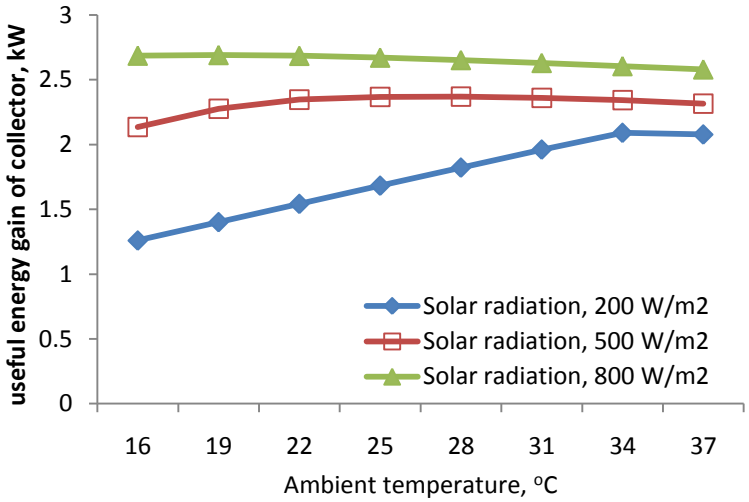

Figure 5.4.3.1 Variation of collector useful energy gain with ambient temperature for different solar radiation.

In the condition of solar radiation of 200W/m^2, useful energy gain increases as ambient temperature increases due to the fact that a large fraction of the total useful energy gain comes from the ambient under low radiation condition, as presented earlier in figure 5.3.3.3 and figure 5.3.3.4. However, under the radiation of 500W/m^2 and 800W/m^2, the total useful energy gain remain constant or even slightly drop with the rise of ambient temperature due to the fact that the temperature of condensed refrigerant after air condenser increased with the rise of ambient temperature. It comes to a conclusion that the ambient tempearature has both positive and negative effect on the collector useful energy gain and the positive effect only dominate in low radiation condition.

Figure 5.4.3.2 shows the variation of collector efficiency as a function of ambient temperature with different solar radiations.

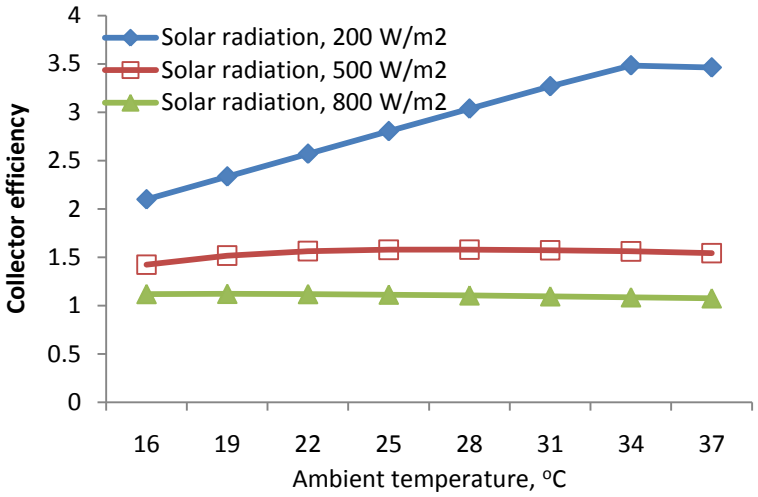

Figure 5.4.3.2 Variation of collector efficiency with ambient temperature for different solar radiation.

In the condition of solar radiation of 200W/m^2, efficiency of the collectors increases as ambient temperature increases due to the increase of useful energy gain of the evaporator-collector. Howeve, ambient temperature does not affect the collectors efficiency much under the radiation of 500W/m^2 and 800W/m^2 due to constancy of total useful energy gain in these two condition, as shown in figure 5.4.3.1.

Figure 5.4.3.3 shows the variation of system COP as a function of ambient temperature with different solar radiations.

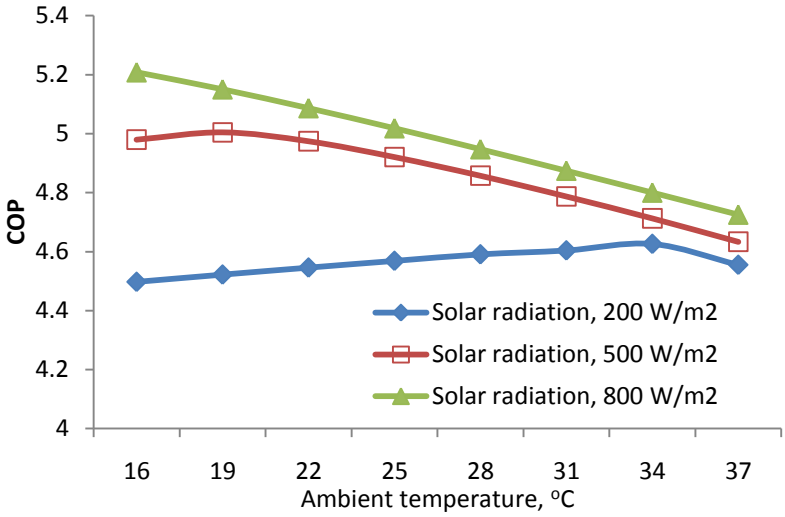

Figure 5.4.3.3 Variation of system COP with ambient temperature for different solar radiation.

In the condition of solar radiation of 200W/m^2, system COP increases as ambient temperature increases due to the increase of useful energy gain by the evaporator-collector. However, under the radiation of 500W/m^2 and 800W/m^2, system COP drops with the rise of ambient temperature due to the fact that the energy released in the air condenser decreased with the rise of ambient temperature, as elaborated in figure 5.4.3.4.

Heat transfer in each system components is plotted against ambient temperature with solar radiatio of 500W/m^2 in figure 5.4.3.4. As seen from the figure, energy released in room evaporator decrease with the rise of ambient temperature due to the rise of temperature of condensed refrigerant after air condenser. However the energy gain by the evaporator-collector remain constant with the rise of ambient temperature due to the benefit of increase of energy gain from ambient.

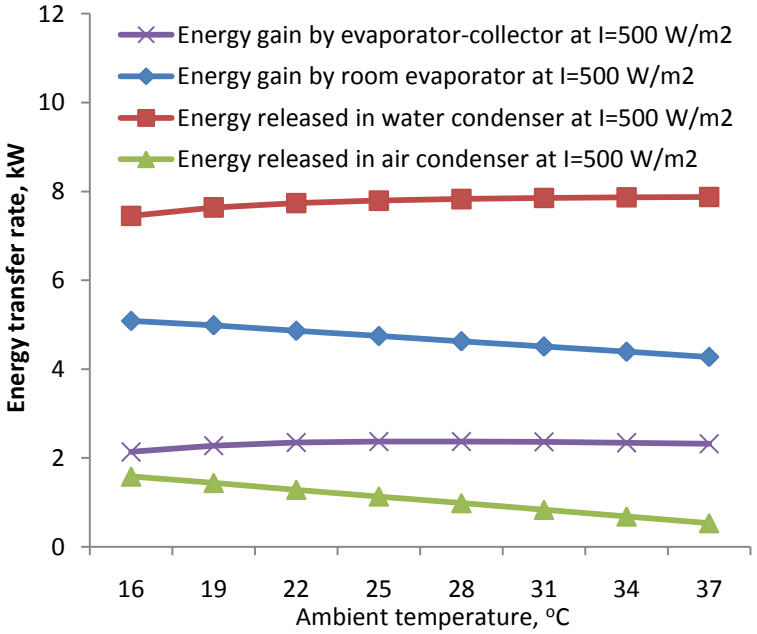

Figure 5.4.3.4 Variation of heat transfer in each component with ambient temperature.

Variation of water temperature rising rate with ambient temperature for different solar radiation is shown in figure 5.4.3.5.

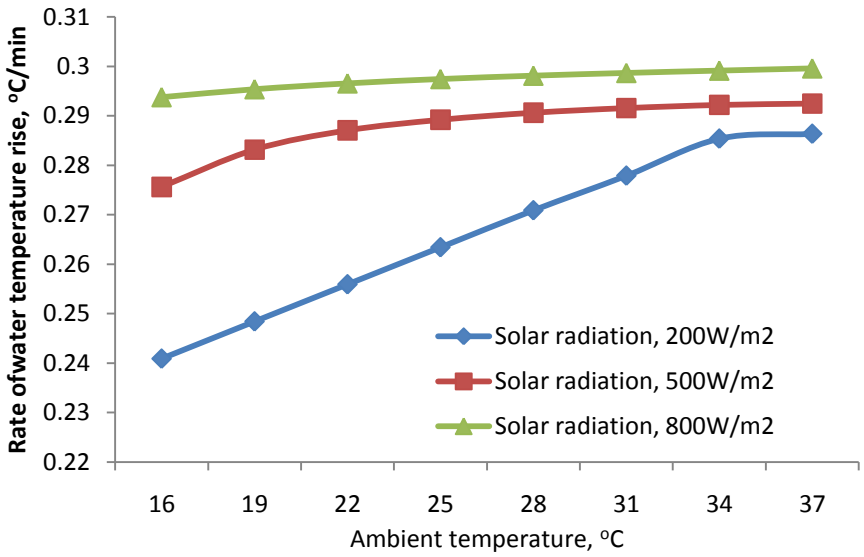

Figure 5.4.3.5 Variation of water temperature rising rate with ambient temperature for different solar radiation.

With the rise of ambient temperature, water temperature increasing rate (℃/min) went up due to the increase of temperature of refrigerant at compressor inlet, as a result for the rise of ambient temperature.

As shown in figure 5.4.3.5, the effect of ambient temperature on the water temperature rising rate in low solar radiation condition is greater than that in high radiation condition. It can be attributed to the fact that the collector useful energy gain increase with the rise of ambient temperature only in low solar radiation condition as discussed in figure 5.4.3.1.

5.4.4 Effect of water temperature

Figure 5.4.4.1 shows the variation of energy released in water condenser and the rate of variation of water temperature for different compressor speed. As water temperature increases, energy released at the condenser decreases leading to a decline in the rate of water temperature rise, which can be attributed to a reducton in temperature difference between the hot refrigerant and the water, as discussed in 5.1.1.

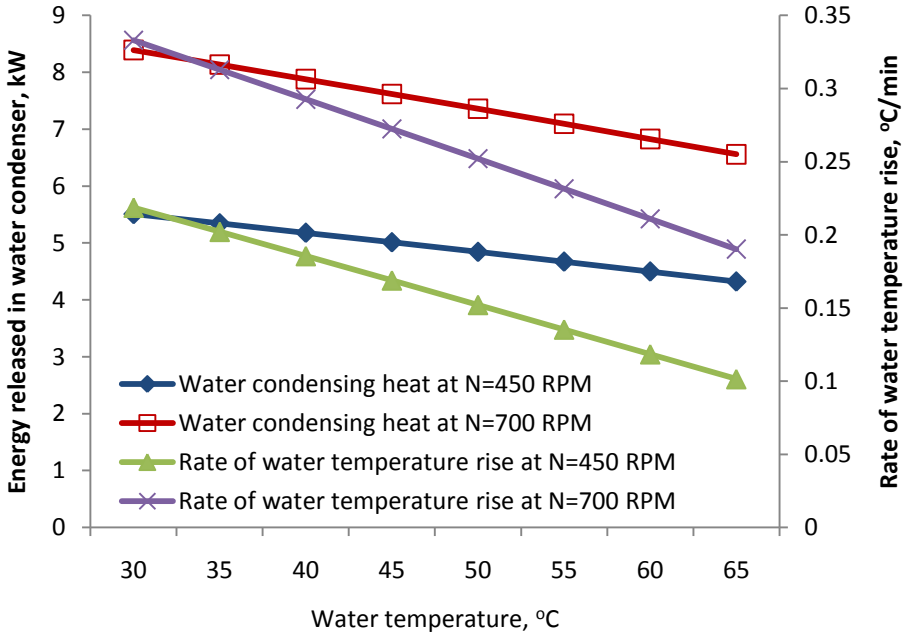

Figure 5.4.4.1 Variation of water condensing heat and water temperature rising rate with water temperature for different compressor speed.

As seen in figure 5.4.4.1, when water temperature rises from 30℃ to 65℃, the condensing heat at compressor speed N=450RPM drops from 5.5kW to 4.3kW and condensing heat at N=700RPM drops from 8.4kW to 6.6kW. As a result, for the water with a volume of 400L, water temperature rising rate at N=450RPM reduces from 0.22℃/min to 0.1℃/min and the water temperature rising rate at N=700RPM reduces from 0.33℃/min to 0.2℃/min

As the energy released in the water condenser reduces with the rise of water

temperature, the enthalpy of refrigerant at air condenser inlet increases, leading to a rise of energy released in the air condenser, as shown in figure 5.4.4.2.

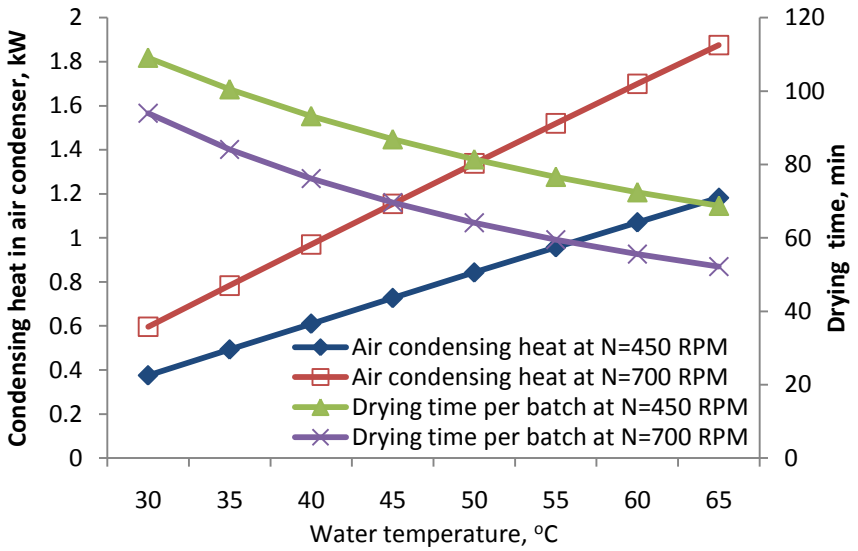

Figure 5.4.4.2 Variation of air condensing heat and drying time with water temperature for different compressor speed.

The time for drying 1.5kg material with initial moisture content of 1.0kg/kg reduces as a result of enhancement of heat released to the air for drying, as shown in figure 5.4.4.2. Drying process is completed when the moisture content is reduced to 0.06kg/kg or lower. When compressor speed is set at 700RPM and water temperature is 65℃, the time for one batch drying is 52 minutes.

Figure 5.4.4.3 shows the Variation of system COP (heating) and COP (cooling) with water temperature when compressor speed is set at 700RPM. With double condensers connected in series, which ensures a full condensation of refrigerant irrespective of water temperature, this integrated solar heat pump system has a relatively constant COP (heating) and COP (cooling), as shown in figure 5.4.4.3. When water temperature rises from 30℃ to 65℃, the COP (heating) reduces from 5.2 to 4.2 and COP (cooling) reduces from 2.8 to 2.1.

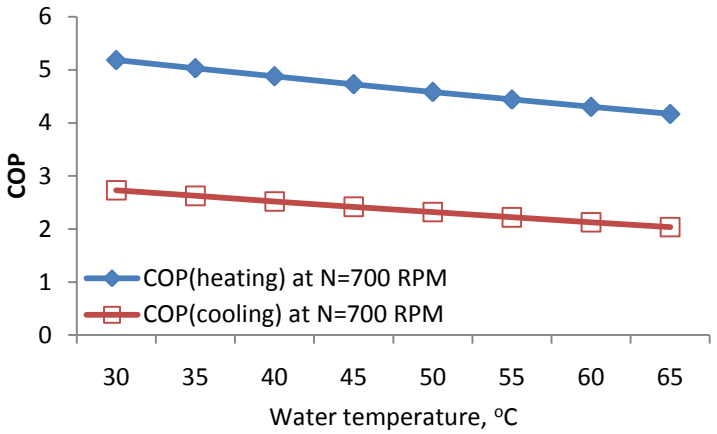

Figure 5.4.4.3 Variation of system COP (heating) and COP (cooling) with water temperature.

Heat transfer in each system components are plotted against water temperature with compressor speed at 700RPM in figure 5.4.4.4.

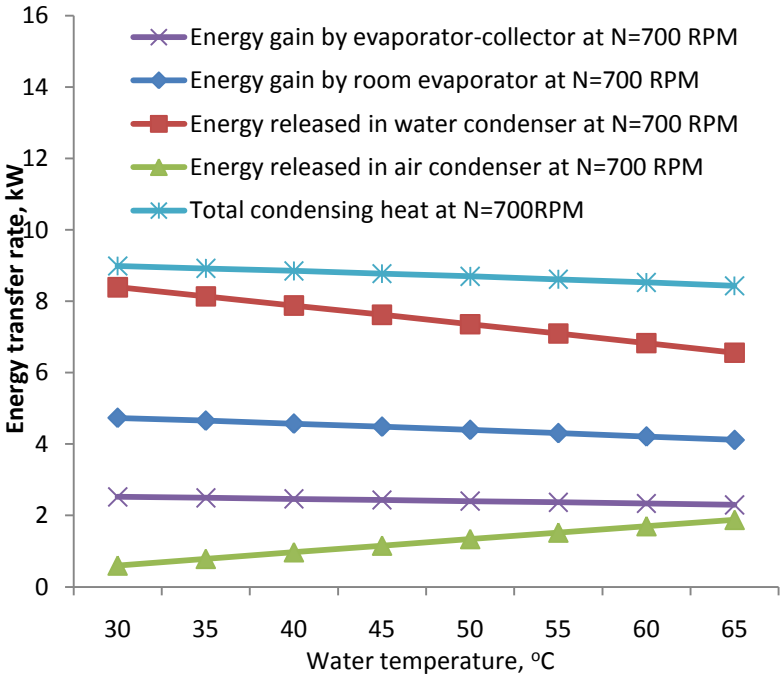

Figure 5.4.3.4 Variation of heat transfer in each component with water temperature.

As seen from the figure, water temperature did not affect the evaporating heat transfers and total condensing heat transfer as much as mass flow rate did.

5.4.5 Effect of air condenser blower speed

When system is operated in the NoWC mode, the water condenser is bypassed and air condenser is the only condenser to ensure a complete condensation of the refrigerant. In this case, the system performance is sensitive to the air condenser performance, which is mainly determined by the air blower speed. In this section, the effect of blower speed in air condenser on system performance under NoWC mode operation is investigated.

Figure 5.4.5.1 shows the variation of drying time as a function of blower speed in air condenser with different compressor speeds in NoWC mode operation.

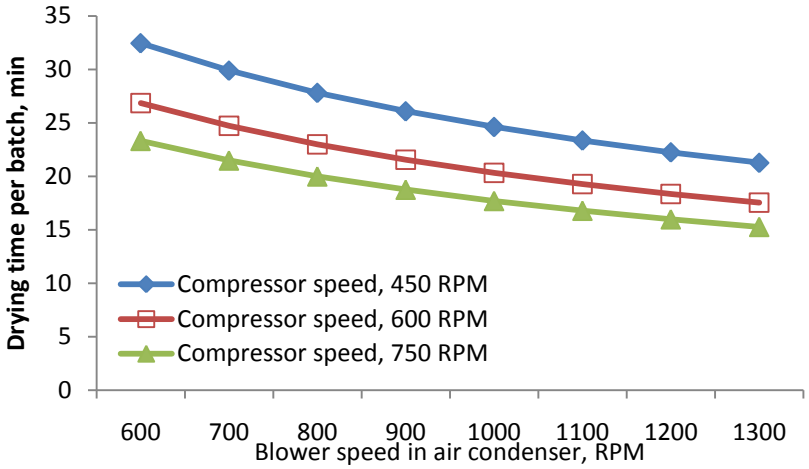

Figure 5.4.5.1 Variation of drying time per batch with blower speed in air condenser for different compressor speed in NoWC mode operation.

As the blower speed increases, time for one batch drying decrease gradually, which is due to a rise of air flow velocity, leadng to the increase of heat released in air condenser and the increase heat transfer coefficient in drying chamber. When compressor speed is set at 750RPM and air condenser blower speed is 1300RPM, the time for one batch drying is only 15.5 minutes.

Figure 5.4.5.2 shows the variation of COP as a function of blower speed in air condenser for different compressor speeds in NoWC mode operation.

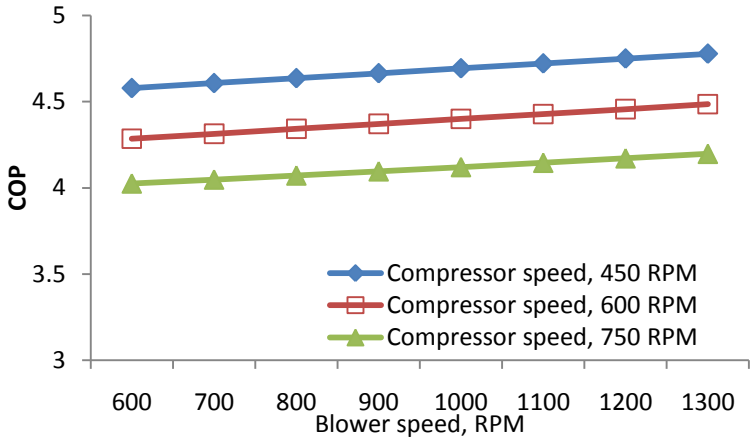

Figure 5.4.5.2 Variation of system COP with drying air blower speed for different compressor speed in NoWC mode operation.

As the blower speed increases, COP increases gradually, which is due to a rise of heat released in air condenser, which is the total condensing heat. When compressor speed is set at 450RPM and blower speed is 1300RPM, COP of the system in NoWC mode operation is 4.8.

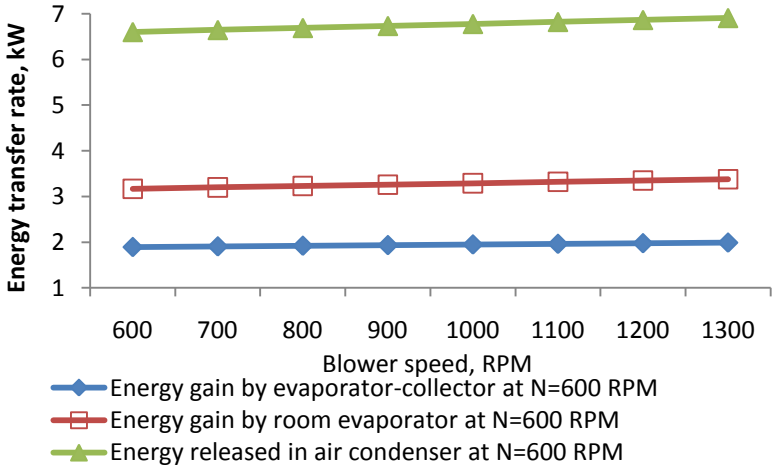

Figure 5.4.5.3 Variation of heat transfer in each component with drying air blower speed in NoWC mode operation.

Heat transfer in each system components in NoWC mode operation are plotted against blower speed with compressor speed at 600RPM in figure 5.4.5.3. As seen from the figure, both energy released in the air condenser and energy gain by the evaporator increase with the rise of blower speed in air condenser.

5.5 System monthly performance

To determine Monthly performance of the system, a series of numerical analysis has been carried out using the meteorological condition of Singapore. In this analysis, the compressor speed was set to 700RPM and collector area of 3m^2 was chosen.

Monthly meteorological data for Singapore

Figure 5.5.1 shows the variation of monthly solar radiation, ambient temperature, relative humidity and wind speed.

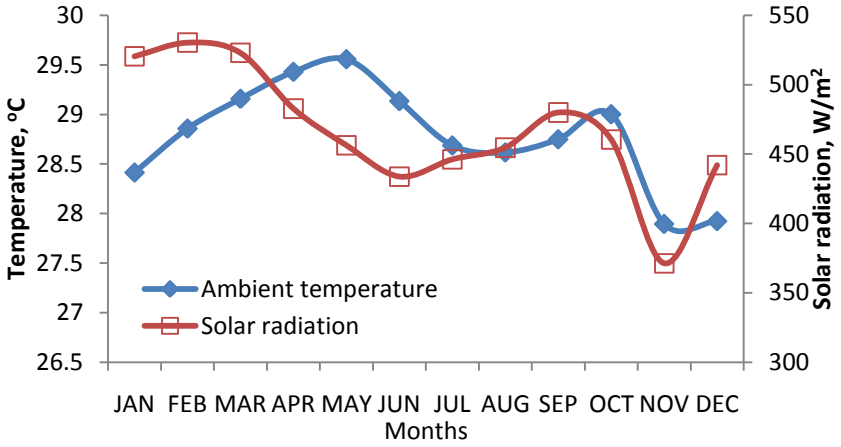

(a) Variation of monthly ambient temperature and solar radiation

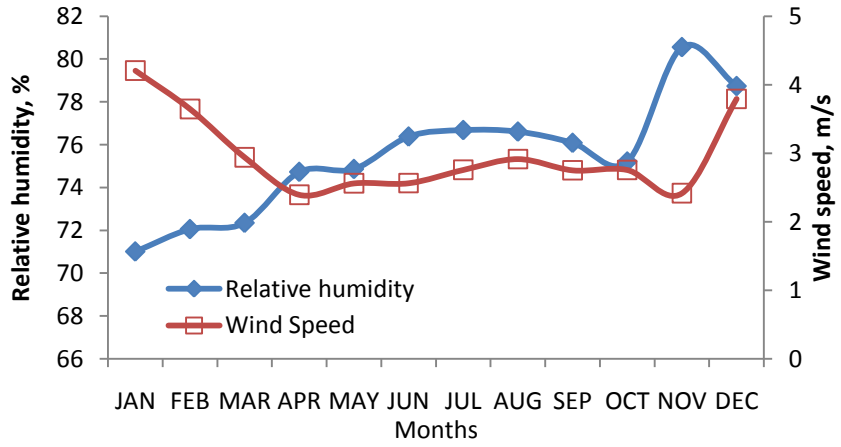

(b) Variation of monthly relative humidity and wind speed

Figure 5.5.1 Variation of Monthly meteorological data for Singapore

It is shown in the figure that the month of March has highest radiation and high ambient temperature, and month of November, which is in the monson season, has lowest radiation, lowest ambient temperature and highest relative humidity. The

fluctuation of meteorological condition of Singapore is not as remarkable as most of the other countries.

Monthly performance of the system

Figure 5.5.2 shows the variation of COP (heating) of the system and solar radiation in different month. As seen from the figure, from February to June, when solar radiation deceases, COP decreases from 4.84 to 4.78 as less energy is received by the evaporator-collector. The lowest COP with value of 4.75 occurs in November, in which solar radiation and ambient temperature are in the lowest point.

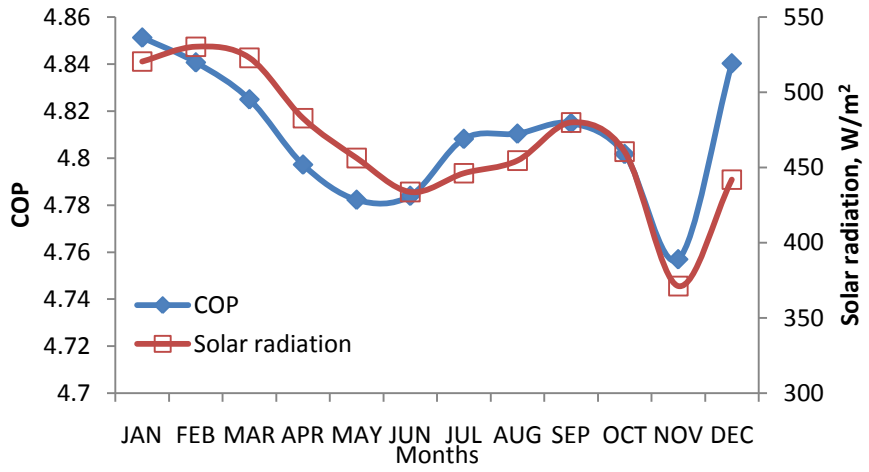

Figure 5.5.2 Variation of system COP (heating) with month

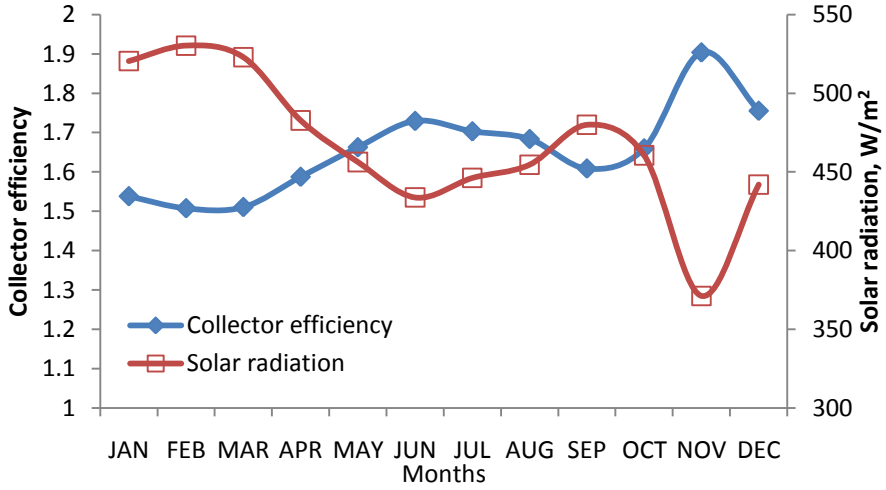

Figure 5.5.3 Variation of solar collector efficiency with month

Figure 5.5.3 shows the variation of monthly collector efficiency and solar radiation. As seen from the figure, from February to June, when solar radiation deceases, collector efficiency increase from 1.5 to 1.72 as the increment of energy received by the evaporator-collector is lower than the increase in radiation heat fall on the collector. The highest collector efficiency with the value of 1.9 occurs in November, in which solar radiation and ambient temperature are in the lowest point.

The efficiency greater than 1 can be attributed to the use of conventional efficiency definition as the ratio of useful energy gain by the collector to the solar energy available on the collector plate ($\eta = \frac{Q_u}{A_c I}$). For the evaporator-collector, the loss term becomes a gain due to low operation temperature of the collector. This collector absorbs solar energy and ambient energy. When the irradiation is low, the contribution of the ambient energy can be significantly high leading to a very high collector efficiency.

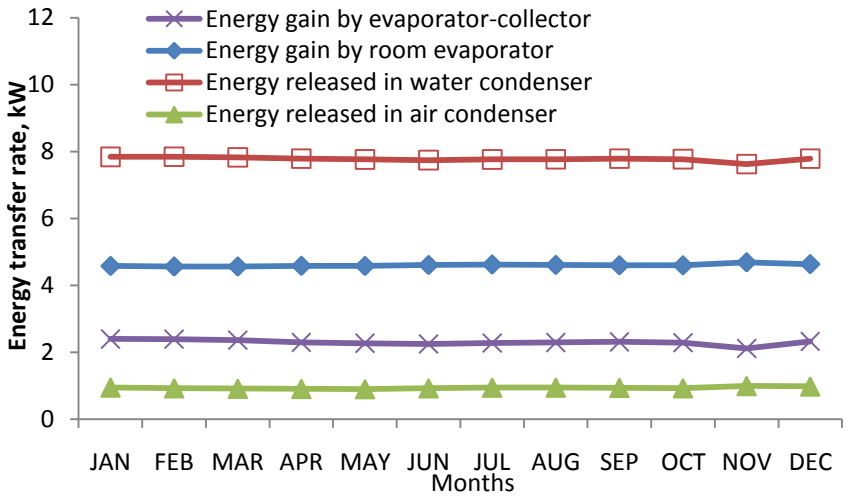

Figure 5.5.4 Variation of heat transfer rate in each component with month

Figure 5.5.4 shows the variation of monthly heat transfer rate in each component of the system. The amounts of energy transfer in each component are quite constant all over the year. The only noticeable drop of energy gain by evaporator-collector

and energy gain in water condenser occur in November, in which solar radiation and ambient temperature are in the lowest point.

Figure 5.5.5 shows the variation of daily (8hours) hot water (50℃) supply and daily (8hours) clothes drying amount with month.

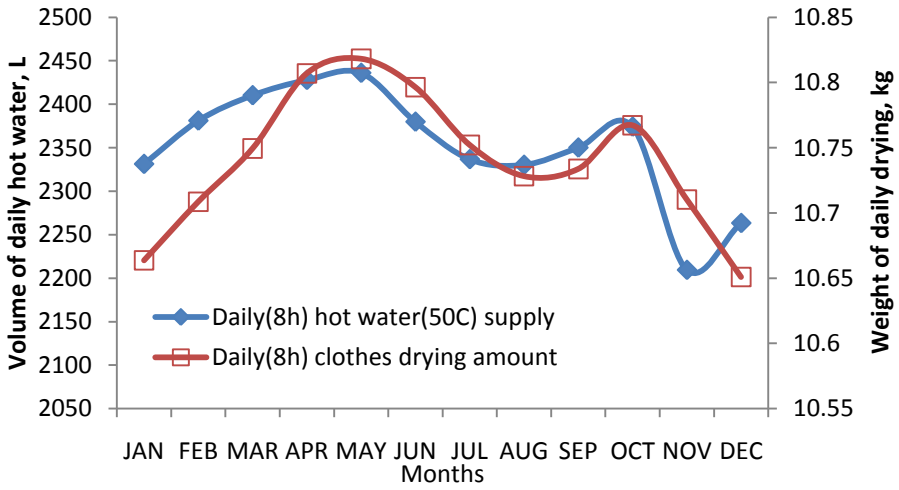

Figure 5.5.5 Variation of daily hot water (50℃) supply amount and daily clothes dying amount (daily operation 8hours) with months

As seen from the figure, the amount of daily hot water (50℃) supply varies from 2435L in May to 2210L in November, due to the variation of solar radiation and ambient temperature. The amount of daily clothes dying varies from 10.65kg in December to 10.85kg in May, mainly due to the variation of ambient temperature, as shown in figure 5.5.5. However the amplitude of fluctuation of amount of daily clothes dying is small due to a combination of energy usage e.g. ambient energy solar energy and air-con waste heat.

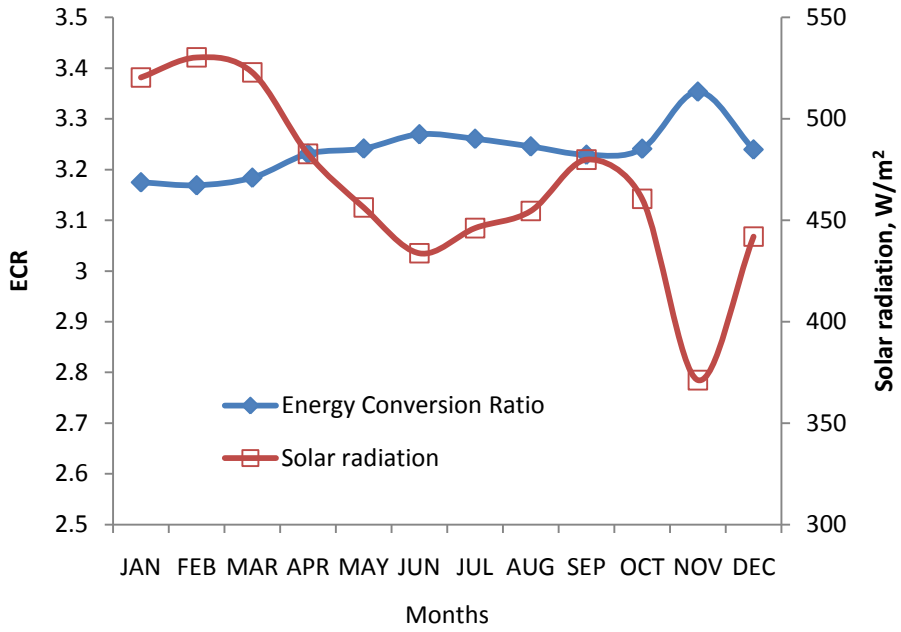

Figure 5.5.6 Variation of Energy Conversion Ratio with month

Figure 5.5.6 shows the variation Energy Conversion Ratio (ECR) of the system and solar radiation in different month. As seen from the figure, ECR is stable in a small range from 3.15 to 3.4 throughout the year. The highest ECR with value of 3.36 occurs in November, in which solar in the lowest point.

5.6 Economic analysis of the system

The conversion of solar energy for useful application requires considerable initial investment compared to a conventional system. Solar systems are normally characterized by a higher initial investment followed by lower operating costs. Therefore, it is necessary to determine whether such an investment is economically competitive when compared with conventional system. To determine the optimum size of the collector, economic analysis has been carried out. It is important to note that, in the calculation of life cycle savings, the future expenses and benefits are expressed in terms of dollars in hand, which requires assumptions on the future discount rate, inflation rate and fuel escalation rate. Therefore, the conversion of all future earnings to present worth dollars involves a certain degree of uncertainty.

System load pattern

For full mode running, the typical values of the economic parameters, used in this study, are given in Table 1. The optimization is for a typical load of a small hotel with the room area of 600m^2 (25 rooms). The air-conditioning load is determined by the room area and the meteorological condition of Singapore.

According to the ASHRAE National Domestic Hot Water Sizing Guidelines [113], in the present study, daily shower water demand for one guest is set as 180L and daily laundry water demand is set as 120L for the bed sheet and clothes of one guest. Daily drying demand is 1.4kg for the washed bed sheets and clothes for one guest. The hot water supply capacity and drying capacity of this system is designed for the consumption of 60 persons in the hotel.

Economic parameters are listed in Table 5.6.1. The system parameters and assumed daily load parameters are listed in Table 5.6.2 and Table 5.6.3. The detail of daily variation of load profile of the system is shown in Figure 5.6.1.

Table 5.6.1 Economic parameters

Inflation rate	0.02
Fuel price escalation rate	0.13
Life cycle of system	20 years
Loan term	8 years
Loan interest rate	0.09
Discount rate	0.07
Solar fraction	0.8
Fuel cost	S$0.03/MJ

Table 5.6.2 System Parameters

Latitude	1°22'N
Collector tilt angle	15°
Collector azimuth	0
Ground reflectance	0.02
Insulation(fiber glass)	0.045 W/m.K
Insulation thickness	0.05 m
Collector absorptivity	0.9
Number of glass covers	0
Collector area	variable
Water specific heat	4130 J/kg K
Heat exchanger efficiency	0.81
Relative humidity	85%
Wind speed	1.5m/s
Daily mean global radiation	15MJ/m^2 [10]
Supply water temperature	25 ℃
Ambient temperature	26 ℃
Heat capacity of collector	10kJ/m^2.K
Initial store temperature	40 ℃
Store volume	18m^3
Heat loss coefficient of store	0.47W/m^2.K

Table 5.6.3 Daily Load Parameters

Air-con room temperature	23 ℃
Air-con room area	600 m^2
Hot water demand temperature	55 ℃
Hot water demand volume	18 m^3

Drying demand weight	90 kg
Temperature of air for drying	40 ℃

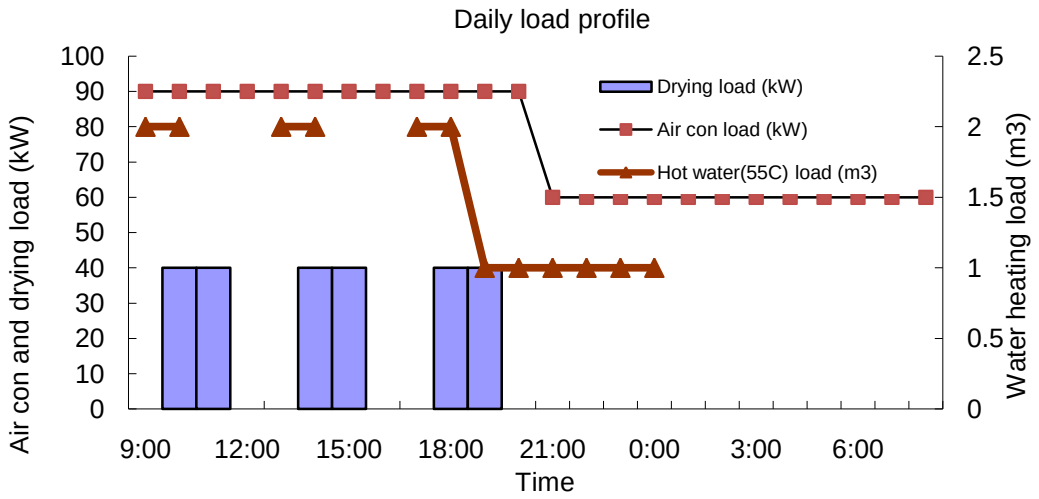

Figure 5.6.1 Load profile of the system

Life cycle savings (LCS) analysis

Figure 5.6.2 shows the life cycle savings as a function of the collector area. Unlike the normal single function solar system, the curve of this integrated system is positive even at the low side of collector area. It is attributed to the factor that the system absorbs the energy not only from collectors but also from air-con rooms.

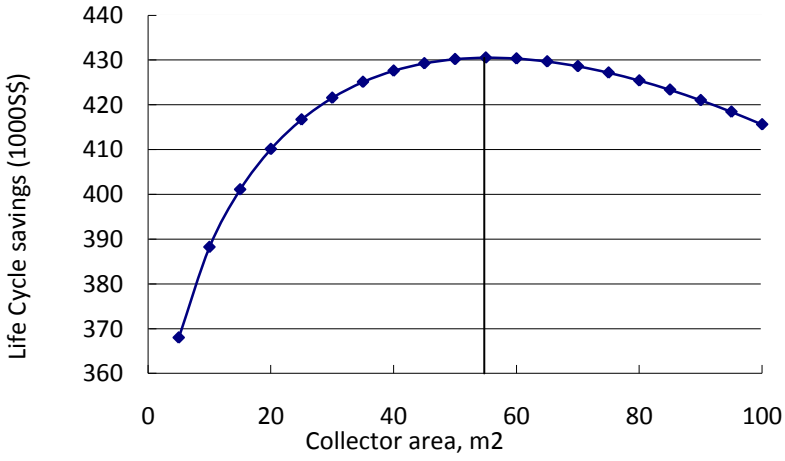

Figure 5.6.2 Variations of life cycle savings as a function of collector area

With increasing collector area, an increased saving can be achieved, until a

maximum at some optimum collector area is reached. For this case, the optimum collector area is 55m^2, as shown in Figure 5.6.2. Further increase in collector area causes the system cost increase excessively, leading to a decrease of solar savings. This decrease is also caused by the fact that solar collector efficiency dropped dramatically when the fluid reaches superheat region [6].

Payback period analysis

The variation of payback period with collector area is shown in Figure 5.6.3.

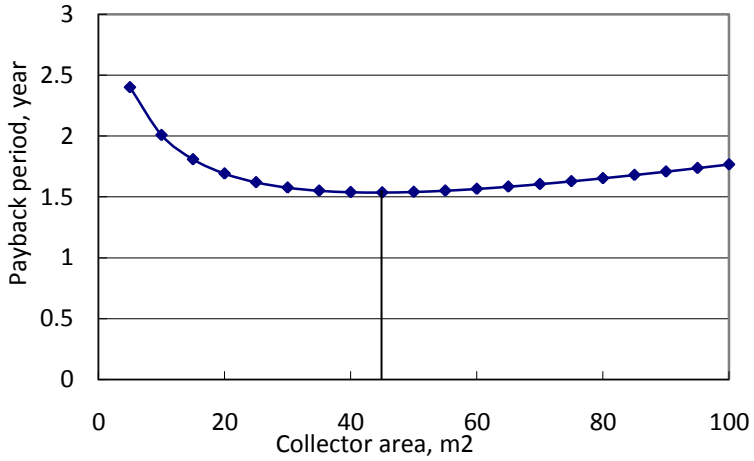

Figure 5.6.3 Variations of payback period as a function of collector area

Payback period decrease sharply with the increase in collector area, since the fuel savings are far greater than the cost increase due to the increasing collector area. It reaches a minimum, a point of optimum collector area, and then increases. Further increase in area causes an increase in cost which is higher than the savings on fuel.

The variation of payback period with collector area shows a large plateau due to the fact that the reduction in fuel consumption is the energy not only from collectors but also from air-con rooms, as discussed in section 4.4. As shown in the figure, when the collector area is 15m^2, the system can achieve a payback period of 1.8 years. Such area can be chosen when the criterion of payback is 2 years.

Payback period method shows that the optimum collector area is 45m^2, which is slightly lower than that obtained from life cycle savings method. The smaller value of the optimal collector area predicted by the payback period may be due to the fact that this model does not consider the cash flows which occur after the point where payback is reached.

CHAPTER 6 CONCLUSIONS

A solar assisted heat pump system for air conditioning, water heating and drying was designed and built to evaluate its performance under the meteorological conditions of Singapore. Based on users' requirement, the system was designed for three modes of operation: air-conditioning, water heating and drying with appropriate control strategies. Under the meteorological conditions of Singapore, a series of experiments were conducted under five different operation modes with the use of control valves to evaluate the system performance:

1. Under the full mode operation (water heating, drying and air-conditioning along with evaporator-collector), the COP values were found between 4 and 7 with the average value of about 5. The values of Energy Conversion Ratio (ECR) were found between 3 and 4 with the average value of about 3.3 for a typical day. The system overall heating performance at the water temperature of 60℃ is better than that of 30℃.

   Comfortable room conditions were obtained with a stabilized room temperature. The rate of heat absorption by the room evaporator was maintained in the range of 6.8kW to 7.8kW. This concludes that the system is able to provide the required cooling capacity.

   The refrigerant from compressor with the temperature of around 90℃ released heat to the water condenser (water tank). The temperature of 400 liters water in the tank could be raised to 60℃ in 75 minutes. The energy released in water condenser is affected mainly by the water temperature. The heat rejection in water condenser is 13kW when water is 30℃ while it is 10kW when water temperature is 60℃.

During the initial period of the system running, the temperature of the drying air increased slowly. The condensing heat rejection in air condenser is 0.7kW when water is at 30℃ while it is 3.5kW when water temperature is 60℃. As a result, the temperature of heated air increases with the increase in energy delivered at the air condenser. When drying air temperature increases, relative humidity of air will drop leading to a lower air partial pressure resulting a higher drying potential. A maximum SMER value of 0.68 kg/kWh was obtained under full mode operation. Furthermore, the two condensers in series ensure complete condensation of the refrigerant with sub-cooling of the refrigerant liquid.

2. When the water condenser is bypassed, single air condenser can still fulfill the requirement that condense the refrigerant to sub-cool status. In this case the moisture content of drying material in the drying chamber can be reduced from 0.9 to 0.09 in 20 minutes in the drying process.

3. When air condenser is bypassed, the temperature of condensed refrigerant (before the expansion valve) is mainly determined by the water temperature in the water condenser. When the water in the water condenser is heated from 30℃ to 60℃, the energy absorbed in both evaporator-collector and room evaporator reduced and the system COP drop to 3.

4. When room evaporator for air conditioning is bypassed, the evaporating heat is only provided by the solar evaporator-collector. In this case, the performances of water heating and drying, which are driven by the condensing heat, are lower than that in full mode and highly affected by solar radiation and ambient temperature.

5. When solar evaporator-collector is bypassed, all the evaporating heat is solely absorbed by the room evaporator. In this case, the energy released in both water condenser and air-condenser are lower than that in full mode and highly affected by the room temperature and cooling load.

The performance of a two-phase unglazed solar evaporator-collector in a solar-assisted heat pump system for cooling, water heating and drying is investigated. It is found that the thermal performance of the two-phase unglazed solar evaporator- collector is affected significantly by refrigerant mass flow rate, solar irradiation, collector area, ambient temperature and relative humidity. Both experimental and analytical results show the fact that the two-phase unglazed solar evaporator-collector, instead of losing energy to the ambient, gained a significant amount due to low operating temperature of the collector. It may be noted that amount of energy gain from the ambient increases when radiation declines. As a result, the collector efficiency attains a value greater than 1, when conventional collector equation is used. With this evaporator-collector, the system can be operated even in the absence of solar radiation at night.

Analytical results show that both heat transfer coefficient and energy gain in two phase region of collector are much higher than those in single phase (saturated vapor) region. And the length of two phase region will increase when the refrigerant mass flow rate decline. This analysis shows that this integrated solar heat pump system with two-phase unglazed solar evaporator-collector has good potential for the application in the tropics

From the parametric study, it was observed that the ambient temperature, solar radiation, relative humidity, compressor speed, area of evaporator-collector and the

temperature of water in water condenser have significant effect on the system thermal performance as well as the evaporator-collector performance.

The results obtained from simulation and experiments are in good agreement under different operation modes. Based on the validated simulation model, an economic optimization was performed to identify the best collector size for a given load and its distribution, using two methods, life cycle savings (LCS) and payback period. The load pattern is determined based on a typical small hotel with the air-con room area of 500m^2, daily hot water demand of 18m^3 and daily drying demand of 90kg. It was seen that the life cycle saving method leads to the prediction of the optimum collector area of 55 m^2. The payback period analyses predicted the optimum collector area of 45 m^2. The minimum payback period is about 1.5 years.

Due to the factor that the integrated solar heat pump system absorbs the energy not only from collectors but also from air-con rooms, the life cycle savings is positive even at lower collector area, where it is negative for conventional single function solar system. The evaporator-collector makes use of two-phase heat transfer processes, where the temperature of the fluid remains constant. The optimum collector area is also affected by the point at which the fluid reaches superheat region due to the fact that the collector efficiency of single phase region is much lower than that of two-phase region. This optimization makes it possible for the integrated solar heat pump system to be commercialized in different industrial and domestic applications.

The original contribution of this work can be summarized as:

a. A comprehensive experimental and theoretical work on the performance of

an innovative integrated solar heat pump system under a series of operation modes.

b. A validated simulation program (design tool) for the system. It is applicable for various conditions and applications.

c. Optimization and economical analysis of the system to prove its promising market potential.

The system shows good potential for implementation in commercial and residential applications and would give a new dimension in the process of replacement of conventional energy with renewable energy sources.

REFERENCES

1. Hawlader, M.N.A., S.K. Chou, and M.Z. Ullah, *The performance of a solar assisted heat pump water heating system.* Applied Thermal Engineering, 2001. 21(10): p. 1049.
2. Sporn, P. and E.R. Ambrose. *The heat pump and solar energy*. in *World symposium on applied solar energy*. 1955. Phonix, Arizona.
3. Chaturvedi, S.K. and Y.J. Shen, *Thermal performance of a direct expansion solar-assisted heat pump.* Solar Energy, 1984. 33(2): p. 155-162.
4. Franklin, J.L., E.W. Saaski, and A. Yamgiwa. *A high efficiency, direct expansion solar plane.* in *Flat-Plate Solar Collector Conference*. 1977. Orlando, Florida
5. Chaturvedi, S.K., Y.F. Chiang, and A.S. Roberts, *Analysis of two phase flow collectors with applications to heat pumps.* ASME Transaction Journal of Solar energy engineering, 1982. 104(4): p. 358-365.
6. Chaturvedi, S.K. and V.C. Mei. *Thermal performance of SAHP system with combined collector/evaporator*. in *AIAA Terrestrial Energy Systems Conference*. 1979. Orlando, Florida.
7. Soin, R.S., et al., *Performance of flat plate solar collector with fluid undergoing phase change.* Solar Energy, 1979. 23(1): p. 69-73.
8. Al-Tamimi, A.I. and J.A. Clark. *Thermal analysis of a solar collector containing a boiling fluid.* in *American Solar Energy Society Annual Meeting*. 1983. America.
9. Al-Tamimi, A.I. and J.A. Clark, *Thermal performance of a solar collector containing a boiling fluid (R-11).* ASHRAE Transcations, 1984: p. 681-693.
10. Wallis, G.B., *One-Dimensional Two-Phase Flow*. 1969, New York: McGraw Hill.
11. Morgan, R.G., *Solar assisted heat pump.* Solar Energy, 1982. 28(2): p. 129-135.
12. Chaturvedi, S.K., D.T. Chen, and A. Kheireddine, *Thermal performance of a variable capacity direct expansion solar assisted heat pump.* Energy Conver Manage, 1998. 39(3-4): p. 181-191.
13. Yamankaradeniz, R. and I. Horuz, *The theoretical and experimental investigation of the characteristics of solar-assisted heat pump for clear days.* International Communications in Heat and Mass Transfer, 1998. 25(6): p. 885-98.
14. Chyng, J.P., C.P. Lee, and B.J. Huang, *Performance analysis of a solar-assisted heat pump water heater.* Solar Energy, 2003. 74(1): p. 33-44.
15. Kuang, Y.H., R.Z. Wang, and L.Q. Yu, *Experimental study on solar assisted heat pump system for heat supply.* Energy Conversion and Management, 2003. 44(7): p. 1089-1098.
16. Chata, F.B.G., S.K. Chaturvedi, and A. Almogbel, *Analysis of a direct expansion solar assisted heat pump using different refrigerants.* Energy Conversion and Management, 2005. 46(15-16): p. 2614-2624.
17. Badescu, V., *Model of a thermal energy storage device integrated into a solar assisted heat pump system for space heating.* Energy Conversion and Management, 2003. 44(10): p. 1589-604.
18. Huang, B.J. and J.P. Chyng, *Integral-type solar-assisted heat pump water heater.* Renewable Energy, 1999. 16(1-4 pt 2): p. 731-734.
19. Huang, B.J. and J.P. Chyng, *Performance characteristics of integral type solar-assisted heat pump.* Solar Energy, 2001. 71(6): p. 403-414.
20. Huang, B.J. and C.P. Lee, *Long-term performance of solar-assisted heat pump water heater.* Renewable Energy, 2004. 29(4): p. 633-639.
21. Huang, B.J. and C.P. Lee, *Performance evaluation method of solar-assisted heat pump water heater.* Applied Thermal Engineering, 2007. 27(2-3): p. 568-75.
22. Hawlader, M.N.A., et al., *Solar-assisted heat-pump dryer and water heater.* Applied Energy, 2003. 74(1-2): p. 185 - 193.
23. Hawlader, M.N.A. and K.A. Jahangeer, *Solar heat pump drying and water heating in the tropics.* Solar Energy, 2006. 80(5): p. 492-499.
24. Axaopoulos, P., P. Panagakis, and S. Kyritsis, *Experimental comparison of a solar-assisted heat pump vs. a conventional thermosyphon solar system.* International Journal of Energy Research, 1998. 22(13): p. 1107-1120.

25. Badescu, V., *First and second law analysis of a solar assisted heat pump based heating system.* Energy Conversion and Management, 2002. 43(18): p. 2539-52.
26. Badescu, V., *Model of a solar-assisted heat-pump system for space heating integrating a thermal energy storage unit.* Energy and Buildings, 2002. 34(7): p. 715-26.
27. Huang, H., X. Ge, and Y. Su, *Theoretical thermal performance analysis of two solar-assisted heat-pump systems.* International Journal of Energy Research, 1999. 23(1): p. 1-6.
28. Kaygusuz, K., *Investigation of a combined solar-heat pump system for residential heating. Part 1: Experimental results.* International Journal of Energy Research, 1999. 23(14): p. 1213-1223.
29. Kaygusuz, K., *Utilization of solar energy and waste heat.* Energy Sources, 1999. 21(7): p. 595-610.
30. Kaygusuz, K., *Calculation of required collector area of a solar-assisted series heat pump for domestic heating.* Energy Sources, 2000. 22(3): p. 247-56.
31. Yumrutas, R. and O. Kaska, *Experimental investigation of thermal performance of a solar assisted heat pump system with an energy storage.* International Journal of Energy Research, 2004. 28(2): p. 163-75.
32. Yumrutas, R., M. Kunduz, and T. Ayhan, *Investigation of thermal performance of a ground coupled heat pump system with a cylindrical energy storage tank.* International Journal of Energy Research, 2003. 27(11): p. 1051-1066.
33. Yumrutas, R. and M. Unsal, *Analysis of solar aided heat pump systems with seasonal thermal energy storage in surface tanks.* Energy (Oxford), 2000. 25(12): p. 1231.
34. Aziz, W., S.K. Chaturvedi, and A. Kheireddine, *Thermodynamic analysis of two-component, two-phase flow in solar collectors with application to a direct expansion solar-assisted heat pump.* Energy, 1999. 24(3): p. 247-259.
35. Cervantes, J.G. and E. Torres-Reyes, *Experiments on a solar-assisted heat pump and an exergy analysis of the system.* Applied Thermal Engineering, 2002. 22(12): p. 1289-1297.
36. Torres Reyes, E., M. Picon Nunez, and J. Cervantes de G, *Exergy analysis and optimization of a solar-assisted heat pump.* Energy, 1998. 23(4): p. 337-344.
37. Torres-Reyes, E., *Optimal performance of an irreversible solar-assisted heat pump.* Exergy, An International Journal, 2001. 1(2): p. 107-111.
38. Torres Reyes, E., M. Picon Nunez, and J. Cervantes de G, *Exergy analysis and optimization of a solar-assisted heat pump.* Energy, 1998. 23(4): p. 337-44.
39. Cervantes, J.G. and E. Torres-Reyes, *Experiments on a solar-assisted heat pump and an exergy analysis of the system.* Applied Thermal Engineering, 2002. 22(12): p. 1289-97.
40. Tong, L.S., *Boiling heat transfer and two-phase flow*. 1965, New York: Jhon wiley and sons, Inc.
41. Chaturvedi, S.K., A.S. Roberts, and V. Mei. *Solar collector as heat pump evaporator*. in *14th Intersociety Energy Conversion Engineering Conference*. 1979. Boston, Mass.: American Chemical Society.
42. Hottel, H. and A. Whillier, *Evaluation of flat-plate solar collector performance*, in *Trans. Conf. Use of Solar Energy ; Vol/Issue: 3 (Thermal Processes) Part 2*. 1955: United States. p. Pages: 74.
43. Spears, R.P. and V.H. Waldin, *ASHRAE 109-A test standard for two-phase solar collectors.* ASHRAE Transcations, 1984: p. 697-706.
44. El-Assy, A.Y. and J.A. Clark, *Thermal analysis of a flat-plate collector in multiphase flows, including superheat.* Solar Energy, 1988. 40(4): p. 345-361.
45. El-Assy, A.Y. and J.A. Clark, *Thermal analysis of a flat-plate boiling collector having sub-cooled inlet and saturated exit states.* Solar Energy, 1989. 42(2): p. 121-132.
46. Freeman, T.L., J.W. Mitchell, and T.E. Audit, *Performance of combined solar-heat pump systems.* Solar Energy, 1979. 22(2): p. 125-135.
47. O'Dell, M.P., J.W. Mitchell, and W.A. Beckman, *Design method and performance of heat pumps with refrigerant filled solar collectors.* Journal of Solar Energy Engineering, 1984. 106(2): p. 159-164.
48. Kishore, V.V.N., M.R. Gandhi, and K.S. Rao, *Analysis of flat-plate collectors charged with phase-changing fluids.* Applied Energy, 1984. 17(2): p. 133-149.
49. Ramos, E., M. Sen, and C. Treviño, *A steady-state analysis for variable area one- and two-phase thermosyphon loops.* International Journal of Heat and Mass Transfer, 1985.

28(9): p. 1711-1719.

50. **Mathur, G.D. and T.W. McDonald, *Simulation program for a two phase thermosyphon loop heat exchanger.* ASHRAE Transcations, 1986. 92: p. 473-485.**
51. **Price, H.W., S.A. Klein, and W.A. Beckman, *Analysis of boiling flat-plate collectors.* Journal Solar Energy Engineering, 1986. 108(2): p. 150-158.**
52. **Yilmaz, T., *Computer simulation of two-phase flow thermosyphon solar water heating system.* Energy Conversion and Management, 1991. 32(2): p. 133-144.**
53. **Morrison, G.L. and D. Gilliaert, *Unglazed solar collector performance characteristics.* Journal of Solar Energy Engineering, 1992. 114(3): p. 194-200.**
54. **Radhwan, A.M. and G.M. Zaki, *Analysis of refrigerant-charged solar collectors with phase change.* Heat Recovery Systems and CHP, 1993. 13(5): p. 429-439.**
55. **Hussein, H.M.S., M.A. Mohamad, and A.S. El- Asfouri, *Transient investigation of a thermosyphon flat-plate solar collector.* Applied Thermal Engineering, 1999. 19(7): p. 789-800.**
56. **Hussein, H.M.S., *Transient investigation of a two phase closed thermosyphon flat plate solar water heater.* Energy Conversion and Management, 2002. 43(18): p. 2479-2492.**
57. **Krakow, K.I. and S. Lin, *A solar source heat pump with refrigerant-cooled solar collectors for cold climates.* International Journal of Refrigeration, 1983. 6(1): p. 20-33.**
58. **Chaturvedi, S.K. and M. Abazeri, *Transient simulation of a capacity-modulated direct expansion, solar-assisted heat pump.* Solar Energy, 1987. 39(5): p. 421-428.**
59. **Krush, E.A., *Performance of heat pump at elevated evaporationg temperatures with application to solar input.* Journal of solar energy engineering, 1980. 102: p. 203-210.**
60. **Shinobu, Y. and K. Matsuki. *Recent technical trends in direct expansion solar heat pump systems.* in *3rd International Energy Agency Heat Pump Conference*. 1990. Tokyo, Japan.**
61. **Ito, S., *Heat pumps with direct expansion solar collectors.* Transcations of the Japanese Association of Refrigeration, 1992. 9(2): p. 101-115.**
62. **Pluta, Z. and W. Pomierny, *The theoretical and experimental investigation of the phase-change solar thermosyphon.* Renewable Energy, 1995. 6(3): p. 317-321.**
63. **Day, A.R. and T.G. Karayiammis, *Solar-assisted heat pump research and development.* Building Services Engineering Research and Technology, 1994. 15: p. 71-88.**
64. **Ito, S., N. Miura, and K. Wang, *Performance of a heat pump using direct expansion solar collectors.* Solar Energy, 1999. 65(3): p. 189-196.**
65. **Joudi, K.A. and A.A. Al-Tabbakh, *Computer simulation of a two phase thermosyphon solar domestic hot water heating system.* Energy Conversion and Management, 1999. 40(7): p. 775-793.**
66. **Weisman, J., et al., *Effects of fluid properties and pipe diameter on two-phase flow patterns in horizontal lines.* International Journal Multiphase Flow, 1979. 5: p. 437-462.**
67. **Pool, R., *The elusive replacements for CFCs.* Science, 1988. 242(4879): p. 666-668.**
68. ***Montreal protocol on substances that deplete the ozone layer.* in *United Nations Conference*. 1987.**
69. **Eckels, S.J. and M.B. Pate, *An experimental comparison of evaporation and condensation heat transfer coefficients for HFC-134a and CFC-12.* International Journal of Refrigeration, 1991. 14(2): p. 70-77.**
70. **Hambraeus, K., *Heat transfer coefficient during two-phase flow boiling of HFC-134a. .* International Journal of Refrigeration-Revue Internationale du Froid., 1991. 14(6): p. 357-362.**
71. **Torikoshi, K., K. Kawabata, and T. Ebisu. *Heat transfer and pressure drop characteristics of R134a in a horizontal heat transfer tube.* in *1992 International Refrigeration Conference*. 1992.**
72. **Torikoshi, K. and T. Ebisu, *Heat transfer and pressure drop characteristics of R134a, R32, and a mixture of R32/R134a inside a tube.* ASHRAE Transcations, 1993. 99(2): p. 90-96.**
73. **Wattlet, J.P., et al., *Evaporative characteristics of R-134a, MP-39, and R-12 at low mass fluxes.* ASHRAE Transactions, 1994. 1: p. 603-615.**
74. **Murata, K. and K. Hashizume, *Forced convective boiling of nonazeotropic refrigerant mixtures inside tubes.* Transcations of the ASME. Journal of Heat Transfer, 1993. 115(3): p. 680-689.**
75. **Kim, Y. and D.L. O'Neal, *The effect of oil on the two-phase critical flow of Refrigerant 134a***

through short tube orifices. International Journal of Heat and Mass Transfer, 1994. 37(9): p. 1377-1385.

76. Kim, Y. and D.L. O'Neal, *A semi-empirical model of two-phase flow of refrigerant-134a through short tube orifices.* Experimental Thermal and Fluid Science, 1994. 9(4): p. 426-435.
77. Bassi, R. and P.K. Bansal, *In-tube condensation of mixture of R134a and ester oil: empirical correlations.* International Journal of Refrigeration, 2003. 26(4): p. 402-409.
78. Liu, X., *Condensing and evaporating heat transfer and pressure drop characteristics of HFC-134a and HCFC-22.* Journal of Heat Transfer, 1997. 119(1): p. 158-163.
79. Natan, S., D. Barnea, and Y. Taitel, *Direct steam generation in parallel pipes.* International Journal of Multiphase Flow, 2003. 29(11): p. 1669-1683.
80. Minzer, U., D. Barnea, and Y. Taitel, *Evaporation in parallel pipes--splitting characteristics.* International Journal of Multiphase Flow, 2004. 30(7-8): p. 763-777.
81. Choi, J., J.T. Chung, and Y. Kim, *A generalized correlation for two-phase flow of alternative refrigerants through short tube orifices.* International Journal of Refrigeration, 2004. 27(4): p. 393-400.
82. Abou-Ziyan, H.Z., et al., *Solar-assisted R22 and R134a heat pump systems for low-temperature applications.* Applied Thermal Engineering, 1997. 17(5): p. 455-469.
83. Esen, M. and H. Esen, *Experimental investigation of a two-phase closed thermosyphon solar water heater.* Solar Energy, 2005.
84. MO, M., *NIST ''REFPROP'' Code, Version 6.01.* 1998, U.S. Department of Commerce, .
85. Wijeysundera, N.E. and J.C. Ho, *Comparison of optimization criteria for solar heating and some energy conservation measures.* Energy Conversion and Management, 1985. 25(3): p. 331-7.
86. Barley, C.D. and C.B. Winn, *OPTIMAL SIZING OF SOLAR COLLECTORS BY THE METHOD OF RELATIVE AREAS.* Solar Energy, 1978. 21(4): p. 279-289.
87. Brandemuehl, M.J. and W.A. Beckman, *Economic evaluation and optimization of solar heating systems.* Solar Energy, 1979. 23(1): p. 1-10.
88. Lunde, P.J., *A simplified approach to economic analysis of solar heating and hot water systems and conservation measures.* Solar Energy, 1982. 28(3): p. 197-203.
89. Chang, H.K. and A. Minardi, *An optimization formulation for solar heating systems.* Solar Energy, 1980. 24(1): p. 99-103.
90. Michelson, E., *Multivariate optimization of a solar water heating system using the Simplex method.* Solar Energy, 1982. 29(2): p. 89-99.
91. Boer, K.W., *Payback of solar systems.* Solar Energy, 1978. 20(3): p. 225-32.
92. Gordon, J.M. and A. Rabl, *Design, analysis and optimization of solar industrial process heat plants without storage.* Solar Energy, 1982. 28(6): p. 519-30.
93. El-Nashar, A.M., *Economics of small solar-assisted multiple-effect stack distillation plants.* Desalination, 2000. 130(3): p. 201-215.
94. Hawlader, M.N.A., et al., *Economic evaluation of a solar water heating system.* Energy Conversion and Management, 1987. 27(2): p. 197-204.
95. Mills, D. and G.L. Morrison, *Optimisation of minimum backup solar water heating system.* Solar Energy, 2003. 74(6): p. 505-511.
96. Kalogirou, S.A., *Optimization of solar systems using artificial neural-networks and genetic algorithms.* Applied Energy, 2004. 77(4): p. 383-405.
97. Kulkarni, G.N., S.B. Kedare, and S. Bandyopadhyay, *Determination of design space and optimization of solar water heating systems.* Solar Energy, 2007. 81(8): p. 958-68.
98. Waje, S.S., B.N. Thorat, and A.S. Mujumdar, *An experimental study of the thermal performance of a screw conveyor dryer.* Drying Technology, 2006. 24(3): p. 293-301.
99. Braun, J.E., P.K. Bansal, and E.A. Groll, *Energy efficiency analysis of air cycle heat pump dryers.* International Journal of Refrigeration, 2002. 25(7): p. 954-65.
100. Conde, M.R., *Energy conservation with tumbler drying in laundries.* Applied Thermal Engineering, 1997. 17(12): p. 1163-72.
101. Sharma, V.K., A. Colangelo, and G. Spagna, *Experimental investigation of different solar dryers suitable for fruit and vegetable drying.* Renewable Energy, 1995. 6(4): p. 413-24.
102. Oktay, Z. and A. Hepbasli, *Performance evaluation of a heat pump assisted mechanical opener dryer.* Energy Conversion and Management, 2003. 44(8): p. 1193-1207.
103. Pendyala, V.R., S. Devotta, and V.S. Patwardhan, *Heat-pump-assisted dryer part 1.*

Mathematical model. **International Journal of Energy Research, 1990. 14(5): p. 479-492.**

104. Pendyala, V.R., S. Devotta, and V.S. Patwardhan, *Heat-pump-assisted dryer part 2. Experimental study.* International Journal of Energy Research, 1990. 14(5): p. 493-507.

105. Chou, S.K., et al., *Performance of a heat-pump assisted dryer.* International Journal of Energy Research, 1994. 18(6): p. 605-622.

106. Best, R., et al., *Evaluation of a rice drying system using a solar assisted heat pump.* Renewable Energy, 1994. 5(1-4 pt 1): p. 465-468.

107. Best, R., et al., *Experimental results of a solar assisted heat pump rice drying system.* Renewable Energy, 1996. 9(1-4): p. 690-694.

108. Florides, G.A., et al., *Review of solar and low energy cooling technologies for buildings.* Renewable and Sustainable Energy Reviews, 2002. 6(6): p. 557-572.

109. Tsoutsos, T., et al., *Solar cooling technologies in Greece. An economic viability analysis.* Applied Thermal Engineering, 2003. 23(11): p. 1427-1439.

110. Tleimat, B.W. and E.D. Howe, *Solar-assisted heat pump system for heating and cooling residences.* Solar Energy, 1978. 21(1): p. 45-54.

111. Khankari, K.K., S.V. Patankar, and R.V. Morey, *Mathematical model for natural convection moisture migration in stored grain.* Transactions of the ASAE, 1995. 38(6): p. 1777-1787.

112. Hawlader, M.N.A., T.Y. Bong, and W. Mahmood, *A method of estimating monthly global radiation for Singapore.* International Journal of Solar Energy, 1988. 5(5-6): p. 279-88.

113. Parsons, R.A., *1995 ASHRAE Handbook: HVAC Applications*. 1995: ASHRAE.

114. Moddiat, R.J., *Describing the uncertainties in experimental results.* Experimental and thermal fluid science, 1988. 1: p. 3-37.

115. Prasertsan, S. Saen-Saby, P. Ngamsritrakul P. and Prateepchaikul, G. Heat pump dryer part 3: Experiment verification of the simulation. International journal of energy research, 1997. Volume 21, p.707-722,

Appendix-A

Coefficients for meteorological data correlation, as indicated in equ. 4.11

Table A.1. Solar radiation coefficients

	January	February	March	April	May	June
a0	1.39E+01	26.299	33.092	2.14E+01	7.55E+00	7.73E+00
a1	-7.0314	-12.174	-15.784	-1.05E+01	-4.26E+00	-4.15E+00
a2	1.1914	2.0026	2.7158	1.82E+00	7.45E-01	6.99E-01
a3	-0.08239	-1.44E-01	-2.09E-01	-1.36E-01	-4.89E-02	-4.36E-02
a4	2.37E-03	4.60E-03	7.37E-03	4.55E-03	1.15E-03	9.13E-04
a5	-2.17E-05	-5.34E-05	-9.76E-05	-5.53E-05	-4.16E-06	-2.94E-07
a6	0	0	0	0	0	0
a7	0	0	0	0	0	0
	July	August	September	October	November	December
a0	3.04E+00	6.58E+00	-4.18E+00	2.11E+01	1.56E+01	1.68E+01
a1	-2.20E+00	-3.82E+00	1.01E+00	-1.03E+01	-8.45E+00	-8.52E+00
a2	3.89E-01	6.74E-01	-1.69E-01	1.77E+00	1.59E+00	1.50E+00
a3	-2.06E-02	-4.46E-02	2.73E-02	-1.33E-01	-1.31E-01	-1.12E-01
a4	1.19E-04	1.10E-03	-1.89E-03	4.48E-03	4.86E-03	3.71E-03
a5	9.64E-06	-5.90E-06	4.24E-05	-5.47E-05	-6.78E-05	-4.39E-05
a6	0	0	0	0	0	0
a7	0	0	0	0	0	0

Table A.2. Temperature coefficients

	January	February	March	April	May	June
a0	2.20E+01	2.21E+01	2.19E+01	2.28E+01	2.40E+01	2.41E+01
a1	2.93E+00	3.35E+00	4.58E+00	3.95E+00	3.08E+00	2.63E+00
a2	-1.39E+00	-1.59E+00	-2.21E+00	-1.98E+00	-1.60E+00	-1.37E+00
a3	2.53E-01	2.92E-01	4.29E-01	3.96E-01	3.22E-01	2.75E-01
a4	-2.01E-02	-2.37E-02	-3.88E-02	-3.68E-02	-2.99E-02	-2.51E-02
a5	7.31E-04	9.10E-04	1.78E-03	1.74E-03	1.40E-03	1.15E-03
a6	-1.07E-05	-1.51E-05	-3.99E-05	-4.08E-05	-3.24E-05	-2.60E-05
a7	2.66E-08	6.79E-08	3.48E-07	3.77E-07	2.94E-07	2.27E-07
	July	August	September	October	November	December
a0	2.40E+01	2.44E+01	2.34E+01	2.30E+01	2.20E+01	2.21E+01
a1	2.26E+00	1.90E+00	2.93E+00	3.28E+00	3.79E+00	3.06E+00
a2	-1.19E+00	-1.04E+00	-1.52E+00	-1.72E+00	-1.92E+00	-1.47E+00
a3	2.43E-01	2.15E-01	3.09E-01	3.51E-01	3.92E-01	2.81E-01
a4	-2.27E-02	-2.01E-02	-2.09E-02	-3.31E-02	-3.75E-02	-2.44E-02
a5	1.07E-03	9.50E-04	1.39E-03	1.57E-03	1.83E-03	1.04E-03
a6	-2.52E-05	-2.22E-05	-3.31E-05	-3.68E-05	-4.46E-05	-2.07E-05
a7	2.36E-07	2.07E-07	3.14E-07	3.38E-07	4.28E-07	1.49E-07

Table A.3. Wind speed coefficients

	January	February	March	April	May	June
a0	6.42E-01	3.43E-01	7.62E-01	3.63E-01	1.24E-01	2.54E-01
a1	2.13E+00	1.94E+00	6.40E-01	2.06E-01	7.65E-01	5.56E-01
a2	-1.04E+00	-9.27E-01	-3.53E-01	-2.50E-02	-3.54E-01	-2.03E-01
a3	2.12E-01	1.82E-01	6.73E-02	-1.18E-02	6.38E-02	2.54E-02
a4	-2.08E-02	-1.68E-02	-5.34E-03	3.63E-03	-4.61E-03	-7.21E-06
a5	1.07E-03	8.07E-04	1.98E-04	-3.33E-04	1.26E-04	-1.57E-04
a6	-2.78E-05	-1.92E-05	-3.31E-06	1.25E-05	-1.37E-07	8.51E-06
a7	2.93E-07	1.92E-07	1.89E-08	-1.69E-07	-3.11E-08	-1.35E-07
	July	August	September	October	November	December
a0	3.71E-02	1.11E-01	1.56E-01	-8.62E-02	3.92E-01	8.28E-01
a1	1.34E+00	1.23E+00	8.69E-01	9.79E-01	1.02E+00	1.62E+00
a2	-6.22E-01	-6.11E-01	-3.52E-01	-3.62E-01	-4.85E-01	-8.49E-01
a3	1.15E-01	1.21E-01	5.45E-02	4.88E-02	9.06E-02	1.76E-01
a4	-9.50E-03	-1.08E-02	-2.77E-03	-1.50E-03	-7.55E-04	-1.70E-02
a5	3.71E-04	4.72E-04	-2.11E-05	-1.20E-04	2.99E-04	8.37E-04
a6	-6.34E-06	-9.83E-06	5.18E-07	8.53E-06	-5.25E-06	-2.06E-05
a7	-1.35E-07	7.65E-08	-1.03E-07	-1.45E-07	2.80E-08	2.03E-07

Appendix-B

Numerical solution of PDE using Crank-Nicholson method

The governing equations of the energy balance on the evaporator collector subject to an initial condition and four boundary conditions are given in the previous chapter. This is to be solved numerically using Crank-Nicholson method.

1. Finite difference approximation for PDE for the interior area of collector.

The partial differential equation for the interior area of collector is expressed as

$$\frac{q_u}{k\delta}+\frac{\partial^2 T}{\partial x^2}+\frac{\partial^2 T}{\partial y^2}=\frac{\rho c_p}{k}\frac{\partial T}{\partial t} \tag{B.1}$$

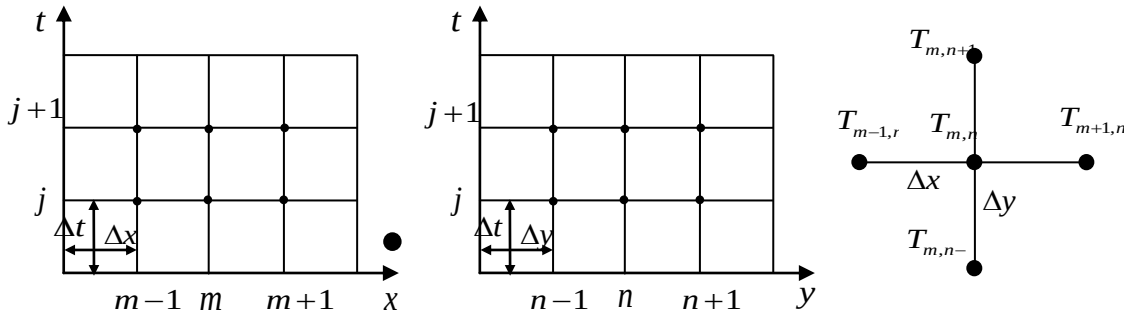

Figure B.1 Graphical form of Crank Nicholson method

Crank-Nicholson method is to consider partial differential equation (PDE) as being satisfied at the midpoint of j and j+1 as shown in Fig 1. Using Crank-Nicholson method, the following terms are expressed as:

$$\frac{\partial^2 T}{\partial x^2}=\frac{1}{2}\left(\left.\frac{\partial^2 T}{\partial x^2}\right|^{j}+\left.\frac{\partial^2 T}{\partial x^2}\right|^{j+1}\right)=\frac{1}{2}\left(\frac{T^{j}_{m+1,n}+T^{j}_{m-1,n}-2T^{j}_{m,n}}{\Delta x^2}+\frac{T^{j+1}_{m+1,n}+T^{j+1}_{m-1,n}-2T^{j+1}_{m,n}}{\Delta x^2}\right)$$

$$\frac{\partial^2 T}{\partial y^2}=\frac{1}{2}\left(\frac{T^{j}_{m,n+1}+T^{j}_{m,n-1}-2T^{j}_{m,n}}{\Delta y^2}+\frac{T^{j+1}_{m,n+1}+T^{j+1}_{m,n-1}-2T^{j+1}_{m,n}}{\Delta y^2}\right)$$

$$T=\frac{1}{2}\left(T^{j+1}+T^{j}\right)$$

$$\frac{\partial T}{\partial t}=\frac{T^{j+1}-T^{j}}{\Delta t}$$

Substituting these terms into equation (B.1), gives

$$\begin{aligned}&\frac{U_L}{2}T_{m,n}^{j+1}-\frac{r}{2}\left(T_{m+1,n}^{j+1}+T_{m-1,n}^{j+1}+T_{m,n+1}^{j+1}+T_{m,n-1}^{j+1}-4T_{m,n}^{j+1}\right)+pT_{m,n}^{j+1}\\&=S-U_L\left(\frac{1}{2}T_{m,n}^{j}-T_a\right)+\frac{r}{2}\left(T_{m+1,n}^{j}+T_{m-1,n}^{j}+T_{m,n+1}^{j}+T_{m,n-1}^{j}-4T_{m,n}^{j}\right)+pT_{m,n}^{j}\end{aligned} \tag{B.2}$$

Where, we define: $r=\frac{k\delta}{\Delta x^2}=\frac{k\delta}{\Delta y^2}$, and $p=\frac{\rho c\delta}{\Delta t}$

Rearrangement of this equation gives

$$\begin{aligned}&T_{m,n-1}^{j+1}+T_{m-1,n}^{j+1}+T_{m+1,n}^{j+1}+T_{m,n+1}^{j+1}+\left(-4-\frac{U_L}{r}-\frac{2p}{r}\right)T_{m,n}^{j+1}\\&=-\left(T_{m,n-1}^{j}+T_{m-1,n}^{j}+T_{m+1,n}^{j}+T_{m,n+1}^{j}\right)+\left(4+\frac{U_L}{r}-\frac{2p}{r}\right)T_{m,n}^{j}-\frac{2}{r}\left(S+U_LT_a\right)\end{aligned} \tag{B.3}$$

Equation (B.3) is the finite difference approximation of the governing equation [1]

2. Finite difference approximation for boundary conditions

The partial differential equation for the boundary at $y=0$ and $0<x<\frac{(W-D)}{2}$ is expressed as:

$$\frac{q_u}{k\delta}+\frac{\partial^2T}{\partial x^2}-\frac{2}{k\Delta y}U_L\left(T-T_a\right)+\frac{2}{\Delta y}\frac{\partial T}{\partial y}=\frac{\rho c_p}{k}\frac{\partial T}{\partial t} \tag{B.4}$$

Using Crank-Nicholson method, the following terms are expressed as:

$$\frac{\partial^2T}{\partial x^2}=\frac{1}{2}\left(\frac{T_{m+1,n}^{j}+T_{m-1,n}^{j}-2T_{m,n}^{j}}{\Delta x^2}+\frac{T_{m+1,n}^{j+1}+T_{m-1,n}^{j+1}-2T_{m,n}^{j+1}}{\Delta x^2}\right)$$

$$T=\frac{1}{2}\left(T^{j+1}+T^{j}\right)$$

$$\frac{\partial T}{\partial y}=\frac{T_{m,n+1}^{j}-T_{m,n}^{j}}{\Delta y}$$

$$\frac{\partial T}{\partial t}=\frac{T^{j+1}-T^{j}}{\Delta t}$$

Substituting these terms into equation (B.4), gives

$$T_{m-1,n}^{j+1}+T_{m+1,n}^{j+1}+\left[-2-\frac{U_L}{r}\left(1+\frac{2\delta}{\Delta y}\right)-\frac{2p}{r}\right]T_{m,n}^{j+1}$$
$$=-\left(T_{m-1,n}^{j}+T_{m+1,n}^{j}+2T_{m,n+1}^{j}\right)+\left[4+\frac{U_L}{r}\left(1+\frac{2\delta}{\Delta y}\right)-\frac{2p}{r}\right]T_{m,n}^{j}-\frac{2}{r}\left(S+U_L T_a\right) \quad \text{(B.5)}$$

Similarly, at $y=L$ and $0<x<\frac{(W-D)}{2}$

$$\frac{\partial T}{\partial y}=\frac{\left(T_{m,n}-T_{m,n-1}\right)}{\Delta y}$$

The partial differential equation (B.1) can be written as:

$$T_{m-1,n}^{j+1}+T_{m+1,n}^{j+1}+\left[-2-\frac{U_L}{r}\left(1+\frac{2\delta}{\Delta y}\right)-\frac{2p}{r}\right]T_{m,n}^{j+1}$$
$$=-\left(T_{m-1,n}^{j}+T_{m+1,n}^{j}+2T_{m,n-1}^{j}\right)+\left[4+\frac{U_L}{r}\left(1+\frac{2\delta}{\Delta y}\right)-\frac{2p}{r}\right]T_{m,n}^{j}-\frac{2}{r}\left(S+U_L T_a\right) \quad \text{(B.6)}$$

At $x=0$ and $0<y<L$, partial differential equation is expressed as:

$$\frac{q_u}{k\delta}+\frac{\partial^2 T}{\partial y^2}-\frac{2}{\Delta x}\frac{\partial T}{\partial x}=\frac{\rho c_p}{k}\frac{\partial T}{\partial t} \quad \text{(B.7)}$$

Use Crank-Nicholson method to write it in finite difference approximation form:

$$T_{m,n-1}^{j+1}+T_{m,n+1}^{j+1}+2T_{m+1,n}^{j+1}+\left(-4-\frac{U_L}{r}-\frac{2p}{r}\right)T_{m,n}^{j+1}$$
$$=-\left(T_{m,n-1}^{j}+T_{m,n+1}^{j}+2T_{m+1,n}^{j}\right)+\left(4+\frac{U_L}{r}-\frac{2p}{r}\right)T_{m,n}^{j}-\frac{2}{r}\left(S+U_L T_a\right) \quad \text{(B.8)}$$

At $x=\frac{(W-D)}{2}$ and $0<y<L$, partial differential equation is expressed as:

$$\frac{q_u}{k\delta}-\frac{2}{D}\frac{\partial T}{\partial x}-\frac{\left(T-T_f\right)}{k\delta D\left(\frac{1}{h_{fi}\pi D_i}+\frac{1}{C_b}\right)}=\frac{\rho c_p}{k}\frac{\partial T}{\partial t} \quad \text{(B.9)}$$

Using Crank-Nicholson method, the following terms are expressed as:

$$T = \frac{1}{2}\left(T^{j+1} + T^{j}\right)$$

$$\frac{\partial T}{\partial x} = \frac{T^{j}_{m,n} - T^{j}_{m-1,n}}{\Delta x}$$

$$\frac{\partial T}{\partial t} = \frac{T^{j+1} - T^{j}}{\Delta t}$$

Substituting these terms into equation (B.9), gives

$$\left(2p + U_L + \phi\right)T^{j+1}_{m,n} = \left(2p - U_L - 4r\frac{\Delta x}{D} - \frac{\phi}{D}\right)T^{j}_{m,n} + 4r\frac{\Delta x}{D}T^{j}_{m-1,n} + 2\left(S + U_L T_a + \frac{\phi}{D}T_f\right) \quad \text{(B.10)}$$

Where $\phi = \dfrac{1}{\dfrac{1}{h_{fi}\pi D_i} + \dfrac{1}{C_b}}$

Appendix-C

EXPERIMENTAL RESULTS

Table C.1. Experimental results plotted in Figure 5.1.1.1 and Figure 5.1.1.2

Time, min	Inlet Refrigerant, ℃	Outlet Refrigerant, ℃	Water in the tank, ℃	Energy released from refrigerant, KW	Energy absorbed by water, kW
0	91.5	33.8	33.0	12.4	11.6
5	89.1	37.3	35.1	12.1	11.4
10	90.1	40.5	37.1	11.9	10.5
15	90.9	44.3	39.0	11.7	10.4
20	91.0	45.2	40.9	11.6	10.5
25	91.2	45.8	42.7	11.6	10.1
30	91.9	51.2	44.5	11.3	10.6
35	92.1	53.3	46.4	11.1	10.8
40	92.6	54.2	48.3	11.1	9.8
45	93.8	58.3	50.1	10.9	10.6
50	93.5	57.3	52.0	10.9	10.4
55	95.1	61.2	53.8	10.8	9.1
60	94.2	63.2	55.5	10.6	9.1
65	93.9	64.6	57.1	10.5	8.6
70	94.3	66.9	58.6	10.4	7.6
75	94.0	68.7	60.0	10.3	7.9

Table C.2. Experimental results plotted in Figure 5.1.1.3

Time, min	Inlet Refrigerant, ℃	Inlet Air, ℃	Heated Air, ℃	Condensing heat, KW
0	33.8	33.3	33.7	0.1
5	37.3	31.7	33.3	0.4
10	40.5	31.7	33.3	0.7
15	44.3	32.5	33.9	1.0
20	45.2	32.2	34.0	1.1
25	45.8	31.8	34.0	1.2
30	51.2	31.3	34.0	1.7
35	53.3	32.3	35.2	1.9
40	54.2	32.1	34.7	2.0
45	58.3	31.0	35.7	2.4
50	57.3	31.5	36.1	2.3
55	61.2	33.0	37.1	2.6

60	63.2	32.8	38.1	2.8
65	64.6	31.4	38.5	3.0
70	66.9	31.7	39.5	3.2
75	68.0	32.8	39.8	3.1

Table C.3. Experimental results plotted in Figure 5.1.1.4

Time, min	Inlet Air, ℃	Heated Air, ℃	Discharged Air, ℃	Moisture Content, kg
0	30.8	34.2	27.9	1.00
5	29.7	35.9	28.5	0.81
10	30.2	35.4	28.7	0.66
15	30.3	35.7	28.9	0.54
20	30.9	35.6	28.3	0.46
25	29.3	35.3	28.7	0.39
30	30.0	36.1	29.0	0.30
35	30.1	35.4	29.6	0.23
40	29.6	35.7	30.5	0.17
45	29.4	35.0	31.4	0.11
50	30.5	35.2	32.0	0.09
55	30.1	36.4	33.3	0.08
60	30.3	34.8	32.8	0.07

Table C.4. Experimental results plotted in Figure 5.1.1.6

Time, min	Ambient temperature, ℃	Room temperature, ℃	Outlet refrigerant, ℃
0	28.0	26.3	23.9
5	29.2	25.4	23.3
10	29.9	24.5	22.1
15	30.1	23.6	21.2
20	30.0	23.5	20.8
25	30.1	23.0	20.1
30	29.9	22.4	19.4
35	29.8	22.2	18.0
40	30.8	21.6	17.6
45	30.4	21.3	14.7
50	30.2	21.1	16.0
55	30.6	20.5	13.8
60	29.6	20.2	13.8
65	31.1	19.7	12.8
70	30.9	19.6	11.3

75	30.7	19.5	12.9
80	29.7	19.3	12.1

Table C.5. Experimental results plotted in Figure 5.1.1.9

Time	Solar Radiation, W/m^2	Plate 1 surface, ℃	Plate 2 surface, ℃
10:00	372.2	6.9	7.9
10:20	201.4	6.8	7.8
10:40	476.2	9.4	13.0
11:00	709.4	10.3	10.4
11:20	337.8	6.8	9.5
11:40	665.2	11.0	12.8
12:00	805.1	13.8	15.7
12:20	898.0	13.1	16.8
12:40	922.0	14.4	16.1
13:00	949.8	15.7	16.8
13:20	934.8	15.7	17.8
13:40	893.0	14.3	16.3
14:00	853.1	14.0	14.8
14:20	783.7	13.4	15.4
14:40	628.2	12.1	16.3
15:00	346.7	6.7	8.7
15:20	497.0	7.4	14.1
15:40	422.4	9.8	12.6
16:00	330.4	7.6	13.0

Appendix-D

CALIBRATION CHART AND EQUATIONS

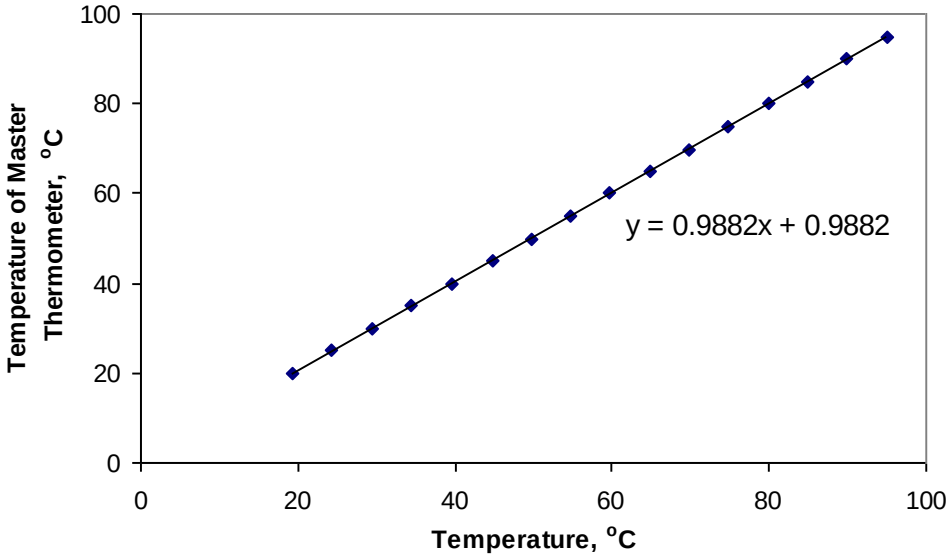

Figure D.1. Thermocouple calibration

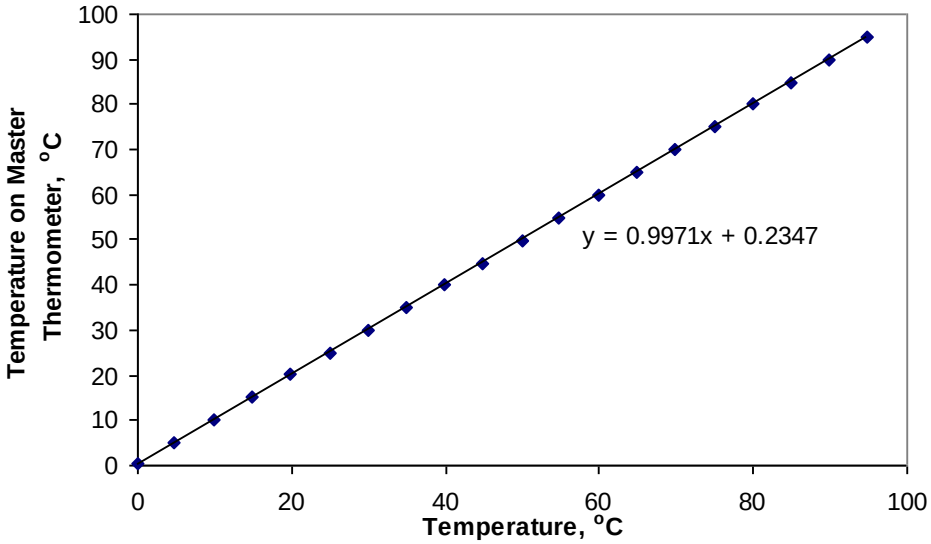

Figure D.2. Thermo probe calibration

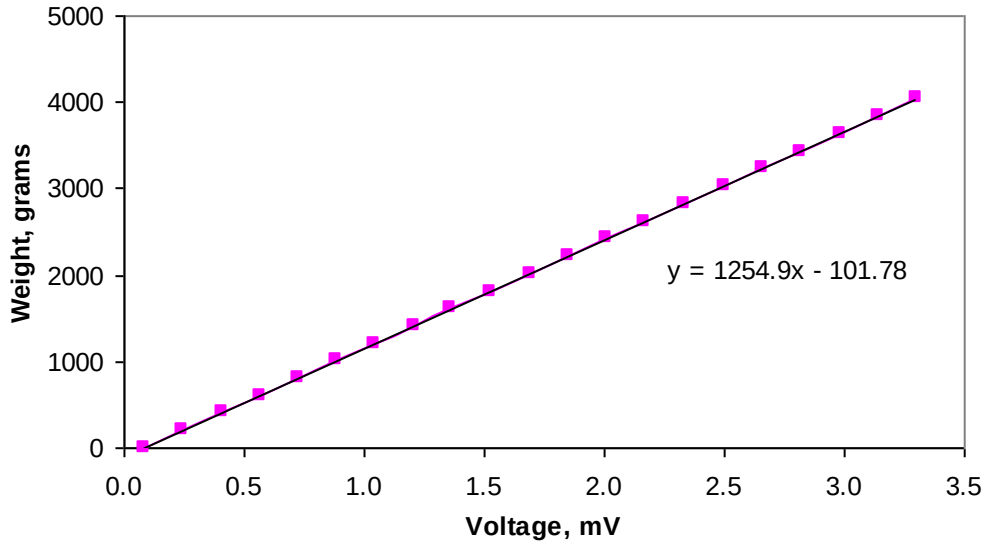

Figure D.3. Load cell calibration chart

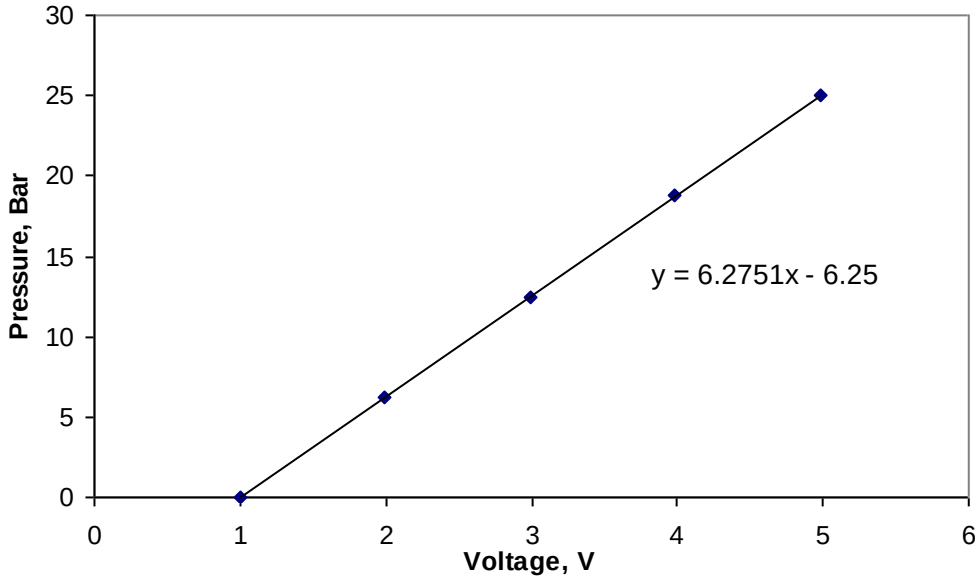

Figure D.4. Pressure transducer calibration chart

Appendix-E

APPENDIX E Error analysis

The thermal performance of the system has been investigated in a test rig in Singapore. In this analysis, collector efficiency and coefficient of performance are two critical parameters. Thus, an error analysis for collector efficiency and COP has been undertaken based on Moffiat' s equation of uncertainty in result [114]. A sample calculation of errors attached to collector efficiency η_c is presented here and all errors are tabulated in Table E-1

The following error is based on the condition of compressor speed=700RPM, collector area=3m^2. Based on Moffiat's equation of uncertainty in result,

$$\partial R = \left[\sum \left(\frac{\partial DIP}{\partial X_i} \partial X_i \right)^2 \right]^{\frac{1}{2}}$$

Where, $\frac{\partial DIP}{\partial X_i}$ stands for the partial derivative of the entire set of equations (DIP) with respect to the variables X_i.

Sample calculation of the efficiency $\partial \eta_c$:

$$\partial \eta_c = \frac{\dot{m}(h_1 - h_4)}{A_c I(\tau\alpha)}$$

With respect to the specifications of each of the instruments, the major errors are shown below.

Table E.1. Tabulation of instrument error

Instrument	∂X
Pyranometoer, S	$\partial S = \pm 1$ W/m^2
Flowmeter, $\dot{m}$	$\partial m = \pm 0.01$ kg/s
Thermocouple, T	$\partial T = \pm 0.2$ ℃
Pressure transducer, P	$\partial P = \pm 0.25$ N/m

For experiment 1, collector inlet temperature, T=5 ^{o}C, collector outlet temperature, T=40 ^{o}C, collector inlet pressure, P=0.4 MPa, collector outlet pressure, P=0.35 MPa, collector inlet enthalpy, h=248 kJ/kg, collector outlet enthalpy, h=419 kJ/kg, mass flow rate m= 0.025 kg/s.

Table E.2. Tabulation of various errors

Values	Errors
η_c	0.89 ±2.1%
COP	6.48±4.9%

Appendix-F

APPENDIX F Property equations of refrigerant R134a

Saturated Temperature

$$T_{sat} = \frac{-2200.9809}{\ln(P) - 21.51297} - 246.61$$

Saturated liquid enthalpy:

$$H_l = 2\times10^5 + 1335.29\times T_{sat} + 1.7065\times T_{sat}^2 + 7.674\times10^{-3}\times T_{sat}^3$$

Saturated vapor enthalpy

$$H_v = 149048 + 249455 + 606.163\times T_{sat} + 1.05644\times T_{sat}^2 - 1.82426\times10^{-2}\times T_{sat}^3$$

Density of saturated liquid refrigerant

$$\rho_l = 1293.7 - 3.264\times T_{sat} - 3\times T_{sat}^2 - 5.21\times10^{-5}\times T_{sat}^3$$

Specific Volume of saturated vapor refrigerant

$$v_v = \frac{1}{\rho_l} = e^{\left(-12.4539 + \frac{2669}{273.15+T_{sat}}\right)}\begin{pmatrix} 1.101357 + 1.06736\times10^{-3}\times T_{sat} \\ -9.2532\times10^{-6}\times T_{sat}^2 - 3.2\times10^{-7}\times T_{sat}^3 \end{pmatrix}$$

Viscosity of saturated liquid refrigerant

$$\mu_l = 3\times10^{-4} - 6\times T_{sat} + 3\times10^{-8}\times T_{sat}^2 - 2\times10^{-10}\times T_{sat}^3 + 5\times10^{-13}\times T_{sat}^4$$

Viscosity of saturated vapor refrigerant

$$\mu_v = \left(575.67\times T_{sat}^{0.5} - 3.619\right)\times10^{-8}$$

Specific heat of saturated liquid refrigerant

$$Cp_l = 1311.6 + 6.018\times T_{sat} - 0.0972\times T_{sat}^2 + 0.0016\times T_{sat}^3$$

Specific heat of saturated vapor refrigerant

$$Cp_v = -5.2575\times10^{-3} + 3.2966\times10^{-3}\times T_{sat} - 2.0173\times10^{-6}\times T_{sat}^2 + 15.8217\times T_{sat}^{-1}$$

Thermal conductivity of saturated liquid refrigerant

$$k_l = 0.0934 - 5\times10^{-4}\times T_{sat} - 4\times10^{-7}\times T_{sat}^2 + 2\times10^{-8}\times T_{sat}^3 + 2\times10^{-10}\times T_{sat}^4 + 1\times10^{-10}\times T_{sat}^5$$

Thermal conductivity of saturated vapor refrigerant

$$k_v = 2.9742 - 0.17962\times T_{sat} - 0.4265\times10^{-3}\times T_{sat}^2$$

Appendix-G

Pressure-Enthalpy Diagram for Refrigerant R134a